University of Bath

UNIVERSITY OF BATH

PHD

Deactivation of PtH-ZSM-5 Bifunctional Catalysts by Coke Formation during Benzene Alkylation with Ethane

Chua, Li Min

Award date:
2010

Awarding institution:
University of Bath

Link to publication

Deactivation of PtH-ZSM-5 Bifunctional Catalysts by Coke Formation during Benzene Alkylation with Ethane

Li Min Chua

A thesis submitted for the degree of Doctor of Philosophy

University of Bath

Department of Chemical Engineering

March 2010

Acknowledgements

Abstract

The alkylation of benzene with ethane was studied at 370 $^{\circ}$C over two Pt-containing ZSM-5 catalysts with SiO_2/Al_2O_3 ratios of 30 and 80. While the benzene and ethane conversion decreased with time-on-stream for the PtH-ZSM-5(30) catalyst, the PtH-ZSM-5(80) catalyst demonstrated a stable performance. The deactivation of the PtH-ZSM-5(30) catalyst was found to be more significant, when compared to the PtH-ZSM-5(80) catalyst as a result of differences in the formation of coke. Results from gas sorption and x-ray diffraction experiments showed that coke is preferentially formed within the channel segments of the PtH-ZSM-5(30) catalyst as opposed to coke deposition on the outside surface of the PtH-ZSM-5(80) crystallites, subsequently blocking entrance to the zeolite channels.

The location of the coke deposition was found to affect the product selectivity of the two PtH-ZSM-5 catalysts. The accessibility functions, derived from nitrogen and argon sorption data, suggested that, with prolonged time-on-stream, the coke molecules build up from the middle of the zeolite crystallites outwards towards the surface, as the reaction was carried out over the PtH-ZSM-5(30) catalyst. Partial blockage of the internal pore structure of the PtH-ZSM-5(30) catalyst decreased the diffusion length within the crystallites. In contrast to the typical effect of coking, where the selectivity of *para-* isomers would be enhanced with coke deposition, the effect of the reduction in the diffusion length of the PtH-ZSM-5(30) crystallites is consistent with the decreasing *para*-selectivity of the diethylbenzene (DEB) isomers with time-on-stream.

An investigation of the causes of coke locations was conducted, and the results suggested that, the spatial distribution of Pt metal was responsible for the different locations of coke observed. Surface reactions initiated coking in the intercrystalline region of the PtH-ZSM-5(80) catalyst, as the Pt particles on the surface of the PtH-ZSM-5(80) crystallites increased the difficulty of access for reactants to the interior of the crystallites. Within the PtH-ZSM-5(30) catalyst, ethane dehydrogenation and benzene alkylation took place in the micropore network as a result of preferential intracrystalline deposition of Pt metal. Further conversions on the active sites within the PtH-ZSM-5(30) crystallites thus lead intracrystalline coking.

List of Publication and Presentations

List of Publication

1. L.M. Chua, T. Vazhnova, T.J. Mays, D.B. Lukyanov, S.P. Rigby. 2010. Deactivation of PtH-MFI Bifunctional Catalysts by Coke Formation during Benzene Alkylation with Ethane. Journal of Catalysis, 271, 401-412.

List of Presentations

1. Chua, LM, Vazhnova, T, Lukyanov, DB, Rigby, SP, (2009), 'Deactivation by Coke Formation of PtH-ZSM-5 Bifunctional Catalyst during Benzene Alkylation with Ethane into Ethylbenzene'. 11th International Symposium on Catalyst Deactivation, 25-28 October 2009, Delft, The Netherlands (Oral Presentation)

2. Chua, LM, Vazhnova, T, Lukyanov, DB, Rigby, SP, (2009), 'Pore Structure Analysis of Bi-functional Zeolite Catalysis for Benzene Alkylation: Effect of Deactivation by Coking'. 5th International Porous Material Workshop: Characterisation of Porous Materials from Angstroms to Millimeters, 24-26 June 2009, New Brunswick, NJ, USA (Poster); Book of Abstracts, p. 87.

3. Chua, LM, Vazhnova, T, Lukyanov, DB, Rigby, SP, (2009), 'Pore Structure Modification by Coking during Benzene Alkylation with Ethane on Bi-functional Zeolite Catalysts'. 5th Pacific Basin Conference on Adsorption Science and Technology (PBAST 5), 25-27 May 2009, Singapore (Poster); Book of Abstracts, Poster 99

4. Chua, LM, Vazhnova, T, Lukyanov, DB, Rigby, SP, (2008), ' Deactivation of Bi-functional Zeolite Catalysts for Benzene Alkylation with Ethane into Ethylbenzene'. 14th International Congress on Catalysis, 13-18 July 2008, Seoul, Korea (Poster); Book of Abstracts, PIII-64-55; Extended Abstracts (CD-ROM)

5. Chua, LM, Vazhnova, T, Lukyanov, DB, Rigby, SP, (2008), 'Pore Structure Modification during Deactivation of Bi-functional Zeolite Catalysts for Benzene Alkylation with Ethane into Ethylbenzene'. 8th International Symposium on the Characterisation of Porous Solids (COPS-VIII), 10-13 June 2008, Edinburgh, UK (Poster); Book of Abstracts, p.85

6. Chua, LM, Vazhnova, T, Lukyanov, DB, Rigby, SP, (2008), 'Studies of The Deactivation of Bi-functional Zeolite-based Catalysts for Benzene Alkylation'. 31st Annual Meeting of British Zeolite Association, 31 March - 2 April 2008, Keele, UK (Oral Presentation)

7. Chua, LM, Vazhnova, T, Lukyanov, DB, Rigby, SP, (2008), 'Characterisation of ZSM-5 Catalyst for Benzene Alkylation with Ethane'. Catalysis: Fundamental and Practice Summer School, 3-7 September 2007, Liverpool, UK (Poster)

Table of Contents

List of Figures

List of Tables

Abbreviation

B	Benzene
BSE	Back-scattered electron
C_2 / C_2H_6	Ethane
DEB	Diethylbenzene
EB	Ethylbenzene
FCC	Fluid catalytic cracking
FTIR	Fourier-transformed infra-red
GC	Gas chromatogram
H^+	Acid site
LDF	Linear driving force
M	Metal site
$M_{x/n}[(AlO_2)_x(SiO_2)_y].zH_2O$	General formula of zeolite
NMR	Nuclear magnetic resonance
PFG	Pulsed field gradient
PPCP	Protonated pseudo-cyclopropane
PSD	Pore size distribution
SBU	Secondary building units
SEM	Scanning electron microscopy
TEB	Triethylbenzene
TEM	Transmission electron microscopy
TGA	Thermogravimetric analysis
TOS	Time-on-stream
TPD	Temperature programmed desorption
XRD	X-ray diffraction

Nomenclatures

$\langle x^2 \rangle$	Mean squared displacement	
$[p]$	Equilibrium pressure	Pa
Δ	Diffusion time	s
a	Sphere radius/diffusion length	m
A_o	Pre-exponential factor	
B_o	Applied magnetic field	Gauss
C_B	Concentration of benzene in the reaction mixture	mol %
C_{B0}	Initial concentration of benzene	mol %
C_{C2}	Concentration of ethane in the reaction mixture	mol %
C_i	Concentration of species i in the reaction mixture	mol %
C_{i0}	Initial concentration of species i	mol %
C_p	Specific heat capacity	kJ mol^{-1} K^{-1}
D	Effective diffusion coefficient	m^2 s^{-1}
D/a^2	Diffusional time constant	s
D_o	Self-diffusivity at zero coverage	m^2 s^{-1}
D_{PFG}	Self-diffusion coefficient measured by PFG experiments	m^2 s^{-1}
D_s	Self-diffusion coefficient	m^2 s^{-1}
D_t	Transport diffusion coefficient	m^2 s^{-1}
E_D	Activation energy for diffusion	J mol^{-1}
F	Accessibility fraction	
f	Total fraction of unplugged pores	
f_b	Bond occupation probability	
f_{bc}	Bond percolation threshold	
f_s	Site occupation probability	
f_{sb}	Site-bond occupation probability	
f_{sbc}	Site-bond percolation threshold	
f_{sc}	Site percolation threshold	
g	Magnitude of the gradient pulse	G cm^{-1}
H	Henry's constant	

I	Nuclear spin quantum number	
k	Mass transfer coefficient	s^{-1}
k_D	numerical factor which depends on the dimensionality of the system	
K_p	Equilibrium Constant	
L	Number of bonds between one side of the lattice and another	
$M(\infty)$	Equilibrium mass uptake	mg
$M(t)$	Mass uptake at time t	mg
P/P_o	Relative pressure	
P_e	Equilibrium pressures	Pa
P_o	Saturation vapour pressure	Pa
q_{exp}	Experimental adsorption capacity	molecule *per* unit cell
Q_{st}	Heat of adsorption	kJ mol^{-1}
q_{theo}	Theoretical adsorption capacity	molecule *per* unit cell
R	Gas constant	J mol^{-1} K^{-1}
R^2	Regression coefficient	
S_i	Selectivity of species i	mol %
t	Time	s
T	Temperature	^{o}C / K
t	Total time for successful and unsuccessful hops	
u	Random number	
$V(t=0)$	Pore volume for the fresh catalyst	cm^3 g^{-1}
$V(t=t)$	Externally accessible pore volume of the coked catalyst at different TOS	cm^3 g^{-1}
$V_c(t=TOS)$	Volume of coke at different TOS	cm^3 g$^{-1}_{cat}$
x	Spatial coordinate	
X_{ben}	Conversion of benzene	%
Y	Yield	%
Z	Coordination number	
Γ	constant amount adsorbed	mg mg^{-1}
γ	Magnetogyric ratio	rad s^{-1} T^{-1}
δ	Gradient pulse duration	s

ΔG	Gibbs free energy	kJ mol^{-1}
ΔH	Differential molar enthalpy of adsorption	kJ mol^{-1}
ΔS	Entropy	kJ mol^{-1} K^{-1}
Δt	Time interval between each attempted hops	
ε	Voidage	
θ	Occupancy	
λ	Jump distance	m
v	Frequency of the Larmor precession	s^{-1}
τ	Correlation time	s
τ_p	Tortuosity	

Chapter 1 : Introduction

1.1 Background

Ethylbenzene (EB) is the key intermediate in the production of styrene. Over 90% of the world's production of EB is used as primary feedstock for the synthesis of polystyrene [1]. The worldwide capacity for EB is estimated to be 23 million tonnes per year in 2001, with an annual growth rate estimated to be approximately 4 % [1, 2]. The existing commercial production of EB is based on benzene alkylation with ethene (the product of steam reforming of ethane and naphtha) [3, 4]. According to Ren et al. [4], the steam cracking process that produces ethene is responsible for approximately 180 - 200 million tons of CO_2 emissions worldwide. In addition, energy input accounts for 70% of the production cost in a typical ethane- or naphtha- based olefin plants [4]. Therefore, a greener and more cost-effective technology for the production of EB was developed by replacing ethene with ethane as the alkylating agent.

$$\text{C}_6\text{H}_6 + C_2H_6 \rightleftharpoons \text{C}_6\text{H}_5\text{-}C_2H_5 + H_2$$

$$(1\text{-}1)$$
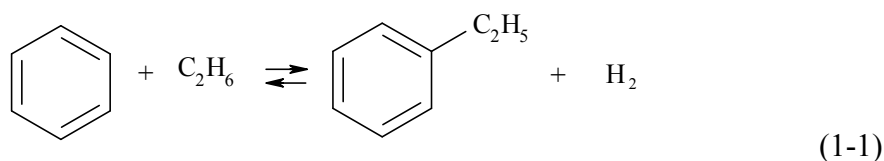
Recent development in the alkylation process of benzene with ethane includes the use of bifunctional zeolite catalysts to enable a one pot synthesis of the valuable alkylaromatic hydrocarbons, ethylbenzene [5-9]. A new bifunctional PtH-ZSM-5 zeolite catalyst has been studied for benzene alkylation with ethane (Equation 1.1), where the optimum reaction temperature (370 ^{o}C) [8], and analysis of the kinetics of the alkylation reaction [9] were discussed. The ZSM-5 type zeolite was chosen because it has become a well-known solid catalyst for acid catalyzed reactions due to its shape-selectivity property [10] and its high resistance to deactivation as compared to other commercial zeolite catalysts [11]. Despite the promising results demonstrated by the PtH-ZSM-5 catalysts for benzene alkylation reaction [8, 9], the deactivation of the catalyst caused by deposition of carbonaceous compounds potentially could limit the development of this process. However, the details of the mechanism of coke formation during the ethylbenzene production process have remained unknown until now.

Catalyst deactivation, as a result of coke formation, has been a challenge in the catalyst industry for many hydrocarbon processes. Extensive studies on the subject of coke and catalyst deactivation were previously carried out on other hydrocarbon processing reactions [10-13], though not for the reaction of benzene alkylation with ethane. Two mechanisms of coking have been identified: pore blocking where coke blocks the access of reactants to active sites, and active site coverage where coke poisons the active sites responsible for the reaction [11, 12].

Modification of the ZSM-5 catalysts by coking has been reported to influence the product distribution of shape selective reactions [11, 14, 15]. The effect of coke deposition on *para*-selectivity was found to be dependent on the location of coke, specifically whether it was located either within the internal pore structure, or on the external surface of the zeolite catalyst [11, 15]. For example, some partially deactivated catalysts have been shown to become less *para*-selective because of coke deposition by pore filling, as demonstrated by Soleto et al. [11], who studied the deactivation of toluene alkylation with methanol reaction on ZSM-5 catalysts. Conversely, Chen et al. [15] showed that, with increasing coke content, *para*-DEB selectivity increased during the disproportionation of ethylbenzene. Similarly, Lin et al. [16] showed that pore blockage as a result of coke formation, caused an increase in the *para*-xylene selectivity with prolonged time-on-stream (TOS). However, this previous work does not consider the effect of intracrystalline coke distribution on the diffusivity and/or diffusion path length, which can then influence product selectivities.

The lack of understanding of the deactivation phenomena during this new process for ethylbenzene production encouraged the work carried out in this research. This study examined new bi-functional zeolite catalysts for benzene alkylation with ethane, and focused on the effect of coking on the accessibility and mass transport within the zeolite catalyst in relation with changes in surface chemistry and network geometry. The aim of this project is to obtain a correlation between the product distribution and the structural evolution of the pore structure of the zeolite catalyst as a result of coke deposition.

1.2   Thesis Structure

This thesis is divided into 8 chapters.

Chapter 2 gives an introduction to zeolites as catalysts. Factors that influence the synthesis of a bifunctional zeolite catalyst will be discussed. Detailed experimental procedures for the preparation of bifunctional PtH-ZSM-5 catalysts will be given in Chapter 2. The alkylation of benzene with ethane over PtH-ZSM-5 catalysts of different SiO_2/Al_2O_3 ratios will be discussed in Chapter 3. The effect of time-on-stream (TOS) and the influence of acidity on the activity and selectivity of PtH-ZSM-5 catalysts are investigated. Chapter 4 examines the pore structure evolution of PtH-ZSM-5 catalysts as a result of coke deposition, using a variety of characterisation techniques such as gas sorption, x-ray diffraction (XRD), thermogravimetric analysis (TGA), scanning electron microscopy (SEM) and infra-red (IR) spectroscopy. The simulation of accessibility and diffusivity in a fresh and partially blocked cubic and ZSM-5 lattice will be performed in Chapter 5. The effect of coke deposition on the thermodynamics and kinetics of the main reactant, ethane will be studied in Chapter 6. Parameters such as heat of adsorption and mass transport coefficient will be determined from the experimental data obtained from ethane adsorption experiments. The use of pulsed field gradient (PFG) NMR technique to study the diffusivity of probe molecules within the H-ZSM-5 and PtH-ZSM-5 catalysts will be discussed in Chapter 7. Finally, the findings of this thesis are summarised in Chapter 8. A proposal for further investigation in this area of research will also be presented.

A schematic representation of the route taken to illustrate the different deactivation mode for the benzene alkylation with ethane reaction is shown in Figure 1.1.
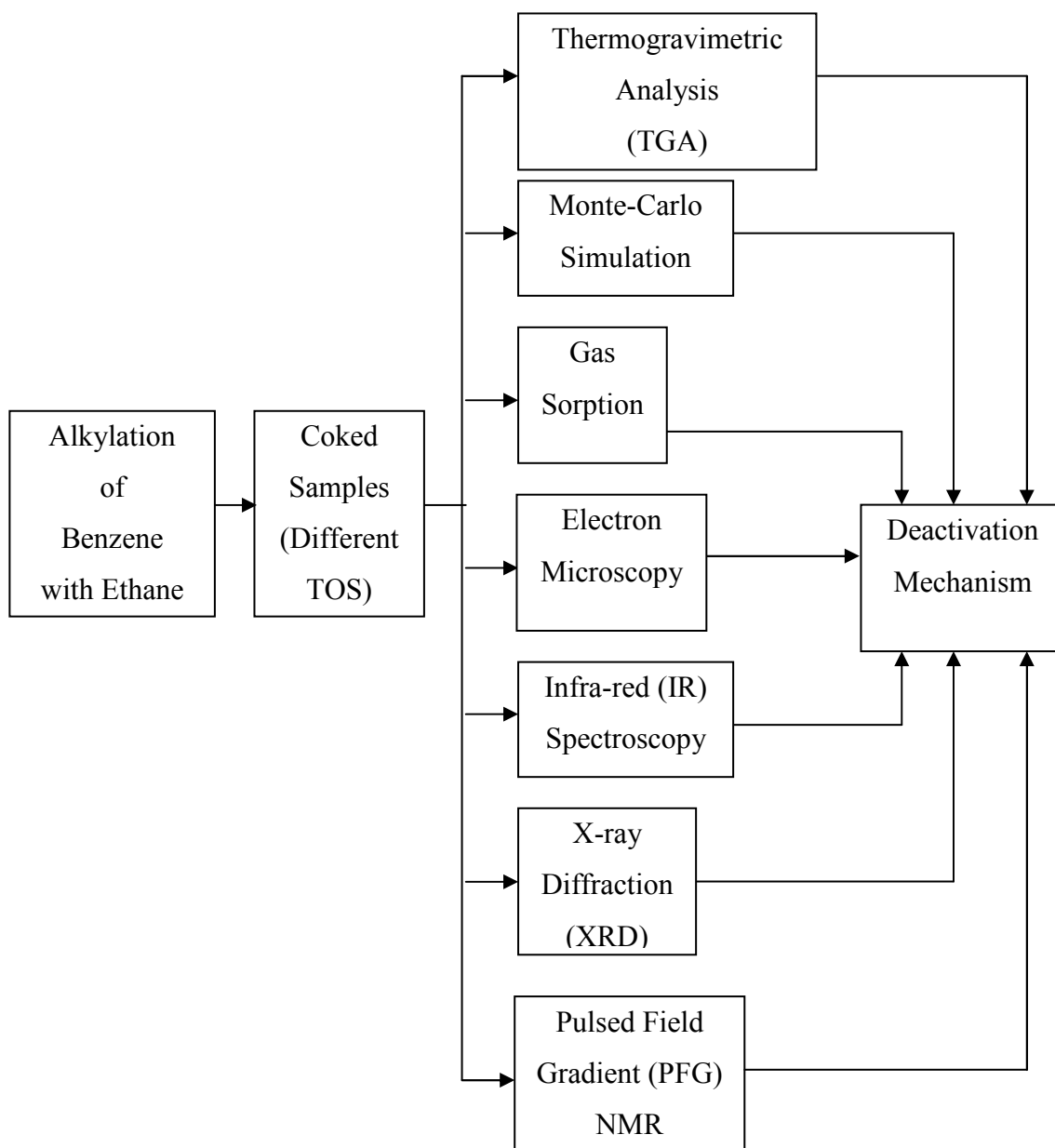
Figure 1.1 – Steps taken to determine the coking behaviour of bifunctional zeolite catalyst during benzene alkylation with ethane

1.3 References

[1]   T.F. Degnan, C.M. Smith, and C.R. Venkat, Applied Catalysis. A, General 221 (2001) 283-294.

[2]   M. Hartmann, Angewandte Chemie International Edition 43 (2004) 5880-5882.

[3]   J.A. Moulijn, M. Makkee, and A. van Diepen, Chemical Process Technology, John Wiley & Sons, Ltd. 109-130.

[4]   T. Ren, M. Patel, and K. Blok, Energy 31 (2006) 425-451.

[5]   S. Kato, K. Nakagawa, N. Ikenaga, and T. Suzuki, Chemistry letters 3 (1999) 207-208.

[6]   S. Kato, K. Nakagawa, N. Ikenaga, and T. Suzuki, Catalysis Letters 73 (2001) 175.

[7]   A.V. Smirnov, E.V. Mazin, E.E. Ponomoreva, E.E. Knyazeva, S.N. Nesterenko, and I.I. Ivanova, Benzene Alkylation with Alkanes over Modified MFI Catalysts, Montpellier, France. 2001.

[8]   D.B. Lukyanov, and T. Vazhnova, Journal of Molecular Catalysis A:Chemical 279 (2008) 128-132.

[9]   D.B. Lukyanov, and T. Vazhnova, Journal of Catalysis 257 (2008) 382-389.

[10]   D.M. Bibby, N.B. Milestone, J.E. Patterson, and L.P. Aldridge, Journal of Catalysis 97 (1986) 493-502.

[11]   J.L. Sotelo, M.A. Uguina, J.L. Valverde, and D.P. Serrano, Applied Catalysis A:General 114 (1994) 273-285.

[12]   A. De Lucas, P. Canizares, A. Durfin, and A. Carrero, Applied Catalysis A: General 156 (1997) 299-317.

[13]   M. Guisnet, and P. Magnoux, Applied Catalysis 54 (1989) 1-27.

[14]   D.H. Olson, and W.O. Haag, ACS Symposium Series 248 (1984) 275-307.

[15]   W.H. Chen, T.C. Tsai, S.J. Jong, Q. Zhao, C.T. Tsai, I. Wang, H.K. Lee, and S.B. Liu, Journal of Molecular Catalysis A:Chemical 181 (2002) 41-55.

[16]   X. Lin, Y. Fan, G. Shi, H. Liu, and X. Bao, Energy and Fuels 21 (2007) 2517-2524.

Chapter 2 : Introduction to Zeolites and Synthesis of Bifunctional Zeolite Catalysts

2.1 Introduction

Zeolites, oxides, complex oxides and ion-exchange resins are the most common types of catalysts used in hydrocarbon processes [1]. According to the study carried out by Tanabe and Holderich [1], zeolites account for approximately 40 % of the types of catalysts used in the chemical and petrochemical industries. The extensive use of zeolites as catalysts in industrial applications is primarily due to their unique physical and chemical characteristics, such as their well defined pore structures and high acidity properties. Therefore, in the present work, zeolites will be used to catalyse the alkylation of benzene with ethane.

2.2 Catalyst Selection for the Production of Ethylbenzene by Benzene Alkylation with Light Alkanes

The transformation of light alkanes (ethane and propane) is an interesting area of research for many research groups as it allows the direct use of these cheap and readily available materials to provide an alternative to processes that are currently based on alkenes and aromatics [2]. Given the low reactivity of light alkanes, the activation of these short-chain alkanes remains a great challenge in catalysis research. In most reactions that involve the functionalisation of light alkanes, such as aromatization, alkylation and isomerisation, zeolites are commonly used as catalysts.

Early studies of aromatization and alkylation reactions were carried out using pure acidic zeolite catalysts. Guisnet et al. [3] reported that the formation of olefinic compounds from dehydrogenation and cracking is the limiting step of the aromatization reaction with these pure acidic catalysts. Kato et al. [4] also mentioned that unloaded zeolites are inactive when light alkanes are used as the alkylating agent. Therefore, to enhance the alkylation and aromatization reaction, bifunctional catalysts were suggested to be significantly more active than pure acid catalyst.

Previous studies clearly show that incorporation of metal particles into the zeolite structure helps to enhance the performance of pure acidic zeolite catalysts [2, 5]. The metal functions as a dehydrogenating agent for the light alkanes. Zinc, platinum and gallium have been demonstrated to improve the zeolite reactivity during alkane activation. However, depending on the reactants used, different metals yield different catalytic activities. According to Guisnet et al. [3], gallium and zinc are the most active dehydrogenating component for the propane aromatization reaction, even though zinc is usually eliminated because of its volatility. This was also pointed out by other authors [2, 6] who reported that the addition of Ga and Zn promotes the dehydrogenation of propane during alkylation and aromatization reactions.

Ga-incorporated zeolite catalysts only showed slight activity for ethane [4, 7], contrary to its higher catalytic activity for propane. Similar to the activity of the Ga-incorporated zeolite catalyst, the performance of other metals such as Ni, Rh and Ru also produce small amounts of ethene [7], which then limits the benzene alkylation reaction. Even though platinum-incorporated zeolite catalysts are less stable and not selective for propane aromatization and benzene alkylation [3], their reactivity is excellent when ethane is used as the reactant during aromatization and benzene alkylation [4, 7].

When a reaction is carried out in the presence of a dual-functional catalyst, the reaction proceeds through a bifunctional reaction pathway where the transformation of light alkanes would initiate with the dehydrogenation reaction to form light alkenes, which will then react with benzene to form alkylbenzenes. Likewise, for benzene alkylation with light alkanes over a metal-incorporated zeolite catalyst, the light alkanes would be dehydrogenated over the metallic site while the formation of the carbenium ion takes place on the acidic site. (The detailed mechanism will be discussed later in Chapter 3).

Therefore, when choosing the catalyst for the alkylation reaction of benzene with ethane, the main consideration would be to enhance : (i) ethane dehydrogenation to ethene and hydrogen and (ii) benzene alkylation with ethene to form ethylbenzene, while suppressing the side reactions such as hydrogenolysis of ethane, oligomerization and cracking as well as ethylbenzene transformation reactions [8]. In addition, the

catalyst chosen should demonstrate stable performance with time-on-stream (TOS) and also be selective to the formation of ethylbenzene. The cost of the catalyst should also be taken into consideration as it influences the production cost of ethylbenzene/stryrene.

In order to determine the most effective zeolite catalyst for benzene alkylation reaction with ethane, Kato et al. [7] carried out experiments to compare the performance of pure and metal-incorporated H-mordenite, H-Y and H-ZSM-5 zeolites. Among the zeolites studied, the Pt/H-ZSM-5 catalyst gave the highest yield of total C8 aromatics [7]. Other zeolites such as the Pt/H-Y and Ga/H-MCM-41 did not yield ethylbenzene and styrene in the product stream. The difference in the catalytic activity of these zeolites was said to be due to the differing acid strengths, as measured by NH_3-TPD.

The ZSM-5 catalyst has a unique catalytic activity in transformation of hydrocarbons to aromatics as it has a low coking rate and it limits the growth of bulky molecules by steric constraints [5, 9-12]. ZSM-5 catalysts have life cycles of 40-60 days before regeneration [13]. In addition to that, their acidic property also makes them a preferred catalyst for these reactions.

Even though platinum incorporated H-ZSM-5 catalyst was demonstrated to be the most promising catalyst for the alkylation reaction of benzene with ethane [4, 7], the high platinum loading used is not economical because of the high cost of platinum. Hence, there is an economic incentive to minimize the amount of platinum used in the preparation of platinum loaded catalysts while maintaining their catalytic activity [14]. This could be achieved by reducing metal loading while increasing the metal dispersion, hence increasing the performance of the catalyst and at the same time, reducing the cost of metal incorporated [14-15].

In addition to increasing the conversion and selectivity of the alkylation reaction, the presence of platinum is also believed to reduce coke formation, because of its role of the entrance of H_2 spill-over [16]. During the H_2 spill-over phenomenon, the olefins and carbenium ions are converted into paraffins, thus suppressing the aromatization reaction which prevents coke formation [17]. With the possibility of controlling coke formation, the lifetime of the catalyst may be increased, therefore making it more stable during the alkylation reaction.

As previous studies have proven that dual-functional catalysts are beneficial to processes that require two different catalytic sites, attempts have been made to employ bifunctional catalysts for benzene alkylation. However, up to now, only a few research groups have carried out the one step synthesis for benzene alkylation with ethane using bifunctional zeolite catalysts [4, 7-8, 18-19]. Recently, Lukyanov and Vazhnova [8, 19] carried out benzene alkylation with ethane over 1 wt % PtH-ZSM-5 catalysts with different SiO_2/Al_2O_3 ratio (SiO_2/Al_2O_3 = 30, 72 and 280). It was shown that the Pt-incorporated H-ZSM-5 catalysts yielded stable catalyst performance, as well as high selectivity into EB (> 90 mol % selectivity in aromatic products). As a result, this study will investigate the alkylation of benzene with ethane on low loading Pt-modified H-ZSM-5 catalysts.

2.3   Zeolites

Zeolites are highly-structured microporous inorganic solids which contain channels and pores of very well-defined sizes, in which catalytic groups are situated [20]. Due to their large application, zeolites have a global market of several million tonnes per annum [21].

Zeolites are crystalline, hydrated aluminosilicates with well-defined structures (Figure 2.1) [21]. Zeolite structures consist of silicon cation (Si^{4+}) and aluminium cations (Al^{3+}) that are linked through by oxygen anions (O^{2-}). Each oxygen anion connects two cations yielding a macromolecular three-dimensional framework. The negative charge arises from the difference in formal valency between silicon- and aluminium cations, and will be located on one of the oxygen anions connected to an aluminium cation [22]. The negative charges on the aluminium-oxygen tetrahedra can be balanced by positive charges to allow the zeolite to be a neutral material [23-25]. The positive charges can be a metal ion or protons, which can be exchanged for other positively charged ions [23].
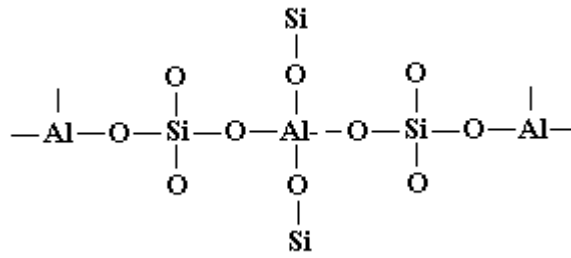
Figure 2.1 - Basic Structure of Zeolite (Adapted from ref [26])

The general formula for zeolite is $M_{x/n}[(AlO_2)x(SiO_2)y].zH_2O$, where M represents the non-framework cation and n is the charge [24].

There are two kinds of zeolites available, natural and synthetic zeolites. Natural zeolites are processed from natural ore bodies. Although natural zeolites are present in large amounts, they have limited range of structures and properties. Therefore, new species of zeolites (synthetic zeolites) which have a wider range of properties and pore architectures than the former counterparts are being manufactured.

Zeolites are built of primary and secondary building units. The primary unit is constructed by joining the $[SiO_4]^{4-}$ and $[AlO_4]^{5-}$ coordination polyhedral. A Si or Al atom sits at the centre of the tetrahedron with 4 oxygen atoms co-valently bonded to the centered Si or Al atom (so-called T-atom). Zeolite structures can be classified by observing the identical repeating structural sub-units which are called the secondary building units (SBU) [27]. A number of secondary building units can be built by a linkage through the oxygen atom covalent bonding, which is called an oxygen bridge. Zeolites with different structures are made possible by varying the arrangements of linked TO_4 (T=Si or Al atom/ion) tetrahedra within the secondary building units. The size of zeolite pores can be classified as narrow-pore, medium-pore or wide-pore zeolites, depending on the ring opening of either 8-, 10- or 12-member rings. The exact diameter of the pore depends on the coordination and the amount of cations and anions present in the ring [22].

2.3.1 Characteristics of Zeolites

Zeolites play an important role in the heterogeneous catalysis field and there has been a significantly rise in the available range of catalysts in the past few decades [28]. The interest in the usage of zeolites as catalysts arises from their unique properties, namely their acid strength and their well-defined pore structure. The high thermal stability of zeolites makes them ideal for use in petrochemical industry, where high-energy transformations are carried out [20, 29].

2.3.1.1 Acidity

The possibility of controlling the acid strength, as well as the density of acid sites, of zeolite catalysts has led to their wide application in the field of oil refining and petrochemistry.

Acidity can be introduced into a zeolite by creating 'hydroxyls' within the pore structure [27]. These hydroxyls are formed either by ammonium or polyvalent cation exchange, followed by a calcination step. They are associated with the negatively charged framework of oxygens linked into alumina tetrahedral, which is the Brønsted acid sites [27].
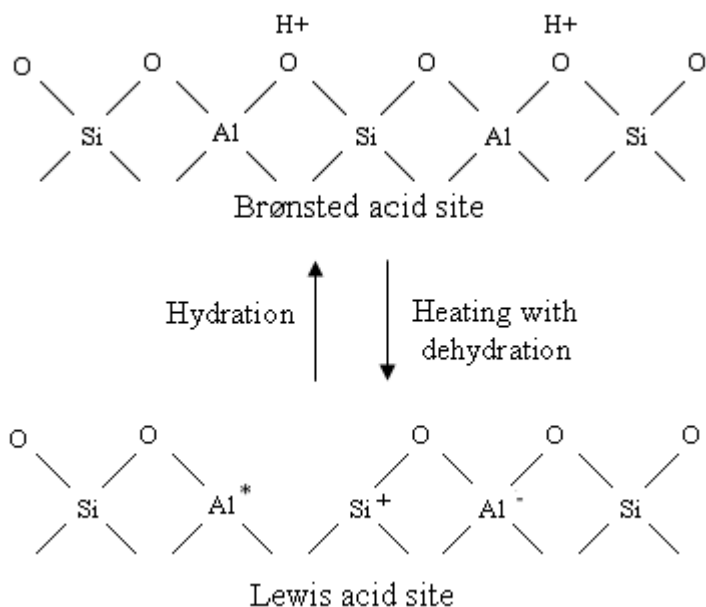
Figure 2.2 - Interconversion of Brønsted and Lewis Acid Sites (Adapted from ref [27])

The Brønsted acid sites have greater mobility at high temperature, thus forming the unstable Lewis acid sites. An annealing process stabilizes the structure by ejecting Al species from the framework and produces so-called 'true' Lewis acid sites [27]. The interconversion of Brønsted and Lewis acid sites can be seen from Figure 2.2.

The effective acidity of the zeolite catalyst is influenced by a few factors such as the total number of Brønsted and Lewis acid sites, their strength distribution and location [28]. The two most commonly used methods to determine the acidic properties of the zeolite catalysts are temperature-programmed desorption (TPD) of ammonia and Fourier transform infrared spectroscopy (FTIR). Theoretically one acid site is generated by substitution of one aluminium atom into the silicalite matrix. The acidity of zeolites is determined by the SiO_2 to Al_2O_3 ratio in the framework. According to Ribeiro et al. [28], the increase in Si/Al ratio increases the number of strong Brønsted acid sites, despite the decrease in the total amount of acid sites. However, the acid site density is reduced with higher Si/Al ratio [29]. Based on NH_3-TPD results, Kato et al. [7] reported that the total acidity of zeolite catalysts increases with the decrease in SiO_2 to Al_2O_3 ratio.

2.3.1.2 *Shape-selectivity*

The pore structure of zeolites is also an important feature in their application as catalysts. Their well-defined pore dimensions can discriminate reactants and products by size and shape when these molecules present significant differences in diffusivity through a given pore channel system [31]. It was pointed out that access to active sites within the zeolite framework is controlled by the oxygen window [30]. With the dimension of pores about the same order of magnitude as many hydrocarbon molecules, zeolite catalysts can control the adsorption of reactants and products, hence inducing shape selectivity. Relative to traditional catalysts, zeolites can be tailored to admit certain reactant molecules which produce selective products [30]. The product distribution when using different types of zeolites as catalyst differs from one another due to the different pore network structure.

Due to the high activity of zeolite catalysts, they are vulnerable to coke deposition, which has been identified as the primary reason for deactivation of the

catalyst during acid-catalysed hydrocarbon reactions [32]. However, the coking process is a shape selective reaction which can be controlled by the pore structure of zeolite catalysts [33]. The build-up of the carbonaceous residues in the microporous channels of the zeolite catalyst can block access of reactants to active sites or products from diffusing out of the zeolite crystallites.

The shape selectivity property of zeolite catalysts can be classified into three categories:

(a) Reactant shape selectivity: due to the complexity of the pore structure of zeolites, only reactants that can penetrate into the pore, or have a favourable shape, will be able to react on the active sites of the catalyst [24, 30]

(b) Product shape selectivity: the size of the product formed must be smaller than the size of the pores structure and intersections [24, 30]

(c) Restricted transition state selectivity: the transition state intermediate product should not be too bulky due to the limited volume available around the active site of the zeolite framework. This will control the shape and size of the product [24, 30]

2.3.2   Zeolite Modification

Zeolites can be treated to optimise their physical and chemical properties to suit the requirement of a desired reaction. Preparation of zeolites having various pore sizes and acidities have been given a lot of attention. The framework of zeolites can be modified by synthesizing zeolites with metal cations other than aluminum and silicon in the framework. According to Perot and Guisnet [29], the characteristics of the zeolite catalyst, i.e. acid strength, density of acid sites, and porosity cannot be modified independently. For example, dealumination decreases the acid site density but increases the acid strength and also changes the porosity of the zeolite [29], where mesopores are created to overcome diffusion problem in microporous zeolite [33].

The size of the zeolite pore channels is a major advantage for separation processes and for applications as adsorbents and heterogeneous catalysts. In some

applications, zeolites with larger pores are required to reduce diffusion limitations on the reaction rate, while in some separation processes channels of microporous dimensions are required. The micropore structure limits the performance of the catalyst due to mass transport limitations of the reactants and products. Therefore, Christensen et al. [35] suggested using mesoporous zeolite single crystals to increase the activity and selectivity of the catalyst while reducing diffusional limitations [35]. These mesoporous zeolites could be obtained by minimizing the size of the zeolite crystals or by increasing the pore size of the zeolite catalyst [36].

Hartmann [36] drew attention to the advantages of the new mesoporous zeolites in relation to their catalytic activity. The author highlighted that these modified zeolites offer higher reaction rates for diffusion-limited reactions which could improve the selectivity of the target product plus slow down deactivation of the catalyst due to pore mouth blockage in the microporous zeolites.

Studies have been carried out to compare the performance of the conventional zeolite and the modified zeolites which has mesopore channels. Rovik et al. [37] showed that the conversion and selectivity of the mesoporous Re/H-ZSM-5 catalyst during the dehydrogenation of propane is much higher than the conventional ReH-ZSM-5 catalyst due to pore blocking of Re on the conventional MFI catalyst. Earlier studies by Christensen et al. [35] also showed an increase in the selectivity of ethylbenzene over a mesoporous MFI catalyst during benzene alkylation with ethene.

2.3.3 ZSM-5 Zeolite

ZSM-5 zeolite is part of the pentasil family of high-silica zeolites [20, 38]. Since the synthesis of ZSM-5 by Mobil scientists, it has been regarded as one of the most versatile zeolites found and used industrially. ZSM-5 zeolite has also been of scientific interest due to its diverse application in heterogeneous catalysis, separation, purification and lately in environmental applications [39]. As mentioned earlier, zeolites account for approximately 40 % of the type of catalysts used in the chemical and petrochemical industries, and out of the 40 %, 42 % of the zeolite catalysts used is the ZSM-5 zeolite [1]. Results from the survey carried out [1] demonstrate the importance of ZSM-5 zeolite as solid acid catalysts.
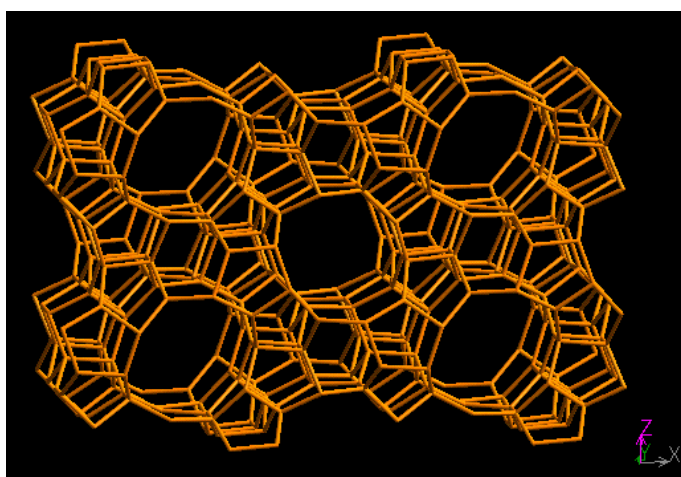
Figure 2.3 - Framework of MFI Type Zeolite [40]

ZSM-5 zeolites consist of two types of pores, both formed by 10-membered oxygen rings (Figure 2.3). The framework contains two intersecting channels, one of the channel structures is straight and elliptical in cross section, whereas the second sort of pores intersect the straight pores at right angles, in a zig-zag pattern and are circular in cross section [11, 41-44]. The sinusoidal and nearly circular opening has a dimension of 5.4 Å x 5.6 Å whereas the straight elliptical opening has a dimension of 5.1 Å x 5.6 Å [30].

Elliptical Straight Channels
(0.51 x 0.56 nm)

Near circular sinusoidal channel
(0.54 x 0.56 nm)
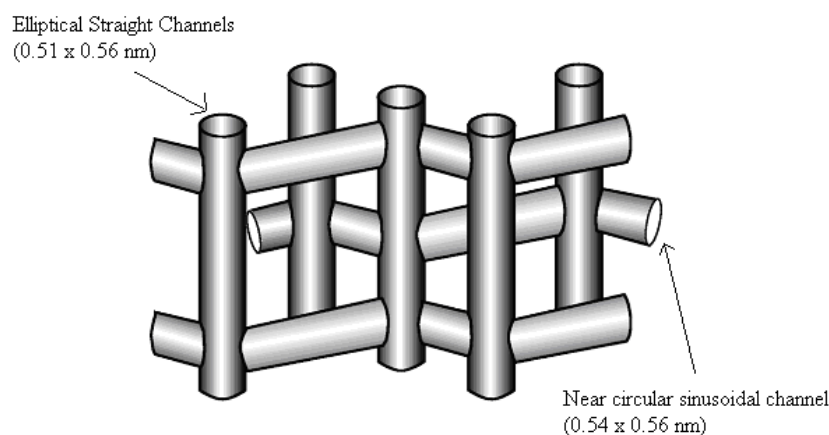
Figure 2.4 - Pore Structure of H-ZSM-5 [20]

The ZSM-5 type zeolite is known to be a shape selective catalyst due to its unique channel structures [42]. The channel opening of the 10-membered ring controls the type of molecules that can have access to the internal zeolite pore channels by its size. The ZSM-5 zeolite is also considered as a remarkably stable acid catalyst due the

absence of large supercages and small windows [29] that are present in other zeolites such as zeolite-Y and zeolite-A. Figure 2.3 shows the framework of MFI type zeolite while the representation of the channel system of ZSM-5 can be seen from Figure 2.4.

The ZSM-5 zeolite was chosen as the preferred alkylation catalyst to other acid catalysts because it induces shape selective catalysis and it has low ageing rates. Amongst them, the steric factor plays a significant role in catalyst selection. The shape selectivity property of the ZSM-5 zeolite can be illustrated by *para*-selectivity enhancement during xylene isomerisation, toluene-methanol alkylation and toluene disproportionation experiments [45] as a result of the higher diffusivity of *para*-isomers compared to *meta*- and *ortho*-isomers in the pores of ZSM-5 catalysts. Compared to other zeolites with larger pore dimensions, the geometry of ZSM-5 imposes constraints to prevent formation of large polynuclear hydrocarbons (by hydrogen transfer or cyclization) which are responsible for coking [29, 46].

2.4 Bifunctional Zeolite Catalysts

The catalytic properties of a bifunctional catalyst depend upon the technique applied and also the preparation method which includes the type of metal precursor used, amount of metal loading, and the calcination and reduction conditions. The preparation step is vital for determining the location of the metal species, metallic dispersion and the particle size of the metal species, which will influence the desired activity, selectivity and life time of the catalyst. The balance between the metal and acid strength is another factor that changes the catalytic activity of the bifunctional catalyst. The types of precursors used to form the bifunctional catalyst have been shown to affect the metallic and acidic properties of the bifunctional catalyst [47].

2.4.1 Preparation Method

Bifunctional catalysts can be prepared via several techniques such as ion exchange [15, 47-49], incipient wetness impregnation [15, 48-49], mechanical mixing and spontaneous monolayer dispersion [48]. However, the two most commonly used techniques for the preparation of bifunctional catalysts are the ion exchange and impregnation method [15]. The ion exchange method is described as an irreversible

chemical reaction where the zeolite is mixed in a soluble salt solution of the desired ingoing cation. The ion from the solution is exchanged with the cation attached to the zeolite particles. If the bifunctional catalyst is prepared via the incipient wetness impregnation method, the zeolite will be immersed in a solution of metal salts of interest, inducing deposition.

Many studies have been carried out to investigate the effect of different metal incorporation techniques on the properties of the bifunctional catalyst. Schulz and Baerns [9] reported that the method of preparation (impregnation or ion exchange) had no influence on the activity of the catalyst during ethane aromatization. However, it was found that the impregnated Ga/H-ZSM-5 catalyst is a more active catalyst when compared with the physical mixed catalyst, for ethane aromatization, due to the close interaction between Ga_2O_3 and the Brønsted acid sites. Likewise, Smirnov et al. [18] found that the mixed platinum modified H-ZSM-5 catalyst has lower activity compared to the ion-exchanged and impregnated catalyst for the alkylation of benzene with propane [18].

In contrast to the findings of Schulz and Baerns [9], Jao et al. [49] found that the isomerization selectivity for the catalyst prepared via ion exchange technique is higher as a result of higher platinum dispersion and smaller platinum particles as compared to the mordenite-supported Pt catalyst prepared by impregnation method. Based on the shift in the Ni reduction temperature to higher temperature for the ion-exchange catalysts, Romero et al. [47] reported that a Ni/H-ZSM-5 catalyst prepared via impregnation method has a lower nickel dispersion compared to one prepared by the ion exchange technique. Their result is in agreement with the conclusions drawn by Jao et al. [49]. It was proposed that the platinum precursors are deposited on the external surface area of the zeolite catalyst after impregnation and these platinum precursors agglomerate during the calcination and/or reduction step [49]. In addition, the shorter distance between the acidic and metal centers [18] also explains the better performance of the ion exchange catalysts.

Ni/H-ZSM-5 catalysts prepared via impregnation method was reported to have a higher activity during n-decane hydroisomerization compared to the one prepared by mechanical mixing. The increase in hydroisomerization activity was because of the

smaller Ni particles formed and the closer interaction between the acid and metal function after impregnation [50].

2.4.2 Calcination and Reduction

The preparation of a bifunctional catalyst usually includes a calcination and reduction step after the metal precursors have been introduced into the zeolite support to activate the catalyst. These heat-treatment procedures have great influence on the performance and properties of the bifunctional catalyst in terms of the position and the size of the metal particles in the catalyst. The calcination step is required to decompose the precursor compound and to form oxide species [6]. The calcined catalyst will usually undergo a reduction step in the presence of a reducing gas such as hydrogen. The calcination and reduction conditions have significant effect on the metal dispersion and the distribution of the metal in the final product [6]. Given the significant influence of the pre-treatment conditions, continuous work has been carried in this area of research.

The study carried out by Folefoc and Dwyer [51] is in agreement with the earlier results obtained by Kubo et al. [52] on the effect of calcination temperature on the size of the platinum particle, where a higher calcination temperature would result in lower platinum dispersion and larger platinum particles. These results are independent of the type of metal and zeolite support used, as observed by Jao et al. [49] for mordenite-supported Pt and Canizares et al. [15] for Pd incorporated on H-ZSM-5. It was proposed that at higher calcination temperature, the metal ions migrate to the outer surface of the zeolite crystallites, where during reduction, the metal atoms sinter to form large particles [51].

The calcination step is usually carried out under flowing air atmosphere. However, de Araujo and Schmal [53] looked into the effect of calcination temperature on the structural properties of Pt/ZSM-5 catalyst under different conditions. In contrast to earlier findings, the authors reported that a catalyst calcined at 350 ^{o}C presented lower Pt dispersion compared to a catalyst calcined at 550 ^{o}C [53]. Based on a mass spectroscopy analysis, it was observed that the lower temperature was not sufficient to

completely decompose the $[Pt(NH_3)_4]^{2+}$ complex, which leads to platinum agglomeration after reduction with hydrogen [53].

The effect of the reduction conditions on the metal dispersion of supported metal-catalysts has also been investigated [14-15, 49]. It was shown that the dispersion is inversely proportional to the reduction temperature for severe reduction temperatures ($>500\ ^{o}$C). Therefore, the higher the reduction temperature, the tendency for sintering of the reduced metal increases, decreasing the isomerization selectivity of the bifunctional catalyst, as pointed out by Jao et al. [49].

2.4.3 Metal Loading

The balance between the acid and metal site density is important in determining the reactivity of a bifunctional catalyst. The activity of the bifunctional catalyst is not proportional to the amount of metal incorporated onto the zeolite support according to M'Kombe et al. [14] and Canizares et al. [15]. Both studies showed that the metal dispersion is inversely proportional to metal loading based on TEM images [14], CO chemisorption [14] and TPR profiles [15]. The reduction in metal dispersion has been associated with the low performance of the bifunctional catalyst because the metal particles are not exposed to the reactants or that the distance between the metal and acid site is very far from one another. Therefore, a low metal loading with high dispersion will not only lead to a higher activity of the catalyst, but also reduce the cost of the raw material. It is also believed that the metal component should be present in excess in order for the reaction on the acid site to be the rate limiting reaction so that the equilibrium between the saturated and unsaturated species is achieved [14, 47].

2.5 Synthesis of the Bifunctional PtH-MFI Catalyst for Benzene Alkylation Reaction with Ethane

Two bifunctional PtH-ZSM-5 catalysts of different SiO_2/Al_2O_3 ratio (30 and 80) were chosen for the alkylation of benzene with ethane investigated in this study. The preparation steps for the PtH-ZSM-5(30) and PtH-ZSM-5(80) catalysts will be described in detail in this section.

2.5.1 Calcination

The parent catalyst of ZSM-5 with different silicon dioxide (SiO_2) to aluminium oxide (Al_2O_3) ratio in the form of NH_4ZSM-5 was calcined to convert the zeolite catalyst from NH_4^+ into H-form zeolite. Approximately 1 g of NH_4^+ form zeolite ZSM-5 was placed in a crucible, and then heated in a muffle furnace following the temperature profile shown in Figure 2.5.

The heating profile was set using the Carbolite temperature programmer by entering the desired temperature profile for the calcination process. The temperature profile was divided into a few segments. The segment where the temperature remains the same for a certain time is called the dwell, while the temperature rising segment is called the ramp.
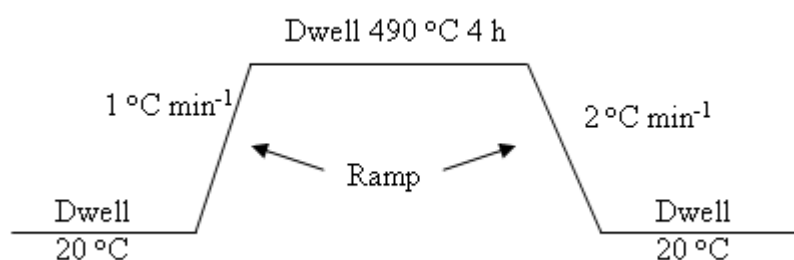
Figure 2.5 – Temperature profile for calcination of NH_4ZSM-5 catalyst

Following the heating of the catalysts, any water residue trapped in the catalysts would be removed. H-ZSM-5 catalyst obtained at the end of the heating process was left to dry in the drying cabinet ($\sim 50^oC$) over the weekend.

2.5.2 Impregnation

In the case of Pt incorporated zeolite catalyst, Pt metal was impregnated onto the H-ZSM-5 catalyst. For this research, Pt loading of 1 wt% was chosen and tetraamineplatinum(II)nitrate, $Pt(NH_3)_4(NO_3)_2$ was used as the platinum precursor.

The amount of platinum precursor required to make 1 wt % PtH-ZSM-5 catalyst can be calculated as shown below:

1 wt % PtH-ZSM-5 catalyst contains 0.99 weight fraction of H-ZSM-5 and 0.01 weight fraction of Pt.

Table 1 – Molecular weight of various components

Component	Molecular Weight (kg kmol^{-1})
Platinum (Pt)	195
Nitrogen (N)	14
Hydrogen (H)	1
Oxygen (O)	16

The molecular weight of $Pt(NH_3)_4(NO_3)_2$ = 387 kg kmol^{-1}

387 g $Pt(NH_3)_4(NO_3)_2 \rightarrow$ 195 g Pt

For 1 g of 1 wt % PtH-ZSM-5,

X g $Pt(NH_3)_4(NO_3)_2 \rightarrow$ 0.01 g Pt

$$\Rightarrow X = \frac{0.01}{195} \times 387 = \underline{0.0198\,g}$$

From the calculation above, it is shown that 0.02 g of $Pt(NH_3)_4(NO_3)_2$ is needed for the preparation of 1 g of 1 wt % PtH-ZSM-5 catalyst.

Pt solution was prepared by mixing 0.02 g of $Pt(NH_3)_4(NO_3)_2$ and 0.8 ml of deionised water, ensuring that the $Pt(NH_3)_4(NO_3)_2$ salt was completely dissolved in water. Then, the solution was added drop by drop using a pipette to the 0.99 g H-ZSM-5 catalysts placed in a crucible. The mixture was left to dry overnight under room temperature. The dried mixture was cracked into powder form using a spatula and was then placed in a crucible for further treatment.

The PtH-ZSM-5 catalyst was calcined in a furnace via the temperature profile shown in Figure 2.6.
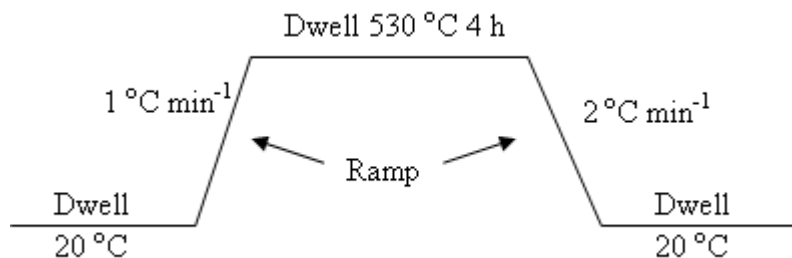
Figure 2.6 - Temperature profile for calcination process

2.5.3 Preparation of Catalyst Fractions

The powdered form catalysts cause a large backpressure (due to lack of voidage in the catalyst bed) which is undesired during the alkylation reaction. Therefore, the powder catalyst is made into the form of small particles referred to as 'fractions' before it was loaded into the reactor.

The catalyst powder samples were pressed into discs, then, crushed and sieved using 250-710 μm meshes, creating size fractions. The catalyst was thus obtained in its final form as used in the reaction studies.

2.6 Conclusion

Zeolites have been extensively used as solid acid catalysts for light alkane activation reactions because of their unique properties; in particular their acidity, microporosity and shape-selectivity. The incorporation of metal or metal oxides onto zeolite catalysts improves their activity in catalysing reactions, but the number of metallic and acidic sites needs to be balanced for optimum performance. The catalyst's active metal ingredient incorporation method and preparation conditions are also important factors to be considered as they affect the activity of the catalyst as well as the selectivity of the products.

A Pt incorporated H-ZSM-5 catalyst was chosen for the current work on benzene alkylation with ethane to produce ethylbenzene. The incorporation of Pt has

been proven to enhance the dehydrogenation reaction of ethane, while the H-ZSM-5 catalyst was reported to be the most promising catalyst, in terms of activity for alkylation reactions. In addition, PtH-ZSM-5 catalysts have also been known to suppress the formation of carbonaceous deposits, which are responsible for catalyst deactivation.

The synthesis of the 1 wt % PtH-ZSM-5 catalyst with SiO_2/Al_2O_3 ratio of 30 and 80 via incipient wetness impregnation method was discussed. The PtH-ZSM-5 catalysts are made in the form of 'fractions' of dimensions between 250-710 μm to prevent large backpressure during the alkylation reaction.

2.7 References

[1]   K. Tanabe, and W.F. Holderich, Applied Catalysis A: General 181 (1999) 399-434.

[2]   E.G. Deruoane, H.Y. He, S.B.D.A. Hamid, and I. Ivanova, Journal of Molecular Catalysis A:Chemical 158 (2000) 5-17.

[3]   M. Guisnet, N.S. Gnep, and F. Alario, Applied Catalysis A: General 89 (1992) 1-30.

[4]   S. Kato, K. Nakagawa, N. Ikenaga, and T. Suzuki, Chemistry letters 3 (1999) 207-208.

[5]   G. Caeiro, R.H. Carvalho, Z. Wanga, M.A.N.D.A. Lemosa, F. Lemos, M. Guisnet, and F.R. Ribeiro, Journal of Molecular Catalysis. A, Chemical 255 (2006) 131-158.

[6]   C. Bigey, and L. Su, Journal of Molecular Catalysis. A, Chemical 209 (2004) 179-187.

[7]   S. Kato, K. Nakagawa, N. Ikenaga, and T. Suzuki, Catalysis Letters 73 (2001) 175.

[8]   D.B. Lukyanov, and T. Vazhnova, Journal of Catalysis 257 (2008) 382-389.

[9]   P. Schulz, and M. Baerns, Applied Catalysis A:General 78 (1991) 15-29.

[10]   S.J. Kulkarni, S.B. Kulkari, P. Ratnasamy, H. Hattori, and K. Tanabe, Applied Catalysis 8 (1983) 43-56.

[11]   D.H. Olson, G.T. Kokotailo, S.L. Lawton, and W.M. Meier, Journal of Physical Chemistry 85 (1981) 2238-2243.

[12] M.A. Uguina, D.P. Serrano, R. Van Grieken, and S. Venes, Applied Catalysis A: General 99 (1993) 97-113.

[13] C. Perego, and P. Ingallina, Catalysis Today 73 (2002) 3-22.

[14] C.M. M'kombe, M.E. Dry, and C.T. O'Connor, Zeolites 19 (1997) 175-179.

[15] P. Canizares, A. De LuCas, F. Dorado, and J. Aguirre, Microporous and Mesoporous Materials 42 (2001) 245-254.

[16] S. Todorova, and B. Su, Journal of Molecular Catalysis A:Chemical 201 (2003) 223-235.

[17] U. Mroczek, K.H. Steinberg, and F. Roessner, Reaction Kinetics and Catalysis Letters 44 (1991) 201-207.

[18] A.V. Smirnov, E.V. Mazin, E.E. Ponomoreva, E.E. Knyazeva, S.N. Nesterenko, and I.I. Ivanova, Benzene Alkylation with Alkanes over Modified MFI Catalysts, Montpellier, France. 2001.

[19] D.B. Lukyanov, and T. Vazhnova, Journal of Molecular Catalysis A: Chemical 279 (2008) 128-132.

[20] D.J. Macquarrie, Philosophical Transactions. Mathematical, Physical, and Engineering Sciences 358 (2000) 419-430.

[21] R.G. Bell. 2001. What are Zeolites? [online] Available from: http://www.bza.org/ [Accessed 7 May 2007].

[22] S. Van Dock. 2002. Adsorption, Diffusion and Reaction Studies of Hydrocarbons On Zeolite Catalysts In Inorganic Chemistry & Catalysis. Utrecht University. 168.

[23] J.W. Ward, Journal of Catalysis 9 (1967) 225-236.

[24] E. Roland, and P. Kleinschmit. 1996. Zeolites. In Ullmann's Encyclopedia of Industrial Chemistry B. Elvers, Hawkins, S., editor. VCH,Weinhem. 314-362.

[25] X. Wu. 2003. Zeolite Catalysts Bound With Silica and Alumina. In Chemical Engineering. Texas A&M University.

[26] B.K. Marcus, and W.E. Cormier, Chemical Engineering Progress 95 (1999) 47-53.

[27] W.M. Meier, and D.H. Olson, Atlas of Zeolite Structure Types. Butterworths, 1987.

[28] F.R. Ribeiro, F. Alvarez, F.L. Henriques, J.M. Lopes, and M.F. Ribeiro, Journal of Molecular Catalysis A: Chemical 96 (1995) 245-270.

[29] G. Perot, and M. Guisnet, Journal of Molecular Catalysis 61 (1990) 173-196.

[30] A. Dyer, An Introduction To Zeolite Molecular Sieves. John Wiley and Sons, 1988.

[31] A. Corma, Journal of Catalysis 216 (2003) 298-312.

[32] L.Y. Fang, S.B. Liu, and I. Wang, Journal of Catalysis 185 (1999) 33-42.

[33] L.D. Rollman, and D.E. Walsh, Journal of Catalysis 56 (1979) 139-140.

[34] R. Lu, H. Tangbo, Q. Wang, and S. Xiang, Journal of Natural Gas Chemistry 12 (2003) 56-62.

[35] C.H. Christensen, K. Johannsen, I. Schmidt, and C.H. Christensen, Journal of the American Chemical Society 125 (2003) 13370-13371.

[36] M. Hartmann, Angewandte Chemie International Edition 43 (2004) 5880-5882.

[37] A.K. Rovik, A. Hagen, I. Schmidt, S. Dahl, I.B. Chorkendorff, and C.H. Christensen, Catalysis Letters 109 (2006) 153-156.

[38] P.A. Jacobs, Zeolites 1 (1981) 161-168.

[39] Y.S. Tao, H. Kanoh, and K. Kaneko, Advanced Materials 17 (2005) 2789-2791.

[40] C.H. Baerlocherm, and L.B. McCusker. Database of Zeolite Structures.

[41] L. Song, and L.V.C. Rees, Microporous and Mesoporous Materials 35-36 (2000) 301–314.

[42] G.T. Kokotailo, S.L. Lawton, and D.H. Olson, Nature 272 (1978) 437-438.

[43] E.M. Flanigen, J.M. Bennett, R.W. Grose, J.P. Cohen, R.L. Patton, and R.M. Kircher, Nature 271 (1978) 512-516.

[44] R.E. Richards, and L.V.C. Rees, Langmuir 3 (1987) 335-340.

[45] L.B. Young, S.A. Butter, and W.W. Kaeding, Journal of Catalysis 76 (1982) 418-432.

[46] D.E. Walsh, and L.D. Rollman, Journal of Catalysis 56 (1979) 195-197.

[47] M.D. Romero, A. De LuCas, J.A. Calles, and A. Rodriguez, Applied Catalysis : A General 146 (1996) 425-441.

[48] L. Qian, and Z.F. Fan, Colloids and Surfaces A: Physicochemical and Engineering Aspects 180 (2001) 311-316.

[49] R.M. Jao, L.J. Leu, and J.R. Chang, Applied Catalysis:A General 135 (1996) 301-316.

[50] M.D. Romero, J.A. Calles, and A. Rodriguez, Industrial & Engineering Chemistry Research 36 (1997) 3533-3540.

[51] G.N. Folefoc, and J. Dwyer, Journal of Catalysis 136 (1992) 43-49.

[52] T. Kubo, H. Arai, H. Tominaga, and T. Kunugi, Bulletin of the Chemical Society of Japan 45 (1972) 607-612.

[53] L.R.R. De Araujo, and M. Schmal, Applied Catalysis A:General 203 (2000) 275-284.

Chapter 3 : Benzene Alkylation with Ethane over PtH-ZSM-5 Catalysts

3.1 Introduction

The complexity of the reaction pathway of benzene alkylation with light alkanes was pointed out by Derouane et al. [1], Bigey and Su [2], and Smirnov et al. [3-4]. Smirnov et al. [3] highlighted that the reaction pathway was determined by the alkylating agent, as well as the types of catalysts used. Therefore, in this chapter, the evaluation of the performance of PtH-ZSM-5 catalysts of different acidity (different SiO_2/Al_2O_3 ratio) on the alkylation of benzene with ethane (Equation 3.1) will be discussed in detail.

$$\text{benzene} + C_2H_6 \rightleftharpoons \text{ethylbenzene}(C_2H_5) + H_2$$

(3-1)
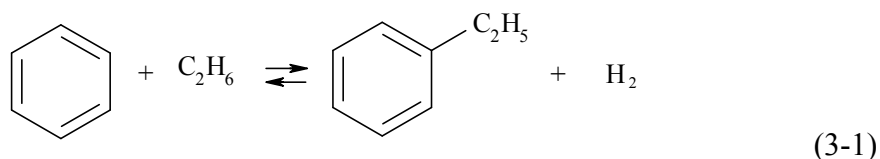
3.2 Catalyst and Process Development in the Commercial Ethylbenzene Production Process

The history of EB manufacturing goes all the way back to the 1930s when the alkylation reaction was performed by reacting benzene and ethene in the presence of a Friedel-Crafts catalyst (i.e. $AlCl_3$-HCl) under mild conditions of 160 ^{o}C [5]. Advances to the EB production technology were made to avoid the use of corrosive liquid-phase acidic catalysts. In the 1940s, the first solid acid catalyst was introduced to enhance the alkylation of benzene with ethene in the vapour phase.

Zeolites were first used as catalysts for alkylation in the 1960s when zeolites with large pores such as REX, HY and REY were used to catalyse the EB formation reaction. The first industrial application of zeolites as catalysts for the production of EB was introduced in 1976. However, commercialisation was achieved in 1980 by Mobil-Badger as the 'second generation Mobil-Badger process' with improved catalyst

lifetime and yield of EB [6] over earlier processes. Since then, the Mobil-Badger vapour phase process is the most widely used zeolite catalysed EB manufacturing process [6].

In later years, developments in EB production focused on the liquid-phase process, where zeolites were catalysing the alkylation reaction of benzene with ethene. Example of the liquid-phase alkylation process is the Mobil-Badger EBMax process with MCM-22 as the zeolite catalyst. In 1989, Unocal-ABB Lummus Crest introduced a liquid-phase process based on a modified Y-zeolite which yields 99.6 % of EB [5-6]. According to Perego and Ingallina [5], 76 % of EB production processes are based on zeolite catalysts, while the remaining 24 % still uses $AlCl_3$-HCl technology. A summary of the EB production processes based on benzene alkylation with ethene was reviewed by Degnan et al. [6] and Perego and Ingallina [5].

The possibility of direct benzene alkylation with light alkanes was first reported by Olah et al. [7], however with the use of fluoroantimonic acid (HF-SbF_5) as the catalyst. Later on, the use of bifunctional zeolite catalysts for benzene alkylation with ethane was reported [3, 8-11]. Detailed discussion on the alkylation of benzene with light alkanes will be presented in the next section.

3.3   Benzene Alkylation with Light Alkanes

The alkylation of benzene with light alkanes has been extensively studied [3-4, 8-11]. Based on previous investigations, it was reported that the direct alkylation of benzene with alkane was possible over a dual-functional catalyst, where metal and acid centres allowed the dehydrogenation and protonation of the light alkanes respectively, to take place at the same time [4, 8]. In comparing the reactivity of different alkanes for the benzene alkylation reaction over modified ZSM-5 zeolite catalyst, it was shown that the reactivity of the alkanes increased as the chain length was increased [3].

A general reaction network (Figure 3.1) for the alkylation of benzene with light alkanes was proposed by Smirnov et al. [3]. In addition to the main alkylation reaction, side reactions also took place simultaneously, influencing the selectivity of the desired product. Therefore, an understanding of the reaction mechanism for benzene alkylation

is necessary in order to suppress these side reactions and maximise the yield of the desired product.
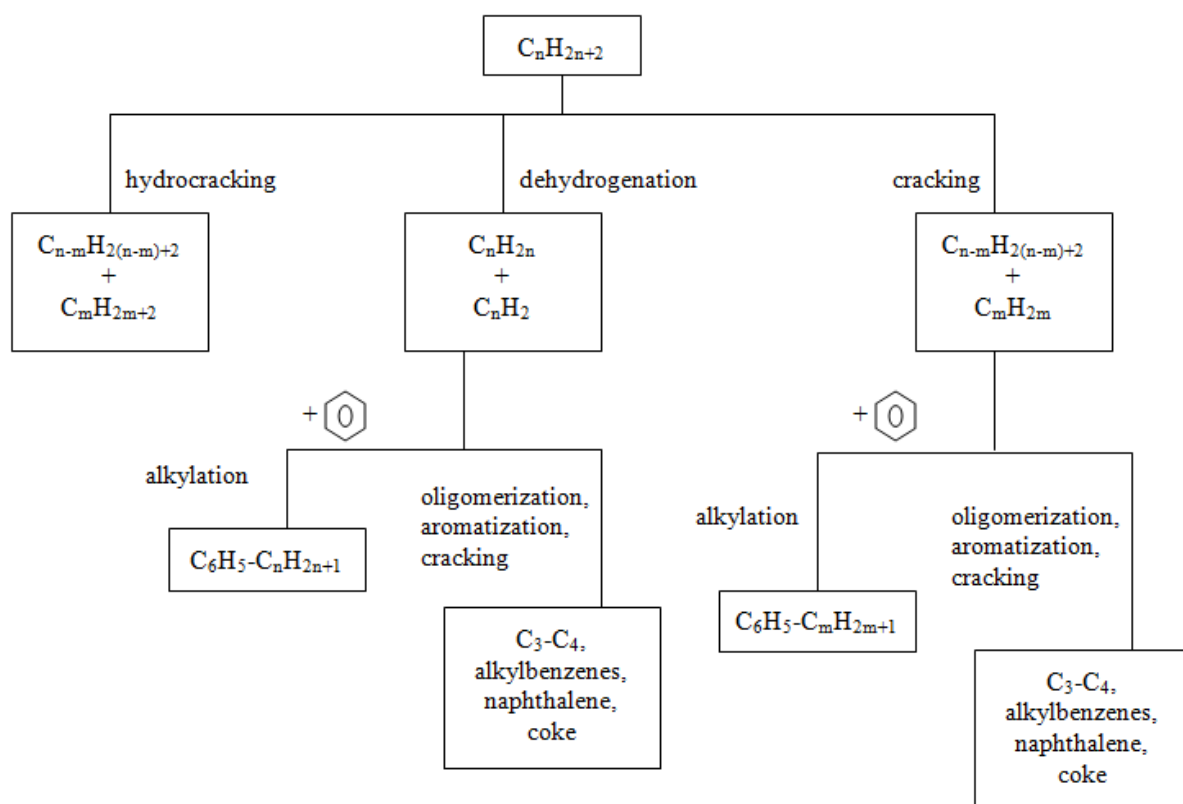
Figure 3.1 - General reaction network for benzene alkylation with light alkanes
Adapted from ref [3]

3.3.1 Conversion of Light alkanes into Light Alkenes and Aromatic Hydrocarbons

Direct benzene alkylation with light alkanes on a bifunctional catalyst includes the initial dehydrogenation reaction of light alkanes forming light alkenes, followed by alkylation of benzene with the alkenes produced [2, 4, 8, 12]. Similarly, in aromatization reactions, short chained alkanes are first dehydrogenated to form light alkenes, then aromatized to form aromatics [12-15]. Kato et al. [8] stated that dehydrogenation of light alkanes is the key reaction in the ethylation of benzene reaction. It was demonstrated that the reactivity of zeolite catalysts in alkane activation was improved significantly by modification with Pt, Ga or Zn [4, 15-16].

The first step in the alkylation reaction with alkanes would be the activation of light alkanes prior to further reactions. According to Buckles and Hutchings [17], the activation of light alkanes on a bifunctional catalyst is a two step reaction that could take place either at the interface between the metal and the zeolite or on the metal oxide [17]. The activation of light alkanes has been extensively studied [1, 15, 17-18] and different reaction mechanisms were proposed. All reaction mechanisms suggested the formation of mono-alkenes from the corresponding feed alkanes [19].

In studying the aromatization reaction of short-chain alkanes on zeolite catalysts, Guisnet and Gnep [18] proposed a reaction mechanism for the activation of propane dehydrogenation reaction carried out over Ga/H-ZSM-5 bifunctional catalyst. The authors suggested that propane was initially dissociated with the formation of gallium hydride and gallium alkoxide species. Then, the propyl carbenium ion was rapidly exchanged with zeolite protons through an alkyl surface migration reaction before propene desorbed from the zeolite surface [18].

In a later study by Derouane et al. [1], the authors reported that the activation of propane by Ga/H-ZSM-5 catalyst occurred via a bifunctional mechanism that involved the formation of cylic protonated pseudo-cyclopropane (PPCP) intermediate. The PPCP intermediate was formed via propane interaction with the Ga^{3+} and O^{2-} ion pair via a positively and negatively charged hydrogen atom respectively, and was further converted into a pseudo-cyclopropane entity which was protonated by the Brønsted acid [1]. The PPCP intermediate then decomposed to form CH_4, C_2H_6, H_2, and methyl, ethyl and propyl carbenium ions which could react with benzene to form alkylbenzenes [1]. The same activation mechanism was also proposed by Bigey and Su [2] when the authors investigated the alkylation of benzene with propane over Ga-modified H-ZSM-5 catalyst.

In the presence of pure acidic catalyst only, alkanes are transformed into alkenes via protolytic dehydrogenation or cracking reactions. The activation of light alkanes can be explained by a monofunctional acid mechanism, which differs from the bifunctional mechanism described earlier. The monofunctional reaction mechanism proposed that alkanes are protonated on Brønsted acid sites of the zeolite catalyst to form the unstable transition state carbonium ions. For propane activation, the carbonium ions were

decomposed to form methane and $C_2H_5^+$ via β-scission, to $C_3H_7^+$ via dehydrogenation or to CH_3^+ and C_2H_6, depending on whether the proton attacks the C-C bond or the C-H bond of the reacting alkane [2, 15, 17].

It was reported by Smirnov et al. [3] that the first reaction step for light alkanes could proceed via three possible routes; dehydrogenation, cracking or hydrocracking. The alkane activation on the strong Brønsted acid sites (H^+) of H-MFI catalysts can be described by the formation of the carbonium ion transition state which will then be transformed either by dehydrogenation (Equation 3.2) or cracking (Equation 3.3) reaction.

$$C_nH_{2n+2} \xrightarrow{H^+} \{C_nH_{2n+3}\}^+ \to \{C_nH_{2n+1}\}^+ + H_2 \qquad (3\text{-}2)$$

$$C_nH_{2n+2} \xrightarrow{H^+} \{C_nH_{2n+3}\}^+ \to \{C_{n-m}H_{2(n-m)+2}\}^+ + \{C_mH_{2m+1}\}^+ \qquad (3\text{-}3)$$
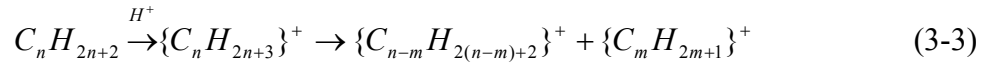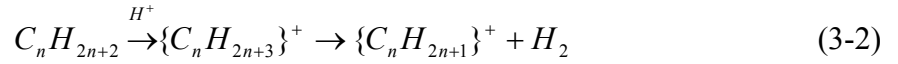
On a metal containing system however, dehydrogenation reaction became the main reaction pathway [3]. The general equation for light alkane dehydrogenation on metal (M) site [3] is as shown below :

$$C_nH_{2n+2} \xrightarrow{M} C_nH_{2n} + H_2 \qquad (3\text{-}4)$$

Alkenes formed on the metal site can be further protonated on the acidic site (H^+) to give carbenium ion (Equation 3.5) which will then be involved in further reactions.

$$C_nH_{2n} + H_2 \xrightarrow{H^+} \{C_nH_{2n+1}\}^+ \qquad (3\text{-}5)$$

The study by Smirnov et al. [3] showed that the reaction pathway for the activation of light alkanes depend on the catalyst in the reaction system. The reactions described by Equation 3.4 and 3.5 takes place on a mixed catalyst system where the metallic and protonic sites are further apart. In the case where the acidic and metallic sites are in close proximity, such as in a bifunctional catalyst, the dehydrogenation and protonation steps occurred on the bifunctional metal-acidic centres (M, H^+) [3], which resulted in a direct formation of a very reactive carbenium ion:

$$C_nH_{2n+2} \xrightarrow{M,H^+} \{C_nH_{2n+1}\}^+ + H_2 \qquad (3\text{-}6)$$
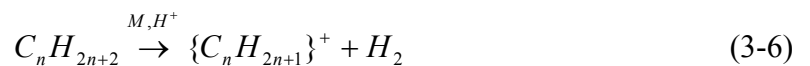
Alkenes formed from the protolysis of light alkanes and/or from hydrogen transfer reactions on the metal centres are very reactive in acid catalysed systems [15]. In addition to reacting with benzene to form alkylbenzene, these alkenes can go through a series of oligomerization, cyclization, and cracking steps on the acidic sites of the zeolite catalyst to form aromatic hydrocarbons [13, 15, 17, 20]. The CH_3^+ carbocation and $C_2H_5^+$ carbenium ion can react further with alkenes and alkanes while the $C_3H_7^+$ carbenium ion can be oligomerized by reaction with alkeneic intermediates.

In addition to promoting the dehydrogenation of light alkanes, the incorporation of metal species on acidic catalysts enhances side reactions such as the hydrogenolysis reaction that takes place on the metallic site of a bifunctional catalyst. Steinberg et al. [20] reported that ethane was converted to methane via hydogenolysis on the Pt surface. Even though Pt is believed to catalyse efficiently the dehydrogenation of ethane, it also supports the hydrogenolysis of alkanes and higher aromatics [14]. It had been reported that hydrogenolysis is a structural sensitive reaction as this reaction depends on the metal type and metal surface [21], as well as metal particle size of the active phase [22].

Hydrogenolysis suppresses the formation of light alkenes via dehydrogenation, which is a disadvantage to the main alkylation reaction as fewer alkene intermediates will then react with benzene to produce alkylbenzenes [23]. The reaction mechanism of ethane hydrogenolysis (Equation 3.7 − 3.10) proposed by Nayssilov [21] was initiated via dissociative adsorption of ethane by breaking the C-H bond and then the obtained ethyl radical undergoes dehydrogenation to the basic surface intermediate $C_2H_x(a)$. This was followed by breaking of the C-C bond in the intermediate and the formation of adsorbed particles containing one carbon atom [21].

$$C_2H_6(g) = C_2H_5(a) + H(a) \tag{3-7}$$

$$C_2H_5(a) + H(a) = C_2H_x(a) + (6-x)H(a) \tag{3-8}$$

$$C_2H_x(a) \rightarrow CH_y(a) + CH_z(a) \tag{3-9}$$

$$CH_y(a) + CH_z(a) + (8-x)H(a) \rightarrow 2CH_4(g) \tag{3-10}$$
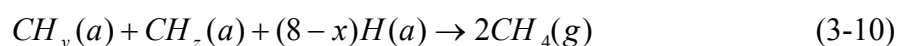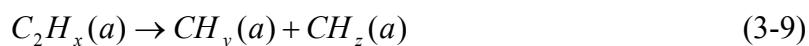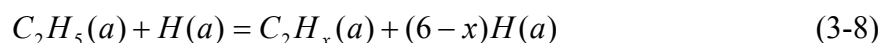
Besides hydrogenolysis, oligomerization and cracking are other side reactions that take place during alkylation. Smirnov et al. [3] mentioned that on Pt incorporated

ZSM-5 type catalysts; the main reaction pathway includes hydrocracking. Hydrocracking produces methane, thus lowering the concentration of ethene for further reactions. The oligomerization of light alkenes leads to the formation of larger alkenes, which will then crack into smaller alkenes. These smaller alkenes will act as alkylating agents for reaction with benzene on the acid sites.

As oligomerization is said to occur faster than dehydrogenation [17], it causes a major problem to most alkylation reactions. Oligomerization is responsible for the growth of bulky molecules in the product stream. These bulky molecules could prevent further reactions from taking place if they are adsorbed on these active sites or if they block access of reactants to these sites.

3.3.2 Benzene Alkylation with Light Alkanes

As the activation of light alkanes takes place on the metallic centre of the bifunctional catalyst, aromatic formation occurs at Brønsted acid sites. The carbenium ions or alkenes produced from the activation of light alkanes (described in the previous section) act as alkylating agents for benzene alkylation reactions.

Derouane et al. [1] reported that the benzene alkylation reaction can be initiated by benzene activation. During the benzene activation process, benzenium ion is formed by benzene protonation on strong acid sites (Equation 3.11). However, if benzene was adsorbed on weak acid sites, it cannot be activated, and the adsorbed carbenium ions cannot react with benzene. The benzenium ion abstracts a hydride ion from the nearest alkane molecule resulting in the formation of alkyl carbenium ion and cyclohexadiene [1]. This benzene activation scheme was supported by Caeiro et al. [15] when investigating the alkylation of benzene with light alkanes over a bifunctional catalyst.

$$\text{(3-11)}$$

33
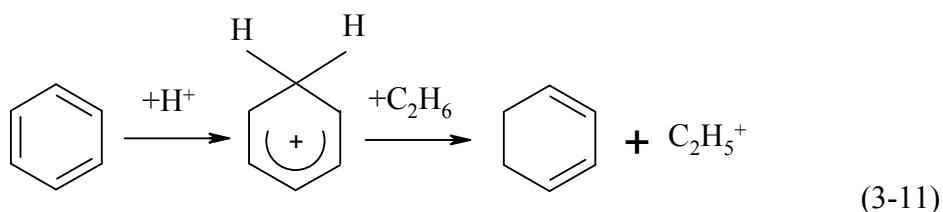
Alkylbenzenes are formed by reactions of benzene with alkyl carbenium ions. Equation 3.12 shows the reaction of carbenium ion with benzene to form alkylbenzene, the desired product.

$$\{C_nH_{2n+1}\}^+ + C_6H_6 \xrightarrow{-H^+} C_6H_5 - C_nH_{2n+1}$$

(3-12)
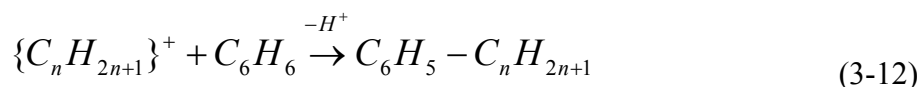
As pointed out earlier, the reaction pathway for light alkanes is dependent on the catalytic system of the alkylation reaction. This suggests that the final product composition will depend on the activation of light alkanes. Activation of propane on a pure acidic catalyst forms propyl-, ethyl- and methylcarbonium ions which further lead to the formation of propyl-, ethyl- and methylbenzenes. Modification of the acidic zeolite catalyst with a metal species increases the activity of the catalyst and selectivity to the desired alkylbenzene as the metal-acid centres can act together to dehydrogenate and protonate the alkane at the same time.

Ethylbenzene formed from the alkylation of benzene with ethene may also undergo polyalkylation reaction to produce diethylbenzenes (DEB) and triethylbenzenes (TEB) as proposed by Perego and Ingallina [5]. The authors pointed out that the polyethylbenzenes can be recycled back to the reactor where transalkylation takes place to form EB until thermodynamic equilibrium is reached [5]. Over a bifunctional zeolite catalyst, EB can be transformed into other products via secondary reactions as described by Moreau et al. [24]. The alkylation of benzene is a reversible reaction. At high reaction temperature and reactant conversion, dealkylation of alkylbenzenes is favoured. This is responsible for the large amount of alkenes in the product stream [15].

The isomerization of EB into xylene isomers has been said to occur through a bifunctional mechanism, and the rate of reaction was dependant on both metallic and acidic sites [24]. Hydrogen was produced when light alkanes are dehydrogenated to alkenes. In the presence of hydrogen, hydrogenolysis of EB takes place on the metallic site of the bifunctional catalyst leading to the formation of toluene and methane. The disproportionation of EB into benzene and diethylbenzene and the transalkylation reaction of EB and xylene into ethyltoluenes and toluene or to dimethylethylbenzenes and benzene are other side reactions that involve the consumption of EB.

The side reactions described could potentially decrease the yield and selectivity of the desired product, EB. Therefore, knowledge of the main and side reaction pathways is required to yield a stable and highly selective reaction. To achieve this, a detailed kinetic study of the benzene alkylation with ethane was carried out. The experimental set-up and results obtained will be discussed in the following sections.

3.4   Experimental Materials and Methodology

3.4.1   Experimental Set-up (Preparing the catalytic rig)

In this study, the alkylation reaction of benzene with ethane was catalysed by Pt incorporated H-ZSM-5 catalysts with different SiO_2/Al_2O_3 ratios. The steps taken to prepare the PtH-ZSM-5(30) and PtH-ZSM-5(80) catalysts were discussed in Chapter 2. In the following section, the operating procedure for the benzene alkylation reaction is described.

3.4.1.1   *Charging the reactor*

The prepared catalyst fractions were loaded into the reactor so that the reaction gas could flow through the catalyst bed. A layer of quartz wool was filled at the bottom of the reactor to support the carborundum which was placed above the quartz wool layer. The catalyst was positioned in the centre of the reactor in between a top and bottom layer of quartz wool which separated the catalyst from the carborundum. The quartz wool that was placed on the top and bottom part of the catalyst was flattened to make a flat bed. A thermocouple, used to measure the temperature of the catalyst bed, was positioned on the upper layer of the quartz wool between the carborundum and the catalyst, and not in the catalyst bed to prevent breaking the catalyst particles. At the upper most part of the reactor, another layer of carborundum was placed. Carborundum layers work to reduce the temperature gradient between the feed gas and the catalyst layers and also ensures constant reaction temperature along the catalyst bed. Figure 3.2 illustrates the schematic diagram of the reactor profile:
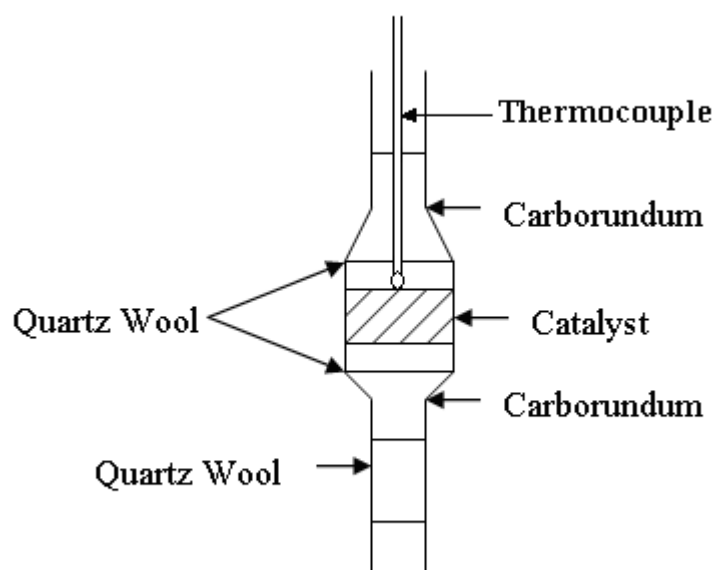
Figure 3.2 - Reactor Profile

3.4.1.2 *Installing the reactor*

The reactor was installed in a furnace, connected to gas pipelines. When the reactor was properly positioned in the middle of the furnace, nitrogen gas was allowed to flow through the reactor. Simultaneously, pipeline connections and joints were checked for gas leakage with soap foams.

Glass wool was used to prevent heat loss at the top and bottom of the furnace in addition to preventing the reactor from being in contact with the edge of the furnace. The outlet of the reactor was not protected and this could lead to heat loss and condensation of products. To avoid condensation of products, naked sections of glass lines were wrapped with glass wool and after that, with heating tape (set to 70-75 ^{o}C).

3.4.2 Catalyst Pre-treatment

Prior to the reaction taking place, catalysts were activated overnight. Activation of the catalyst was done by flowing air through the catalyst bed under the temperature profile shown in Figure 3.3. The airflow rate was 30 ml min^{-1} and was maintained by a purgemeter at a constant flow rate throughout the whole activation process. The initial

temperature was 20 °C and the temperature was increased to 530 °C at a rate of 1 °C min^{-1}. During the heating process, water was released. Therefore, to avoid damaging the catalyst structure, the rate of heating was kept low. The catalyst was kept at 530 °C for 4 hours before it was reduced to 200 °C at a rate of 2 °C min^{-1}.
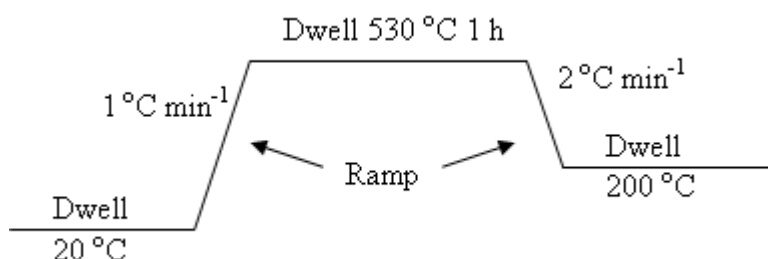
Figure 3.3 - Catalyst Activation with Air Temperature Profile

The next step after activation in air was hydrogen pre-treatment. However, before H$_2$ was allowed to flow through the reactor, the system was purged with N$_2$ to remove all the air from the furnace so that an explosion resulting from the mixture of air and H$_2$ does not occur. N$_2$ was set to a flow rate of 50 ml min^{-1} using a purgemeter, and was left for an hour to purge the reactor.

If the traces of O$_2$ in the reactor were negligible, the flow of N$_2$ was switched to H$_2$ at a flow rate of 50 ml min^{-1}. The hydrogen reduction step was carried out following a temperature profile shown in Figure 3.4.
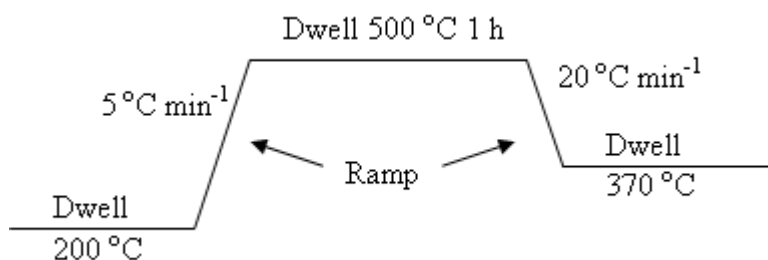
Figure 3.4 – Hydrogen Treatment Temperature Profile

3.4.3 Catalytic Experiments

3.4.3.1 *Reaction gases mixture set-up*

The reaction gases were mixed in the by-pass line so that the gas mixtures were at the right composition and condition before being in contact with the catalyst. The ratio of benzene to ethane concentration (mol %) in the experiment was 1:9. Ethane gas (Grade N2 99.99 % purity) was bubbled through a perforated tube into a saturator that contained liquid benzene (99.9+ % HPLC grade). Ethane flow rate was kept constant at 16 ml min^{-1} while the saturator temperature was maintained at 20 ^{o}C. The ratios of the reactants are affected by the vapour pressure of the volatile liquid reactant, which is highly influenced by temperature. As a result, the saturator is placed in a thermo flask to keep the liquid phase benzene at a specific temperature throughout the experiment. At 20°C, atmospheric pressure, the ratio of ethane to benzene (mol %) is 1:9.

3.4.3.2 *Kinetic Studies*

Benzene alkylation with ethane was carried out at atmospheric pressure in a continuous flow reactor at 370 ^{o}C. The reaction time starts once the gas mixtures were allowed through the reactor. Catalyst loading of 500 mg was used. The gas stream was redirected to the reactor channel once the desired composition of the reactant mixture was achieved. The first GC injection was made at 1 hour on stream, on the Varian CP-3800GC. Further injections were made automatically at a certain time interval. Before any injection was made, the flow rates of ethane and benzene were determined. After being run for different times-on-stream the reactor was purged with N$_2$ (30 ml min $^{-1}$) for 0.5 h at the reaction temperature and then cooled down to room temperature in a nitrogen atmosphere. The catalysts were then unloaded from the reactor for further analyses.

3.4.3.3 *Analysis of products*

The product composition was analyzed by on-line GC, which was equipped with a molecular sieve 13X packed column and a thermal conductivity detector (TCD) for analysis of H2, and a 25 m long PLOT Al$_2$O$_3$/KCl capillary column with a flame ionization detector (FID) for analysis of hydrocarbons (argon was used as a carrier gas in both columns). The GC was calibrated once a year to ensure accurate analysis of

product compositions. An example of a typical GC trace obtained from the TCD and FID detector is shown in Appendix A1.

3.5 Calculations

3.5.1 Conversion and selectivity calculations

The feed conversion is defined as the percentage of total products produced from the initial feed reactant:

$$X_i = \frac{C_{i0} - C_i}{C_{i0}} \times 100\%$$
(3-13)

where C_{i0} is the initial concentration of species i; C_i is the concentration of species i in the reaction mixture.

Therefore, benzene conversion was calculated based on the ratio of the total amount of benzene converted into aromatics to the total amount of benzene fed into the reactor:

$$X_{ben} = \frac{\sum C_{AR}}{\sum C_{AR} + C_B} \times 100\%$$
(3-14)

where C_{AR} is the aromatic product concentration; C_B is the concentration of benzene in the reaction mixture.

Likewise, ethane conversion was determined from the amount of ethane converted during the alkylation reaction, i.e. the ratio of ethane converted to the total ethane feed.

$$X_{C2} = \frac{\sum C_i}{\sum C_i + C_{C2}} \times 100\%$$
(3-15)

where C_i is the product concentration, and C_{C2} is the ethane concentration

In this work, two different selectivities were defined; the selectivity of products formed from ethane, S_{C2} (Equation 3.16) and the selectivity of products formed from benzene, S_B (Equation 3.17).

$$S_{C2} = \frac{C_i}{100 - C_B - C_{C2}} \times 100\%$$
(3-16)

$$S_B = \frac{C_i}{\sum C_{AR}} \times 100\% \qquad (3\text{-}17)$$

where C_{AR} is the concentration of aromatic products.

The reaction yield is the amount of desired product formed in a chemical reaction. Therefore, in the benzene alkylation reaction, the yield is the total amount of EB formed (Equation 3.18).

$$Y = \frac{C_{EB}}{\sum C_{AR} + C_B} \times 100\% \qquad (3\text{-}18)$$

3.5.2 Thermodynamic Conversion Calculations

The alkylation of benzene with ethane over bifunctional zeolite catalysts is a two-step reaction which involves the dehydrogenation of ethane on the metallic centre and the alkylation of benzene with ethene on acidic sites. Both reactions are reversible reactions governed by thermodynamic equilibrium. Therefore, the thermodynamic equilibrium conversion of these reactions should be known in order to analyse the performance of the catalyst used. Detailed calculations for the equilibrium conversion of the dehydrogenation and alkylation reactions are presented in Appendix A2.

The enthalpy, ΔH and entropy, ΔS of the reaction at a specific temperature can be calculated using the standard enthalpy and entropy values given in Table 3.1.

Table 3-1 – Thermodynamic data at 298 K [25]

Components	Specific Heat Capacity, Cp (J mol^{-1} K^{-1})	Enthalpy, ΔH (J mol^{-1})	Entropy, ΔS (J mol^{-1} K^{-1})
Ethane	52.5	-84000	229.12
Ethene	42.9	52400	219.3
Hydrogen	28.8	0	130.57
Benzene	81.67	82880	269.3
EB	128.41	29920	360.63

The standard enthalpy and entropy of a reaction can be calculated using the equations below:

$$\Delta H_{rxn}(298K) = \Delta H_{products} - \Delta H_{reac\tan t} \qquad (3\text{-}19)$$

$$\Delta S_{rxn}(298K) = \Delta S_{products} - \Delta S_{reac\tan t} \qquad (3\text{-}20)$$

For calculation of enthalpy and entropy of reaction at a specific temperature, the following equations were used:

$$\Delta H_{rxn}(T_{rxn}) = \Delta H_{rxn(298K)} + C_{p(products-reac\tan ts)} \times (T_{rxn} - T_{298K}) \qquad (3\text{-}21)$$

$$\Delta S_{rxn}(T_{rxn}) = \Delta S_{rxn(298K)} + C_{p(products-reac\tan ts)} \times \ln\left(\frac{T_{rxn}}{T_{298K}}\right) \qquad (3\text{-}22)$$

The equilibrium constant (Equation 3.24) can be determined using the Gibbs free energy equation (Equation 3.23):

$$\Delta G_{rxn} = \Delta H_{rxn} - T_{rxn}\Delta S_{rxn} \qquad (3\text{-}23)$$

$$\Delta G_{rxn}(T_{rxn}) = -RT_{rxn}\ln K_{p(rxn)} \qquad (3\text{-}24)$$

3.5.2.1 Dehydrogenation of ethane

The equilibrium conversion of the dehydrogenation of ethane (Equation 3.24) was determined from the pure ethane feed.

$$C_2H_6 \;\rightleftarrows\; C_2H_4 + H_2 \qquad (3\text{-}25)$$

The calculation for the conversion of ethane dehydrogenation reaction gives an equilibrium conversion of 0.52 % at reaction temperature of 370 $^{\circ}$C. (See Appendix A2-2)

3.5.2.2 Alkylation of benzene with ethane

The alkylation reaction of benzene with ethane (Equation 3.25) was carried out with feed ratio of 90 mol% of ethane and 10 mol% of benzene. The same calculation steps were followed to determine the equilibrium conversion of the alkylation reaction. The equilibrium conversion was calculated to be 13.2 %. (See Appendix A2-1)

41

$$\text{(benzene)} + C_2H_6 \rightleftharpoons \text{(ethylbenzene, } C_2H_5) + H_2$$

(3-26)
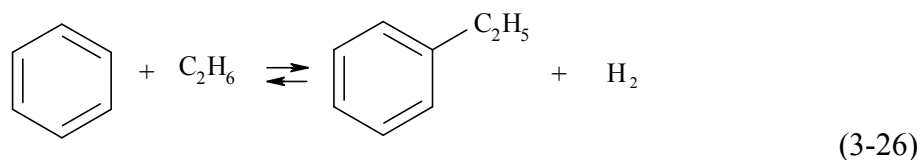
3.6 Results and Discussions

The alkylation of benzene with ethane was carried out over two different 500 mg loadings of PtH-ZSM-5 catalyst with SiO_2/Al_2O_3 ratios of 30 and 80 respectively. The ratio of benzene to ethane concentration (mol %) in this experiment was 1:9. The experimental data for benzene alkylation with ethane are presented in Appendix A3.

3.6.1 Effect of time-on-stream (TOS) on the performance of the 1 wt% PtH-ZSM-5(30) catalyst

On the plot:
$y = 12.22 + 8.67\, e^{-0.035t}$

$y = 2.69 + 4.18\, e^{-0.079t}$
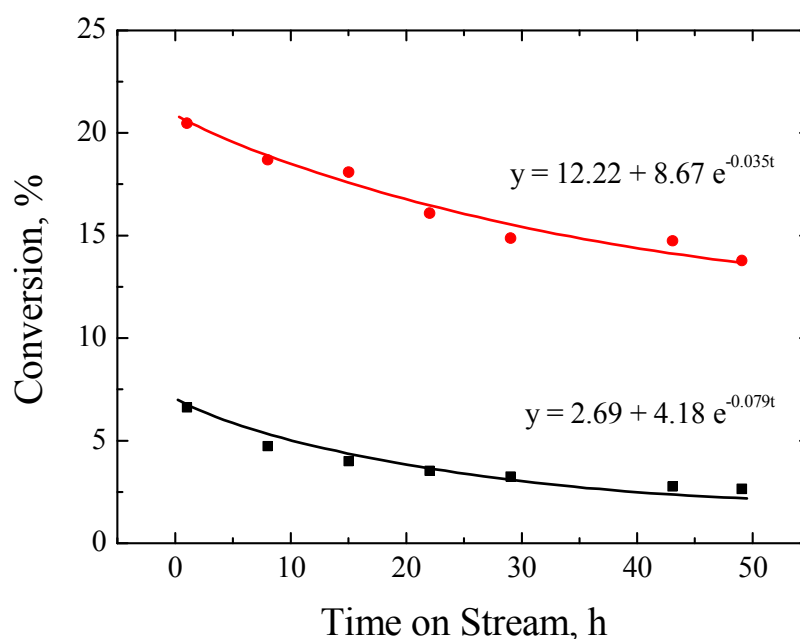
Figure 3.5 – Effect of TOS on ethane (-■-) and benzene (-●-) conversion

Figure 3.5 demonstrates the performance of the PtH-ZSM-5(30) catalyst used in this work for benzene alkylation with ethane. The activity of the PtH-ZSM-5(30) catalyst decreased with TOS, as shown by the decreasing benzene and ethane conversion with TOS. The conversion of ethane decreased more rapidly compared to

the drop in benzene conversion during the 48 h on-stream as demonstrated by the fitted exponential decay time constants of 0.079 ± 0.009 h^{-1} for ethane and 0.035 ± 0.014 h^{-1} for benzene. This demonstrates the unstable performance of the PtH-ZSM-5(30) catalyst. The conversion of benzene is higher than the conversion of ethane, since ethane is available in excess, in the feed stream, compared to benzene.

As discussed in the literature review, ethane undergoes dehydrogenation (Equation 3.26) over platinum sites of the bifunctional zeolite catalyst. At the reaction temperature (370 $^{\circ}$C), equilibrium conversion for the dehydrogenation of ethane was calculated to be 0.52 %. Ethane conversion was observed to be higher than the equilibrium conversion (Figure 3.5) for the PtH-ZSM-5(30) catalyst. On highly acidic catalysts, such as PtH-ZSM-5(30), the alkylation of benzene with ethene would be enhanced, hence pulling the ethane dehydrogenation reaction forward.

$$C_2H_6 \rightleftharpoons C_2H_4 + H_2$$

$$(3\text{-}27)$$
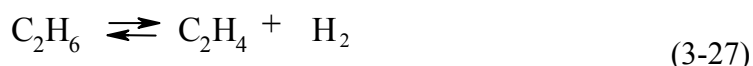
Similarly to the conversion of ethane, benzene conversion into EB was also limited by thermodynamics, and the equilibrium conversion (Equation 3.27) was calculated to be 13.5 % (Section 3.5.2.2). The conversion of benzene over the PtH-ZSM-5(30) catalyst exceeded this equilibrium conversion to give a benzene conversion of 20.5 % at the start of the reaction, suggesting that, apart from the transformation of benzene into EB, benzene was also converted into other aromatic products.

$$(3\text{-}28)$$
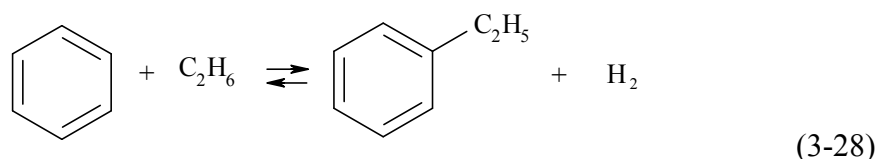
Figure 3.6 shows the variation of ethene concentration in the product stream with TOS. The increasing concentration of ethene could be due to the enhanced alkylation of benzene on the highly acidic PtH-ZSM-5(30) catalyst, as discussed earlier. The high concentration of ethene led to side reactions such as oligomerization and cracking which produces large amount of alkenes. It was previously reported that coking occurred rapidly from alkenes due to the high reactivity of the adsorbed species

(carbenium ions) formed from alkenes [26]. Therefore, the low stability of the PtH-ZSM-5(30) catalyst, illustrated by the drop in reactant's conversions (see Figure 3.5), could result from the poisoning of the complex metal-acid centre of the PtH-ZSM-5(30) catalyst by the irreversibly chemisorbed coke precursors [27].
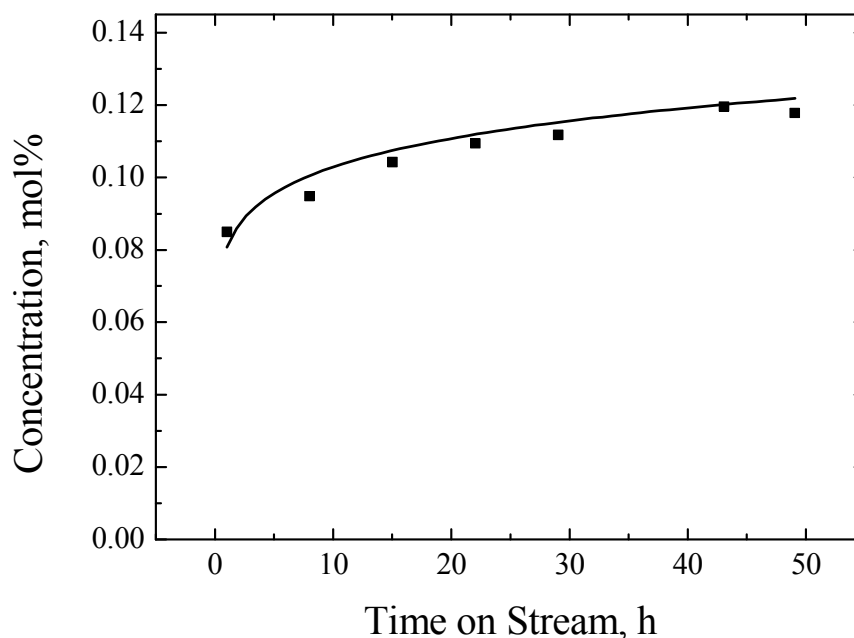
Figure 3.6 – Effect of TOS on the ethene (-■-) concentration
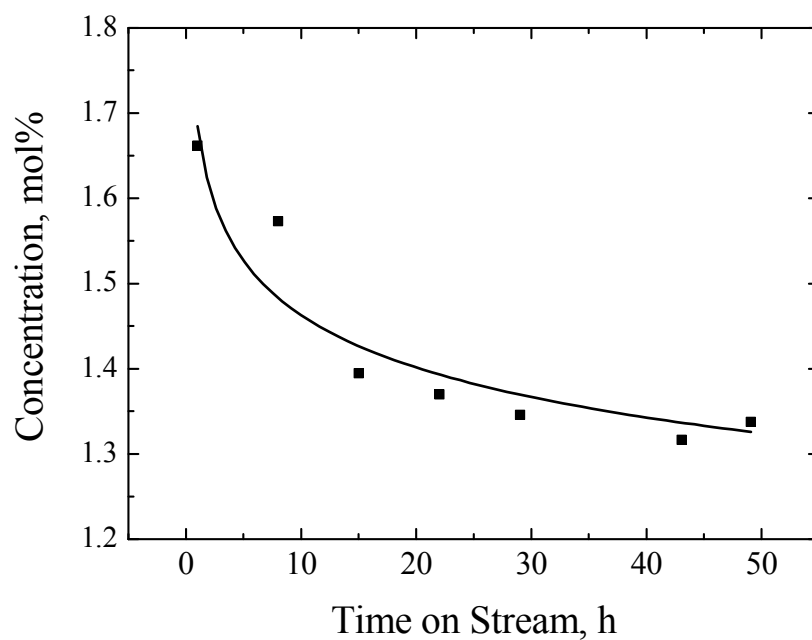
Figure 3.7 – Effect of TOS on hydrogen (-■-) concentration

The incorporation of platinum on H-ZSM-5 catalyst was reported to enhance the dehydrogenation, but it also supports hydrogenolysis of alkanes and alkylaromatics [14]. The high concentration of ethene at low TOS indicated that ethane was dehydrogenated into ethene, producing hydrogen at the same time. Hence this explains the large amount of hydrogen detected by the GC at low TOS as shown in Figure 3.7. As the dehydrogenation reaction of ethane produces equimolar concentration of ethene and hydrogen (Equation 3.26), the concentration of hydrogen would be expected to increase with TOS. However, the contrary was observed. The concentration of hydrogen decreased with TOS, suggesting that the hydrogen produced during the dehydrogenation reaction could be consumed by side reactions such as hydrogenolysis and hydrogenation reactions.

Hydrogenolysis only takes place in the presence of hydrogen. The existence of hydrogen will influence the reaction pathway during the alkylation reaction [20]. The hydrogen produced during dehydrogenation would be adsorbed on platinum metal species, catalysing hydrogenolysis (Equation 3.28) which produces methane (Figure 3.8). Previous study pointed out that large amounts of methane were formed on Pt-loaded catalysts due to their strong hydrogenolysis activity [28].

$$C_2H_6 + H_2 \rightleftharpoons 2CH_4$$

(3-29)
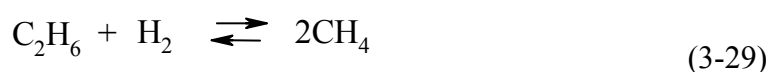
As methane was not supplied in the reaction feed, the concentration of methane detected could be a result of side reactions that took place during the alkylation of benzene. The concentration of methane decreased rapidly with TOS, from 6 mol % to 3.5 mol % in the first 8 hours of alkylation. Due to the depleting concentration of hydrogen (Figure 3.7), the rate of hydrogenolysis was also reduced. This resulted in a decrease in the concentration of methane. Hydrogenolysis is a 'structural-sensitive' reaction where the specific rate of alkane hydrogenolysis is highly dependent on the metal particle size of the active phase [22].
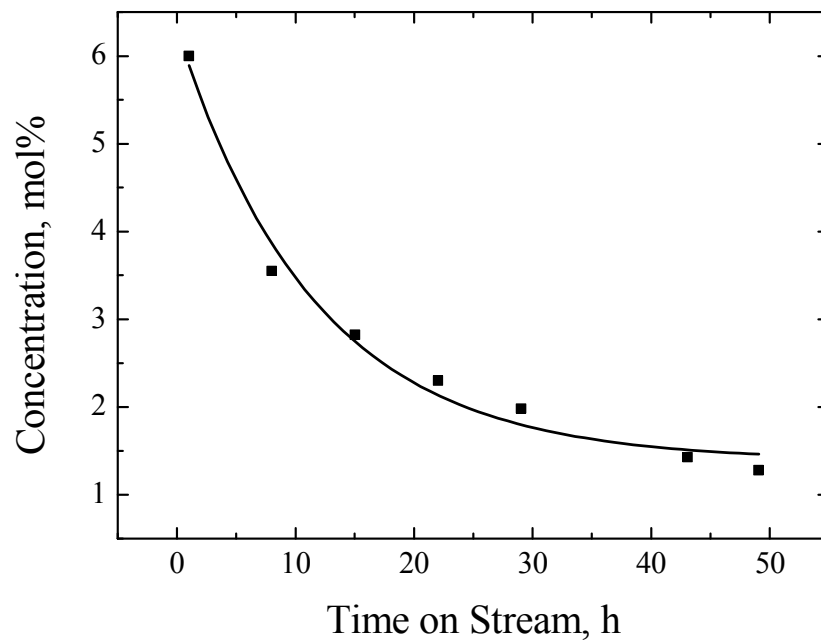
Figure 3.8 – Effect of TOS on methane (-■-) concentration
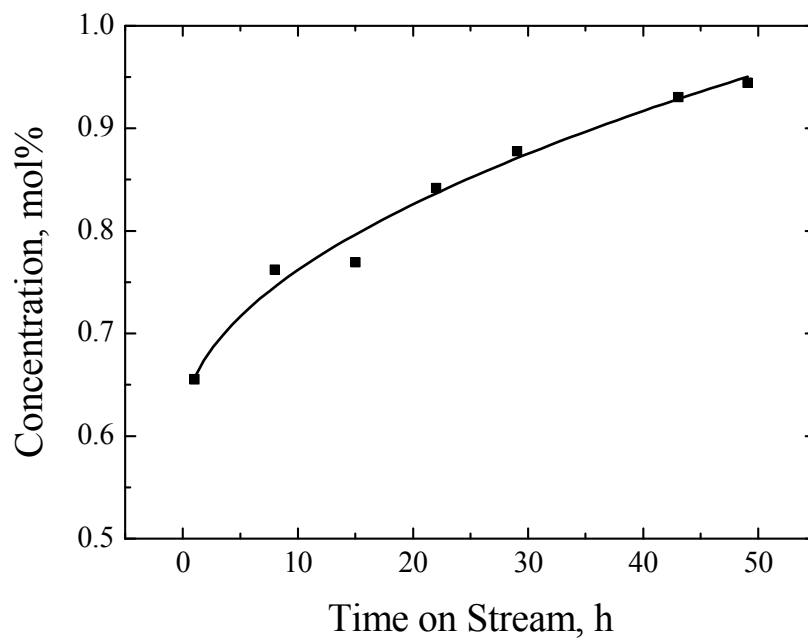
Figure 3.9 – Effect of TOS on EB (-■-) concentration

The alkylation of benzene with ethane was reported to proceed via two consecutive reactions steps; the dehydrogenation reaction of ethane to form ethene over

metallic platinum sites and the alkylation of benzene with ethene over Brønsted acid sites [11]. Even though the activity of PtH-ZSM-5(30) catalysts (based on benzene conversion) decreased from 20.5 % to 13.8 %, the selectivity of EB increased by 30 % to yield a selectivity of 80 % at 48 h TOS. Ethene, being the intermediate product formed on the metal centre would proceed to the acid sites of the catalyst for further reactions [20]. The desired pathway for ethene molecules would be alkylation with benzene to form EB. The production of EB was dependent on the intermediate product, ethene. Thus, the increase in EB concentration observed in Figure 3.9 could be related to the increase in concentration of ethene with TOS. In addition, the drop in the concentrations of toluene and triethylbenzene (TEB) could explain the increment in EB concentration with TOS.
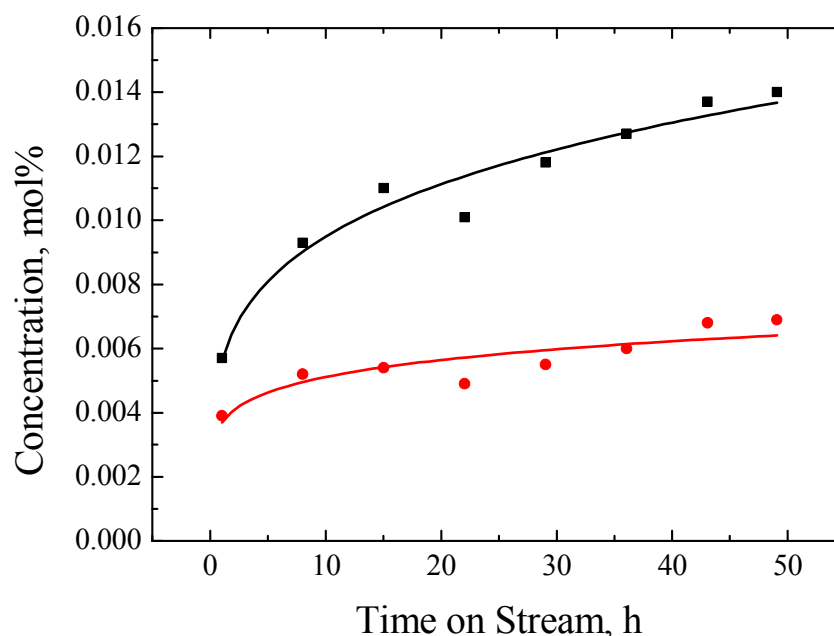
Figure 3.10 – Effect of TOS on *meta*-DEB (-■-) and *para*-DEB (-●-) concentration

Further alkylation of EB with ethene produces diethylbenzene (DEB). DEB could also be formed via disproportionation of EB [29]. Due to pore restrictions within the ZSM-5 channels, it is more likely that DEB was formed via alkylation than disproportionation as the disproportionation of EB required two EB molecules as opposed to alkyation reaction which required only one [30]. The concentration of the DEB isomers; *meta*- and *para*-DEB shown in Figure 3.10 varied with TOS. The differences in the mobility rate of the DEB isomers inside the catalyst's framework

47

could have influenced the concentration of the DEB isomers at the reactor's outlet. The changes in the selectivity of the DEB isomers with TOS will be discussed in the next section.

Besides the main reactions (dehydrogenation of ethane and alkylation of benzene), side reactions also took place. These side reactions have a negative effect on the EB selectivity. An example of a competing reaction is hydrogenolysis discussed previously. The high concentration of ethene could contribute to the presence of by-products from oligomerization, cracking and isomerization, which eventually led to decrease in catalytic performance of PtH-ZSM-5(30) catalysts.

Propane and propene were observed in the product stream and their concentration decreased as the reaction progressed. The possible route for propene formation is from oligomerization of ethene to form higher hydrocarbons, then followed by a cracking reaction. Steinberg et al. [20] reported that propene was formed via the oligomerization reaction of ethene to form hexene (Equation 3.29), which was then cracked to produce propene (Equation 3.30). Instead of the direct formation of hexene from ethene oligomerization, hexene was formed from the reaction of ethene with butene (Equation 3.31 – 3.32). Hexene was then involved in cracking reaction to produce propene (Equation 3.30). Propene would then be converted into propane by hygrogenation on the platinum dispersed on H-ZSM-5 catalysts (Equation 3.33).

$$3C_2H_4 \rightleftharpoons C_6H_{12} \tag{3-30}$$

$$C_6H_{12} \rightleftharpoons C_3H_6 + C_3H_6 \tag{3-31}$$

$$C_2H_4 + C_2H_4 \rightleftharpoons C_4H_8 \tag{3-32}$$

$$C_2H_4 + C_4H_8 \rightleftharpoons C_6H_{12} \tag{3-33}$$

$$C_3H_6 + H_2 \rightleftharpoons C_3H_8 \tag{3-34}$$
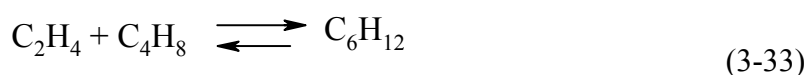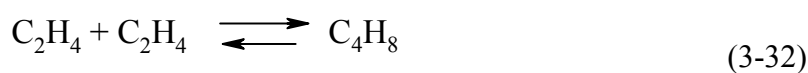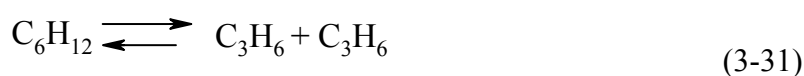
Hexene was produced as an intermediate during oligomerization and cracking reactions to form propane. However, hexene was not present in the product distribution. This may possibly be because of the low concentration of hexene in the product stream.

Hexene is a very reactive molecule and cracks immediately into propene, and is therefore not detected by the GC.

The concentrations of propane and propene both decreased, while the concentration of isopropylbenzene increased with TOS. The propene concentration remained low throughout the course of the reaction as it was being consumed during the alkylation of benzene with propene. In addition, the decreasing concentration of propane and propene could also result from the lower cracking reactions, since Wang and Manos [31] concluded that strong acid sites, which were responsible for the cracking reactions, were preferably poisoned by coke.

Toluene was the most abundant aromatic formed after EB. The formation of toluene is undesirable as it affects the selectivity to the desired product, EB. Toluene could possibly be formed via hydrogenolysis of EB and alkylation of benzene with methane. In addition, Smirnov et al. [3] suggested that transalkylation reaction of EB with benzene or the direct alkylation of benzene with ethane could lead to the high concentration of toluene at the reactor outlet. However, at the reaction conditions used, the reactivity of methane is very low. Therefore, toluene was possibly formed from the hydrogenolysis of EB and transalkylation of EB and benzene. As the hydrogen concentration decreased with TOS, hydrogenolysis reaction of EB was unlikely to take place. Hence, the concentration of toluene decreased with time.

While the selectivity towards DEB increased with TOS, it decreased with benzene conversion. The decrease in the selectivity of DEB could be associated with the increasing selectivity of ethyltoluene and TEB in the product distribution. Ethyltoluene could either be formed from hydrogenolysis of DEB or it could also be a product of alkylation of toluene with ethene. Due to the high concentration of toluene, compared with the concentration of DEB, ethyltoluene was most likely formed from the alkylation of toluene with ethene.

3.6.2 Effect of TOS on shape selectivity reactions for the 1 wt% PtH-ZSM-5(30) catalyst

The variations in the shape selective reactions that took place during the alkylation of benzene with ethane, such as the alkylation of EB with ethene to form DEB and the EB hydroisomerization to produce xylenes demonstrate the effect of catalyst deactivation with TOS.
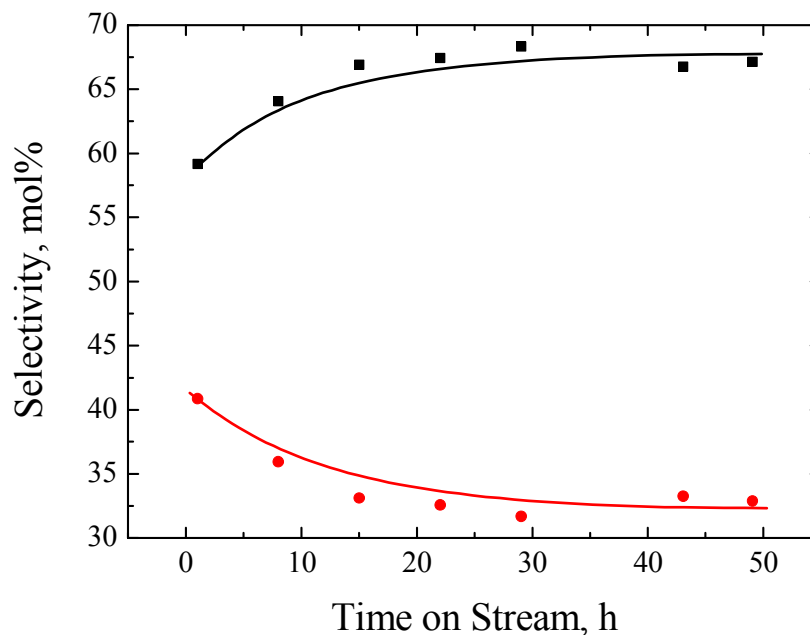
Figure 3.11 – Effect of TOS on the selectivity of *meta*-DEB (-■-) and *para*-DEB (-●-)

The product distribution of the isomers of DEB; *meta-* and *para-* DEB is shown in Figure 3.11. The ratio of *meta*-DEB to *para*-DEB expected at thermodynamic equilibrium at 370 $^{\circ}$C is 1.81. Due to steric constraints of the two ethyl groups, *ortho*-DEB was not observed in the product distribution. According to Schumacher and Karge [32], *para*-DEB diffuses much faster to the outside of the pores of the catalyst than the other 2 isomers. In addition, a previous study also found that the selectivity of *para*-isomers should be enhanced as coke deposition reduces the effective channel size of the catalyst and increases the diffusion resistance [33]. This should have resulted in an enhancement of selectivity to *para*-isomers as the diffusivity of *para*-DEB was not hindered by geometrical constraints. Despite this, the selectivity to *para*-DEB decreased

while the selectivity to *meta*-DEB increased with TOS in this work. This finding is rare in comparison with the typical effect of coking.

It was proposed that, due to thermodynamic limitations, *para*-DEB is converted to *meta*-DEB via isomerization [29]. This led to a higher *meta*-DEB selectivity in the product distribution. However, a different explanation was given for the enhancement of the *para*-DEB selectivity when the alkylation reaction of benzene with ethene was carried out over ZSM-5 catalyst. Kaeding [34] pointed out that large ZSM-5 crystals gave higher concentrations of *para*-DEB as compared with small ZSM-5 crystallites [34]. In large crystallites, *meta*-DEB and *ortho*-DEB isomers were isomerized to *para*-DEB because of the longer residence time of DEB isomers in the crystallites [34]. Given that there are two possible explanations for the variation of DEB isomers with TOS, no conclusion will be proposed for the observed trend until the effect of pore structure has been taken into consideration.
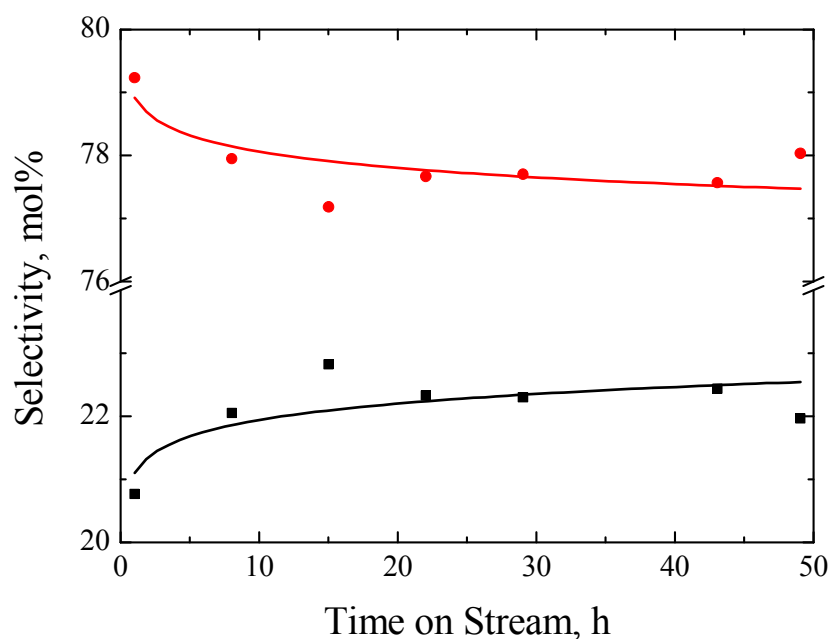
Figure 3.12 – Effect of TOS on the selectivity of *ortho*-xylene (-■-) and *meta*- +
***para*- xylene (-●-)**

The formation of xylenes could be explained by the isomerization of EB, as described by Lukyanov and Vazhnova [11]. The ratio of *para*- + *meta*-xylene to *ortho*-xylene expected at thermodynamic equilibrium at 370 $^{\circ}$C is 3.24. The relationship

between the selectivity of xylene isomers with TOS (Figure 3.12) illustrates that *ortho*-xylene selectivity increased, while *meta-* + *para-* xylene selectivity decreased with TOS. This result is consistent with earlier research by Sotelo et al. [35], who reported the decrease in selectivity to *para*-xylenes with TOS during the alkylation of toluene with methanol over Mg-modifed ZSM-5 catalyst. They suggested that pore blockage by coke molecules was responsible for the observed trend [35].

Further explanation for the product distribution variation of the shape selectivity reactions will be given in Chapter 8 after taking into consideration the effect of coke deposition on the structural and transport properties of PtH-ZSM-5 catalysts.

3.6.3 Effect of Acidity on Benzene Alkylation with Ethane

In this section, the difference between the catalytic activities of PtH-ZSM-5(30) and PtH-ZSM-5(80) catalysts will be discussed.

Figures 3.13 and 3.14 compare the conversion of benzene and ethane for the two bi-functional zeolite catalysts used in this work. The activity of the PtH-ZSM-5(30) catalyst decreased with TOS, as shown by the decreasing ethane and benzene (Figure 3.13) conversion with TOS. As for the PtH-ZSM-5(80) catalyst, a small drop in benzene and ethane conversion was observed initially, but the benzene and ethane conversion remained stable after 15 hours on stream. The difference in the activity of the two PtH-ZSM-5 catalysts could be due to deactivation of different active sites, where the deactivation of the Pt sites could lead to the drop in the activity of the PtH-ZSM-5(80) catalyst, while coke deposition on the acid sites could possibly dominate the deactivation of the PtH-ZSM-5(30) catalyst. Further work is required to conclude the cause of catalyst deactivation, and this will be discussed in the future work section in Chapter 8.
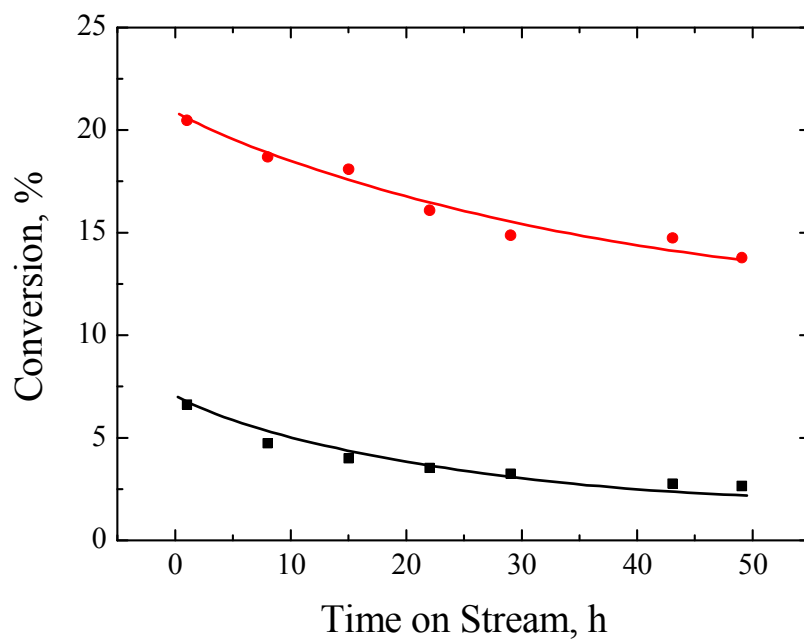
Figure 3.13 – Comparison of ethane (-■-) and benzene (-●-) conversion on PtH-ZSM-5(30) catalyst
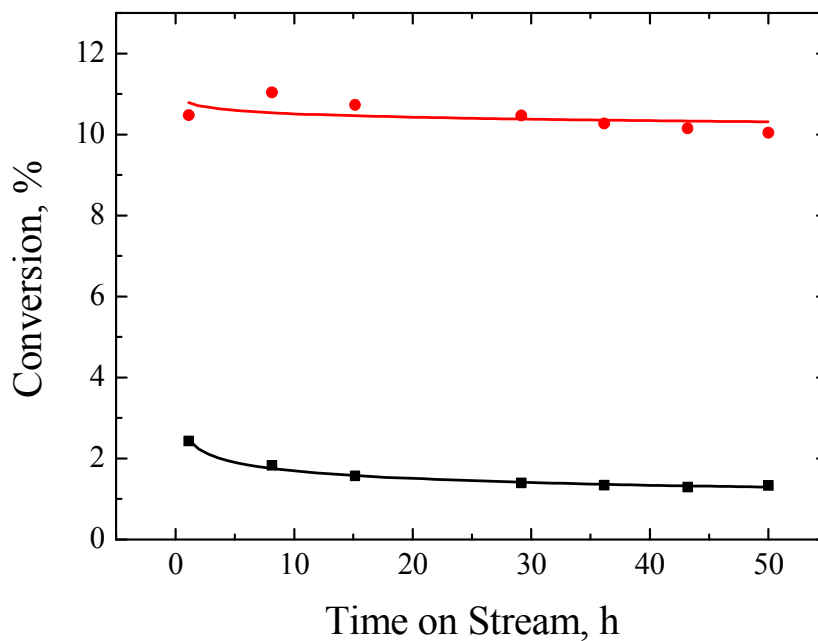
Figure 3.14 – Comparison of ethane (-■-) and benzene (-●-) conversion on PtH-ZSM-5(80) catalyst
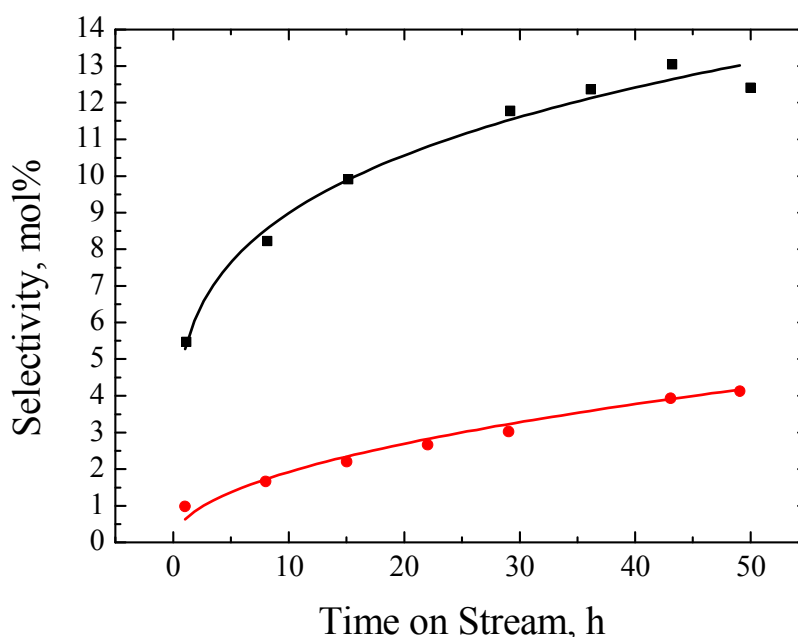
Figure 3.15 – Comparison of ethene selectivity in the aromatic products for PtH-ZSM-5(30) (-●-) and PtH-ZSM-5(80) (-■-) catalyst

The conversion of ethane for both the catalysts studied was higher than the equilibrium conversion of ethane dehydrogenation (0.52 %). The PtH-ZSM-5(30) catalyst yielded a larger ethane conversion, but lower stability as illustrated by the drop in the conversion of the reactants with time. With higher acidity for the PtH-ZSM-5(30) catalyst, the alkylation of benzene with ethene was enhanced, hence pushing ethane dehydrogenation forward. Even though the conversion of ethane is higher on the PtH-ZSM-5(30) catalyst, the selectivity of ethene is lower compared with the PtH-ZSM-5(80) catalyst. The lower selectivity of ethene (Figure 3.15) for the PtH-ZSM-5(30) catalyst than the corresponding selectivity for the PtH-ZSM-5(80) catalyst could be due to the higher bimolecular ethene dimerization steps, which are the initial steps in alkane oligomerization and cracking reactions [10].

Similarly, benzene conversion is greater on the PtH-ZSM-5(30) catalyst than the PtH-ZSM-5(80) catalyst. This result is consistent with previous work which proved that the catalytic activity increased when the SiO_2/Al_2O_3 ratio decreased, as a result of increasing acidity of the zeolite catalyst [4, 10]. The higher acidity of the PtH-ZSM-5(30) catalyst also enhanced other reactions involving benzene apart from its

transformation into EB. Therefore, benzene conversion was greater than the equilibrium conversion (13.5 %) evaluated for benzene alkylation at 370°C. As for the PtH-ZSM-5(80) catalyst, the catalyst demonstrated stable performance during the alkylation. This could be attributed to lower concentrations of alkenes which helped suppress side reactions that lead to coke formation and catalyst deactivation.

3.6.4 Effect of acidity on product distribution

Even though Kato et al. [8] reported the effect of SiO_2/Al_2O_3 on the alkylation of benzene with ethane in terms of the yield of EB and styrene, their work did not include the effect of acidity on reactant's conversion as well as product selectivities. In this section, the variations in product selectivities due to different acidities of the PtH-ZSM-5 catalyst are discussed.

The alkylation of benzene with ethane over bifunctional PtH-ZSM-5 catalysts is dominated by two consecutive reactions; ethane dehydrogenation into ethene, catalyzed by platinum sites and benzene alkylation with ethene, taking place on Brønsted acid sites. In Figure 3.15, it is shown that the selectivity of ethene is higher when the reaction was carried out with the PtH-ZSM-5(80) catalyst. The lower ethene selectivity indicated that ethene was involved in side reactions such as oligomerization and cracking over Brønsted acid sites of the PtH-ZSM-5(30) catalyst.

The sequence of oligomerization and cracking reactions led to the production of different alkenes such as propenes, butenes, pentenes and hexenes. However, only propenes and butenes were detected by GC in the product stream. The higher concentration of propenes and butenes in the product distribution of the PtH-ZSM-5(30) catalyst compared to the PtH-ZSM-5(80) catalyst explained the lower selectivity to ethene observed for the two different catalysts. The higher concentration of these alkenes promoted side reactions leading to coke formation which consequently reduces the performance of the catalyst. The formation of propene is unfavourable as it competes with ethene to react with benzene. The alkylation reaction of benzene with propene produces propylbenzene. The selectivity of propylbenzene increased with TOS for both bifunctional PtH-ZSM-5 catalysts although the selectivity of propylbenzene is lower for the PtH-ZSM-5(30) catalyst.
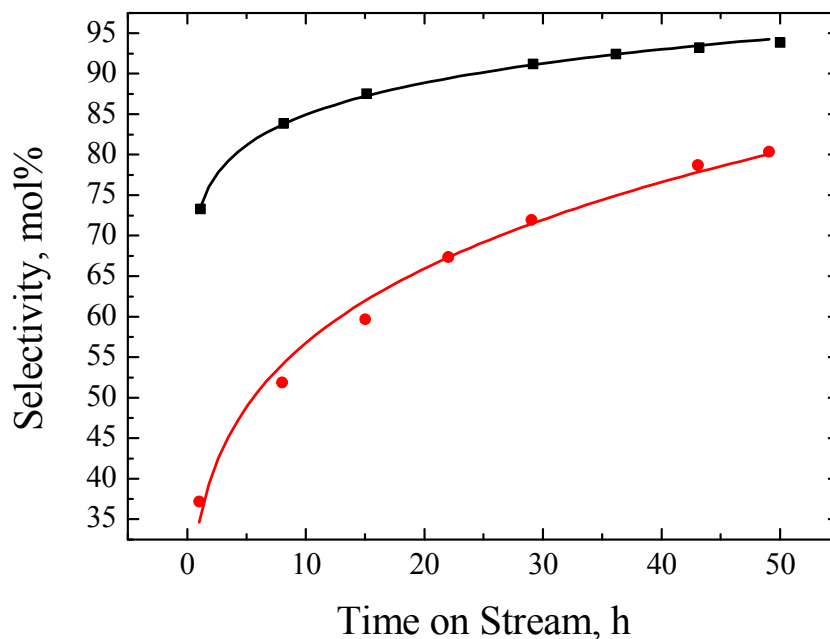
Figure 3.16 – Comparison of EB selectivity in the aromatic products for PtH-ZSM-5(30) (-●-) and PtH-ZSM-5(80) (-■-) catalyst

From Figure 3.16, it follows that the selectivity of the desired product, EB was increasing with TOS for both zeolite catalysts. The gain in EB selectivity could be associated with the decrease in selectivities of side products such as toluene, xylene, triethylbenzene, and ethyltoluene. The EB selectivity is lower for the PtH-ZSM-5(30) catalyst when compared with the corresponding selectivities observed with the PtH-ZSM-5(80) catalyst. The higher acidity of the PtH-ZSM-5(30) catalyst could possibly be responsible for the transformation of EB to other aromatic products, hence decreasing the selectivity of EB.

As benzene conversion increased, the selectivity of EB in the aromatic products decreased. The decreasing selectivity of EB could result from the transformation of EB into secondary and tertiary products such as toluene, DEB, xylenes, TEB and ethyltoluene which demonstrated increasing selectivity with benzene conversion. Since the concentration of toluene is much higher than the concentration of methane for the PtH-ZSM-5(80) catalyst, it was proposed that toluene could be formed from other reactions such as the transalkylation of EB with xylene to produce toluene and

ethyltoluene, apart from EB hydrogenolysis over platinum sites on the H-ZSM-5 catalyst.

From the experimental data, it was observed that the selectivity of the tertiary product, TEB was higher when the alkylation reaction was carried out with the PtH-ZSM-5(30) catalyst. As a result, the selectivity to DEB was reduced as TEB was formed via alkylation of DEB with ethene. The effect of acidity on selectivites of DEB isomers are illustrated in Figures 3.17 and 3.18. For the reaction that was carried out over the PtH-ZSM-5(80) catalyst, the selectivity of the *meta*-DEB and *para*-DEB isomers remained constant with TOS. However, this was not the case for the reaction over the PtH-ZSM-5(30) catalyst, where the selectivity of *meta*-DEB isomer increased at the expense of the selectivity of the *para*-DEB isomer with TOS. The difference observed is believed to be related to the deactivation of the catalyst by coke molecules, which could either poison the active sites or block access to these active sites. Further investigations were carried out to understand these observations. They will be discussed in Chapter 8.
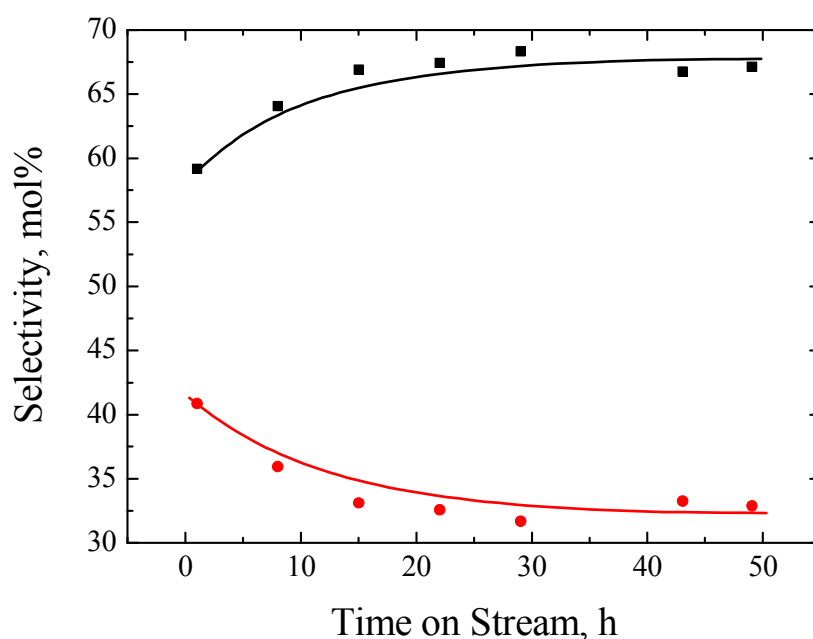
Figure 3.17 – Variations of *meta*-DEB (-■-) and *para*-DEB (-●-) isomer selectivity with TOS over PtH-ZSM-5(30) catalyst
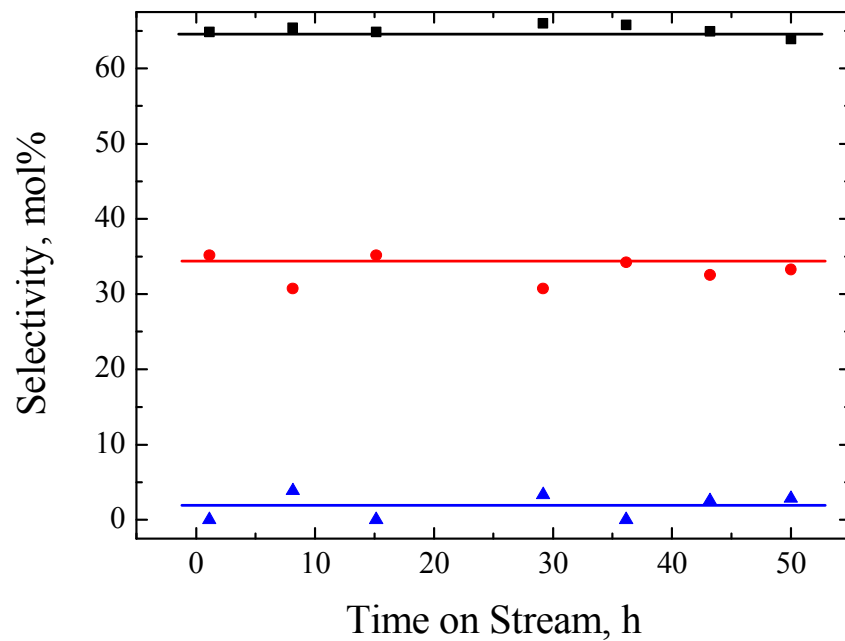
Figure 3.18 – Variations of *meta*-DEB (-■-), *para*-DEB (-●-) and *ortho*-DEB (-▲-) isomer selectivity with TOS over PtH-ZSM-5(80) catalyst
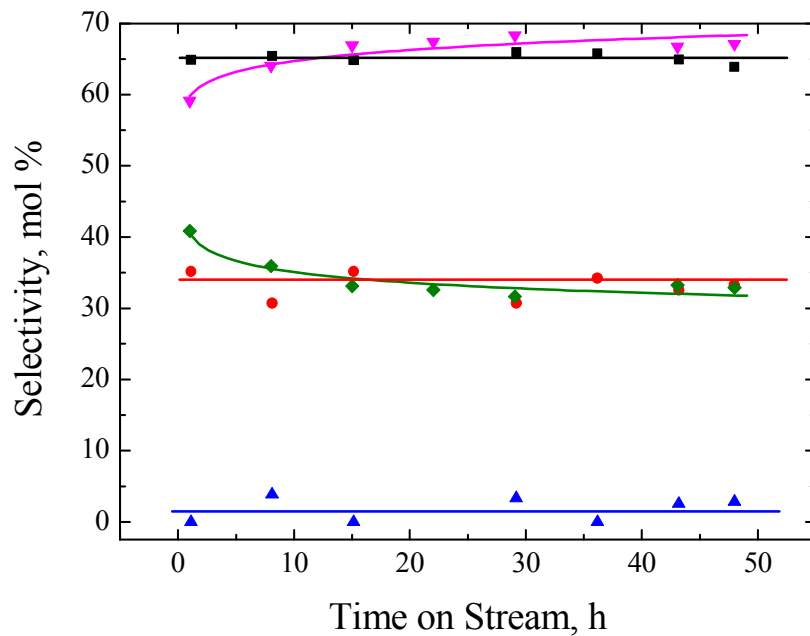
Figure 3.19 – Comparison of *meta*-DEB (-■-), *para*-DEB (-●-) and *ortho*-DEB (-▲-) isomer selectivity over PtH-ZSM-5(80) catalyst with *meta*-DEB (-▼-) and *para*-DEB (-♦-) isomer selectivity over PtH-ZSM-5(30) catalyst, with TOS

Figure 3.19 combines the selectivites of DEB isomers for both the PtH-ZSM-5 catalysts studied. It can be seen that the PtH-ZSM-5(30) catalyst was more *para*-selective when compared with the PtH-ZSM-5(80) catalyst at the start of the reaction. However, at higher TOS, the enhanced *para*- selectivity observed for the PtH-ZSM-5(30) catalyst disappears, and the *para*- and *meta*- DEBs selectivities obtained over the PtH-ZSM-5(30) and PtH-ZSM-5(80) catalysts are approximately the same.

3.7 Conclusions

The alkylation of benzene with ethane over two PtH-ZSM-5 catalysts of different SiO_2/Al_2O_3 was analysed in this study. Due to the difference in acidities, the performance of these PtH-ZSM-5 catalysts differs in terms of the reactant conversion and product selectivities. However, detailed analysis of the product distributions/selectivities confirmed that for both reactions, EB was formed via two consecutive reactions, (i) dehydrogenation of ethane into ethene and hydrogen on platinum sites and (ii) benzene alkylation with ethene over Brønsted acid sites.

The deactivation of the PtH-ZSM-5(30) catalyst was found to be more significant when compared with the PtH-ZSM-5(80) catalyst as a result of lower ethene and/or alkene concentration in the latter, which is responsible for the formation of coke. During the alkylation of benzene with ethane over the PtH-ZSM-5(30) catalyst, it was observed that the partially deactivated catalysts were more *para*-selective than the fresh PtH-ZSM-5(30) catalyst. On the contrary, the selectivity of the DEB isomers remained constant with TOS when the reaction was carried out over the PtH-ZSM-5(80) catalyst. The difference in the selectivity changes of the DEB and xylene isomers with TOS for the shape selective reactions of the two PtH-ZSM-5 catalysts was suggested to be caused by the effect of coke deposition during alkylation.

3.8 References

[1]   E.G. Deruoane, H.Y. He, S.B.D.A. Hamid, and I. Ivanova, Journal of Molecular Catalysis A:Chemical 158 (2000) 5-17.

[2]   C. Bigey, and L. Su, Journal of Molecular Catalysis. A, Chemical 209 (2004) 179-187.

[3]   A.V. Smirnov, E.V. Mazin, E.E. Ponomoreva, E.E. Knyazeva, S.N. Nesterenko, and I.I. Ivanova, Benzene Alkylation with Alkanes over Modified MFI Catalysts, Montpellier, France. 2001.

[4]   A.V. Smirnov, E.V. Mazin, V.V. Yuschenko, E.E. Knyazeva, S.N. Nesterenko, I.I. Ivanova, L. Galperin, R. Jensen, and B. S., Journal of Catalysis 294 (2000) 266-277.

[5]   C. Perego, and P. Ingallina, Catalysis Today 73 (2002) 3-22.

[6]   T.F. Degnan, C.M. Smith, and C.R. Venkat, Applied Catalysis. A, General 221 (2001) 283-294.

[7]   G.A. Olah, P. Schiling, J.S. Staral, Y. Halpern, and J.A. Olah, Journal of American Chemical Society 97 (1975) 6807-6810.

[8]   S. Kato, K. Nakagawa, N. Ikenaga, and T. Suzuki, Catalysis Letters 73 (2001) 175.

[9]   S. Kato, K. Nakagawa, N. Ikenaga, and T. Suzuki, Chemistry letters 3 (1999) 207-208.

[10]   D.B. Lukyanov, and T. Vazhnova, Journal of Molecular Catalysis A: Chemical 279 (2008) 128-132.

[11]   D.B. Lukyanov, and T. Vazhnova, Journal of Catalysis 257 (2008) 382-389.

[12]   A. Krogh, A. Hagen, T.W. Hansen, C.H. Christensen, and I. Schmidt, Catalysis Communications 4 (2003) 627-630.

[13]   P. Schulz, and M. Baerns, Applied Catalysis A:General 78 (1991) 15-29.

[14]   L.R.R. De Araujo, and M. Schmal, Applied Catalysis A:General 203 (2000) 275-284.

[15]   G. Caeiro, R.H. Carvalho, Z. Wanga, M.A.N.D.A. Lemosa, F. Lemos, M. Guisnet, and F.R. Ribeiro, Journal of Molecular Catalysis. A, Chemical 255 (2006) 131-158.

[16]   Y.V. Joshi, and K.T. Thomson, Catalysis Today 105 (2005) 106-121.

[17]   G.L. Buckles, and G.J. Hutchings, Catalysis Today 31 (1996) 233-246.

[18]   M. Guisnet, N.S. Gnep, and F. Alario, Applied Catalysis A: General 89 (1992) 1-30.

[19]   M.M. Bhasin, J.H. McCain, B.H. Vora, T. Imai, and P.R. Pujad, Applied Catalysis A: General 221 (2001) 397-419.

[20]   K.H. Steinberg, U. Mroczek, and F. Roessner, Applied Catalysis : A General 66 (1990) 37-44.

[21] G.N. Nayssilov, Advances in Colloid and Interface Science 47 (1993) 25-57.

[22] S.D. Jackson, G.J. Kelly, and G. Webby, Journal of Catalysis 176 (1998) 225-234.

[23] U. Mroczek, K.H. Steinberg, and F. Roessner, Reaction Kinetics and Catalysis Letters 44 (1991) 201-207.

[24] F. Moreau, N.S. Gnep, S. Lacombe, E. Merlen, and M. Guisnet, Applied Catalysis : A General 230 (2002) 253-262.

[25] C.L. Yaws. 2003. Yaws' Handbook of Thermodynamic and Physical Properties of Chemical Compounds. Knovel, Norwich, N.Y.

[26] M. Guisnet, and P. Magnoux, Catalysis Today 36 (1997) 477-483.

[27] W. Reschetilowski, U. Mroczek, and K.H. Steinberg, Applied Catalysis A:General 78 (1991) 257-264.

[28] T. Komatsu, M. Mesuda, and T. Yashima, Applied catalysis A:General 194-195 (2000) 333-339.

[29] N. Arsenova-Hartel, H. Bludau, R. Schumacher, W.O. Haag, H.G. Karge, E. Brunner, and U. Wild, Journal of Catalysis 191 (2000) 326-331.

[30] S. Alireza, S. Rezai, and Y. Traa, Catalysis Letters 122 (2008) 91-97.

[31] B. Wang, and G. Manos, Industrial & engineering chemistry research 47 (2008) 2948-2955.

[32] R. Schumacher, and H.G. Karge, Microporous and Mesoporous Materials 30 (1999) 307-314.

[33] X. Lin, Y. Fan, G. Shi, H. Liu, and X. Bao, Energy and Fuels 21 (2007) 2517-2524.

[34] W.W. Kaeding, Journal of Catalysis 95 (1985) 512-519.

[35] J.L. Sotelo, M.A. Uguina, J.L. Valverde, and D.P. Serrano, Applied Catalysis A: General 114 (1994) 273-285.

Chapter 4 : Pore Structure Modification by Coking during Benzene Alkylation with Ethane

4.1 Introduction

The loss in activity of a catalyst could be due to the formation of coke, blocking the pore structure as well as active sites, poisoning of the catalyst's active sites by strongly adsorbing molecules, or sintering of the active phase, which results in the loss of metal surface area. In the previous chapter, it was suggested that the deactivation of the PtH-ZSM-5 catalysts was due to the formation of carbonaceous residues, called 'coke'. Coke components can be classified into two kinds, coke precursor (soft coke) and hard coke. The character of coke precursors can be determined from their ability to be removed from the catalyst. 'Small' coke precursors can be removed rapidly at lower temperatures while 'large' coke precursors are removed at higher temperatures, at a lower rate [1]. Wang and Manos [2] have shown that the thermogravimetric (TG) methodology could differentiate between coke precursors and hard coke from the total amount of coke deposited, because coke precursors can usually be removed from the catalyst sample through volatilisation in inert nitrogen, where as hard coke is removed by burning the coke in an air flow at high temperatures. This coke classification was determined by raising the burning temperature from 473 K to 873 K under flowing nitrogen, then switching the gas flow from nitrogen to air at 873 K. The difference in the mass of the catalyst before and after switching the gases gives the amount of hard coke present in the catalyst.

The carbonaceous deposits formed can be olefinic, saturated or aromatic compounds. For the elucidation of the nature of coke, infrared (IR) spectroscopy has been widely used. Previous studies have demonstrated that changes in the positions and intensities of the IR peaks in regions between 1300 and 1700 cm^{-1} with coke deposition [3-6] could give information regarding the chemical nature of coke compounds. Shape changes of IR bands between 1359 and 1485 cm^{-1} was suggested to be due to the presence of saturated species, formed at low reaction temperatures (300 - 500 K) [3]. Uguina et al. [4] and Sotelo et al. [5] observed an intense double peak at 1365 and 1380

cm^{-1}, suggesting that the coke deposits have a certain paraffinic character. At higher reaction temperatures and increasing TOS, 'coke' bands around 1594 – 1592 cm^{-1}, which were ascribed to polyolefins and/or aromatics such as alkylnaphthalenes and polyphenylenes [10-12], were observed. It was also reported that the IR band at 1585 cm^{-1} was attributed to C=C stretching vibration of microcrystalline graphitic carbon structures, hence the carbonaceous residue formed has the structure of highly unsaturated polycyclic aromatic hydrocarbons [6].

Deactivation by coking can occur in two ways; site coverage or pore blockage [7-11]. Deactivation by site coverage is due to irreversible adsorption of coke on the acid sites of a zeolite catalyst. As pore sizes of zeolites are close to the size of organic molecules, only a few atoms of carbon are required to block the pores [9]. Two types of pore blockage have been identified – (i) blockage of the channels or intersections by coke molecules located at that site, and (ii) pore mouth plugging, which leads to accessibility blockage to channels and intersections in which there are no coke molecules. Coke deposition by pore blockage would eventually affect the architecture of the catalyst. Therefore, the study of catalyst deactivation has to account for the changes to the catalyst pore structure, to gain insight to the way in which pore structure evolves with coke deposition.

The influence of coke on the pore structure of the catalyst has been studied by various techniques, which includes adsorption of gases and x-ray diffraction (XRD) studies. The most commonly used method for the characterisation of the catalysts is the adsorption of gases, followed by the calculation of surface area, pore volume and pore size distribution [10]. From nitrogen sorption results, Lin et al. [10] showed that both micro- and mesopore volume of zeolite catalysts were affected by increasing coke content. Shifts in the differential pore size curves were observed by Hopkins et al. [9] when coke content increased to 4 wt % during n-hexane cracking, and by Schuurman et al. [8], when the effect of coke deposition in FCC catalysts was studied.

However, not only does the modifications of the architecture of the catalyst matter, the identification of the particular location of coke deposits is important to understanding the mechanism of coking. Depending on the loss of adsorption capacity of the coked catalyst and the amount of coke formed, Bibby et al. [12] were able to

determine the broad location of coke deposition. From the linear relationship between the adsorption capacity, S and coke content, C (Equation 4.1), the different location of coke deposition on ZSM-5 catalysts during methanol conversion were identified [12]. The authors proposed the possible distributions of coke in a ZSM-5 pore network with relation to the coefficient k, in the linear relationship given by Equation 4.1 [12]:

$$S = kC + V_o \qquad (4\text{-}1)$$

When coke fills the zeolite channels in a regular way, where the volume of coke is equal to the loss in sorption capacity, the value of k is equal to 1, but when coke is deposited on the external surface of the crystallite, k is found to be smaller than 1. The coefficient k is greater than 1 when internal coke isolates part of the zeolite pores so that a small amount of coke can have a large effect on the sorption capacity. In later years, Guisnet and Magnoux [11] were able to identify the different modes of deactivation by the loss of adsorption capacity of the coked catalyst and the amount of coke formed. The ratio of the pore volume made inaccessible to adsorbates by coke molecules, V_{NA}, to the volume really occupied by coke, V_C as a function of coke content were evaluated and it was found that pore blockage occurs if the ratio of V_C/V_{NA} is smaller than 1, while pore filling takes place if the ratio of V_C/V_{NA} is ~1. This method was then employed by other researchers [4-5, 13] to further understand the effect of coke formation in different catalytic reactions.

With coke deposition within the crystallites, deformations of the zeolite lattice have been detected. These modifications in the framework of the crystallites can be detected by x-ray diffraction, by the changes in the diffraction pattern. Fyfe et al. [14] showed the perturbation of a zeolite structure, when sorbate molecules were present in the zeolite framework, from changes in the diffraction patterns. Their finding was in agreement with earlier findings of Bibby et al. [12] when the MFI lattice was occluded by template ions. This demonstrates that the XRD technique is capable of differentiating between internal [10, 12] and external [4, 13] coke deposition.

Even though adsorption and diffraction studies have been shown to be capable of determining the locus of coke deposition, i.e. internal pore structure vs external surface of the crystallites, they are unable to account for the distribution of coke molecules within the crystallites. Therefore, in this study, the percolation method will

be employed to identify the intracrystalline spatial distribution of coke, and this will be discussed in the next Chapter. This percolation method employed will give a more comprehensive analysis of the coking phenomena as compared to the previous models described earlier [11-12], which only made use of the data given by adsorption measurements. In addition, a multi-component adsorption model will be employed in this work. The multi-component adsorption model does not only allow the determination of the location of coke deposition, but also gives information about the changes in the adsorption capacities within and on the external surface of the crystallites, which will then be used for the percolation study.

The previous studies discussed have shown that it is not satisfactory to understand the coking mechanism by one technique. A combination of experimental techniques is necessary in order to gain a further knowledge of the catalyst deactivation. Therefore, in order to understand the effect coke formation during the alkylation of benzene with ethane, the fresh and spent PtH-ZSM-5 catalysts were investigated by several analytical techniques. The coke content on the zeolite catalysts was determined via combustion of the carbonaceous residues by thermogravimetric analysis (TGA). The nature of the coke content was analysed by infra-red (IR) spectroscopy. The sorption measurements with various probe molecules on the fresh and coked catalysts were carried out to determine the location of the coke deposition as well as the modification of the pore structure of the zeolite catalyst as a result of coke deposition. The effect of coke on the zeolite lattice could be observed by x-ray diffraction, while electron microscopy images give evidence for the occlusion of platinum, on the external crystallite surface, by coke deposition.

4.2 Theory

4.2.1 Gas Sorption

Depending on the types of pores present in the material, different characterisation methods are applied. Examples of the different types of characterization methods are physisorption of gases and liquids, radiation scattering, mercury porosimetry and calometric methods [15]. Among the examples given, gas sorption is

the routinely used for pore structure characterisation as it is a well-established method and it allows a wide range of pore sizes to be accessed.

4.2.1.1 Definition, Terminology and Pore Classification

The pores within the porous materials vary in sizes and shapes within the solids and between one solid and another. In 1985, the International Union of Pure and Applied Chemistry (IUPAC) produced a classification of pore size which gives a guideline for pore widths descriptions applicable to all forms of porosity. Pores are categorised according to their pore sizes:

1) macropores – pores with widths more than 50 nm (500 Å)
2) mesopores – pores of intermediate size of 2 nm < width < 50 nm
   (20 Å < width < 500 Å)
3) micropores – pores with width not exceeding 2 nm (20 Å)

In many catalysts the different types of pores are all present. The pores can be closed, blind or through, and each pore can be isolated or connected to other pores to form a porous network (Figure 4.1).
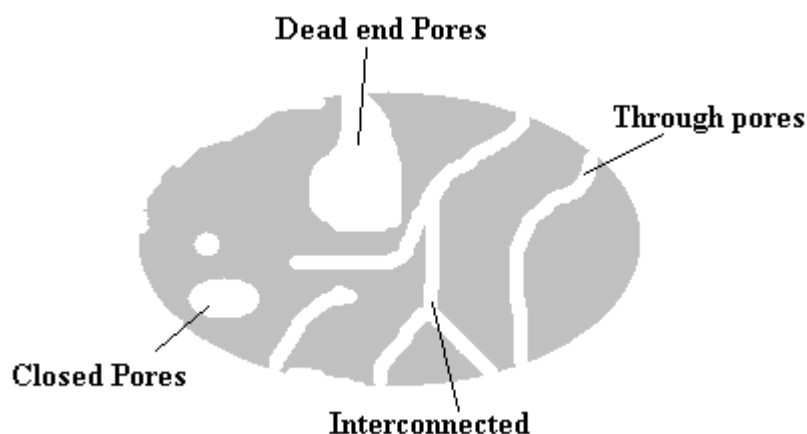
Figure 4.1 – Various types of pores. Modified from ref [16]

Prior to further discussions of the characterisation techniques, the main terms and definition for the study of surface area and porosity should be understood. Some important definitions are given in Table 4.1:

Table 4-1 – Definition associated with porous solids [17]

Term	Definition
Porous Solid	Solid with cavities or channels which are deeper than wide
Open Pore	Cavity of channel with access to the surface
Interconnected Pore	Pore which communicates with other pores
Closed Pore	Cavity not connected to the surface
Void	Space between particles
Pore Size	Pore width – minimum dimension
Pore Volume	Volume of pores determined by stated method
Porosity	Ratio of pore volume to apparent volume of particle or granule
Surface Area	Extent of total surface area as determined by given method under stated conditions
Specific Surface Area	Surface area per unit mass of powder, area determined under stated conditions
External Surface Area	Area of surface outside pores
Internal Surface Area	Area of pore wall
Tortuosity	The path available for diffusion through a porous bed in relation to the shortest distance across the bed

4.2.1.2 Adsorption

The term 'adsorption' was first used by Kayser to explain the condensation of gases on surfaces, in contrast to gas absorption in which gas molecules penetrate the bulk phase of the absorbing solid [18]. Then, McBain proposed the term 'sorption' as a complete description of mass transport into a solid, encompassing surface adsorption, absorption by penetration into the solid and condensation within pores [18]. According to Rouquerol et al. [16], when a solid is exposed to a gas/vapour in a closed space, the enrichment in the interfacial layer brought about by the interactions between the solid and the molecules in the fluid phase is defined as adsorption.

Adsorption can be divided into two categories; physical adsorption, or van der Waals adsorption, and chemisorption. Physisorption is applicable to all adsorbate-

adsorbent systems provided the conditions of pressure and temperature are suitable whereas chemisorption may only occur if the system is capable of making a chemical bond. The comparison between physical and chemical adsorption is given in Table 4.2 [16].

Table 4-2 - Comparison of Physical and Chemical Adsorption

ADSORPTION		
Property	**Physical**	**Chemical**
Forces	van der Waals (mainly dispersion interaction)	Chemical bonds formed between adsorbent and adsorbate
Specificity	Non-specific	Specific
Heat of Adsorption	5-50 kJ mol^{-1}	50-100 kJ mol^{-1}
Activation Energy	Rare	60-100 kJ mol^{-1}
Reversibility	Fast and reversible	Slow and irreversible
Extent	Multilayer	Monolayer

4.2.1.3   *Physisorption of Gas*

Physical adsorption is defined as adsorption in which the forces involved are intermolecular forces (van der Waals forces) and which do have a significant amount of change in electronic orbital patterns of the species involved.
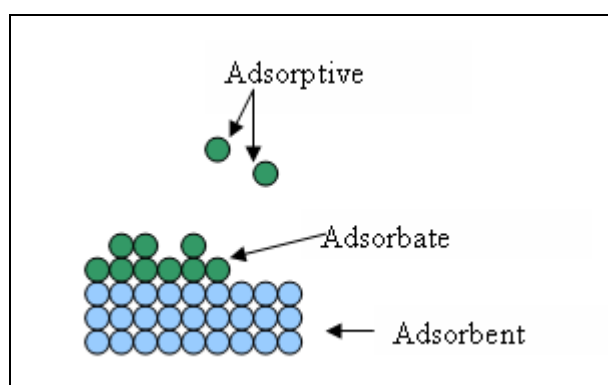
Figure 4.2 - Adsorption Process

The solid acts as the adsorbent, while the gas being adsorbed on the surface is the adsorbate when adsorption occurs at a solid/gas interface. The amount of adsorbate

adsorbed on the adsorbent surface increases with the increase in gas pressure and decreases with increasing temperature. The term adsorptive is used for the bulk phase and/or the phase that is capable of being adsorbed (Figure 4.2).

During physical adsorption, no chemical bond is formed. However, attraction between the adsorbate and adsorbent exists because of the formation of intermolecular electrostatic interactions, such as London dispersion forces, or van der Waals forces from induced dipole-dipole interactions [18]. The molecules in the adsorbed layer do not only interact with the solid surface, but also with the neighbouring molecules within the layers. As the fractional coverage of the surface is increased, the effect of adsorbate-adsorbate interaction becomes more significant and should be taken into consideration [16, 18].

A variety of probe gases can be used for the characterisation of a porous materials, but nitrogen is the most widely used adsorptive for adsorption measurements. The nitrogen molecule is recommended for determining the surface area and pore volume because it is small enough to penetrate into pores of most adsorbent. In addition, there is also a large amount of literature concerning the properties of nitrogen relating to physical adsorption [19]. Besides nitrogen, argon, carbon dioxide, helium, oxygen and other hydrocarbons have also been used for pore structure characterisation.

4.2.1.4 Adsorption Isotherm

The graphical relationship between the amount of gas adsorbed, and the pressure or relative pressure at a constant temperature, is known as the adsorption isotherm. The amount of gas adsorbed expressed in moles *per* gram of solid, *n*, depends on the temperature, *T*, the equilibrium pressure, *P*, and the nature of the gas-solid system. This can be represented by the equation:

$$n = f(P,T,gas,solid) \qquad (4\text{-}2)$$

For an adsorption system where the gas is adsorbed on a particular solid at a constant temperature, the expression below can be used:

$$n = f(P)_T \qquad (4\text{-}3)$$

If the particular gas is below its critical temperature and the adsorbent is maintained at a fixed temperature, the equation above simplifies to:

$$n = f\left(\frac{P}{P_o}\right)_T \qquad (4\text{-}4)$$

where P_o is the saturation pressure of the adsorptive at temperature T.

During the adsorption process, the adsorptive condenses in the pores in order of increasing pore size to form a liquid-like phase in a process known as capillary condensation. The condensation pressure is an increasing function of the pore size, where in smaller pores the adsorptive condenses at lower pressures. The adsorption process may be followed by desorption where the pressure is progressively decreased from its maximum value. During desorption, the liquid phase vaporises from the pores. Vaporization can only take place if a pore has access to the vapour phase and is large enough for vaporisation to be thermodynamically favourable (i.e. the applied pressure is below the condensation pressure for a pore of that size). The desorption curve generally lies above the adsorption isotherm over a range of pressures, forming a hysteresis loop.
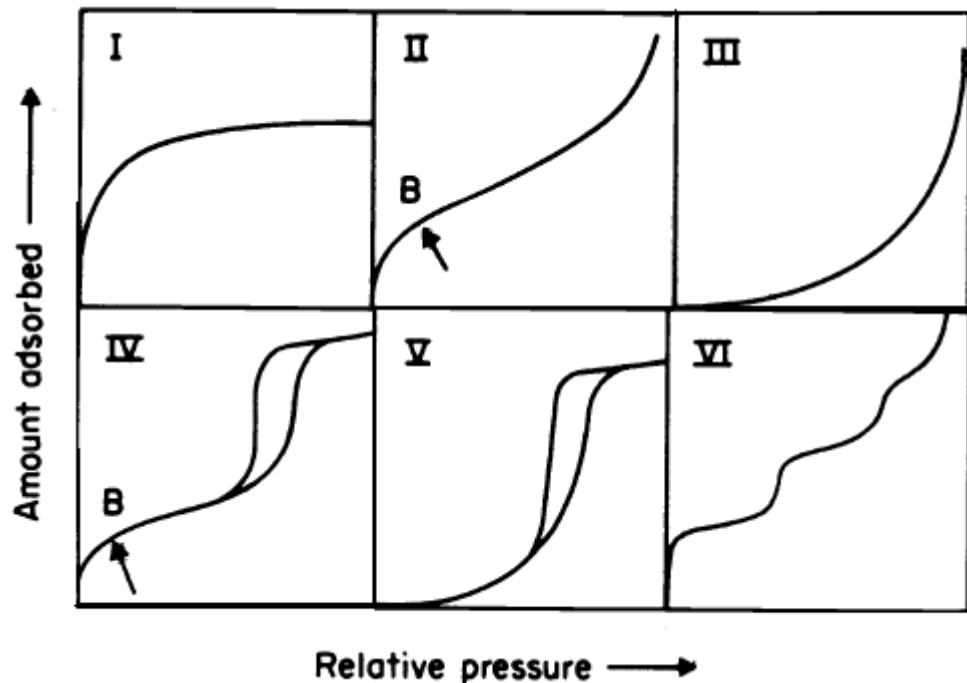
Figure 4.3 – The six main types of physisorption isotherms, according to IUPAC classification [15]

The first step in the interpretation of the isotherm is the examination of the isotherm shape. The shape of the isotherm reveals information about the nature of the porosity of the sample examined. According to the IUPAC 1985 classification, there are 6 main types of isotherms [15]. The isotherms are shown in the Figure 4.3 [16] and are classified as Type I, II, III, IV, V or Type VI isotherms. Type I isotherms are characteristic of microporous adsorbents such as zeolites [20]. The adsorption takes place at very low relative pressures because of strong interactions between the pore walls and adsorbate. The adsorption energy increases, and the relative pressure at which the micropore filling occurs decreases, when the micropore width decreases [16]. The Type I isotherm is reversible and the shape of the isotherm is concave with respect to the relative pressure axis. The amount adsorbed rises steeply, indicative of micropore filling, reaching a plateau and the isotherm approaches a limiting value as P/P_o tends to 1. A low slope of the plateau as the saturation pressure is approached is due to multilayer adsorption on the small external surface area.

The Type II isotherm is a characteristic of non-porous and macroporous adsorbents. Initially, a monolayer is formed and then, this is followed by multilayer adsorption at high P/P_o. The thickness of the adsorbed layer increases progressively until the condensation pressure is reached. The monolayer and multilayer formation processes are always overlapping. When the equilibrium pressure is equal to the saturated vapour pressure, the adsorbed layer becomes a bulk solid or liquid. If the knee of the isotherm is sharp, the uptake at point B (seen in Figure 4.3) indicates completion of monolayer coverage and the beginning of multilayer adsorption. The location of Point B gives an estimate of the amount of adsorbate required to cover the surface with a complete monolayer.

The reversible Type III isotherm is convex to the P/P_o axis over the complete range; hence the isotherm does not have a knee. The type III isotherm is a characteristic of a non-porous or macroporous solid which has weak adsorbent-adsorbate interactions.

The shape of a Type IV isotherm is very similar to Type II isotherm at the start of the isotherm, but differs at high P/P_o. The hysteresis loop is associated with capillary condensation taking place in mesopores and the limiting uptake over the high P/P_o range. The exact shape of the Type IV hysteresis loop differs from one adsorption

system to another, but the uptake is always greater along the desorption branch at any given P/P_o [18].

As with Type III isotherms, Type V isotherms are rare. They have similar characteristics of weak adsorbent-adsorbate interactions, but Type V isotherms exhibit hysteresis loops. The Type V isotherms represent mesoporous solids.

Stepped isotherms are classified as Type VI isotherm. The steepness of the steps depends on the system and the temperature. The stepped isotherms represent adsorption in porous solids that contain highly uniform surfaces. [16]

4.2.1.5   Assessment of Microporosity

Microporous solids are defined as materials with pore width less than 2 nm. Adsorption on microporous solids occurs at very low P/P_o because of the strength of adsorbate-adsorbent interactions. The mechanism for physisorption in very fine pores is unlike filling in mesopores due to the close proximity of the opposite pore wall. To differentiate between the primary filling of pore spaces from the secondary process of capillary condensation in mesopores, the term ' micropore filling' is used [15].

Micropore filling capacity is dependent on the available pore volume as well as the packing of the adsorbed molecule [16]. It was reported that there are two different micropore filling mechanisms; the first stage occurs at very low relative pressures (P/P_o < 0.01) and is termed 'primary micropore filling' while the second takes place in wider micropores and at higher relative pressures ($P/P_o \approx$ 0.01-0.2). The initial adsorption is related to monolayer adsorption on each micropore wall, whereas the secondary process is related to the filling of the residual space in between the opposite monolayers on the micropore walls [21].

In primary micropore filling, adsorbates fill pores of width equivalent to no more than two or three molecular diameters [20, 22]. This stage of micropore filling leads to the distortion of the shape of the isotherm in the monolayer region [17]. In the second phase of micropore filling, the interaction between the adsorbent and adsorbate

is very small, and thus the increase in adsorption energy is due to the cooperative adsorbate-adsorbate interaction [17].

As discussed in the previous section, microporous solids produce type I isotherms which are reversible and have a long horizontal plateau which extends up to $P/P_o \rightarrow 1$. The micropore capacity, n_p is the amount adsorbed at the plateau. From the micropore capacity, the micropore volume, V_p, can be calculated assuming that pores are filled with liquid adsorptive, and thus using the density of the adsorptive liquid at the adsorption temperature [22].

Some microporous materials have very complex textures, where an appreciable amount of surface area lies outside the micropores, i.e. in the form of external and/or mesopore surface [22]. In that case, the type I isotherm has a finite slope in the multilayer region [8, 33]. An isotherm that has Type IV appearance is due to the presence of mesopores in some microporous adsorbents.

4.2.1.6   *Assessment of Mesoporosity*

The study of mesoporous solid is closely related with the concept of capillary condensation and the Kelvin equation (Equation 4.5) [17-18]. The Kelvin equation describes the capillary condensation process, where it relates the curvature of the meniscus present in a pore to the P/P_o value associated with condensation.

$$r_k = \frac{-2\sigma v_1}{RT\ln(P/P_o)} \tag{4-5}$$

where r_k is the Kelvin radius, v_l is the molar volume of the liquid condensate and σ is the surface tension of the liquid condensate

The presence of the hysteresis loop observed for Type IV isotherms is associated with capillary condensation in the mesopore structures. During desorption, the adsorbates vaporise from pores at the surface, and as the pressure decreases, the vapour phase increasingly penetrates the solid. When the percolation transition is reached, desorption is rapid and when the pressure is decreased further, all the liquid-filled pores have access to the vapour phase, which corresponds to the closure of the hysteresis loop [23].

Figure 4.4 shows 4 different types of hysteresis loop for Type IV isotherms. Type H1 is usually associated with porous materials consisting of agglomerates or materials that have narrow pore size distributions [15], for example open-ended tubular pores as in MCM-41 [16] while H2 hysteresis represents a more complex pore structure which tends to be made up of interconnected network of different size and shape pores [16]. Type H3 and H4 do not exhibit any limiting adsorption at high P/P_o which indicate that the adsorbent does not possess a well-defined mesopore structure. Type H3 is often observed with plate-like materials where as narrow slit-shaped pores produces isotherms with Type H4 hysteresis loop.
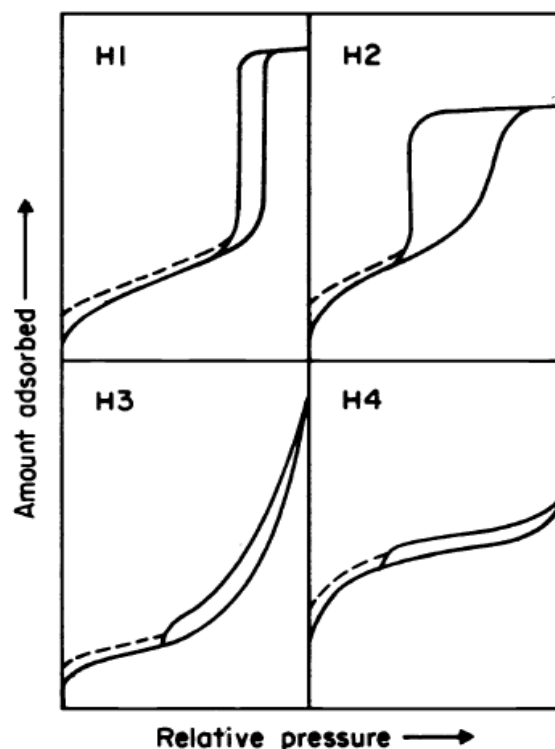
Figure 4.4 – Types of Hysteresis Loop [15]

4.2.1.7 Surface Area Determination

4.2.1.7.1 Langmuir Method

The BET method is the most widely used technique for surface area determination. However, the BET method lacks applicability in the case of microporous materials. It was reported by Seifert and Emig [24] that some researchers doubt the use of BET theory to determine the surface area of a test material containing a certain amount of micropores. BET theory states that it is applicable to multilayer physisorption

of vapour/gas in macropores and on the external surface in mesopores. The pores in microporous materials are so narrow that they often cannot accommodate more than one single molecular layer on their wall [18, 25]. Besides that, the monolayer volume computed by the BET equation corresponds to micropore volume plus the monolayer volume on the external surface of micropores [26]. Therefore, type I isotherms were assumed to conform to the Langmuir equation.

According to the Langmuir theory, the limiting adsorption at the plateau represents completion of a monolayer and can therefore be used for the calculation of surface area [15]. Two stages are involved in calculating the surface area by the Langmuir method. The first stage involves constructing the Langmuir plot and from it, the derivation of a value of monolayer capacity, n_m. Then, the specific surface area, A is calculated.

The linear form of the Langmuir equation is given by:

$$\frac{P}{n} = \frac{1}{n_m b} + \frac{P}{n_m}$$ (4-6)

where n is the specific amount adsorbed at the equilibrium pressure P, n_m is the monolayer capacity and b is the 'adsorption coefficient'.

The plot of (P/n) versus P yields a straight line with slope, m and intercept, i. By solving the two simultaneous equations, the monolayer capacity, n_m (Equation 4.7) and adsorption coefficient, b (Equation 4.8) can be determined.

$$n_m = \frac{1}{m}$$ (4-7)

$$b = \frac{m}{i}$$ (4-8)

The calculation of the specific surface area, $A(Langmuir)$ requires the molecular cross-sectional area of the adsorbate molecule in the complete monolayer, σ. The values of σ depend upon the temperature and the nature of the interactions between the adsorbent and adsorptive. For adsorption with nitrogen at 77 K, the σ value is 0.162 nm^2 assuming that the nitrogen monolayer is close-packed. When argon is used as the

adsorptive, the cross-sectional area is evaluated to be $\sigma(Ar) = 0.138$ nm^2. The specific surface area, A is given by:

$$A = n_m L \sigma \qquad (4\text{-}9)$$

where L is the Avogadro constant and σ is the average area occupied by each molecule in the completed monolayer.

4.2.1.7.2 BET Model

The BET equation is applicable to multilayer adsorption of vapours in macropores and on external surfaces, as well as in mesopores before capillary condensation. The adsorbed molecules on the surface of the material can act as new adsorption sites for further adsorption. The BET model was developed assuming that the heat of adsorption of the first monolayer is constant and that the lateral interaction between the adsorbed molecules is negligible. The heat of adsorption of all layers but the first is said to be equal to the heat of condensation.

The validity of the BET equation is only limited to a restricted part of the isotherm, which is usually not outside of the range of $0.05 < P/P_o < 0.3$. The failure of the BET plot at very low P/P_o ($P/P_o < 0.05$) is because of the influence of high adsorption potentials in the micropores. Even though the BET method is widely used to determine surface areas of solids, it is criticised by many for the assumptions made when developing the BET model. Some of the criticisms of the BET theory were reported in the literature [18, 27].

The BET equation is given by:

$$\frac{P/P_o}{n(1 - P/Po)} = \frac{1}{n_m C} + \frac{C-1}{n_m C}\frac{P}{P_o} \qquad (4\text{-}10)$$

where n_m is the monolayer capacity and C is the BET constant energy parameter.

In order to determine the surface area, a graph of $(P/P_o)/[n(1- P/P_o)]$ vs P/P_o is required. As mentioned, the range where the straight line is fitted is generally between $0.05 < P/P_o < 0.3$, though, this may vary with different adsorption system. The values of n_m and C can be solved from the values of the slope and the intercept of the linear BET

plot. The specific area based on the BET method, *A(BET)* can then be calculated using Equation 4.9 given in the previous section.

Due to the high microporosities in some materials, the BET plot deviates from linearity, which could lead to meaningless negative values of the BET constant energy parameter value [24]. Therefore, two criteria were proposed for the selection of the *P/P_o* range where the modified-BET equation is applied: (i) the pressure range chosen is in the region where n(P_o-P) is increasing with increase in *P/P_o* and (ii) the y-intercept of the linear region must be positive in order to give a meaningful value to BET constant, *C* [28-29].

4.2.1.8   *Pore Volume Determination*

The simplest method to determine the pore volume of a porous material is known as the Gurvitsch method, which is independent of the pore geometry of the material. The plateau in an isotherm at high relative pressure corresponds to the complete filling of the meso- and micropores (if present) [26]. According to the Gurvitsch rule, the pore volume is determined from the quantity adsorbed at the plateau assuming the adsorbate density to be the liquid density of the adsorbate at the temperature of adsorption [18, 26].

Several methods including t-plot, α_s-plot, Horvath-Kavazoe (HK), density functional theory (DFT) and Dubinin-Radushkevich (DR) method could be used to evaluate the micropore volume of a porous solid. The t-plot method is the easist method to determine the total micropore volume [26]. The t-plot can be used to assess the micropore capacity provided that the standard multilayer thickness curve has been determined on a non-porous reference material with a similar surface structure to that of the microporous sample [16]. The plot of volume adsorbed, *V* against *t*, statistical thickness of the adsorbed layer will indicate the type of pores present in the adsorbent. A non-zero intercept from the straight line indicates the presence of micropores while vertical plots reveal mesopores [20]. The micropore volume of the adsorbent can be obtained by extrapolating the straight line to a positive intercept on the y-axis of the t-plot.

In the case of mesoporous solids, the t-plot could still be applied to calculate the mesopore volume. An upward deviation from the linearity corresponds to when capillary condensation is observed. A straight line with a slope corresponding to the external surface area is obtained. The intercept of this line with the y-axis gives the mesopore and micropore (if present) volume [26]. In addition to the t-plot, an α_s-plot or the BJH algorithm could also be used to determine the pore volume of a mesoporous material.

4.2.1.9 Pore Size Distribution

To predict if diffusion through pores is likely to have a limiting effect on the observed rate of reaction within a porous medium, it is necessary to know the pore size distribution of a porous material [24]. Depending on the types of pores present in a solid, different methods are used to compute the pore size distribution. If meso- and macropores are present, the Kelvin equation is said to be a useful model for the transformation of the adsorption data into a pore size distribution. The Kelvin equation is only limited to pore radius greater than 2 nm [25]. In the later years, the Barret, Joyner and Halenda (BJH) algorithm was developed for PSD determination, corrected from the Kelvin equation and a t-layer to take into consideration of the multilayer adsorption in meso- and macropores.

According to Storck et al. [20], it is necessary to use the Horwath-Kawazoe (HK) model to characterise the pore-size distribution data for isotherms obtained at very low P/P_o (P/P_o < 0.1) [20]. The HK method of analysis is based on a quasi-thermodynamic approach, where the P/P_o required for the filling of micropores of a given size and width is directly related to the adsorbent-adsorbate interaction energy [1, 4, 12]. The original HK model only applies for nitrogen isotherms determined on molecular sieve carbons. However, modifications were made so that the HK model is now extended to argon and nitrogen adsorption in cylindrical and spherical pores [16, 20]. As a result, porous materials like zeolites, oxides and aluminophosphates can now be characterised using the HK method.

It was reported that the use of argon as the adsorbate is preferred for the determination of the micropore size distribution in zeolites compared with nitrogen. The

presence of quadrupole moment in N_2 leads to enhanced interaction between the zeolite surface and nitrogen molecules, which could make it difficult to discriminate between zeolites of different pore sizes [27, 29, 40-41]. Besides that, N_2 adsorption in micropores starts at lower P/P_o compared with Ar, which makes the measurement of micropores less accurate for N_2. Groen et al. [30] also pointed out that Ar adsorption at 77 K shows limited application for mesopore size determination, because the temperature of adsorption is below the bulk triple point, hence pore condensation vanishes when the pore diameter exceeds 12 nm [30].

Even though previous studies have indicated that Ar is in favour over N_2 for micropore size distribution, Schuurman et al. [8] recommended the use of N_2 to observe the modifications of micropore populations following coke deposition in FCC catalysts due to the smaller cross-section of the N_2 molecules [8]. Nevertheless, the authors mentioned that the micropore diameter deduced from Ar adsorption is more realistic than the N_2 adsorption because of the interaction between N_2 and pore walls of zeolite, leading to smaller micropore size diameter [8], in agreement with previous findings [7, 16].

It is the aim of this chapter to investigate the effect of coke deposition on the pore structure of PtH-ZSM-5 catalysts during benzene alkylation with ethane. Previous works have shown that N_2 sorption is a useful method for the characterisation of fresh and coked catalysts [8-10, 31]. In this study, Ar sorption was also carried out in addition to the sorption of N_2, for comparison since N_2 posses a quadrupole moment, which can preferentially interact with certain surface sites on the zeolite catalyst. Results from N_2 and Ar sorption were then related to the data obtained from TGA, IR, SEM, and XRD studies, and detailed discussion will be given in the following sections.

4.3   Experimental Methods

4.3.1   Fourier Transform Infrared (FT-IR)

IR measurements of fresh and coked PtH-ZSM-5 samples have been performed to characterise carbonaceous residues formed during benzene alkylation with ethane. The zeolite samples were pressed into wafer thin self-supporting disks (~10 mg), and

then placed into the IR cell holder. Prior to the IR experiments, the samples were heated up to 350 °C with a heating rate of 1 °C min⁻¹, and holding it at 350 °C for 2 hours, before cooling it down to room temperature at a rate of 2 °C min⁻¹. The spectra for coked PtH-ZSM-5 samples were obtained by subtraction of that corresponding to the fresh PtH-ZSM-5 sample.

The IR experiments were carried out by Tanya Vazhnova from the Department of Chemical Engineering, at the University of Bath.

4.3.2 Thermogravimetric Analysis (TGA)

Thermogravimetric analysis of the coke content on the discharged PtH-ZSM-5 catalysts was performed in a Setaram TGA92 thermogravimetric analyzer. Coked samples were heated from room temperature to 900 °C at a rate of 10 °C min⁻¹ in flowing, dry air. The first step observed was due to the desorption of water, and the plateau at 300 °C gives indication that the sample was free from water. Further loss in the sample mass (between 300 °C and 900 °C) is a result of the burning of carbonaceous deposits.

4.3.2.1 Calculations

The mass percentage of the coke per mass of pure zeolite was calculated as follows:

$$Coke\ Content\ (mass\ \%) = \frac{w_{300} - w_{900}}{w_{900}} \times 100\% \qquad (4\text{-}11)$$

where w_T is the mass of sample at temperature T

The volume of coke deposition in a deactivated sample was calculated using Equation 4.12.

$$Volume\ of\ Coke, V_c\ (cm^3 g_{cat}^{-1}) = \frac{Coke\ Content\ (g_{coke}\ g_{cat}^{-1})}{Density\ of\ Coke\ (g_{coke}\ cm^{-3})} \qquad (4\text{-}12)$$

4.3.3 X-Ray Diffraction (XRD)

Powder X-ray diffraction experiments were carried out using a D8 Advance Bruker X-ray diffractometer. Diffraction patterns were recorded using Cu Kα radiation at 40 kV, 30 mA, and a scan rate of $1\ ^{\circ}\ min^{-1}$.

The diffraction experiments were carried out by Dr Gabriele Kociok-Kohnin from the Department of Chemistry, at the University of Bath.

4.3.4 Electron Microscopy

Scanning electron microscopy experiments were conducted on a JEOL JSM6480LV system operating at 15 kV. The samples were coated with a thin carbon layer to complete the electric circuit required for electron transfer before the imaging analyses were carried out. Gold was not used to coat the samples due to the low resolution of the images obtained. The use of carbon coating did not affect the data for the H-ZSM-5(30) samples (see page 92). The effect of coke deposition on the platinum particles impregnated onto the H-ZSM-5 catalysts was studied by backscatter electron imaging.

4.3.5 Gas Sorption

Nitrogen and argon sorption experiments were performed using a Micrometric Accelerated Surface Area and Porosimetry (ASAP) 2020 apparatus. The gas sorption experiment for pore analysis consists of three steps; sample preparation, adsorption analysis and free space analysis. These steps are independent of the adsorptive gases used for the analysis.

4.3.5.1 Sample Preparation

Approximately 100 mg of the PtH-ZSM-5 catalysts were placed in a sample flask and a seal frit was used to seal the opening of the tube. The tube was then placed in the degassing port to expose the surface of the adsorbent to high vacuum. Prior to the adsorption analysis, it is necessary to remove any physisorbed species from the surface of the adsorbent by exposing the surface to high vacuum at elevated temperature. The

outgassing conditions (temperature and duration) should be controlled to prevent changes in the structure of the catalyst.

The samples were heated at 250 ^{o}C for 4 hours. The sample was allowed to cool down before reweighing the sample in the sample tube. The heating process was repeated until the mass of the degassed samples has reached a constant value.

4.3.5.2   Adsorption Analysis

The prepared sample was transferred from the degassing port to the analysis port where it is positioned in a liquid nitrogen dewar. For both; nitrogen and argon adsorption, the adsorption temperature was set at 77 K.

4.3.5.3   Free Space Analysis

A free space analysis was performed at the end of the analysis to determine the 'dead volume' of the sample and sample cell from the relationship between pressure and volume added. The dead space refers to the volume of the sample tube excluding the sample itself. Helium was added to the system continuously, through a flow of controller, for the determination of the dead volume in order to reduce the measurement time. [32]

At the end of the adsorption analysis, the samples were degassed. Once the vacuum condition is reached, the samples were heated at 250°C for 4 hours to prepare the sample for the free space analysis. Then, free space analysis was performed.

4.3.5.4   Calculations

4.3.5.4.1   Renormalising uptake of nitrogen/argon

The total sorption capacity measured from gas sorption experiments gives the amount of nitrogen/argon sorbed *per* unit mass of the sample. For coked samples, the sample mass includes PtH-ZSM-5 catalysts as well as the mass of coke formed during the reaction. Therefore, it is necessary to take into account of the coke content before comparing isotherms of the fresh and coked PtH-ZSM-5 catalysts.

All the uptake values for the isotherms of the coked samples were renormalized to give the amount of gas sorbed *per* unit mass of the catalyst.

$$\mathrm{Re}\,normalised\;Volume,\,V = \frac{V}{1 - Coke\;Content(\%)}\,cm^3 g^{-1} \qquad (4\text{-}13)$$

4.3.5.4.2 Pore Volume Calculation

The sorption capacities, α obtained from the sorption analyses were specified at STP (101.3 kPa, 273.15 K). The pore volume is defined as the volume of adsorbed materials which fills the pores, expressed in terms of bulk liquid at atmospheric pressure and at the temperature of adsorption.

The pore volume of the fresh and coked PtH-ZSM-5 catalysts based on nitrogen adsorption at 77 K was calculated based on Equation 4.14.

$$Pore\;Volume,\,V = \frac{\alpha M}{\rho \overline{V}} = (\alpha \times 1.54 \times 10^{-3})\,cm^3 g^{-1} \qquad (4\text{-}14)$$

When argon was used as the adsorptive gas, Equation 4.14 is modified and the pore volume at 77 K was calculated using Equation 4.15.

$$Pore\;Volume,\,V = \frac{\alpha M}{\rho \overline{V}} = (\alpha \times 1.276 \times 10^{-3})\,cm^3 g^{-1} \qquad (4\text{-}15)$$

4.3.5.4.3 Modified-BET surface area

BET surface areas of the fresh and partially deactivated PtH-ZSM-5 catalysts were calculated based on the method proposed by Rouquerol et al. [29] as this method gives a more accurate surface area for microporous solids. According to the authors, the pressure range for the application of the BET analysis should have values of *V(P_o-P)* increasing with *P/P_o* and the y-intercept of the linear region should be positive to give a meaningful value of the *C* parameter, which should be greater than zero. From the graph of *V(P_o-P)* vs *P/P_o*, the maximum *P/P_o* was used as the upper boundary for the BET plot (Figure 4.5).

With the pressure range known, the BET analysis was performed by plotting *P/P_o/(V(1-P/P_o))* versus *P/P_o*. From the slope *(C-1)/n_mC* and the y-intercept *(1/n_mC)*, the

monolayer capacity, n_m and the constant, C can be calculated. The surface area, $A(BET)$ is then calculated using Equation 4.9.
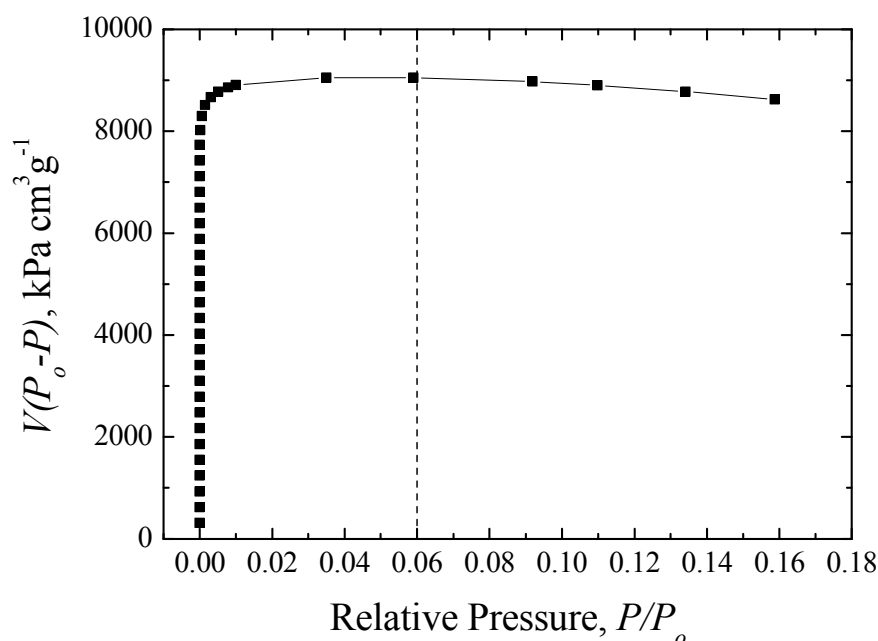
Figure 4.5 – $V(P_o\text{-}P)$ vs P/P_o for the fresh PtH-ZSM-5(30) catalyst.
Only the range below $P/P_o = 0.06$ satisfies the first criterion for application of the
BET theory

4.4   Results

4.4.1   IR Spectroscopy

Figure 4.6 compares the IR spectra of the fresh and 48 h coked PtH-ZSM-5(30) sample in the region between 1300 and 1700 cm^{-1}. The appearance of new IR bands in the CH deformation and C=C stretching regions in the spectrum of the coked catalyst gives evidence of hydrocarbon species being deposited on or inside the zeolite catalyst. The intense IR band at 1600 cm^{-1}, which is assigned to C=C stretching vibrations of microcrystalline graphitic carbon structure, is clearly seen in the spectra for the PtH-ZSM-5(30) sample after 48 hours on-stream, indicating the presence of polyalkenes and/or polyaromatic species. IR bands ascribed to alkylnaphthalenes or polyphenylene structures between 1500 and 1540 cm^{-1} [33] was observed. A doublet at 1369 and 1382 cm^{-1}, which is typical of branched alkanes was also observed, suggesting that the coke

deposits have some paraffinic character (e.g. alkyl chains attached to polyaromatics). No IR bands were detected for wavenumber above 1700 cm^{-1}.
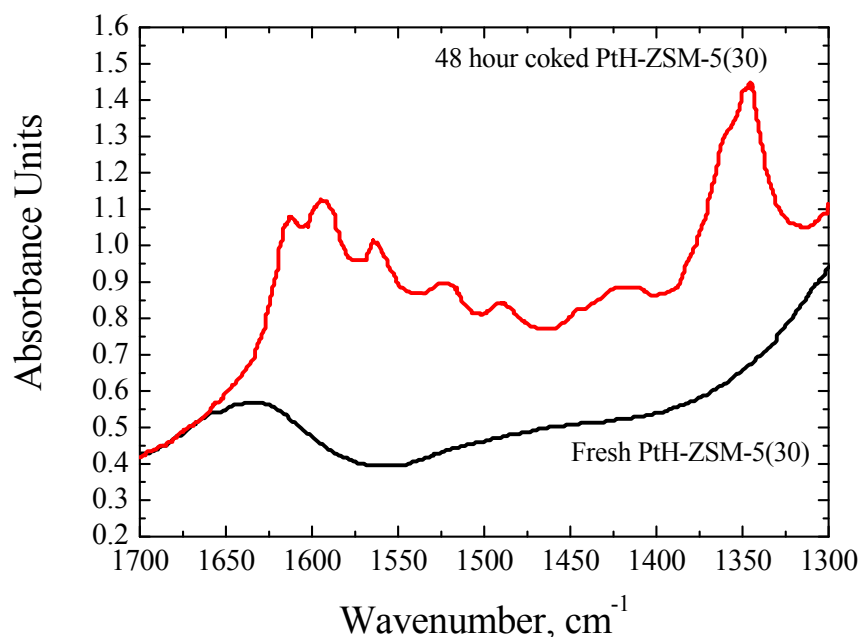
Figure 4.6 – IR spectra of fresh (—) and 48 hour coked (—) PtH-ZSM-5(30) catalysts

Quantitative analysis of the IR spectra found that the ratio between the intensity of the coke band at 1585 cm^{-1} and that of the doublet at 1365 cm^{-1} and 1380 cm^{-1} increased with coke content.

4.4.2 Thermogravimetric Characterisation of Coke Component

The mass percentages of the coke deposits on the spent PtH-ZSM-5 catalysts were determined via thermogravimetric analysis. Figures 4.7 and 4.8 show the change in the mass of PtH-ZSM-5 catalysts with temperature. Two distinct mass loss steps were observed for coked catalysts. The first mass loss step was attributed to desorption of water, while the second step, between temperatures of 300 $^{\circ}$C and 900 $^{\circ}$C, was a result of oxidation of the carbonaceous deposits arising from the reaction. The drop in the mass of PtH-ZSM-5 catalysts after 4 h TOS at the start of the experiment, when there was no rise in temperature, could possibly be due to the samples not thoroughly purged with N$_2$ at the end of the reaction experiments (see Figures 4.7 and 4.8).
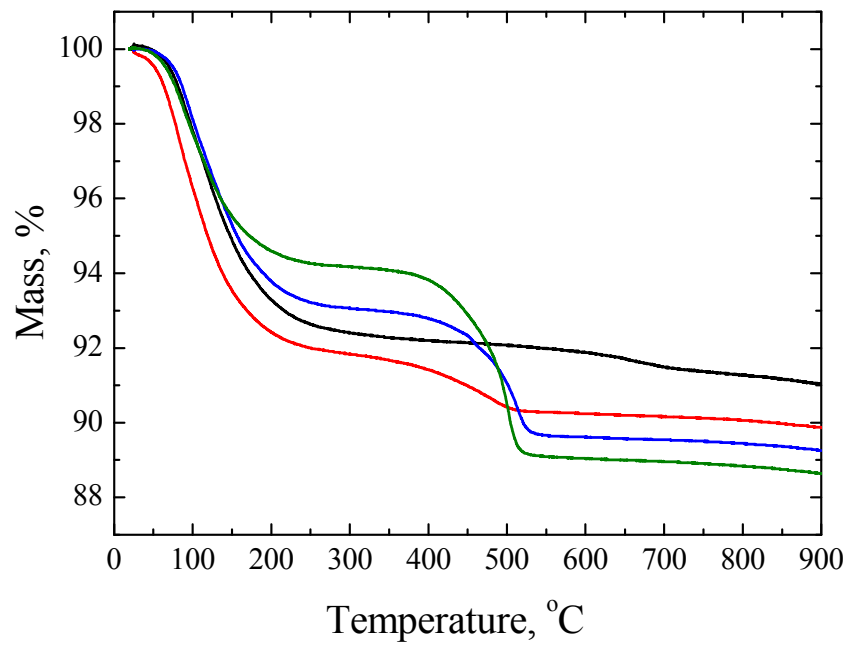
Figure 4.7 – Thermogravimetric (TG) profile for fresh (—), 4 h (—), 24 h (—) and 48 h (—) coked PtH-ZSM-5(30) catalysts
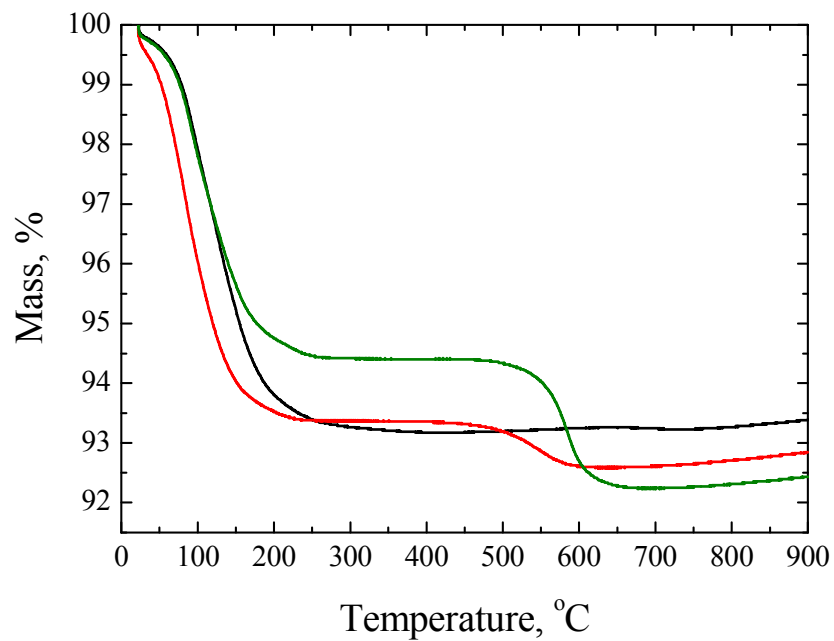
Figure 4.8 – Thermogravimetric (TG) profile for fresh (—), 4 h (—), and 48 h (—) coked PtH-ZSM-5(80) catalysts

The amount of coke formed at different TOS is summarized in Table 4.3. In spite of an increase in the coke content, the rate of coke deposition declined with time after a rapid increase in the amount of carbonaceous deposits at 4 h TOS. The highest amount of coke deposition was 5.61 mass % on the PtH-ZSM-5(30) catalyst after 48 hours on-stream. Comparing the total amount of coke formed at the same TOS, the bifunctional zeolite catalyst with lower SiO_2/Al_2O_3 ratio yields a greater amount of coke.

Table 4-3 – Values of coke content for PtH-ZSM-5 catalysts after different TOS. The coke content measured has a standard error of ± 0.03 %.

Time on Stream (h)	Total Coke (mass %)	
	PtH-ZSM-5(30)	PtH-ZSM-5(80)
4	1.83	0.76
24	3.39	-
48	5.61	2.00

Table 4-4 – Volume of coke deposited in PtH-ZSM-5 catalysts

Time on Stream (h)	Coke Volume, V_c (cm^3 g^{-1}_{cat})	
	PtH-ZSM-5(30)	PtH-ZSM-5(80)
4	1.44E-2 ± 4.08E-4	6.41E-3 ± 1.81E-4
24	2.72E-2 ± 7.71E-4	-
48	4.49E-2 ± 1.27E-3	1.60E-2 ± 4.53E-4

In order to calculate the volume of coke (V_c) given in Table 4.4 using Equation 4.3, the density of coke must be known. The IR spectrum of the 48 hour coked PtH-ZSM-5(30) sample showed IR bands which were ascribed to coke molecules [4, 5]. Given that the IR bands observed for the coked catalyst in Figure 4.6 appeared at the same wavenumber region as the IR bands reported by Uguina et al. [4] for ZSM-5 sample coked with toluene, and Sotelo et al. [5], for Mg-modified ZSM-5 samples coked during alkylation of toluene with methanol, the nature of the coke deposit was assumed to be the same. Hence, coke of density in the range between 1.2 g cm^{-3} and 1.3

g cm^{-3} [4-5, 13] was assumed. The uncertainties in the coke densities were taken into account when evaluating the standard errors in coke volume, V_c (Table 4.4).
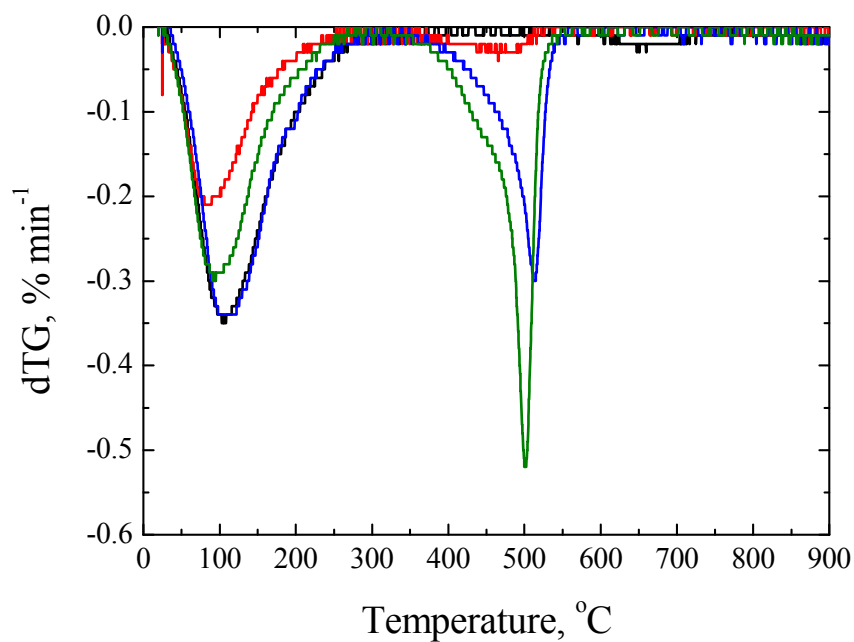
Figure 4.9 – dTG profile for fresh (—), 4 h (—), 24 h (—) and 48 h (—) coked PtH-ZSM-5(30) catalysts
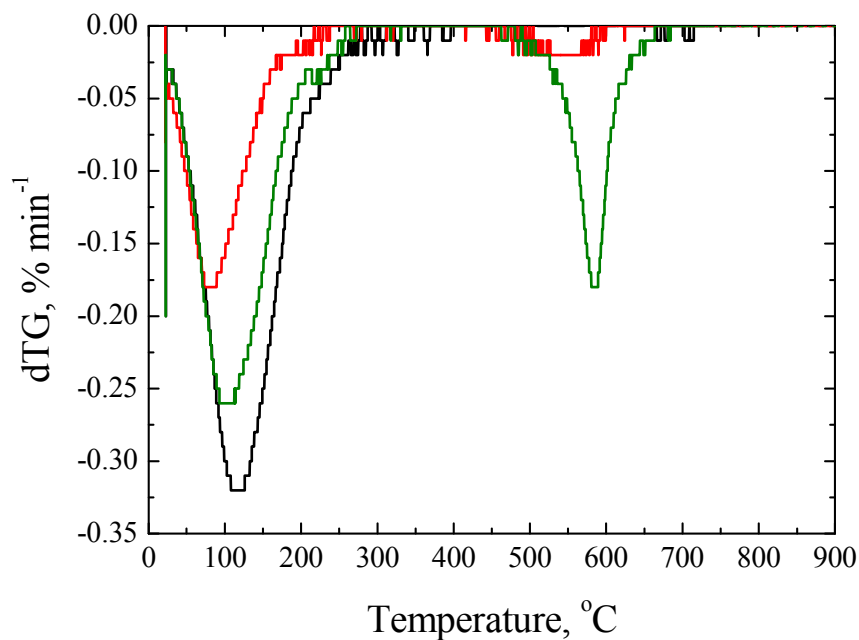
Figure 4.10 – dTG profile for fresh (—), 4 h (—), and 48 h (—) coked PtH-ZSM-5(80) catalysts

Derivative thermogravimetric (dTG) curves, expressed as mass loss rates, are also shown in Figures 4.9 and 4.10. Two maximum peaks were observed in the dTG curves, which correspond to the two steps in the TGA curve (Figures 4.7 and 4.8). The peaks for the coked samples differ in their positions and intensities when compared with the fresh catalyst. The observed shift in the second maximum peak to higher temperature with TOS (particularly comparing 4 h and 48 h TOS in Figure 4.10) could be an indication of the presence of more heavy species/aromatics in the coked catalysts, or that the coke being oxidised was then in regions which were more inaccessible, and therefore required higher temperature for removal from the catalyst bed. It is also possible that the shifts in dTG peaks to higher temperatures indicate a higher degree of structural order in the deposited cokes, and hence lower oxidation reactivity. The shape of the second maximum peak for the 24 h and 48h TOS dTG curves in Figure 4.9 is very similar. Therefore, it is possible to conclude that the nature of coke is the same, and hence the same densities were used to determine the coke volume for 24 h and 48 h coked samples.

4.4.3   X-Ray Diffraction
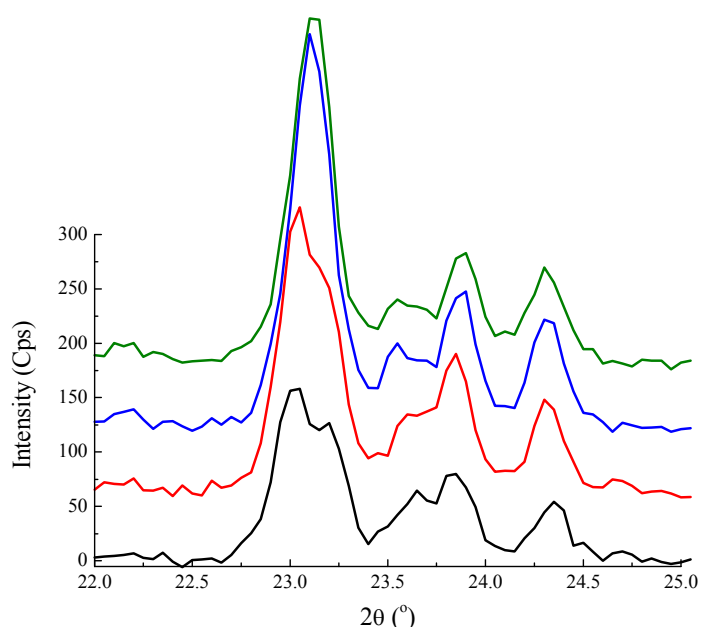
Figure 4.11 – XRD data for fresh (─) and coked PtH-ZSM-5(30) samples after 4 h (─), 24 h (─) and 48 h (─)TOS
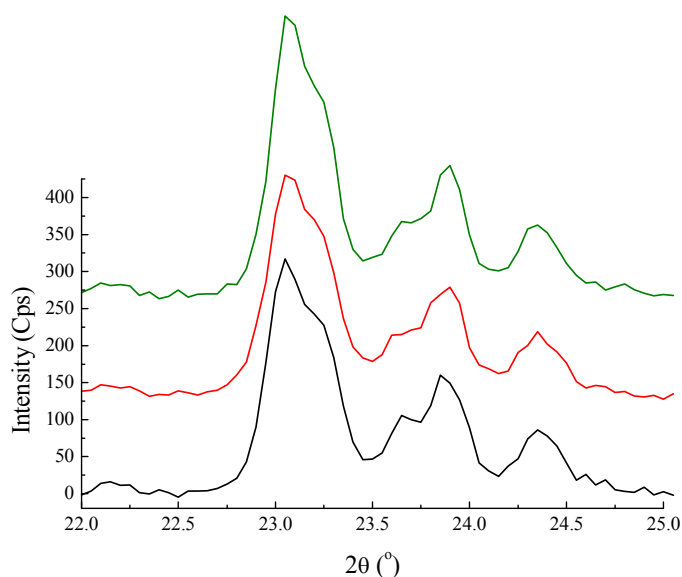
Figure 4.12 – XRD data for fresh (—) and coked PtH-ZSM-5(80) samples after 4 h (—), and 48 h (—) TOS

Figure 4.11 compares the diffraction patterns of the fresh and coked PtH-ZSM-5(30) catalysts. The characteristic bands at $2\theta = 22^{o}$ to 25° were the main difference between the diffraction pattern of the coked catalysts and that of the fresh ones, so the spectra in these regions were expanded for clarity. The changes in the relative intensities and diffraction peak positions were compared for the fresh and deactivated samples. With increasing TOS, the doublet nature of the peak at $2\theta = 23^{o}$-23.2^{o} region collapsed onto one peak at $2\theta = 23.12^{o}$ with increasing intensity.

In contrast to the behaviour of the PtH-ZSM-5(30) catalyst, the position and the nature of the doublet peak was retained for the PtH-ZSM-5(80) (Figure 4.12) catalyst even as the amount of coke formed increased with TOS. Since previous studies [4, 10] have attributed the distortion of the diffraction peaks to coke formation within the crystallites, the lack of this distortion suggests that no deformation of the zeolite framework was detected when coke is formed during benzene alkylation with ethane over PtH-ZSM-5(80) catalysts.

4.4.4 Scanning Electron Microscopy

SEM images of PtH-ZSM-5 catalysts were taken to investigate the changes in the morphology of the zeolite crystallites with coking. Due to the resolution of this technique, only the surface of the zeolite crystallites was captured.

Platinum was impregnated on the H-ZSM-5 catalyst since it is known to be an active dehydrogenation catalyst. Since Pt has a higher atomic number (heavy element) in comparison with other elements on the surface of the ZSM-5 crystallites (Si, Al, O), it will backscatter electrons more strongly than the light elements, and, hence, appears brighter in the BSE images. Typical examples of the BSE microscopy images of PtH-ZSM-5 catalysts at different TOS are shown in Figures 4.13 – 4.14. In the backscattered images, the bright white dots represent the platinum particles on the surface of the zeolite crystallites. On pure H-ZSM-5 catalysts however, no white dots were detected as Pt is not present on the catalyst (Figure 4.15).
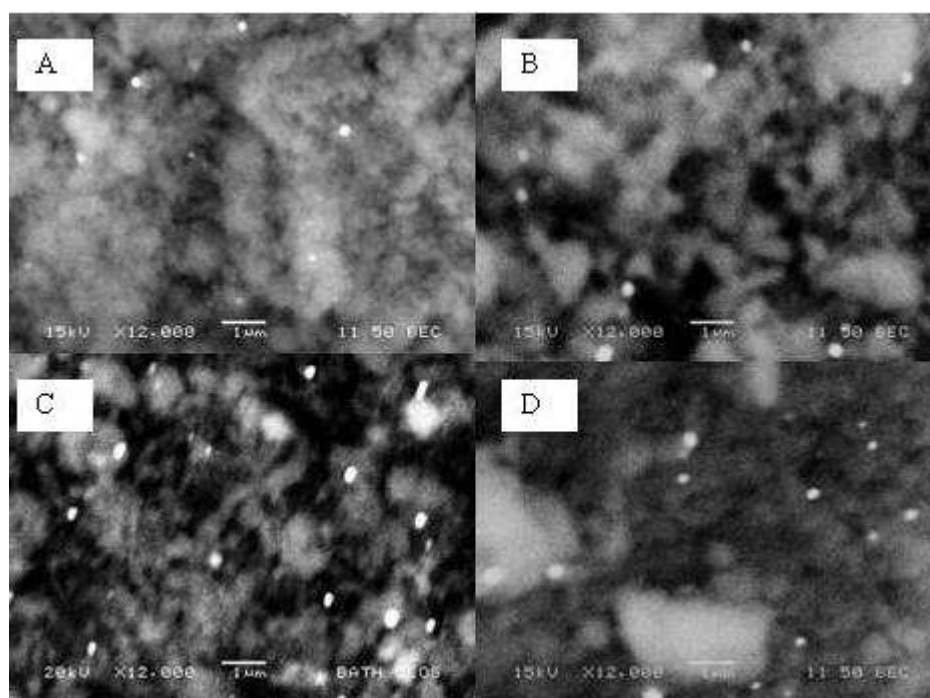
Figure 4.13 – Backscattered images of fresh (A), 4 h coked (B), 24 h coked (C), and 48 h coked (D) PtH-ZSM-5(30) catalysts
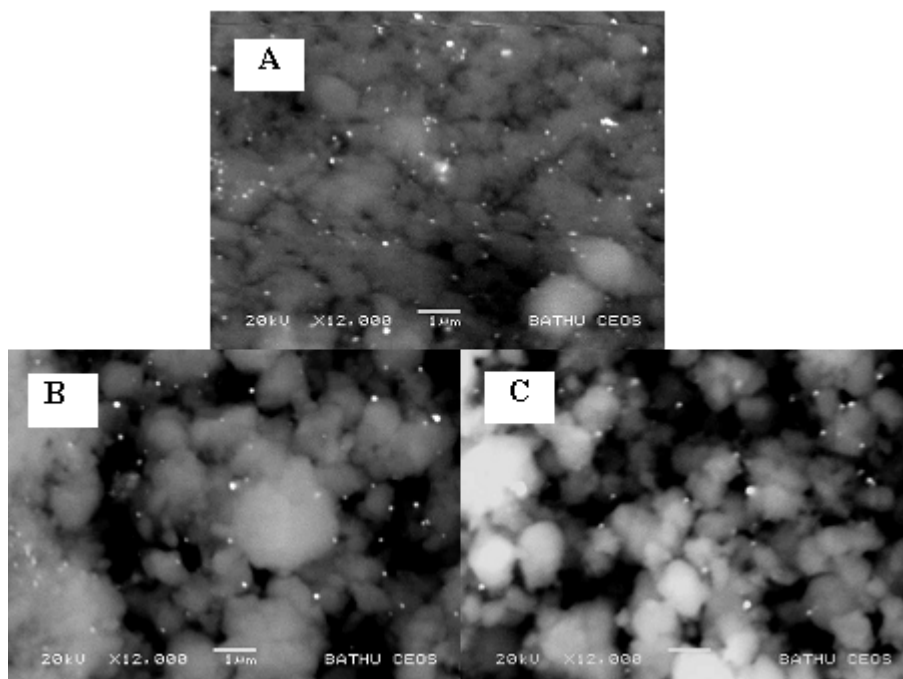
Figure 4.14 – Backscattered images of fresh (A), 4 h coked (B), and 48 h coked (C) PtH-ZSM-5(80) catalysts
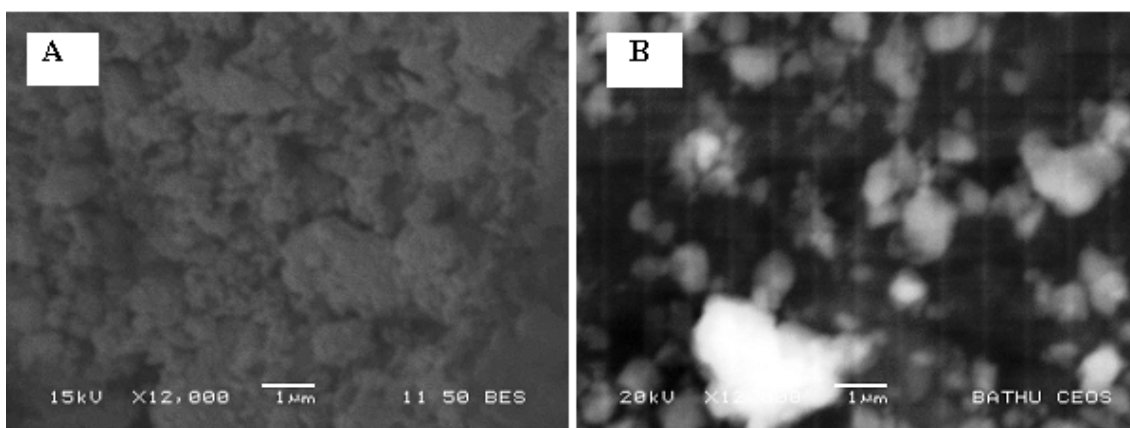
Figure 4.15 – Backscattered image of H-ZSM-5(30) (A) and H-ZSM-5(80) (B) catalysts
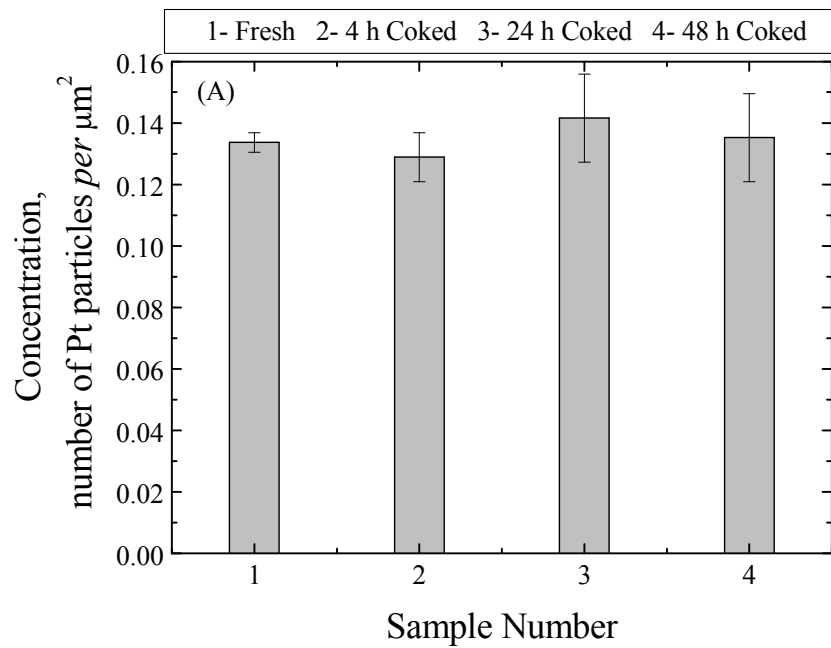
Figure 4.16 – Effect of TOS on the concentration of Pt particles on the surface of the PtH-ZSM-5(30) crystallites
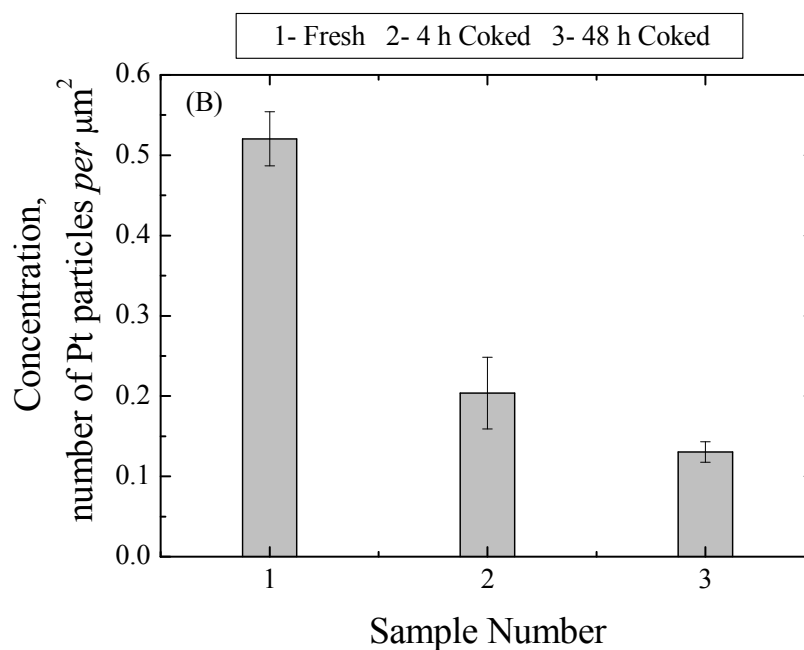
Figure 4.17 – Effect of TOS on the concentration of Pt particles on the surface of the PtH-ZSM-5(80) crystallites

If coke was deposited on the surface of the zeolite crystallite, it would be expected that some of the Pt particles would be obscured by coke molecules, and hence not detected on the micrographs. A quantitative analysis was carried out on the BSE images obtained to investigate the effect of coke deposition on the Pt particles present on the surface of the zeolite crystallites. From, typically, images of three or more different, but identically-sized, regions of the zeolite surface for each sample at different TOS, the number of Pt particles on the surface of the crystallites was calculated. The sampling errors in the surface Pt concentrations are given by the error bars shown in Figures 4.16 and 4.17.

The average concentration of Pt on the surface of PtH-ZSM-5(30) crystallites remained the same before and after coking (Figure 4.16). Conversely, a reduction in the Pt concentration on the surface of the PtH-ZSM-5(80) crystallites with TOS (Figure 4.17) was observed.

4.4.5 Nitrogen and argon sorption

4.4.5.1 Preliminary Checks

It was pointed out by Eleftherious and Theocharis [34] that by increasing the thermal pre-treatment temperature, more space is created for nitrogen adsorption, as more water was removed from zeolite pores. However, it was not mentioned that the heating temperature and duration could possibly change the nature of the adsorbent. Preliminary investigations were carried out to examine the reproducibility of the gas sorption results, as well as the effect of sample preparation conditions on PtH-ZSM-5 samples. It is important to avoid changing the structure of the coked catalysts prior to sorption analysis in order to examine the real effect of coke on the catalyst's pore structure.
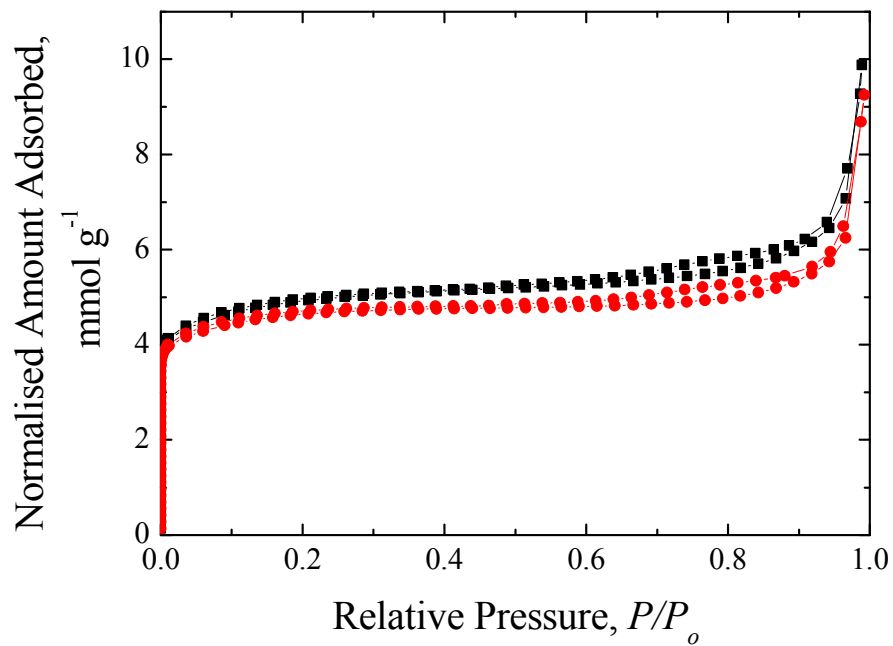
Figure 4.18 – Nitrogen sorption isotherms at 77 K: (-■-) H-ZSM-5(30) heated until sample weight remained constant, (-●-) H-ZSM-5(30) heated overnight
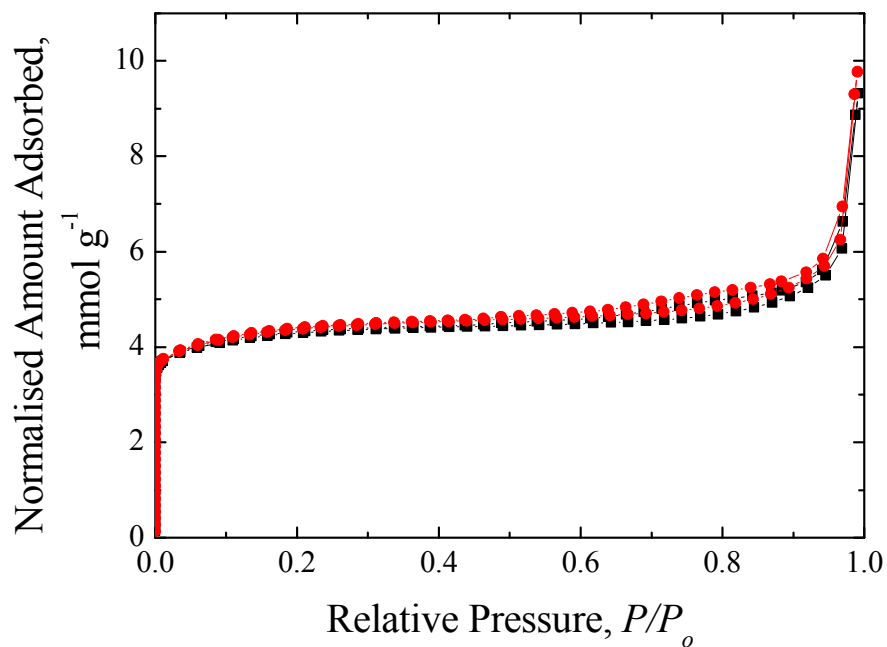
Figure 4.19 – Nitrogen sorption isotherms at 77 K: (-■-) 4h coked PtH-ZSM-5(30) heated until sample weight remained constant, (-●-) 4 h coked PtH-ZSM-5(30) heated overnight

Figures 4.18 and 4.19 compare the nitrogen sorption isotherms for H-ZSM-5(30) and 4h coked PtH-ZSM-5(30) samples that were heated at 250 ^{o}C for different durations. The temperature of 250 ^{o}C was chosen based on results from the thermogravimetric analysis where at this temperature, water was shown to be desorbed from the sample as discussed in Section 4.4.2. Despite different heating durations, the shape of the isotherms remained the same. The difference between the sorption capacities in Figure 4.18 is very small while the two isotherms in Figure 4.19 lie on top of one another. The sorption results revealed that the pore structure of the zeolite catalysts were not affected by the different heating durations, provided that the temperature of pre-treatment is less than the temperature at which the reaction was carried out.
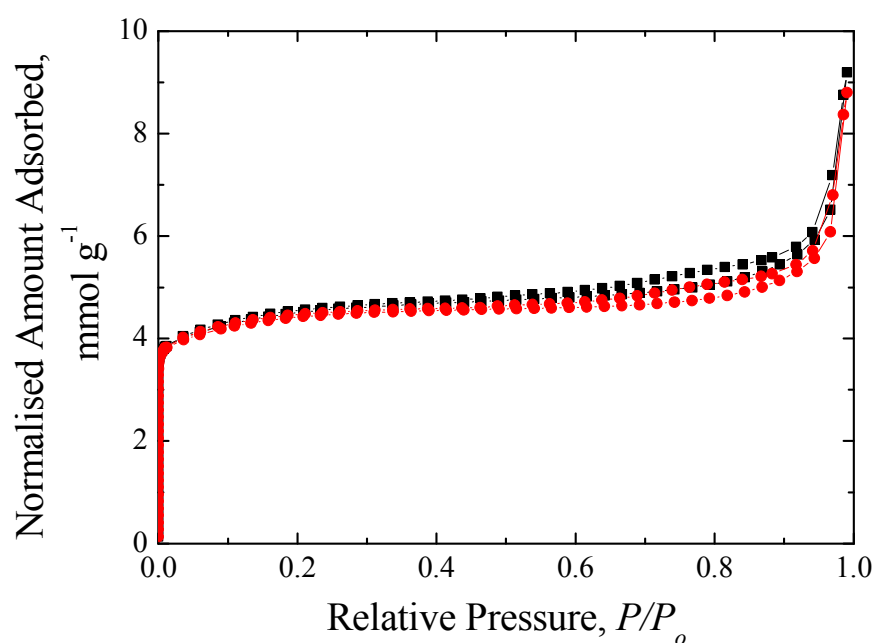
Figure 4.20 – Reproducibility of nitrogen sorption isotherms of PtH-ZSM-5(30) :
(-■-) Isotherm 1, (-●-) Isotherm 2
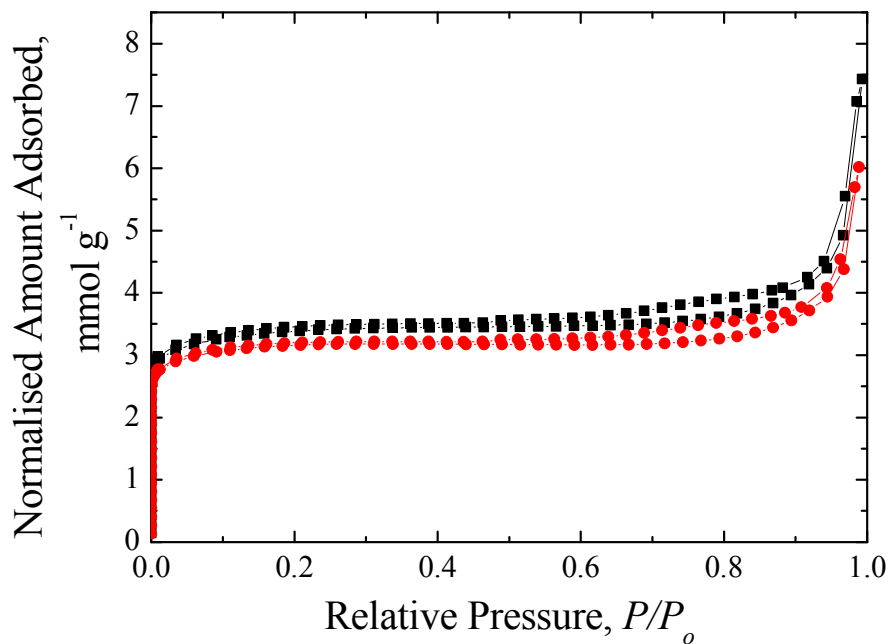
Figure 4.21 – Reproducibility of nitrogen sorption isotherms of 48 h coked PtH-ZSM-5(30): (-■-) Isotherm 1, (-●-) Isotherm 2

The architecture of porous solids could possibly be altered after the sorption analysis. Hence, isotherms obtained are not reproducible and the sample cannot be reused. Several experiments were carried out to ensure that the pore structures of PtH-ZSM-5 catalysts were not destroyed by the first sorption analysis. Duplicate nitrogen sorption isotherms for the fresh and coked PtH-ZSM-5(30) catalysts are shown in Figures 4.20 and 4.21. The sorption isotherms overlap each other at low P/P_o, and showed a small variation between sorption capacities as the P/P_o increases. However, the difference observed was considered to be negligible in comparison with the effect of coking illustrated in Figures 4.25 – 4.28. Hence, the reproducibility of sorption isotherms applies to both, fresh zeolite catalysts as well as zeolite catalysts that were coked during benzene alkylation.
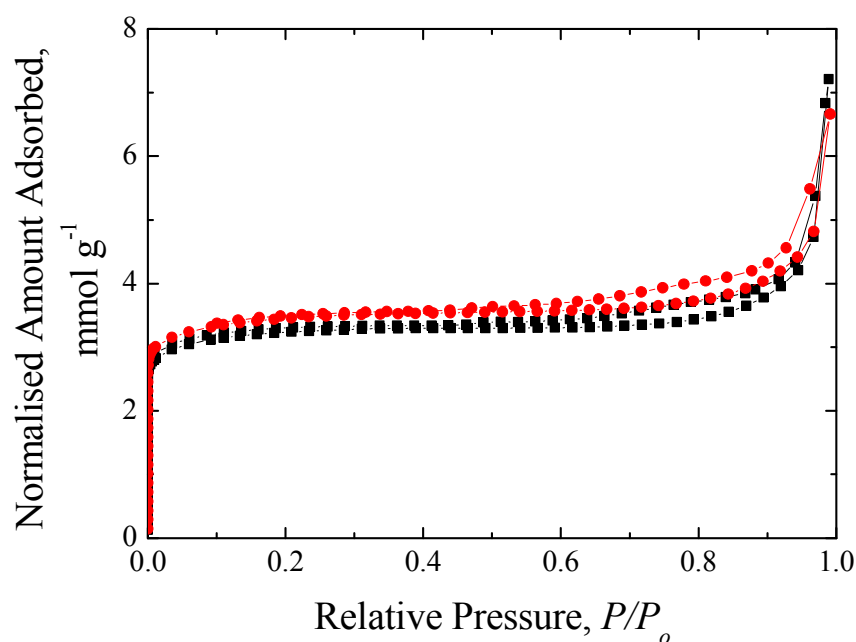
Figure 4.22 – Nitrogen sorption isotherms for 48 h coked PtH-ZSM-5(30) catalysts (-■-) freshly prepared and (-●-) samples kept for 1 year

As the series of PtH-ZSM-5 catalysts were involved in many experiments throughout the duration of this project, the effect of time on coked catalysts was also examined. Comparing sorption isotherms of freshly prepared coked samples with coked samples that have been kept for 1 year in Figure 4.22, it was confirmed that the pore characteristics of the coked catalysts were not affected by time, and any differences observed in the sorption isotherms was not due to the effect of time.

4.4.5.2   N₂ and Ar Sorption Isotherms

Figure 4.23 shows the nitrogen (77 K) and argon (77 K) sorption isotherms for the PtH-ZSM-5(30) catalyst. Isotherms plotted are of type IV classification. PtH-ZSM-5 samples exhibit a high uptake of gas at very low P/P_o, which is a characteristic of adsorption in pores of molecular dimensions, with further adsorption on the external crystal surface of the zeolite catalyst. The isotherms do not give the standard Type I isotherm (for microporous adsorbents) with a horizontal plateau, but the isotherms are convex to the P/P_o axis at high P/P_o due to the high adsorption on the external and/or mesopore surface. The small step in the nitrogen sorption isotherm of the PtH-ZSM-

5(30) sample at $P/P_o \sim 10^{-7}$ was considered as noise in the data due to the low sensitivity of pressure measurements at such low pressure region.
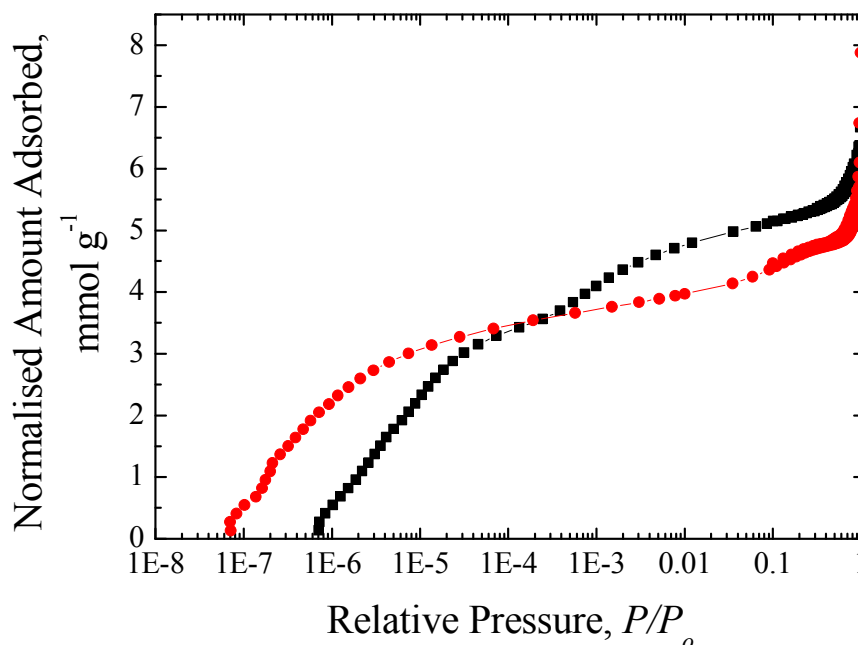
Figure 4.23 – Nitrogen (-●-) and argon (-■-) sorption isotherms for fresh PtH-ZSM-5(30) catalyst

The shape of the isotherms obtained for ZSM-5 zeolites in this present work is similar to that reported by other researchers [9, 12, 35]. According to Hudec et al. [35], the further adsorption of nitrogen at high P/P_o was due to metal loading on the ZSM-5 catalyst, which significantly increases the external surface area of zeolite crystallites. Gervasini [25] subsequently reported that the deposition of metal on ZSM-5 leads to an increase in surface area outside of the micropores, which is consistent with earlier results of Hudec et al. [35]. Therefore, the high uptake of nitrogen and argon when P/P_o approaches unity (as seen in Figure 4.23), could be associated with the increase in external surface area as a result of Pt metal impregnated on the ZSM-5 catalyst.

Hysteresis loops were present in the nitrogen and argon sorption isotherms obtained. The hysteresis loop observed for PtH-ZSM-5 catalysts may possibly indicate the presence of a mesopore network which allowed capillary condensation. Adsorption in void spaces in the intercrystalline region could also result in the presence of hysteresis loop in argon and nitrogen isotherms. The P/P_o of the hysteresis loop of N_2

and Ar isotherms are in the same range, and the low pressure ($P/P_o \sim$ 0.1-0.15) hysteresis loop described in earlier research [22, 36-37] was not observed in this work.

Stepped isotherms were reported by previous studies for argon and nitrogen adsorption on MFI type zeolites [48-51]. However, in this work, no obvious steps were observed in nitrogen sorption isotherms, but a slight step was seen for argon sorption isotherms for P/P_o range of 10^{-4} and 10^{-3}. It was reported that the step observed is due to successive filling of channels and intersections [38]. The stepwise adsorption isotherm for nitrogen adsorption on ZSM-5 crystals was later interpreted by Muller [39], and Carrott and Sing [36] as localized adsorbate molecules in channel site and channel interactions.

Based on molecular simulations and experimental work, it was suggested that the step-like isotherm is due to progressive changes in the structure of the zeolite adsorbent, from monoclinic to orthorhombic, as adsorbate loading increases [40]. On the other hand, some researchers associate the transition to the densification of the adsorbate phase [36, 37, 39, 42]. The densification of the adsorbate is linked with the phase change of the adsorbate to a state of increased order, from a disordered phase to a lattice fluid like phase as seen from diffraction patterns [41]. It was further suggested that the relaxation of zeolite is accompanied by the ordering of the adsorbed phase [40].

4.4.5.3   *Comparison of N$_2$ and Ar isotherms*

Nitrogen and argon were used for characterisation of PtH-ZSM-5 catalysts by gas sorption. The two gases have similar molecular diameter and polarizability, but different potential interactions with the surface of porous solids. While a quadruole moment is present in nitrogen, it is absent in argon. The difference between these two gases allowed the investigation of the effect of quadrupole moment on the sorption isotherms and the characteristics of the zeolite sample.

Figure 4.23 compares the nitrogen and argon adsorption isotherm for the fresh PtH-ZSM-5(30) catalyst. The nitrogen isotherm is shifted an order of magnitude towards lower P/P_o in comparison to the argon adsorption isotherm, consistent with previous findings [17, 42]. The quadrupole moment of the nitrogen molecule leads to

stronger interaction between nitrogen molecules and pore walls of zeolite catalysts as compared to the non-specific adsorptive property of argon.

4.4.5.4 *Comparison of adsorption isotherm for PtH-ZSM-5 catalysts with different SiO₂/Al₂O₃ ratio*
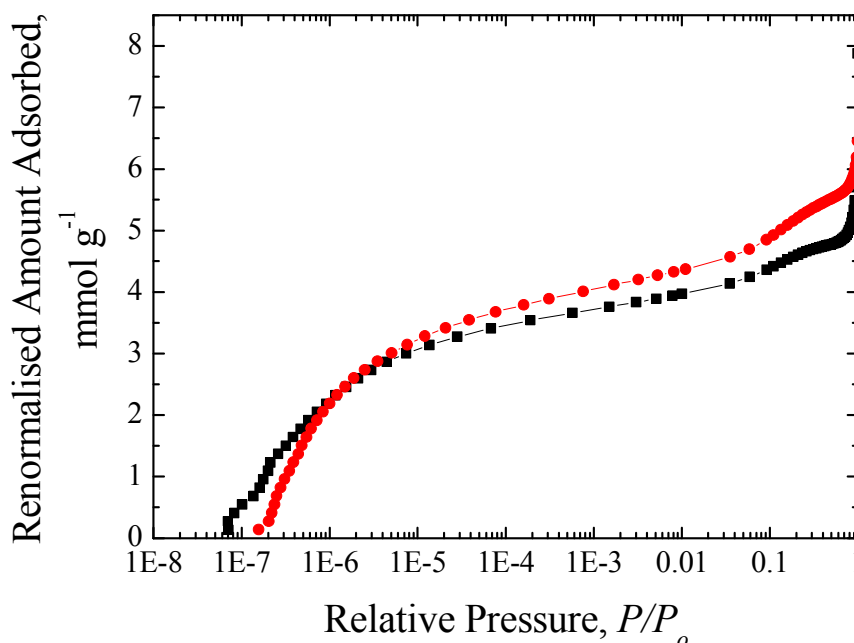
Figure 4.24 – Nitrogen adsorption isotherms for fresh PtH-ZSM-5(30) (-■-) and PtH-ZSM-5(80) (-●-) catalysts

In this study, the alkylation of benzene with ethane was carried out over two PtH-ZSM-5 catalysts of different SiO_2/Al_2O_3. Variations in the SiO_2/Al_2O_3 ratio have been said to affect the crystal size of the ZSM-5 zeolite [35] and hence, the shape of the isotherms. It was previously reported that, decreasing the Si/Al ratio affects the transition P/P_o where the isotherm step occurs, as well as making it more diffuse [42-43]. However, the aluminium content will only affect the transition when adsorbate loading supplied for adsorption is large [42].

From the isotherms presented in Figure 4.24, it can be deduced that adsorption took place at lower P/P_o for the PtH-ZSM-5 catalyst that contains higher aluminium content. This could possibly be due to the interaction of the quadrupole moment of

101

nitrogen molecules with the Al-sites (polar sites) present in the microporous channels of ZSM-5 zeolites.

4.4.5.5 *Effect of Coke on Nitrogen and Argon Adsorption*

In the previous section, it was demonstrated that sorption isotherms were reproducible and that the samples can be reused for further analysis. Following the establishment of the experimental procedure for sorption measurements, the effects of coke on the surface and structural properties of PtH-ZSM-5 catalysts were studied.

Nitrogen and argon adsorption isotherms for the fresh and partially deactivated PtH-ZSM-5(30) catalysts are shown in Figures 4.25 - 4.28 while those of PtH-ZSM-5(80) are illustrated in Figures 4.29 - 4.32. The overall shapes of the isotherms remained the same before and after coking. The main difference observed between the fresh and coked catalysts was the total adsorption capacity of the PtH-ZSM-5 catalysts. On the linear isotherm plot, only a steep rise of amount adsorbed was observed at very low P/P_o range. The slope of the isotherm is very steep, indicating adsorption in pores of molecular dimensions at these P/P_o. It was recommended to plot the amount adsorbed against log (P/P_o) to identify the presence of micropores by the point of inflection in the high-resolution isotherm at low P/P_o [20, 44]. As suggested, the amount of nitrogen and argon adsorbed was plotted against the P/P_o range on a logarithmic scale on the x-axis to allow a detailed observation of the micropore region. The logarithmic graph showed the characteristic 'S' shaped curves of microporous solids as compared to the steep rising region on the linear isotherm plot. The difference in the isotherms observed at low P/P_o indicated that the semi-logarithmic plot was clearly more informative for micropore filling than the linear isotherm plot.
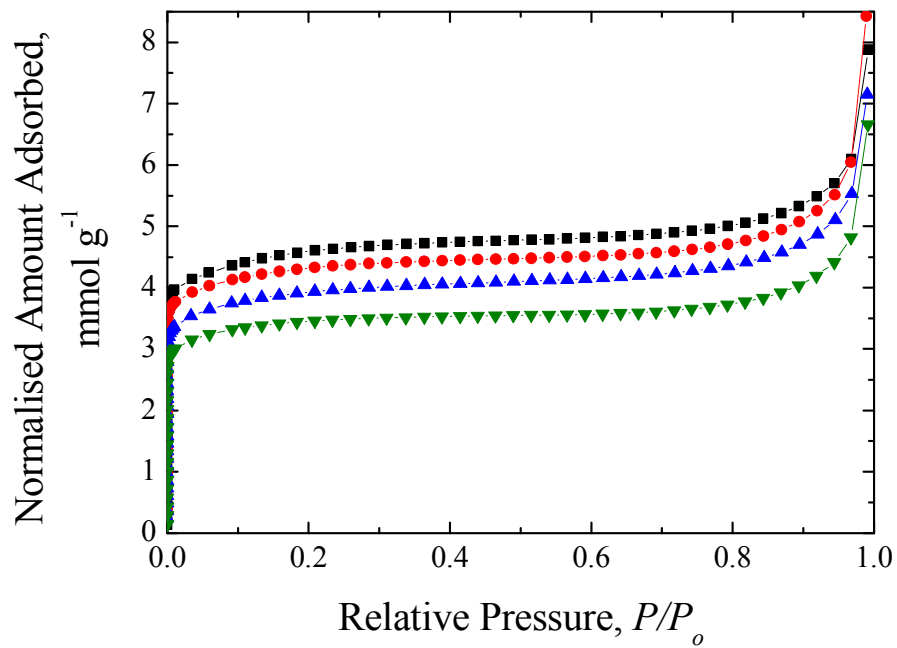
Figure 4.25 – Nitrogen adsorption isotherms for fresh (-■-), 4 h (-●-), 24 h (-▲-) and 48 h (-▼-) coked PtH-ZSM-5(30) catalysts
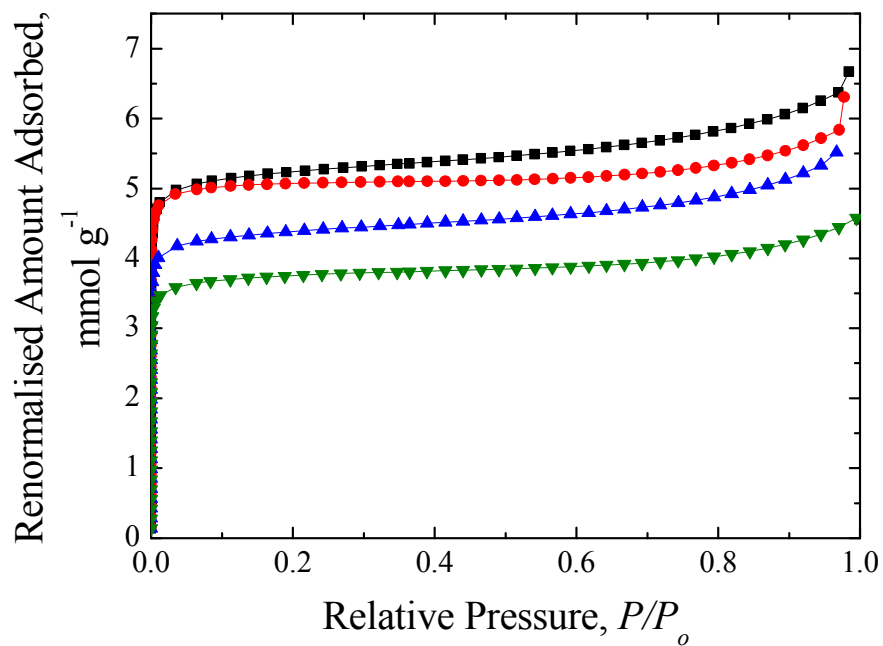
Figure 4.26 – Argon adsorption isotherms for fresh (-■-), 4 h (-●-), 24 h (-▲-) and 48 h (-▼-) coked PtH-ZSM-5(30) catalysts
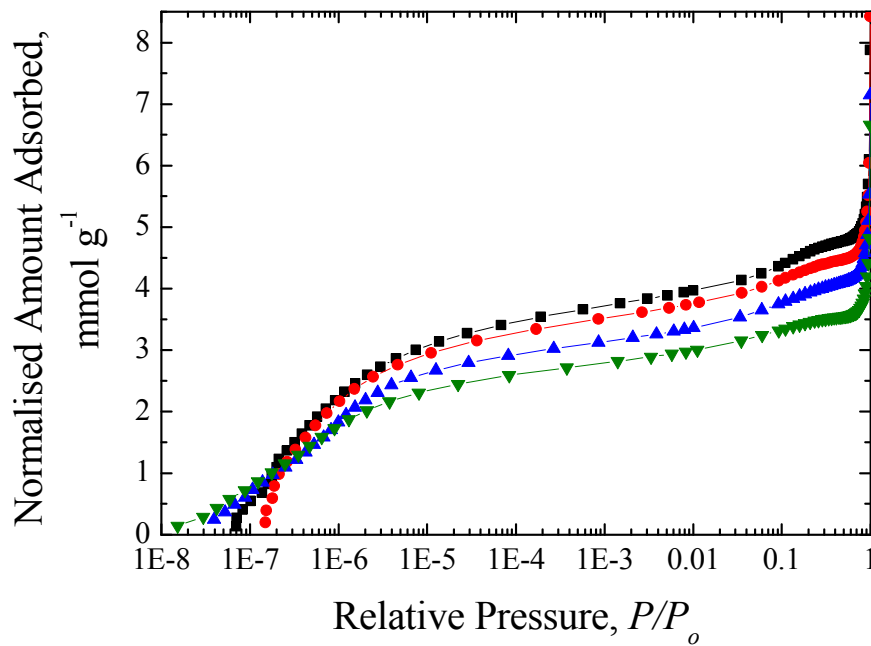
Figure 4.27 – Semi log plot of nitrogen adsorption isotherms for fresh (-■-), 4 h (-●-), 24 h (-▲-) and 48 h (-▼-) coked PtH-ZSM-5(30) catalysts
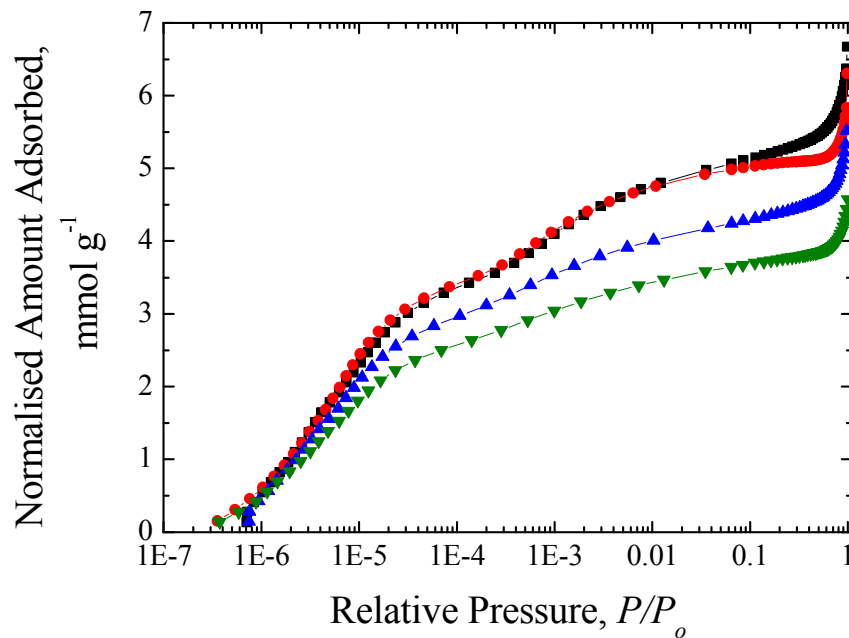
Figure 4.28 – Semi log plot of argon adsorption isotherms for fresh (-■-), 4 h (-●-), 24 h (-▲-) and 48 h (-▼-) coked PtH-ZSM-5(30) catalysts
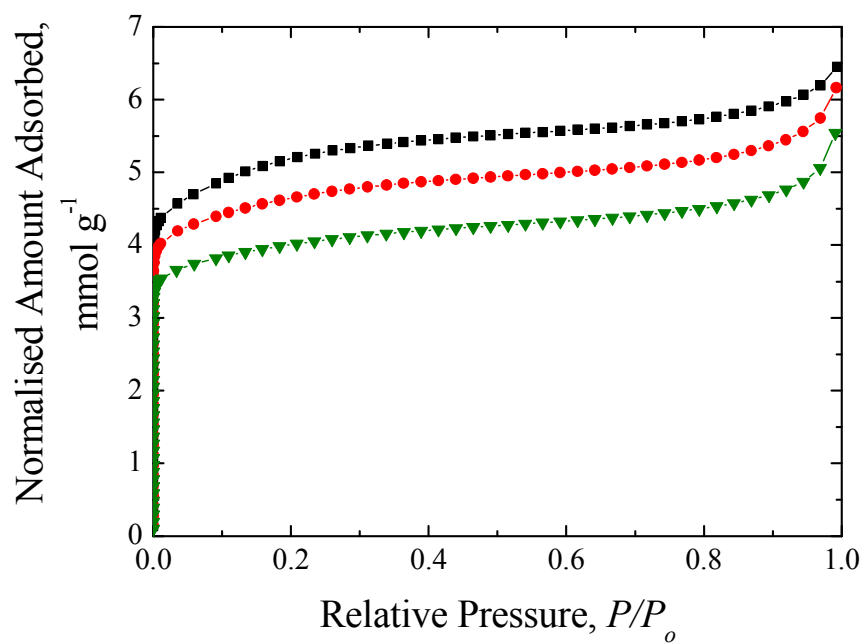
Figure 4.29 – Nitrogen adsorption isotherms for fresh (-■-), 4h (-●-) and 48h (-▼-) coked PtH-ZSM-5(80) catalysts
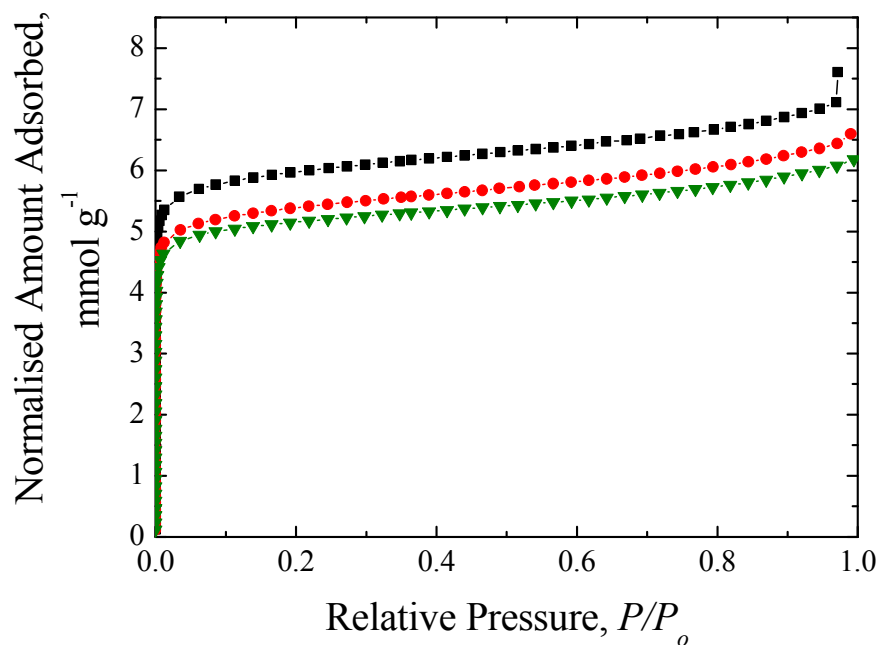
Figure 4.30 – Argon adsorption isotherms for fresh (-■-), 4h (-●-) and 48h (-▼-) coked PtH-ZSM-5(80) catalysts
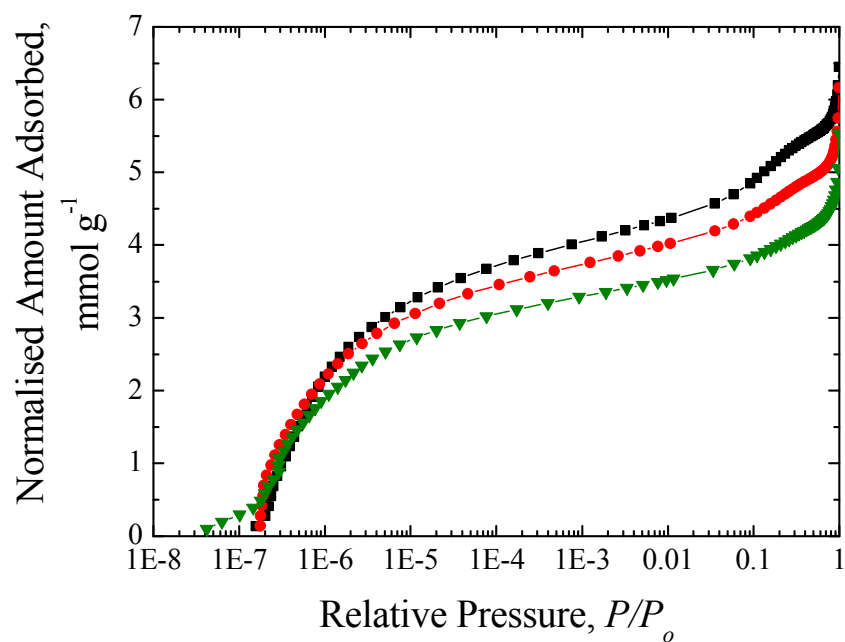
Figure 4.31 – Semi log plot of nitrogen adsorption isotherms for fresh (-■-), 4h (-●-) and 48h (-▼-) coked PtH-ZSM-5(80) catalysts
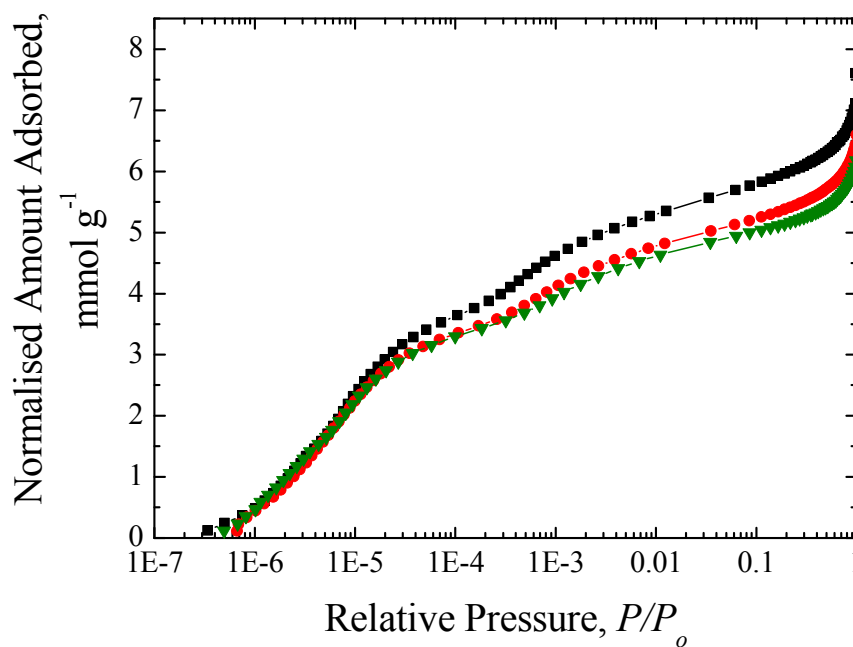
Figure 4.32 – Semi log plot of argon adsorption isotherms for fresh (-■-), 4h (-●-) and 48h (-▼-) coked PtH-ZSM-5(80) catalysts

As with the results obtained from the PtH-ZSM-5(30) catalyst, the adsorption capacity for the PtH-ZSM-5(80) also decreased with TOS (Figures 4.29 – 4.32). As mentioned earlier, the coked sample isotherms for PtH-ZSM-5(30) were shifted to lower P/P_o as a result of coke deposition. However, this shift was not obvious for the isotherms obtained for the PtH-ZSM-5(80) catalysts. The coked isotherms lie on top of the fresh sample isotherms at low P/P_o, and, only at higher P/P_o, was the difference in the adsorption capacity observed.

The adsorption isotherms for PtH-ZSM-5(30) catalysts (Figures 4.25 – 4.28) showed a progressive decline in the total amount of argon and nitrogen adsorbed in the microporous region ($P/P_o<0.2$). The difference between the total adsorption capacity of the fresh and coked catalysts was believed to be associated with the coke content indicated by the TGA results. Comparing the isotherms for the fresh and coked PtH-ZSM-5(30) samples, it was observed that the initial part of the isotherm was shifted to lower P/P_o for coked samples. The isotherm shift observed (Figure 4.27 and 4.28) for the coked catalysts could possibly be due to the effect of coke deposition during the reaction.

Table 4.5 shows the calculated values of the modified-BET surface area for the fresh and coked PtH-ZSM-5 ($SiO_2/Al_2O_3 = 30$ and 80) catalysts. The modified-BET surface area decreased with TOS, indicating that parts of the zeolite pore network were blocked or isolated by coke molecules formed.

Table 4-5 – Modified-BET Surface Area for PtH-ZSM-5(30) and PtH-ZSM-5(80) catalysts at different TOS

Time-on-Stream (TOS), h	Modified-BET Surface Area, $m^2 g^{-1}$			
	PtH-ZSM-5(30)		PtH-ZSM-5(80)	
	Nitrogen	Argon	Nitrogen	Argon
0	369.13	389.73	428.63	444.64
4	347.84	347.20	384.79	398.12
24	322.06	321.47	-	-
48	282.15	277.80	339.62	383.91

4.4.5.6   Langmuir-BET model fit

The reversible regions of the experimental adsorption isotherms were fitted to a two-component model comprising of Langmuir and BET components to distinguish between the adsorption in the dual pore system of the zeolite catalyst. Since PtH-ZSM-5 catalysts are made up of micropores within the zeolite crystallites and mesopores surrounding the zeolite crystallites, the Langmuir (Type I) model was used to represent adsorption within the microporous region, while a BET (Type II) model was used for adsorption in the pores outside of the zeolite crystallites

To determine the adsorption capacity parameters corresponding to the micropores and mesopores in the PtH-ZSM-5 catalyst, the adsorption data were fitted to Equation 4.16:

$$V = \frac{z \times V_m \times K_L \times (P/P_o)}{1 + (K_L \times P/P_o)} + \frac{(1-z) \times (V_m \times K_{BET} \times P/P_o)}{(1 - P/P_o) \times (1 - P/P_o + K_{BET} \times P/P_o)} \qquad (4\text{-}16)$$

where V= volume adsorbed, z= fraction of pores corresponding to Langmuir component, K_L= Langmuir constant, P/P_o= relative pressure , V_m= monolayer capacity, K_{BET}= BET constant

The ratios of the respective fitted adsorption capacity parameters to the total value for both components for the fresh catalyst were determined. From Tables 4.6(i) and 4.6(ii), it can be seen that the ratio of the BET component adsorption capacity parameter showed little change with TOS relative to the Langmuir component for the PtH-ZSM-5(30) catalysts.

In contrast to results for the PtH-ZSM-5(30) catalyst, a more significant drop was observed for the adsorption capacity ratio for the BET component, with TOS for PtH-ZSM-5(80) samples (Tables 4.6(i) and 4.6(ii)). Since only the ratio of the BET component adsorption capacity parameter was changing with TOS, and little variation was observed for the Langmuir component, a different deactivation mechanism was proposed for the PtH-ZSM-5(80) catalyst.

Table 4-6 – Results of Langmuir and BET composite model fit to (i) nitrogen and argon (ii) adsorption isotherms for PtH-ZSM-5(30) and PtH-ZSM-5(80) catalysts. Notes: W/W_o is the ratio of the adsorption capacity parameter of the relevant component, W, for the coked sample, to the corresponding total value, W_o, for the fresh catalyst

(i) Nitrogen

Time on Stream (TOS), h	W/W_o (Langmuir)		W/W_o (BET)	
	PtH-ZSM-5(30)	PtH-ZSM-5(80)	PtH-ZSM-5(30)	PtH-ZSM-5(80)
0	0.79 ± 0.05	0.75 ± 0.02	0.21 ± 0.02	0.25 ± 0.01
4	0.71 ± 0.05	0.67 ± 0.01	0.21 ± 0.02	0.22 ± 0.01
24	0.66 ± 0.05	-	0.21 ± 0.02	-
48	0.56 ± 0.04	0.67 ± 0.01	0.19 ± 0.02	0.19 ± 0.01

(ii) Argon

Time on Stream (TOS), h	W/W_o (Langmuir)		W/W_o (BET)	
	PtH-ZSM-5(30)	PtH-ZSM-5(80)	PtH-ZSM-5(30)	PtH-ZSM-5(80)
0	0.76 ± 0.02	0.68 ± 0.01	0.24 ± 0.01	0.32 ± 0.01
4	0.74 ± 0.02	0.64 ± 0.01	0.25 ± 0.01	0.25 ± 0.01
24	0.61 ± 0.01	-	0.23 ± 0.01	-
48	0.55 ± 0.01	0.63 ± 0.01	0.20 ± 0.01	0.23 ± 0.01

4.5 Discussion

4.5.1 Variation in the Characteristic of Coke Deposits with TOS

From Table 4.3, it was shown that as TOS was increased to 48 hours, coke deposition increased to 5.61 mass % and 2 mass % for PtH-ZSM-5(30) and PtH-ZSM-5(80) catalysts, respectively. The formation of coke detected by TGA was believed to

be responsible for the drop in the activity of the PtH-ZSM-5 catalysts. The greater amount of coke formed, and higher rate of coke formation for the PtH-ZSM-5(30) catalyst compared with the PtH-ZSM-5(80) catalyst could be due to the greater number of acid sites on the PtH-ZSM-5(30) catalyst, or due to the difference in the spatial location and distribution of platinum as seen from the BSE images in Figures 4.13 and 4.14.

It was pointed out in Chapter 3 that, benzene conversion for the PtH-ZSM-5(30) catalyst decreased rapidly at the start of the reaction, when compared with the drop in benzene conversion at higher TOS. The plot of benzene conversion against TOS, together with coke loading, for PtH-ZSM-5(30) catalyst is shown in Figure 4.33. At the same time as when the activity of the PtH-ZSM-5(30) catalyst is deactivating drastically, the corresponding coke content strongly increased (to 1.83 mass %) within the first 4 hours of the benzene alkylation. This result implied that only a small amount of coke was required to have such a large effect on the catalytic activity of the PtH-ZSM-5(30) catalyst. Even though the amount of coke formed during benzene alkylation over PtH-ZSM-5(80) catalyst was increasing with TOS, the benzene conversion remained constant.
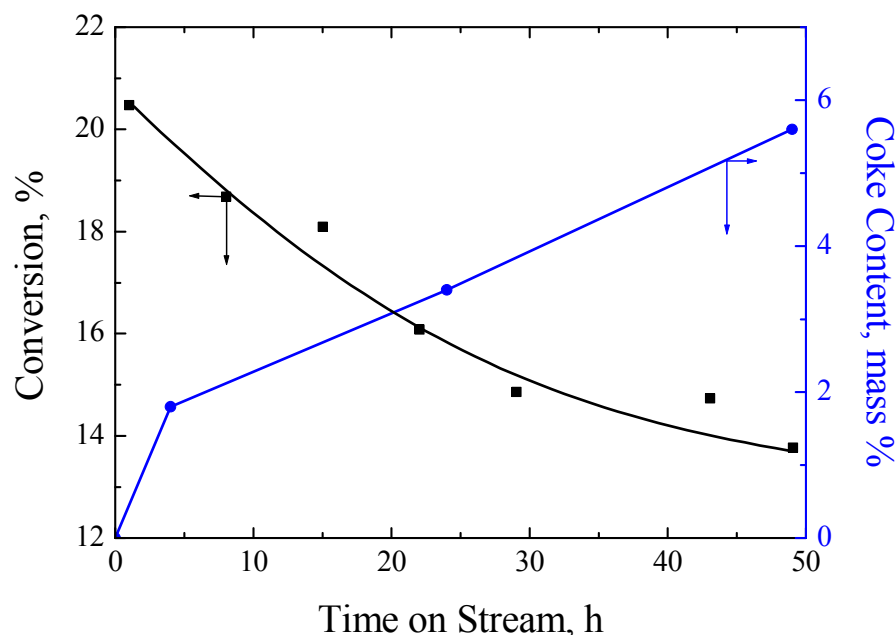
Figure 4.33 – Conversion of benzene (-■-) vs coke content (-●-) with TOS for the PtH-ZSM-5(30) catalyst

IR investigations of the 48 hour coked PtH-ZSM-5(30) catalyst demonstrate that the nature of coke deposits from the alkylation of benzene with ethane have both polyaromatic and paraffinic characters, as seen from the appearance of the IR bands at 1600 cm^{-1} and in the regions between 1300 and 1500 cm^{-1}. However, the ratio between the intensity of the 'coke band' at 1600 cm^{-1} and that of the doublet at 1369 cm^{-1} and 1382 cm^{-1} increased with coke content, which indicates the increase in polyaromatic character of coke with TOS.

4.5.2 Pore Structure Evolution with Deposition of Coke

Modifications of the pore architecture of PtH-ZSM-5 catalysts with coking were observed from nitrogen and argon adsorption results. The adsorption isotherms, comparing the fresh and spent PtH-ZSM-5 catalysts, indicated that, as TOS is increased, the amount of nitrogen and argon adsorbing is decreasing. The difference between the total adsorption capacity of the fresh and deactivated catalysts is believed to be associated with the increasing coke content at higher TOS. The loss of accessible pore volume suggests that the internal pore structure of the catalyst and/or the surface chemistry have been modified in some ways [45].
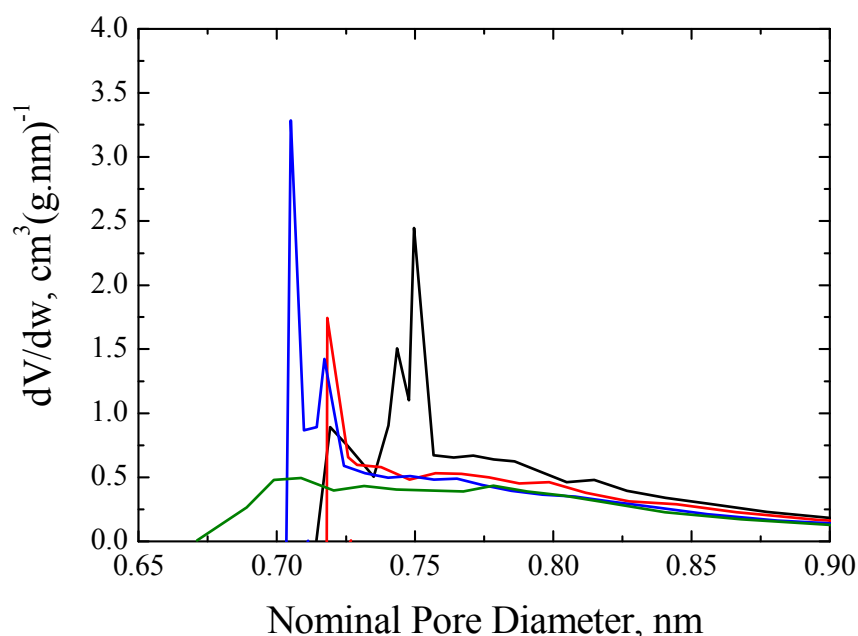
Figure 4.34 – Pore size distribution for fresh (—), 4 h (—), 24 h (—) and 48 h (—) coked PtH-ZSM-5(30) catalysts

From the nitrogen adsorption data, the pore size distribution (PSD) for the PtH-ZSM-5(30) catalyst was predicted using Horwath-Kawazoe cylindrical pore model. It should be noted that due to the simple description of the adsorbate-adsorbent interactions in the HK model, the PSD generated from it probably does not give a correct absolute pore size for the MFI catalyst. Hence, only the relative shift in the PSD is taken into account, which may reflect geometric or chemical changes, or both together. The effect of coke on the micropore size distribution of the fresh and coked PtH-ZSM-5(30) catalysts is shown in Figure 4.34. The differential pore volume plot of the fresh catalyst showed three peaks at 0.725 nm, 0.743 nm and 0.749 nm. As the carbon content increased, the three peaks progressively decreased, and the PSD was shifted to smaller pore diameters.

A significant apparent increase in the micropore volume was observed at a pore diameter of 0.72 nm for the 4 h coked catalyst and 0.71 nm for the 24 h coked catalyst. In the case of the PtH-ZSM-5(30) catalyst coked for 4 and 24 h, the modification of the micropore size distribution could result from coke deposition onto the walls of larger micropores, hence apparently creating more smaller pores. A general trend towards apparently smaller pores with increased TOS might also arise from the increasing formation of more dead-end pores as coke is deposited within the core of the crystallites. This is because adsorption occurs more readily (at lower pressure) in dead-end pores due to the increased pore potential. After 48 hours on-stream, a significant loss in micropore volume was observed, possibly induced by the diminution of the number of pores accessible to nitrogen.

4.5.3 Location of Coke Deposition

While the diffraction patterns for PtH-ZSM-5(30) catalysts changed from a doublet peak at $2\theta = 23^{\circ}\text{-}23.2^{\circ}$ for the fresh catalyst into a singlet with increasing intensity when coke is formed, the doublet peak remained so for coked samples of PtH-ZSM-5(80) catalysts. Changes in the relative position and intensities of the XRD peaks have previously been suggested to result from the distortion of the ZSM-5 lattice when it was occluded by template ions [12], or when carbonaceous residues were deposited within the zeolite pores [10]. The similar changes, observed in Figure 4.11, to those reported in the recent study by Lin et al. [10] provided evidence that the deposited coke

was located inside the zeolite crystallites, as opposed to the external location of the coke formed during the reaction over the PtH-ZSM-5(80) catalyst.

As hypothesized earlier, if coke was formed on the surface of the zeolite crystallites, it ought to obscure at least some Pt particles, but this was not observed for the PtH-ZSM-5(30) catalyst. Therefore, it can be assumed that coke was deposited inside the crystallites of the PtH-ZSM-5(30) catalyst. The reduction in the apparent surface Pt concentration with TOS (Figure 4.17) suggests the deposition of coke on the surface of the PtH-ZSM-5(80) crystallites.

The change in the ratios of the adsorption capacity parameters, from the two-component (Langmuir and BET) adsorption fits, with TOS suggested that that the deposition of coke within the PtH-ZSM-5(80) catalyst was predominantly located in the mesopore network thus giving rise to pore blockage, where the entrance to the zeolite channels was blocked by coke forming on the outside of the zeolite crystallite. However, a different mechanism was proposed for the catalyst with higher acidity and activity (PtH-ZSM-5(30)), since only the ratio of the Langmuir component adsorption capacity parameter was changing with TOS, and no variation was observed for the BET component adsorption capacity. Hence, only the pores within the zeolite crystallites were modified by coke, supporting the proposed location of coke deposition by the XRD spectra.

4.6 Conclusions

Thermogravimetric analysis showed that the amount of coke deposited on the PtH-ZSM-5 catalysts increased with TOS. As a result, the total adsorption capacity for nitrogen and argon decreased for the partially deactivated PtH-ZSM-5 catalysts, as compared with the fresh catalysts. With coke deposition on the walls of larger micropores, more smaller pores are generated, hence shifting the PSD of the coked PtH-ZSM-5(30) catalysts towards smaller pore diameters.

The diffraction pattern, together with the sorption data of different probe molecules (nitrogen and argon), suggested that coke is deposited inside the pore network of the PtH-ZSM-5(30) catalyst. In addition, the back-scattered electron images

also showed that the coke molecules formed did not obstruct the Pt particles located on the surface of the crystallites, which supports the diffraction and sorption results.

In contrast to the findings of PtH-ZSM-5(30) catalyst, coke is mainly formed in the intercrystalline regions of the PtH-ZSM-5(80) catalysts, as shown by the diffraction patterns and the decrease in BET component adsorption capacity parameters from the Langmuir-BET fit, with TOS.

4.7 References

[1]   B. Wang, and G. Manos, Journal of Catalysis 250 (2007) 121-127.

[2]   B. Wang, and G. Manos, Industrial & Engineering Chemistry Research 47 (2008) 2948-2955.

[3]   H.G. Karge, and E. Boldingh, Catalysis Today 3 (1988) 379-386.

[4]   M.A. Uguina, D.P. Serrano, R. Van Grieken, and S. Venes, Applied Catalysis A: General 99 (1993) 97-113.

[5]   J.L. Sotelo, M.A. Uguina, J.L. Valverde, and D.P. Serrano, Applied Catalysis A: General 114 (1994) 273-285.

[6]   D. Eisenbach, and E. Gallei, Journal of Catalysis 56 (1979) 377-389.

[7]   P. Dejaifve, A. Auroux, P.C. Gravelle, J.C. Vedrine, Z. Gabelica, and E.G. Derouane, Journal of Catalysis 70 (1981) 123-136.

[8]   Y. Schuurman, C. Delattre, I. Pitault, J.P. Reymond, and M. Forissier, Chemical Engineering Science 60 (2005) 1007-1017.

[9]   P.D. Hopkins, J.T. Miller, B.L. Meyers, G.J. Ray, R.T. Roginski, M.A. Kuehne, and H.H. Kung, Applied Catalysis A: General 136 (1996) 29-48.

[10]   X. Lin, Y. Fan, G. Shi, H. Liu, and X. Bao, Energy and Fuels 21 (2007) 2517-2524.

[11]   M. Guisnet, and P. Magnoux, Applied Catalysis 54 (1989) 1-27.

[12]   D.M. Bibby, N.B. Milestone, J.E. Patterson, and L.P. Aldridge, Journal of Catalysis 97 (1986) 493-502.

[13]   A. De Lucas, P. Canizares, A. Durfin, and A. Carrero, Applied Catalysis A: General 156 (1997) 299-317.

[14]   C.A. Fyfe, G.J. Kennedy, C.T. De Shutter, and G.T. Kokotailo, Journal of Chemical Society-Chemical Communication 8 (1984) 541-542.

[15] K.S.W. Sing, D.H. Everett, R.A.W. Haul, L. Moscou, R.A. Pierotti, J. Rouquerol, and T. Siemieniewska, Pure and Applied Chemistry 57 (1985) 603-619.

[16] F. Rouquerol, J. Rouquerol, and K. Sing, Adsorption By Powders and Porous Solids Principles, Methodology and Applications San Diego, Calif. ; London : Academic Press, 1999.

[17] G. Ertl, H. Knozinger, and J. Weitkamp, editors. 1997. Handbook of Heterogeneous Catalysis. VCH : Weinheim.

[18] S.J. Gregg, and K.S.W. Sing, Adsorption, Surface Area and Porosity. London : Academic Press, 1982.

[19] A.F. Venero, and J.N. Chiou, Materials Research Society Symposium Proceedings 111 (1987) 235-240.

[20] S. Storck, H. Bretinger, and W.F. Maier, Applied Catalysis A: General 174 (1998) 137-146.

[21] A. Gil, Adsorption 4 (1998) 197-206.

[22] K.S.W. Sing, Colloids and Surfaces 38 (1989) 113-124.

[23] H. Liu, L. Zhang, and N.A. Seaton, Journal of Colloid and Interface Science 156 (1993) 285-293.

[24] J. Seifert, and G. Emig, International Chemical Engineering - New York 31 (1991) 29-41

[25] A. Gervasini, Applied Catalysis A: General 180 (1999) 71-82.

[26] G. Leofanti, M. Padovan, G. Tozzola, and B. Venturelli, Catalysis Today 41 (1998) 207-219.

[27] S. Lowell, and J.E. Shields, Powder Surface Area and Porosity. Chapman and Hall, London, 1984.

[28] K.S. Walton, and R.Q. Snurr, Journal of The American Chemical Society 129 (2007) 8552-8556.

[29] J. Rouquerol, P. Llewellyn, and F. Rouquerol, Characterization of Porous Solids VII : Proceedings of the 7th International Symposium on the Characterization of Porous Solids (COPS-VII) Elsevier, Amsterdam ; London 2007, 49-56.

[30] J.C. Groen, L.A.A. Peffer, and J. Perez-Ramirez, Microporous and Mesoporous Materials 60 (2003) 1-17.

[31] D. Chen, H.P. Rebo, K. Moljord, and A. Holmen, Chemical Engineering Science 51 (1996) 2687-2692.

[32] E. Maglara, A. Pullen, D. Sullivan, and W.C. Conner, Langmuir 10 (1994) 4167-4173.

[33] H.G. Karge, W. NieBen, and H. Bludau, Applied Catalysis A: General 146 (1996) 339-349.

[34] M.-E. Eleftheriou, and C.R. Theocharis in: B. McEnaney, Mays, T.J., Rouquerol, J., Rodriguez-Reinoso, F., Sing, K.S.W., Unger, K.K., (Ed.), An Anomalous Adsorption of ZSM-5 Zeolites, Royal Society of Chemistry, University of Bath. 1997, 475-490.

[35] P. Hudec, A. Smieskova, Z. Zidek, M. Zubek, P. Schneider, M. Kocirik, and J. Kozankova, Collection of Czechoslovak Chemical Communications 63 (1998) 141-154.

[36] P.J.M. Carrott, and K.S.W. Sing, Chemistry and Industry 22 (1986) 786-787.

[37] K.S.W. Sing, Unger, K.K., Chemistry and Industry 5 (1993) 165-166

[38] P.A. Jacobs, Zeolites 1 (1981) 161-168.

[39] U. Muller, E. Robens, K.K. Unger, Y. Grillet, F. Rouquerol, J. Rouquerol, D. Pan, and A. Mersmann, Fresenius' Journal of Analytical Chemistry 333 (1989) 433-436.

[40] D. Douguet, R.J.M. Pellenq, A. Boutin, A.H. Fuchs, and D. Nicholson, Molecular Simulation 17 (1996) 255-288.

[41] P. Llewellyn, Coulomb, J.P., Reichert, H., Patarin, J., Grillet, Y., Rouquerol, J., Langmuir 9 (1993) 1852-1856.

[42] P. Llewellyn, Coulomb, J.P., Reichert, H., Patarin, J., Grillet, Y., Rouquerol, J. , Langmuir 9 (1993) 1846-1851.

[43] Y.S. Tao, H. Kanoh, and K. Kaneko, Advanced Materials 17 (2005) 2789-2791.

[44] X. Guo, Y. Han, Y. Zou, D. Li, J. Yu, S. Qiu, and F. Xiao, Microporous And Mesoporous Materials 42 (2001) 325-336.

[45] J. Wang, F. Hassan, P.I. Chigada, S.P. Rigby, B. Al-Duri, and J. Wood, Industrial & Engineering Chemistry Research 48 (2009) 7899-7909.

Chapter 5 : Monte Carlo Simulation

5.1 Introduction

In the previous chapter, the location of coke deposition, either within the zeolite crystallite or in the intercrystalline region, has been identified. However, the distribution of coke inside the zeolite crystallite is still not known. It is believed that the interconnectivity of the zeolite pore structure influences the diffusivity and accessibility within the zeolite crystals. In order to study the effect of coke on the accessibility of a molecule in a blocked pore network, the percolation theory was adapted in this work. The effect of pore blockage on the self-diffusivity in zeolite crystallites was also studied by Monte Carlo simulation.

5.2 Percolation Theory

Percolation theory is commonly used to describe the effect of connectivity and accessibility in porous materials. The key concept of percolation theory is the occupation of sites or bonds, which indicates if a site or bond is available for diffusion i.e. open (unoccupied) or close (blocked or occupied) [1]. Sites and bonds are randomly selected as blocked with probability f and empty with probability $(1-f)$ [2].

Percolation theory was developed for three different types of occupation: bond percolation where the bond between neighbouring lattice sites can be closed with a probability f_b or open with a probability of $(1-f_b)$, site percolation where the intersections between bonds are closed or open with a probability f_s and $(1-f_s)$ respectively. Lastly, site-bond percolation where both sites and bonds are blocked or remain empty randomly with a probability f_{sb} and $(1-f_{sb})$, respectively.

The pore structure of any porous medium can be mapped onto an equivalent three-dimensional network of random bonds connected to each other by sites/nodes of the network [5]. Several models are available to describe the structure of porous media and study the deactivation of catalysts at a particle level. Cubic and random stochastic pore networks, fractal pore structures, and Bethe-tree networks [6] are a few examples. The simplest model consists of a regular network of nodes or sites connected by identical bonds, as in the case of cubic tessellation or Bethe network, as shown in Figure

5.1. In the cubic lattice and Bethe network, only the accessible volume and connectivity are changed, but the pore radii and diffusivity remain constant [6]. The cubic lattice is widely used as it takes into account isolated inaccessible pore clusters which are responsible for rapid deactivation [6]. The Bethe network does not give a realistic representation of the real pore structure since pores present in the network are connected through a central node. As a result, most models are now using more connected lattice networks to mimic pore structures within the crystallites.
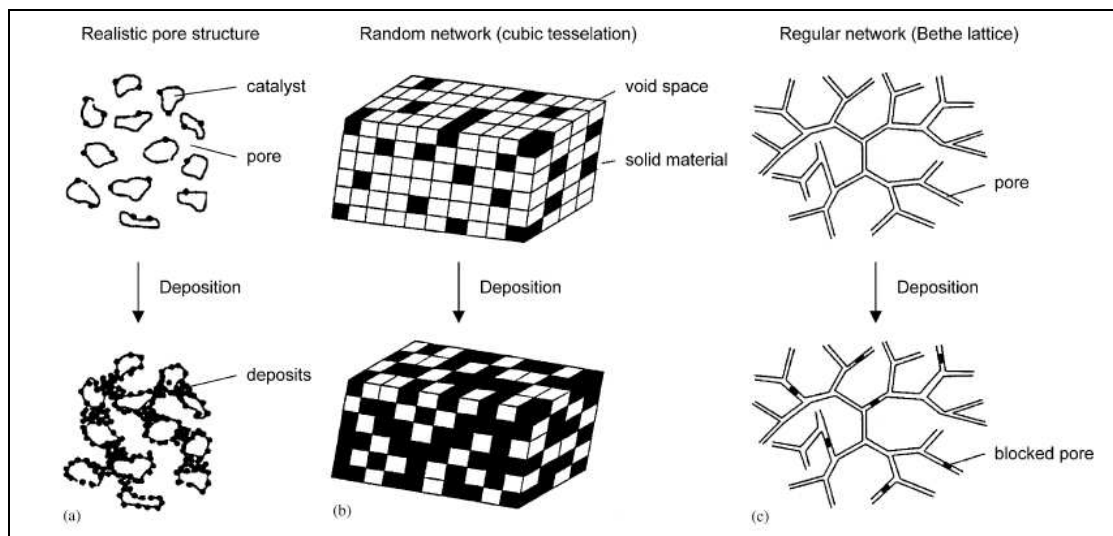
Figure 5.1 – Representation of real pore structure on a cubic and Bethe lattice – adapted from reference [6]

The complexity of the architecture of a porous medium can be represented by an array of lattices. Both two and three dimensional lattices consist of an array of sites which are connected to their neighbouring sites by bonds, and can be described in terms of L, number of bonds between one side of the lattice and another and Z, the coordination number (connectivity), i.e. the number of bonds that are connected to one node. Even though the cubic lattice is mostly used, other types of lattices such as the triangular lattice, honeycomb lattice, and the diamond lattice can also be applied to mimic the pore structure of a porous material.

If a pathway exists for a molecule to move from one side of the lattice to the other, then, a percolation cluster is said be present in the lattice. Figure 5.2 shows a square lattice with a bond probability of (a) 0.25 and (b) 0.5. The bond probability is defined as the number of occupied bonds divided by the total number of bonds. As the

bond probability increases (transition from Figure 5.2a to 5.2b), larger clusters are formed until a percolation cluster is formed, where the cluster is large enough to span the lattice [7]. The phenomenon, when this spanning cluster is formed, is known as the percolation threshold.

(a) $f_b = 0.25$　　　　　　　　(b) $f_b=f_{bc}=0.5$
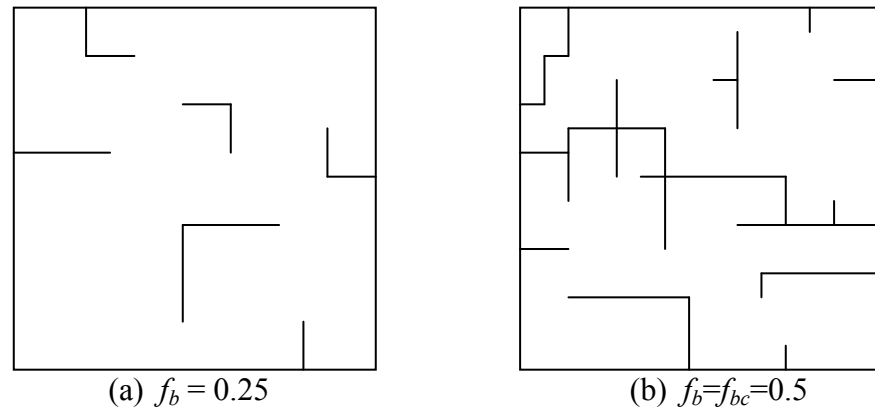
Figure 5.2 – Square lattice with different bond occupational probability, p_b

5.2.1 Application of percolation theory in this study

The connection between the deactivation process and percolation theory is made by relating the state of bonds or sites in the lattice with coke deposition. Therefore, three types of pores are defined in terms of pore content:

a) Pores that are open or unblocked – can be accessed by reactants/products
b) Pores that are occupied or blocked pores by coke molecules – cannot be accessed by reactant/products
c) Pores that are open or unblocked but are only accessed through other pores blocked by coke molecules (isolated pores) – cannot be accessed by reactant/products

The probability of a bond/site being blocked, f is the ratio of the number of blocked bonds/sites to the total number of bonds/sites (Equation 5.1). The accessibility or percolation fraction, F is the probability that network bonds/sites are in the spanning cluster (Equation 5.2). As the fraction of unblocked pores decreases, the connectivity of the lattice decreases, and eventually the molecules are unable to penetrate through the pore network from the bulk of the lattice. The minimum fraction of unblocked pores

that still allows a percolation cluster to exist in the lattice is termed percolation threshold. The percolation threshold determines the critical porosity at which most of the pore space becomes completely isolated, and the transport diffusivity/accessibility is reduced to zero. In terms of catalyst deactivation, the catalyst becomes deactivated when the percolation threshold is reached because of general inaccessibility to the interior of the catalyst pore volume.

$$f = \frac{Total\ number\ of\ free\ sites/bonds}{Total\ number\ of\ sites/bonds} \qquad (5\text{-}1)$$

$$F = \frac{Total\ number\ of\ accessible\ sites/bonds}{Total\ number\ of\ sites/bonds} \qquad (5\text{-}2)$$

5.2.2 Analysis of catalyst deactivation by coke formation in a ZSM-5 lattice – a percolation approach

During the catalyst deactivation process, coke formed can either deactivate active sites or block access to the active centres. Deactivation by coking which results in active site loss has been comprehensively studied over the years, but little information is available for deactivation by pore blocking. According to Beyne and Froment [3], pore blockage depends on the geometrical and topological characteristics of the pore network. The connectivity of a lattice plays an important role in determining the behaviour of the catalyst in terms of catalyst lifetime. It was previously shown that a catalyst has higher resistance to deactivation when the pores are more interconnected [5]. Since the gradual build up of coke within the pore cavities during the deactivation process cause changes in the morphology of the porous medium, the concept of percolation was applied to describe this occurrence. Sahimi and Tsotsis [5] were the first to identify catalyst deactivation as a percolation phenomenon. From that study, percolation models of catalyst deactivation were developed by other researchers to investigate reaction and diffusion in a porous catalyst. [3, 6, 8-9].

The ZSM-5 zeolite is widely used because of its unique catalytic property, in particular its high resistance to deactivation by coke formation. As a result, there has been increasing interest in understanding transport within the ZSM-5 zeolite. In order to

simulate diffusion and reaction in the ZSM-5 zeolite, Beyne and Froment [3, 8-9] made use of the diamond lattice to mimic the network of pores inside the ZSM-5 zeolite crystallites in a series of studies. The use of diamond lattice which has a coordination number of four is possible only if site percolation is taken into account as the connectivities of the sites (intersections) and bonds (channels) of a ZSM-5 lattice are not equal. In later years, the diffusion and reaction in ZSM-5 catalysts was studied by Monte Carlo simulation based on a more realistic model of the ZSM-5 lattice as shown in Figure 1 in reference [10]. According to Trout et al. [10], the inherent anisotropy in ZSM-5 lattice could not be captured by the isotropic model such as square, diamond or cubic lattices. Therefore, the authors modelled the ZSM-5 lattice in such a way that the sites have a coordination number of four while the coordination number of the bonds is two. It was reported that the effect of pore blockage on diffusivity is more pronounced on the ZSM-5 lattice employed compared with the two-dimensional square and three-dimensional cubic lattice. In addition, the critical percolation probability (percolation threshold) for the ZSM-5 lattice employed by Trout et al. [10], which consists of sites both in the channels and intersections (site-bond percolation) was evaluated to be 0.64.

5.3 Diffusion in Zeolites

The diffusion of molecules can be classified in a number of different regimes depending on the pore diameter of the porous material (Figure 5.3). Most applications of zeolites (in catalysis and separation processes) involve the migration of sorbates within the crystallite. The separation of mixtures is based on the differences in their diffusion coefficients, while in catalytic applications, diffusion of reactants to the active site can be a rate limiting step [11]. Therefore, diffusion behaviour in zeolites has been studied extensively over the years. Transport in zeolites is beyond the molecular and Knudsen diffusion regions and takes place in the configurational diffusional regime. When discussing diffusion in zeolites, two situations are involved: (i) diffusion within the zeolite crystal and (ii) diffusion in between zeolite crystals, in the pellet.
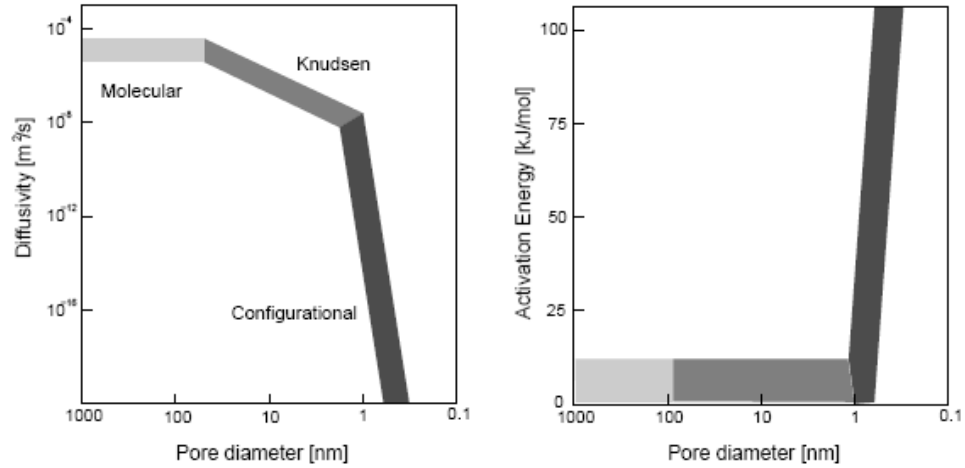
Figure 5.3 – Effect of pore diameter on diffusivity and diffusional activation energy. Adapted from reference [12]

Transport diffusion results from a concentration gradient, while self-diffusion takes place in the absence of a chemical potential gradient. Transport diffusivity can be described by Fick's first law:

$$J = -D_t \left(\frac{\partial C}{\partial x} \right) \tag{5-3}$$

where C is the concentration, x is the spatial coordinate and D_t is the transport diffusion coefficient.

Self diffusivity monitors the diffusion path of a tagged molecule placed in the centre of the lattice over a preset number of steps [13]. Equation 5.4 can be used to describe the flow of the tagged component:

$$J_i^* = -D_s \left(\frac{\partial C^*}{\partial x_i} \right) \Bigg|_{C=cons\tan t} \tag{5-4}$$

in which * refers to the labelled component, and D_s is the self-diffusion coefficient.

The self-diffusion coefficient could be related to the mean square displacement (defined by Einstein equation) after time t by Equation 5.5:

$$\left\langle \left| \vec{r}^i(t) - \vec{r}^i(0) \right|^2 \right\rangle = \left\langle \left| r^2(t) \right| \right\rangle = 6D_s t \tag{5-5}$$

122

where $\overset{\rightarrow i}{r}(t)$ is the position of particle i at time t (average of the squared distance travelled by a particle at time t.

For diffusion in inhomogeneous frameworks such as the ZSM-5 type zeolite, Equation 5.5 is modified to:

$$\left\langle \left| r_\alpha(t) - r_\alpha(0) \right|^2 \right\rangle = 2D_s^\alpha t \qquad (5\text{-}6)$$

where α denotes the displacement along x, y or z direction and $D_s = \dfrac{D_s^x + D_s^y + D_s^z}{3}$

In a current review on diffusion in zeolites, Smit and Maesen [11] pointed out the difficulty in measuring the diffusion coefficient, and that the diffusion coefficient measured could differ by orders of magnitude depending on the particular experimental technique used. Therefore, theoretical predictions of diffusivity at the molecular level were performed. This computational modelling has provided useful information on the mobility of a probe molecule in a lattice.

The diffusion of molecules can be affected by several factors, such as the size of adsorbate molecules, the connectivity of a lattice, the molecular occupancy, the interaction between the molecule and the lattice, and pore blockage. The effects of lattice topology and occupancy on the self-diffusivity of a molecular species was studied by Coppens et al. [4]. The diffusivity variation with occupancy differs for each lattice with different coordination number, Z. However, the value of self-diffusivity at zero coverage is independent of connectivity as molecules do not encounter each other in the lattice. It was found that the dependency of diffusivity on occupancy is non-linear because at high occupancies and low connectivities, the probability of a molecule returning to its original site is high as a result of molecules blocking the sites.

Theoretical investigations have also provided useful information on the transport properties in a catalyst as a result of coke deposition. The earliest study of diffusion and reaction in blocked ZSM-5 catalysts was carried out by Theodorou and Wei [14] using a random walk approach. It was found that the intracrystalline diffusivity is sensitive to the blocking modes applied, either pore blocking or surface/border blocking. This study was then extended to investigate the effect of reactant pressure on the modes of catalyst

deactivation [15-16]. The effect of blocked sites on self-diffusivity was investigated by Trout et al. [10] for a ZSM-5 catalyst. Results generated by Monte Carlo simulations indicated that the occupancy effect is more significant on a ZSM-5 lattice than on a two-dimensional square or three-dimensional cubic lattice. In addition, the normalised diffusivity was reported to decrease with increasing fraction of blocked sites as a result of reduced accessibility of the molecules.

It is the purpose of this chapter to understand the effect of coking on the mass transport within the catalyst pellets studied, as well as identifying the distribution of coke molecules formed during the reaction. In the next section, the models and simulation methodology will be presented, followed by discussion of the results obtained.

5.4   Construction of Lattices

In order to model the diffusion/accessibility in a catalyst particle, the pore structure of the catalyst can be represented either by two or three dimensional lattice networks constructed by bonds and sites. All the pore volumes of the pore space can be assigned to the bonds or sites, or both the bonds and sites inside the lattice. A simple cubic network and ZSM-5 lattice was employed in this study.

5.4.1   Cubic Lattice

The cubic lattice is generated by a network of cylindrical pores as described by Liu et al. [17]. At the start of the simulation, each site has a coordination number, Z of 6, but changes when the bonds and/or sites are blocked at random. The cubic lattice used in the simulations for this study is illustrated in Figure 5.4, where the black dots represent sites and the grey dots signify bonds in the cubic lattice.
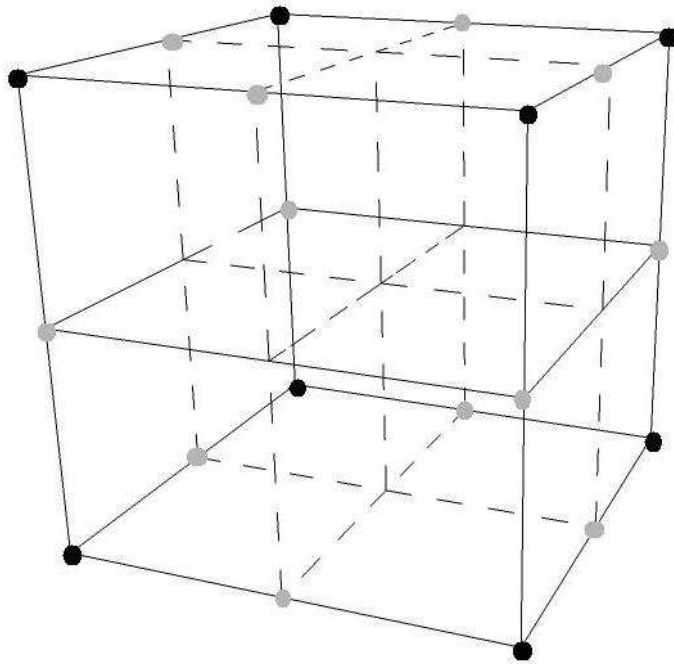
Figure 5.4 – Cubic lattice model; (-●-) sites and (-●-) bonds

5.4.2 ZSM-5 Lattice

As described in Chapter 2, the ZSM-5 structure contains the circular sinusoidal channel (0.54 x 0.56 nm) and straight elliptical channel (0.51 x 0.55 nm) which are connected by a spherical intersection (~ 0.8 nm). The model of the ZSM-5 lattice used is adapted from previous work by Trout et al. [10] and is presented in Figure 5.5. The black dots represent the adsorption sites in the intersections (sites) while the gray dots represent the straight/zig-zag channels (bonds). There are 12 lattice points *per* unit cell; four in the intersections (there being four intersections in the unit cell) and eight in the straight and zig-zag channels [10].
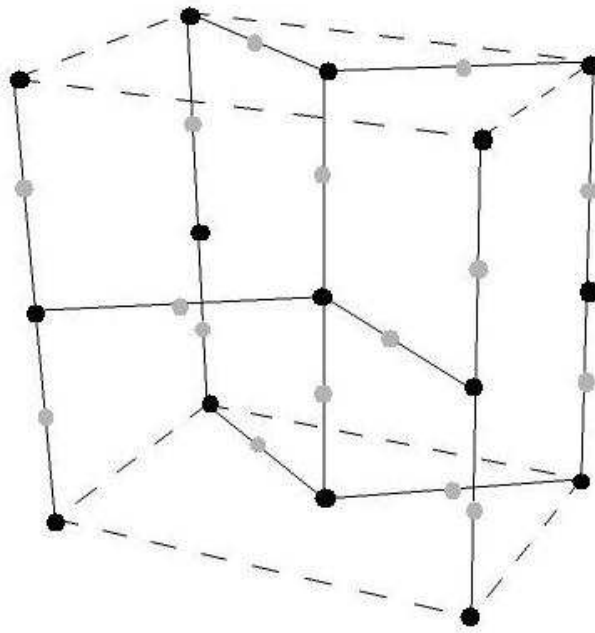
Figure 5.5 – Lattice model of ZSM-5; (-●-) sites and (-●-) bonds

The coordination numbers of the intersections and channels of the ZSM-5 lattice are not equal to one another. If a particle/molecule is in the channel, it has only 2 neighbours hence it only has 2 directions of hop. In the straight channels, a particle can only move in the up (UP) or down (DN) direction, while in the zig-zag channels, the directions of northeast (NE)/southwest (SW) or northwest (NW)/southeast (SE) can be chosen. If however, a particle sits in the channel intersection, it has 4 neighbours. Therefore it has 4 directions (UP, DN, NE and NW or SE and SW) of hop.

5.5 Simulation Methods

The accessibility and self-diffusion simulations described in the following sections were computed by an in-house computer program written using Fortran 95 (Appendix A4).

5.5.1 Accessibility Simulation

The deactivation phenomenon was represented by the blocking of the bonds and intersections of the lattice generated. In this study, bond-site percolation was

investigated for the ZSM-5 lattice. The intersections and bonds that were blocked were chosen at random according to a probability weighted by their volume in the real zeolite. The coke molecules could only occupy the bonds and intersections if they were previously empty. Once a bond or intersection was occupied by coke, no further occupancy was allowed.

For calculations of accessibility, a layer of diffusing molecules was placed along the boundaries of the lattice to represent the nitrogen (or argon) bulk phase during adsorption. These molecules then penetrated into the pore network to identify accessible bonds and sites. Any pores plugged with coke were considered inaccessible and potentially barred the way for further penetration. If pores were unplugged, or not blocked by coke molecules, but were completely surrounded by blocked pores, these isolated clusters were also considered as not accessible.

In this study, bond and site percolation was studied on a simple cubic lattice while bond-site percolation was investigated for a ZSM-5 lattice. The network size, L was also varied in this study to investigate its effect on the accessibility for a constant coordination number of the network, Z. Simulations were repeated for sets of new lattices, and random number seeds, and average values for the accessibility fraction were taken, in order to obtain a typical result for random dispersion/distribution of coke molecules in the lattice/crystallites.

5.5.2 Self-diffusivity Monte-Carlo Simulations

The simulation of self-diffusivity was carried out on a simple cubic lattice ($Z=6$) of lattice size, $L = 21$ and on a ZSM-5 pore network of lattice size, $L = 24$. The simulation of self-diffusivity in the ZSM-5 lattice is based on previous work by Trout et al. [10] and Coppens et al. [4].

The occupancy θ of the lattice ($0 \leq \theta \leq 1$) is defined as the number of simultaneously diffusing molecules divided by the number of lattice sites [4]. Initially, a certain number of molecules, corresponding to θ, occupy randomly chosen sites on the grid. Before the displacement of the molecules is sampled, the molecules are allowed to hop for a certain equilibration time so that the diffusivity does not change as a function

of number of hops. When steady state diffusion in the lattice is achieved, the clock is reset to zero and the positions of the particles are recorded. The particles are then allowed to hop for an average of 3000 successful hops per particle.

A particle is selected at random to make a hop. Each particle can migrate to the neighbouring sites with equal probability. The direction at which the particle hops to is selected at random and the jump probability in each direction is the same. It is also assumed that there is no interaction between the molecules or a molecule and the zeolite lattice. If the direction chosen corresponds to the zeolite wall, the particle selected does not move. If another particle occupies the particular site that was chosen, the particle also does not move. The time interval between each attempted hops, Δt is calculated from a Poisson distribution where $\Delta t = -\dfrac{1}{k\ln(u)}$, where u is a random number between 0 and 1. Even if the hop is unsuccessful and the molecule returns to its original site, the clock is advanced by the time, Δt. However, if the site chosen is empty, the particle hops to its adjacent lattice point and the successful hop counter is incremented.

Periodic boundary conditions are used to avoid finite size effects, where a particle/molecule on the border of the grid exiting the simulation lattice can hop to the symmetrically opposite site. Nevertheless, the real coordinates of each molecule are updated and saved, as if the lattice were infinite [4]. Simulations are performed at different occupancy, θ to study the influence of θ on self-diffusivity, D_s.

5.6 Calculations

5.6.1 Accessibility Study

5.6.1.1 Calculating volume of ZSM-5 lattice

The total volume of 1 unit cell of ZSM-5 lattice is modelled by the total volume occupied by 4 straight cylindrical channels, 4 zig-zag cylindrical channels and 4 spherical intersections [1]. The dimensions for the channels and intersections for the ZSM-5 lattice are taken from reference [18].

Table 5-1 – ZSM-5 channel dimensions [18]

Channel Type	Length (nm)	Diameter (nm)
Straight	0.46	0.55
Zig-zag	0.66	0.53
Intersection	0.54	0.80

Table 5-2 – Volume of ZSM-5 channels in 1 unit cell

Channel Type	Volume of 1 channel (nm^3)	Volume of 1 channel (cm^3)	Total volume of channels in 1 unit cell (nm^3 *per* unit cell)	Total volume of channels in 1 unit cell (cm^3 *per* unit cell)
Straight	0.109	1.09E-22	0.437	4.37E-22
Zig-zag	0.146	1.46E-22	0.583	5.83E-22
Intersection	0.268	2.68E-22	1.072	1.07E-21
Total volume of 1 unit cell of ZSM-5				**2.09E-21**

5.6.1.2   *Analysis of Experimental Data*

Pore blockage due to coke formation on the PtH-ZSM-5 catalysts was accounted for by changes in the pore volumes determined from the nitrogen and argon adsorption isotherms. The pore volume obtained from these adsorption experiments comprises the volume of micro- and mesopores. However, in this work, the percolation model only applies to the zeolite crystallite, hence only pore volumes inside the crystallites which consist of straight and zig-zag channels and intersections are taken into account.

In order to distinguish between the internal and external pore volume of the zeolite crystallites, the graphs of cumulative pore volume as a function of pore diameter from nitrogen and argon adsorption experiments were used. It was assumed that the micropores within the ZSM-5 crystal were less than 2 nm while pore volume between 2 and 50 nm was occupied by mesopores. The mesopore volume loss was assumed to be occupied by coke molecules. This volume of coke was then subtracted from the total coke volume determined from TGA so that the coke content in the micropores could be evaluated.

129

Equations 5.1 and 5.2 were modified in order to incorporate the adsorption experiment data for the accessibility plot. The values of F and f are determined by the following equations:

$$F = \frac{V(t = TOS)}{V(t = 0)}$$

(5-7)

where F is the accessibility fraction, $V(t=0)$ is the pore volume for the fresh catalyst and $V(t=t)$ corresponds to the externally accessible pore volume of the coked catalyst at different times-on-stream (t). The total fraction of unplugged pores, f, is given by:

$$f = \frac{V(t = 0) - V_c(t = TOS)}{V(t = 0)}$$

(5-8)

where $V_c(t=TOS)$ is the volume of coke at different TOS (t). The uncertainties in V_c as a result of coke density values used (as described in Chapter 4) were taken into account when evaluating the standard errors in the fraction of unplugged pores, f, and are given by error bars shown in Figures 5.10 and 5.11.

5.6.2   Calculating/Estimation of Self-Diffusion Coefficient, D_s

The self-diffusivity was computed by calculating the mean squared displacement of the molecule using Einstein equation: $\langle x^2 \rangle = 2D_s t$ where $\langle x^2 \rangle$ is the mean square displacement of the molecule between the position at time t and the initial position of that particle, D_s is the self-diffusion coefficient and t is the total time for successful and unsuccessful hops.

From the Monte-Carlo simulation, a linear plot of mean square displacement, $\langle x^2 \rangle$ against time t was obtained. The slope of the graph corresponds to $2D_s$, where the self-diffusion coefficient, D_s can be calculated.

The self-diffusivity at zero coverage, D_o is required to determine the normalised self-diffusivity value. In order to evaluate D_o, the diffusivity at low loading (20 molecules) was simulated. Then, normalised self-diffusivity, D/D_o was calculated.

5.7 Results and Discussion

5.7.1 Accessibility

5.7.1.1 Validation of the accessibility program

The accessibility program was initially written for a simple cubic lattice. In order to validate the program, simulated results were compared with published data.

Figure 5.6 shows the bond percolation simulation results on a simple cubic lattice of network size, $L = 61$. On the same graph, the simulated result is also compared with previously reported data on accessibility in a cubic lattice [17]. The agreement between the simulated results and those of Liu et al. [17] validates the Fortran program written.
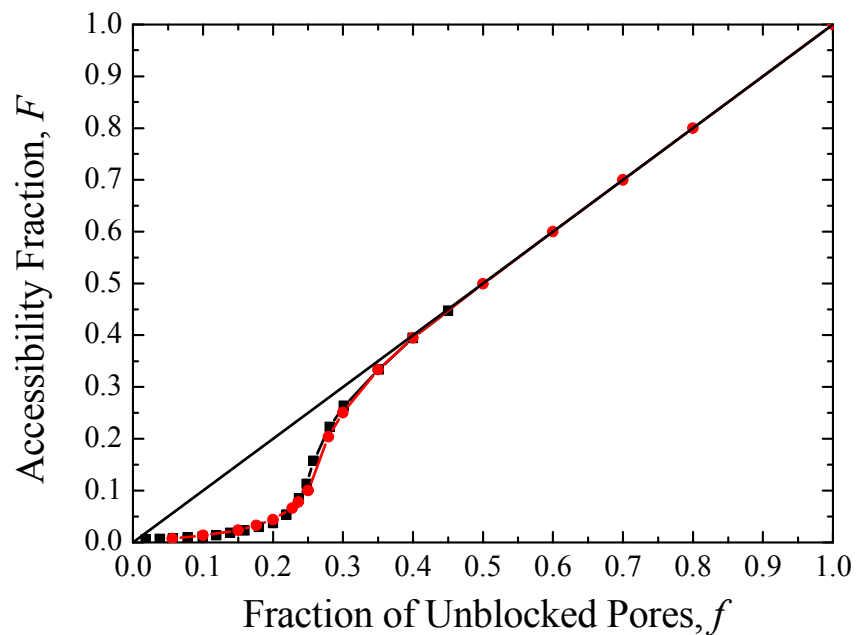
Figure 5.6 – Accessibility fraction, *F* as a function of unblocked pores, *f* for bond percolation on a simple cubic lattice : Comparison of results from Liu et al. [17] (-■-) and our simulated data (-●-)

The effect of network size, L on the percolation transition is shown in Figure 5.7. As the network size decreases, the percolation transition is more diffuse when

compared with a bigger network size. According to Liu et al. [17], as the network size is decreased, the surface cluster dominates the accessibility of the network [17].
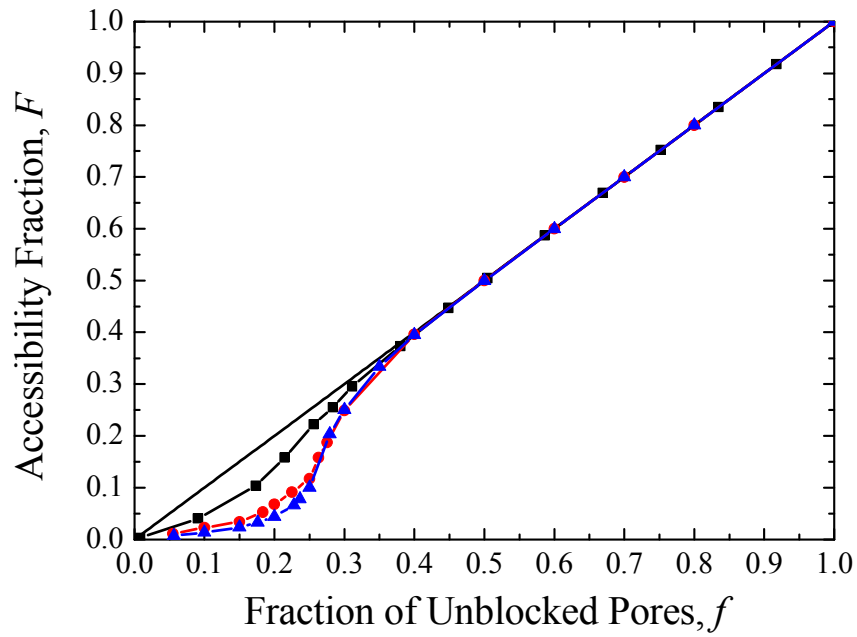
Figure 5.7 – Effect of network size on the accessibility for *Z*=6: *L*=21 (-■-), *L*=41 (-●-) and *L*=61 (-▲-)
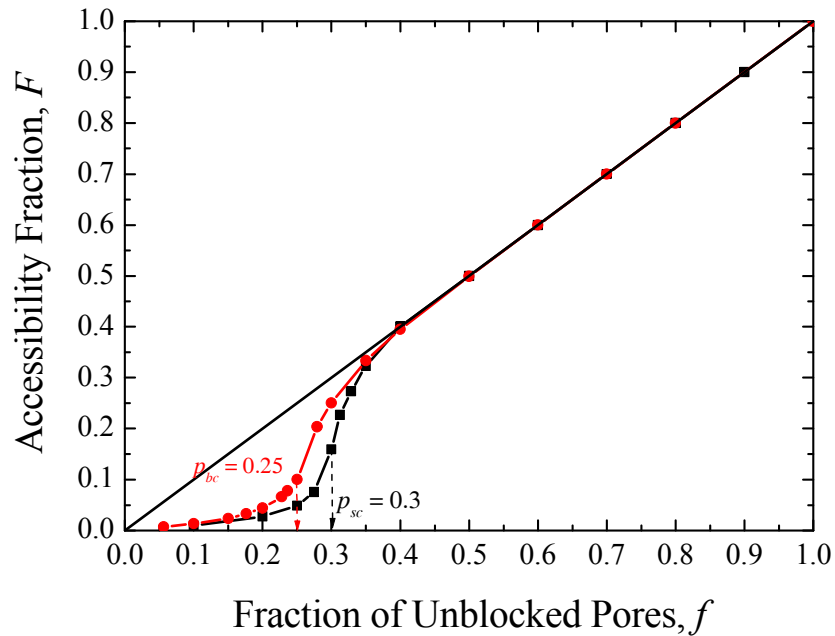
Figure 5.8 – Accessibility fraction, *F* as a function of unblocked pores, *f* for site (-■-) and bond (-●-) percolation on a simple cubic lattice

The bond percolation program was then modified to investigate site percolation on a simple cubic lattice. Figure 5.8 compares the accessibility of a molecule in a cubic lattice for bond and site percolation. The percolation study on a simple cubic lattice has been extensively studied, and the percolation threshold, f_c for the bond percolation was said to be f_{bc}=0.2492 while the percolation threshold for site percolation was reported to be f_{sc}=0.3117 [2]. Consistent with published literature, simulations from this work yields percolation threshold values of f_{bc}=0.25 and f_{sc}=0.3.

5.7.1.2   *Determination of the lattice size, L for a ZSM-5 network*

Based on the accessibility program written for a cubic lattice, the program was modified in order to investigate pore blockage effects on a ZSM-5 lattice. No previous work have developed a bond-site percolation model for the ZSM-5 lattice shown in Figure 5.5 using a volume weighted probability, hence the accessibility plot for the ZSM-5 lattice was generated in this study. Two types of occupation positions are present in the ZSM-5 lattice; one in the intersection and another in the straight/zig-zag channels.

The previous section pointed out the effect of surface clusters on the accessibility function of a cubic lattice. A large lattice size was used to represent a large zeolite crystallite to avoid finite size effects on the percolation accessibility function. Simulations were carried out by varying the network size, L (from 24 to 96). Figure 5.9 shows the effect of network size, L on the percolation transition in a ZSM-5 lattice for site-bond percolation. As the network size decreases, the percolation transition becomes more diffuse, consistent with results obtained for a cubic lattice.

It was found that by increasing the lattice size above 48×48×48, the accessibility function did not then change significantly with lattice size at the percolation limit. The simulation work in this study was carried out on a 96×96×96 lattice with 13 824 unit cells, giving a total of 165 888 accessible lattice points.
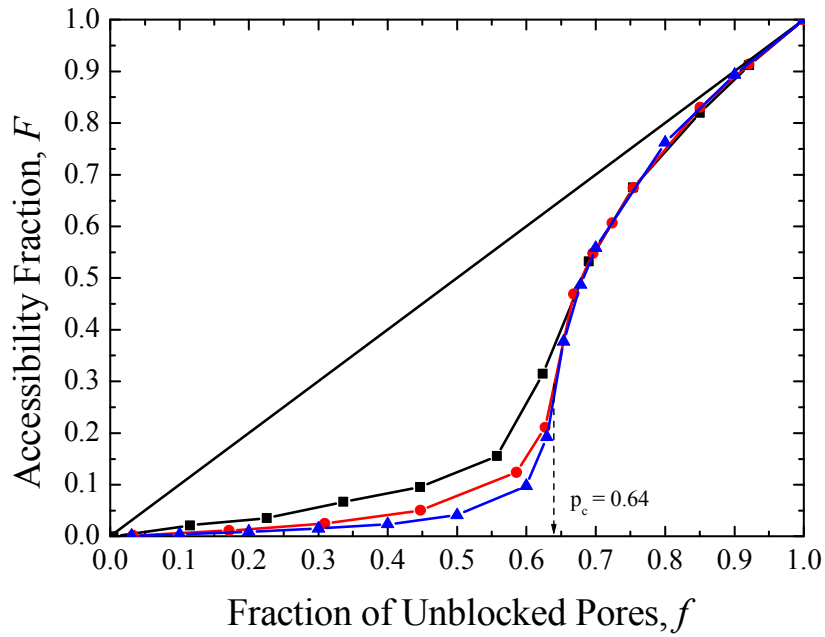
Figure 5.9 – Effect of network size on the accessibility for ZSM-5 lattice : *L*=24 (-■-), *L* =48 (-●-), *L* =96 (-▲-)

5.7.1.3 *Determination of percolation threshold, p_c*

In terms of pore blockage, the percolation threshold, p_c is defined as (1 − maximum blockage probability) that still allowed accessibility across the lattice. Percolation threshold of different lattices was determined from the accessibility plot generated by Monte Carlo simulations.

Table 5-3 – Percolation threshold, p_c for simple cubic and ZSM-5 lattice

Lattice	Type of percolation	Percolation Threshold, p_c	
		Literature	Current work
Cubic Lattice	Site (f_{sc})	0.3117 [2]	0.30
	Bond (f_{bc})	0.2492 [2, 17]	0.25
ZSM-5	Site-bond (f_{sbc})	0.64 [10]	0.64

The percolation thresholds of a cubic lattice and ZSM-5 lattice are listed in Table 5.3. Results obtained from the current work are consistent with the percolation threshold values reported for simple cubic [2, 17] and ZSM-5 lattice [10].

5.7.1.4 *Comparison of accessibility function from experimental results and simulated data*

The changes in the accessibility of nitrogen and argon molecules determined from adsorption studies were compared with the accessibility plot simulated assuming that coke molecules are deposited in both the straight and zig-zag channels, and in the intersections of the ZSM-5 lattice.
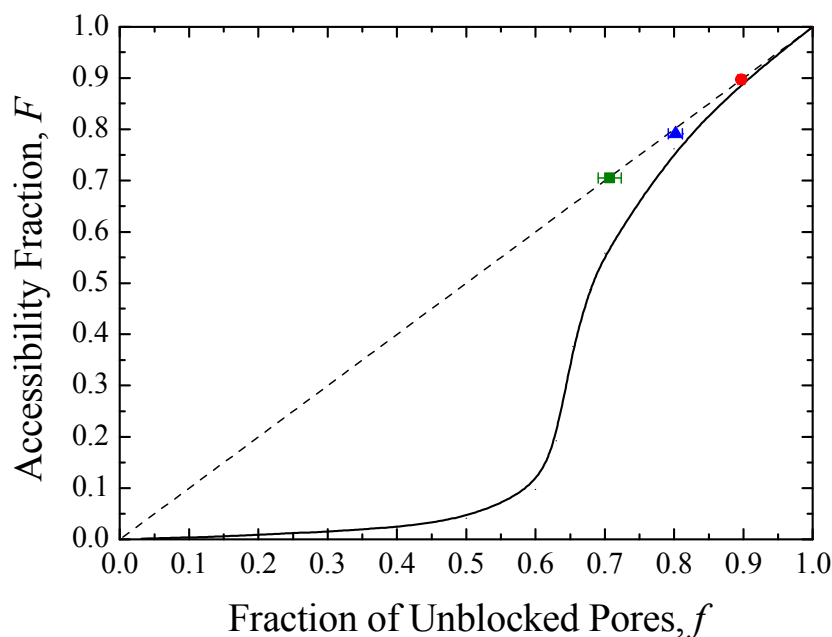
Figure 5.10 – Accessibility plot – No percolation (Dash line), Accessibility in a ZSM-5 lattice assuming random deposition of coke (Solid line), nitrogen adsorption data for PtH-ZSM-5(30) coked samples after 4 h (●), 24 h (▲), and 48 h (■) TOS

In the case of the PtH-ZSM-5(30) catalysts at different TOS, the experimentally measured accessibility of the micropore lattice to nitrogen and argon still remained high even when the value of f corresponding to the percolation threshold, f_{sbc} of the ZSM-5 lattice, assuming randomly distributed deposition of coke, is reached. This indicated that even with increasing coke deposition, all of the unblocked pores are still in the percolating cluster of the ZSM-5 network. The results thus showed that the potential scenario of random deposition of coke in the ZSM-5 crystallites during the alkylation reaction is incorrect.
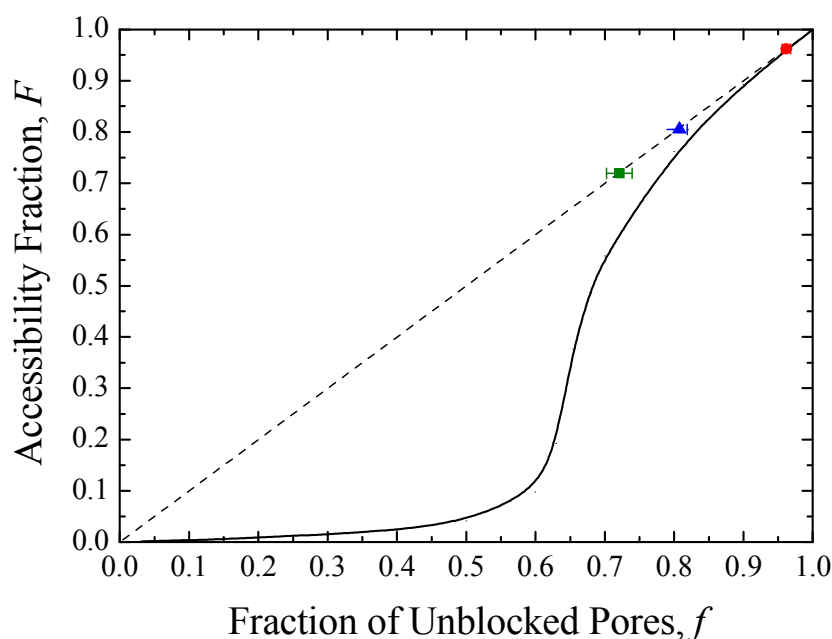
Figure 5.11 – Accessibility plot – No percolation (Dash line), Accessibility in a ZSM-5 lattice assuming random deposition of coke (Solid line), argon adsorption data for PtH-ZSM-5(30) coked samples after 4 h (●), 24 h (▲) and, 48 h (■) TOS

If the coke were blocking access to pores which did not contain coke molecules, then the difference between the accessibility fraction and the fraction of unplugged pores (Figure 5.10 and Figure 5.11) would have been significant. In the case of pore mouth plugging, a small amount of coke on the surface of the zeolite crystallite can lead to a large decrease in the accessibility of the molecules to the center of the catalyst. In addition, if the percolation threshold (f_{sbc}) of the lattice was reached, the pore network would lose its connectivity, resulting in the complete loss in accessibility. However, this was not observed in our results for the PtH-ZSM-5(30) catalysts even when the percolation threshold for the lattice, assuming a random distribution of coke, was reached. Figure 5.10 and Figure 5.11 show that the PtH-ZSM-5(30) pore network remained highly accessible to nitrogen and argon even when the percolation threshold for random deposition was reached. Two different gases with different potential interactions with the surface were used. Nitrogen has a permanent quadrupole moment, while argon is a spherically symmetric (though polarisable) molecule. Since both gases gave similar results, this suggests that accessibility was not affected by chemistry.

The bond-site percolation threshold (f_{sbc} = 0.64) for the ZSM-5 catalyst was evaluated from blocking the bonds and sites randomly with coke molecules. Comparing the theoretical and experimental accessibility plots (Figure 5.10 and Figure 5.11), the results suggested that the coke molecules were initially formed in the core of the crystallite, and as the coke content increased, these coke molecules block the channels and intersections in such a way that the coke was progressively building up from the middle of the structure, moving outwards towards the crystallite surface, hence decreasing the diffusion length of the zeolite crystallites. Such mode of pore blocking would not obstruct the accessibilities of nitrogen and argon molecules, hence the accessibility fraction remained high.

5.7.2 Random walk / Mean square displacement

5.7.2.1 Effect of Lattice Topology
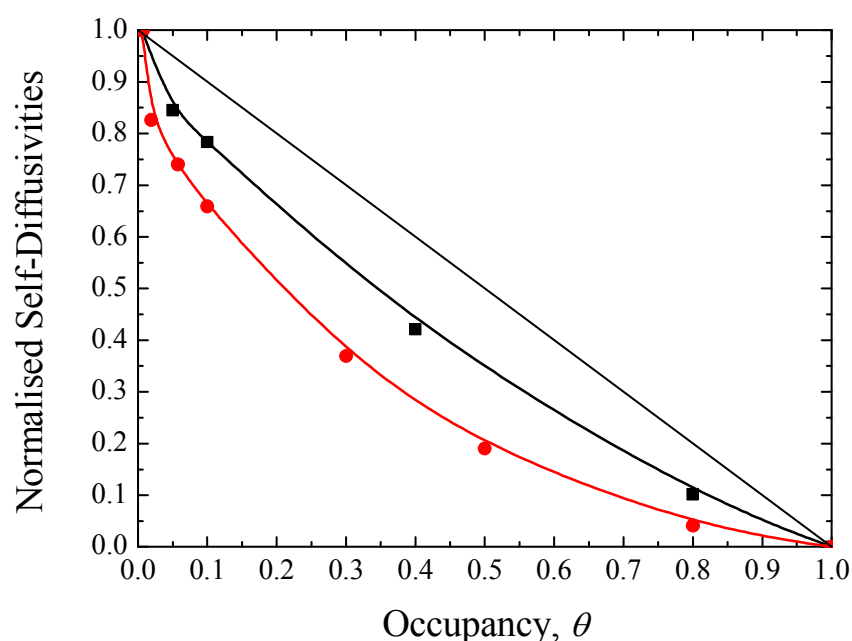
Figure 5.12 – Self-diffusivities as a function of occupancy for a simple cubic (-■-) and a ZSM-5 (-●-) lattice

The effect of topology and occupancy on the self-diffusivity was investigated in this study. A simple cubic lattice with connectivity, Z=6 and a ZSM-5 lattice with

average connectivity, $Z = \dfrac{(4 \times 2) + (4 \times 2) + (4 \times 4)}{12} = \dfrac{8}{3} = 2.67$. The connectivity of a ZSM-5 lattice is much lower than the connectivity of a cubic lattice. Figure 5.12 shows the relationship between the normalised self-diffusivities, D_s/D_o and occupancy, θ for the two different lattices examined in this study.

Results showed that the normalised diffusivities do not decrease linearly with fractional occupancy for both, cubic and ZSM-5 lattice. When the number of molecules in the lattice increases, the molecules hindered each other as one site can only be occupied by one molecule. As a result, the molecule returned to its original site when the chosen site was not vacant. The probability of this scenario taking place was greater at higher occupancies and also at low connectivites as the tendency of the molecule return to its original site was higher. Therefore, the deviation from linearity was more significant for a ZSM-5 lattice when compared with a cubic lattice (due to lower connectivity of the ZSM-5 lattice compared with cubic lattice) as demonstrated in Figure 5.12. These results are consistent with those of Coppens et al. [4], who compared the effect of connectivity, Z on the self-diffusivity for various lattices.

Previous studies on the diffusion in a ZSM-5 type zeolites were approximated by a 2-dimensional square lattice ($Z=4$) or even a 3-dimensional cubic lattice ($Z=6$), which have much higher connectivities. The difference between the variation of self-diffusivity with occupancy for a cubic and ZSM-5 lattice showed in this work (Figure 5.12) implies that the approximated lattice to represent the ZSM-5 catalyst in previous work may lead to inaccuracies in the results obtained.

5.7.2.2 *Effect of Pore Blockage on Self-Diffusivity, D_s*

In order to determine the relationship between the self-diffusivity and extent of pore blocking, pores are blocked at random in the interior of the zeolite crystallite. Similar to the accessibility study, the straight/zig-zag channels and intersections are blocked at random. Figure 5.13 shows the normalised self-diffusivity as a function of fractional occupancy for different fractions of blocked sites.
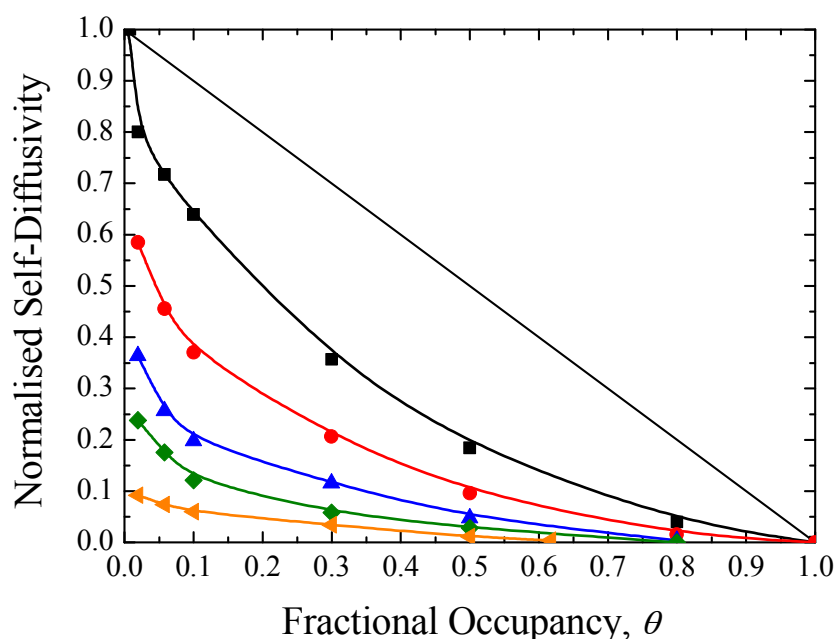
Figure 5.13 – Normalised diffusivity for various fractional occupancies and different percentages of blocked sites in ZSM-5 lattice model: (-■-) 0% blocked, (-●-) 10% blocked, (-▲-) 20% blocked, (-◆-) 30% blocked and (-◄-) 36% blocked. (The lines shown are to guide the eye).

Similar to the findings of Trout et al. [10], simulation results showed that, for the same occupancy, D_s/D_o decreases with increasing fraction of blocked sites. This could be a direct consequence of lower connectivity of the zeolite channel system when sites were blocked to represent the deposition of coke molecules.

In the previous section, the percolation threshold in a ZSM-5 lattice where straight/zig-zag channels and intersections are blocked at random was evaluated to be $f_{sbc} = 0.64$. Therefore, the diffusivity of a molecule should reduce to a great extent if 36% of the pores within the zeolite lattice are blocked by coke molecules. The results (Figure 5.13) from the random walk simulation in a ZSM-5 model showed that, when coke molecules occupy 36 % of the total lattice space, D_s/D_o decreased rapidly, hence consistent with what would be expected at the percolation limit.

5.8 Conclusion

The structural modifications of PtH-ZSM-5 catalysts during deactivation were investigated using percolation theory by Monte Carlo simulations. A three-dimensional lattice with a more realistic representation of the ZSM-5 pore network was used for the simulations in this study. Percolation analysis of nitrogen and argon adsorption data obtained in Chapter 4 indicated that the random distribution of coke inside the zeolite crystallite is incorrect for the catalytic PtH-ZSM-5(30) system. Results for PtH-ZSM-5(30) catalysts showed that the straight/zig-zag channels and intersections within the ZSM-5 catalyst remained highly accessible to nitrogen and argon even when the percolation threshold assuming randomly distributed deposition of coke is reached.

Based on Monte Carlo simulations, it was found that the relationship between the self-diffusivity with molecular occupancy, θ is non-linear. The non-linearity is more significant for a lattice with lower connectivity, as demonstrated by the comparison between a simple cubic lattice and a ZSM-5 lattice. The dependency of self-diffusion on occupancy at different degree of pore blockage was also examined. The intracrytalline diffusivity decreased with increasing pore blockage, but dropped rapidly when the percolation limit is reached.

5.9 References

[1]   J. Holakovsky, I. Kratochvilova, and M. Korcirik, Microporous and Mesoporous Materials 91 (2006) 170-171.

[2]   D. Stauffer, Introduction to Percolation Theory. Taylor and Francis, London and Philadelphia, 1985.

[3]   A.O.E. Beyne, and G.F. Froment, Chemical Engineering Science 48 (1993) 503-511.

[4]   M.-O. Coppens, A.T. Bell, and A.K. Chakraborty, Chemical Engineering Science 53 (1998) 2053-2061.

[5]   M. Sahimi, and T.T. Tsotsis, Journal of Catalysis 96 (1985) 552-562.

[6]   B.M. Vogelaar, R.J. NBerger, B. Bezemer, J. Janssens, A.D. van Langeveld, S. Eijsbouts, and J.A. Moulijn, Chemical Engineering Science 61 (2006) 7463-7478.

[7]   N.A. Seaton, Chemical Engineering Science 46 (1991) 1895-1909.

[8]   A.O.E. Beyne, and G.F. Froment, Chemical Engineering Journal 82 (2001) 281-290.

[9]   A.O.E. Beyne, and G.F. Froment, Chemical Engineering Science 45 (1990) 2089-2096.

[10]   B.L. Trout, A.K. Chakraborty, and A.T. Bell, Chemical Engineering Science 52 (1997) 2265-2276.

[11]   B. Smit, and T.L.M. Maesen, Chemical Reviews 108 (2008) 4125-4184.

[12]   D.M. Ruthven, and M.F.M. Post, in: H. van Bekkum, E.M. Flanigen, P.A. Jacobs, and J.C. Jansen, (Eds.), Introduction to Zeolite Science and Practise Elsevier, Amsterdam. 525-578.

[13]   B. Frank, K. Dahlke, G. Emig, E. Aust, R. Broucek, and M. Nywlt, Microporous Materials 1 (1993) 43-56.

[14]   D. Theodorou, and J. Wei, Journal of Catalysis 83 (1983) 205-224.

[15]   P.H. Nelson, D.M. Bibby, and A.B. Kaiser, Zeolites 11 (1991) 337-344.

[16]   X. Guo, Z. Liu, and B. Zhong, Microporous and Mesoporous Materials 23 (1998) 203-209.

[17]   H. Liu, L. Zhang, and N.A. Seaton, Journal of Colloid and Interface Science 156 (1993) 285-293.

[18]   R.E. Richards, and L.V.C. Rees, Langmuir 3 (1987) 335-340.

Chapter 6 : Ethane Adsorption and Mass Transport Kinetics

6.1 Introduction

Modification of the pore structure of zeolite catalysts by coking usually leads to transport resistance for reactants and products, as well as hinders accessibility to active sites, as described in the work of several researchers [1-3]. It is therefore important to understand the effects of coke on equilibrium and kinetics of adsorption/mass transport rates in zeolites. Detailed investigations of the evolution of the catalyst pore structure, and its effects on the thermodynamics and kinetics of adsorption of ethane, a key reactant molecule during benzene alkylation was studied and will be discussed in this Chapter.

6.2 Theory

Adsorption kinetics in porous materials can be described by a variety of models such as Fickian, linear driving force (LDF), and a combined barrier resistance/Fickian diffusion model [4]. The LDF model was originally proposed by Glueckauf and Coates [5] for adsorption chromatography. In a later study, Sircar and Hufton [6] showed that the LDF model gives a good approximation to the Fickian solution for diffusion within an adsorbent particle.

For the solution of Fick's second law of diffusion within a sphere, the total amount of diffusing substance entering the sphere at time *t,* can be determined using Equation 6.1 [6]:

$$\frac{M(t)}{M(\infty)} = 1 - \frac{6}{\pi^2} \sum_{n=1}^{\infty} \left(\frac{1}{n^2}\right) \exp(-Dn^2\pi^2 t / a^2) \qquad (6\text{-}1)$$

where *M(t)* the mass uptake at time *t* (mg), *M(∞)* is the equilibrium mass uptake (mg), *a* is the radius of sphere (m), and *D* is the effective diffusion coefficient ($m^2 s^{-1}$).

For the fraction of uptake *M(t)/M(∞)* > 0.5, Equation 6.1 can be simplified and the uptake data fitted to Equation 6.2. The simplified form is called the LDF model.

$$\frac{M(t)}{M(\infty)} = 1 - \exp(-kt) \qquad (6\text{-}2)$$

where k is the mass transfer coefficient, MTC (s^{-1}) and $M(\infty)$ is the equilibrium uptake of ethane.

The mass transport coefficient, k is related to the effective diffusivity, D ($m^2\,s^{-1}$) and a (m) is the sphere radius (diffusion length):

$$k = \frac{15D}{a^2} \qquad (6\text{-}3)$$

Figure 6.1 illustrates the method to obtain the values of $M(t)$ and $M(\infty)$ from the plot of sample mass/pressure versus time.
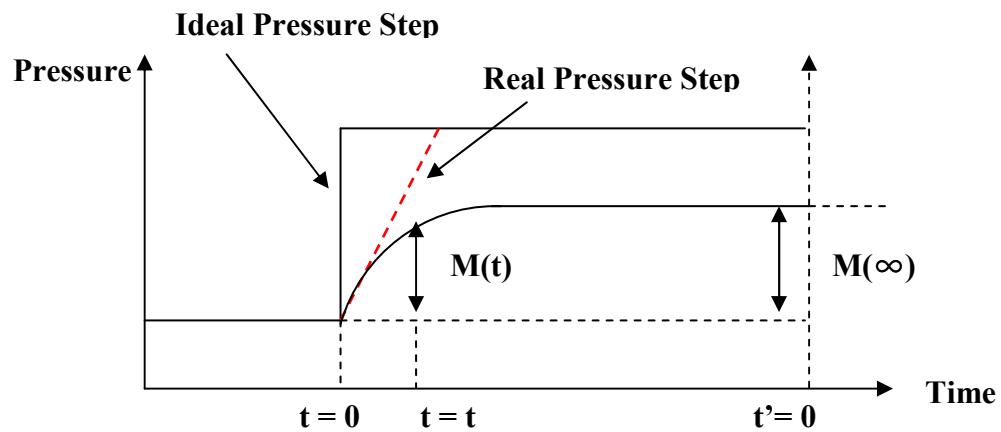
Figure 6.1 – Schematic diagram of an ideal and real pressure step, and the corresponding change in the mass of the sample with time

The development of the LDF model is based on assumptions which may lead to inaccuracy in the calculations of the mass transport coefficient. An ideal pressure step is assumed for the LDF model (vertical step increase). The real pressure step during the adsorption experiment is not vertical as expected in the LDF model. A diagram to illustrate this is shown in Figure 6.1. In addition, the solution to the LDF equation assumes isothermal behaviour, and this is not always the case since adsorption is an exothermic process.

6.3 Previous Studies

The formation of coke in zeolites usually leads to transport resistance as well as hinders the access of reactants and/or products to the active sites. Many experiments have shown the effect of coke deposition on the diffusion rate of a probe molecule [2-3, 7-8]. In addition to reducing the diffusion coefficient (D), coke may change the diffusional pathway (a) within the crystallite, depending on the location of coke deposition during the reaction.

The diffusivity of a probe molecule usually decrease with increasing coke content when intracrystalline coking dominates. This was demonstrated by Karger et al. [7] for coking with n-hexane and Paweewan et al. [3] when the authors studied the mode of coke formation during ethene conversion over USY zeolite. In addition, Chen et al. [2] and Schuurman et al. [8] reported that, at low coke content, the decrease in the intracrystalline diffusivity could explain the decrease in the diffusion time constant (D/a^2). However, when coke is deposited on the surface of the catalyst, the diffusional time constant, (D/a^2) is lowered, as a result of an increase in the diffusion length of a probe molecule, as illustrated by Figure 4 in the work of Uguina et al. [9]. Similarly, later studies [2, 8] showed that, when coke deposition in the pores resulted in pore blockage, the decrease in the diffusion time can be explained by the decrease in diffusion path length.

These studies showed that, by measuring the influence of coke on the diffusivity of a probe molecule, it is possible to distinguish between surface and intracrystalline coking. Therefore, analysis of ethane mass transport in the fresh and coked zeolite catalysts investigated in Chapter 3 could give information on the mode of coke formation, and the effect of coke on the pore structure of the zeolite catalysts. The adsorption of ethane will be discussed in the following sections.

6.4 Experimental Procedure

Ethane adsorption experiments were performed on an Intelligent Gravimetric Analyser (IGA) supplied by Hiden Ltd U.K.

6.4.1 Sample Preparation

Approximately 100 mg of PtH-ZSM-5 catalysts were loaded on a sample pan and the reactor chamber was then sealed tightly. The system was out gassed until vacuum was reached. Then, the sample was heated at 250 $^{\circ}$C until no further weight loss was observed. The reactor chamber was then allowed to cool to room temperature.

6.4.2 Adsorption Analysis

A stainless steel cylinder containing ethylene glycol, connected to a water bath was attached to the reactor to maintain the temperature of the reactor at the desired temperature for analysis. The isothermal analysis was performed once the temperature of the reactor had reached the desired temperature.

6.4.3 Calculations

6.4.3.1 Ethane Adsorption Capacity (molecule per unit cell)

The adsorption capacity of ethane was expressed in terms of molecules of ethane adsorbed *per* unit cell of the zeolite catalyst and effective chain length of sorbate molecules *per* unit cell (nm *per* unit cell) (Equation 6.4) instead of the mass of ethane adsorbed *per* unit mass of the zeolite catalyst as it gives a more helpful understanding of the adsorption process according to Richard and Rees [10].

$$chain\ length \times \frac{molecule}{unit\ cell} = \frac{total\ chain\ length}{unit\ cell} \qquad (6\text{-}4)$$

The theoretical adsorption capacities were calculated from the channel lengths of the ZSM-5 zeolite (Table 6.1) and the length of ethane molecule based on the sorption of one or two ethane molecules adsorbed *per* intersection.

Table 6-1 – ZSM-5/Silicalite-1 Channel Lengths [10]

Channel Type	Channel Length (nm *per* unit cell)[a]
Sinusoidal channels and intersections only	4.83
Linear channels and intersections only	3.98
Sinusoidal and linear channels and intersections (1 molecule *per* intersection)	6.65
Sinusoidal and linear channels and intersections (2 molecules *per* intersection)	8.81

[a] Unit cell parameters: a=2.007, b=1.992, c=1.342 nm

6.4.3.2 Heat of Adsorption

The differential molar enthalpy of adsorption, also known as the 'isosteric heat of adsorption' (Q_{st}). Q_{st} is positive when adsorption occurs and heat is evolved. [11]. The differential enthalpies of adsorption can be calculated from a series of adsorption isotherms at different temperatures. The difference between the temperature at which the adsorption experiments were carried out should be small enough to justify the assumption that isosteric heat of adsorption, Q_{st} is independent of temperature [11].

Equation 6.5 relates the equilibrium pressure to the differential heat of adsorption at which a certain amount is adsorbed on the surface of the adsorbent.

$$\left(\frac{\partial}{\partial T} \ln[p] \right)_{\Gamma} = -\frac{\Delta H_{T,\Gamma}}{RT^2} \tag{6-5}$$

and therefore,

$$\Delta H_{T,\Gamma} = R \left(\frac{\partial(\ln[p])}{\partial(1/T)} \right)_{\Gamma} \tag{6-6}$$

where ΔH is the differential molar enthalpy of adsorption (kJ mol^{-1}), R is the gas constant (J mol^{-1} K^{-1}), T=temperature (K), $[p]$= equilibrium pressure (Pa) corresponding to the amount adsorbed, Γ=constant amount adsorbed (mg mg^{-1})

Integration of Equation 6.6 allows the calculation of *ΔH* from adsorption isotherm obtained experimentally at two or more temperatures (assuming constant temperature).

$$\ln\left(\frac{p_2}{p_1}\right) = \frac{-\Delta H}{R}\left(\frac{1}{T_2} - \frac{1}{T_1}\right)$$
(6-7)

ΔH can be can be calculated by plotting the graph of $ln(p)$ as a function of $\frac{1}{T}$ for the same amount adsorbed at all the different temperatures. The calculation for *ΔH* (Equation 6.7) is applicable to only a particular amount adsorbed, therefore, the calculation is repeated for different amount adsorbed in order to obtain the variation of *ΔH* with loading.

6.4.3.3 Mass Transfer Coefficient
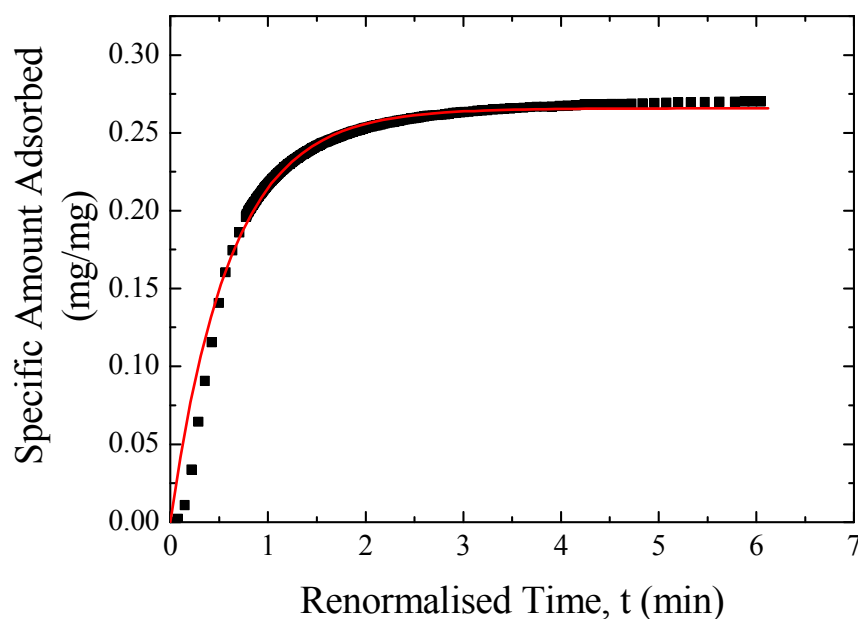
Figure 6.2 – Mass up take curve (■) for pressure step from *P/P_o* of 0.00172 to 0.00196 from ethane adsorption experiment on PtH-ZSM-5(30) sample after 48 hours on-stream.
The solid line (—) shown is a fit of the LDF model to the experimental data, R^2=0.9766

The uptake kinetics of gases on porous solids is usually used to determine the adsorption rate/mass transport coefficient. The increment in mass uptake was due to the small pressure steps introduced to the adsorption system. The data from the uptake curves of each pressure step was fitted to the LDF model (Equation 6.2) to estimate the values of $M(\infty)$ and k.

The data points from the isotherms were checked to ensure that it had reached equilibrium by checking that the fitted parameter $M(\infty)$ from the LDF model agreed with the mass uptake values in the final plateau of the uptake curves. A diagram to illustrate the experimental data fit with the LDF model is as shown in Figure 6.2. The equilibrium uptake, $M(\infty)$ calculated from LDF model is compared with the experimental value. In general, even though the LDF fit only applies for $M(t)/M(\infty) >$ 0.5, it still gives a reasonable fit to the lower part of the curve as illustrated in Figure 6.2.

The mass transport coefficient was calculated by using the kinetic data that corresponds to the beginning of the isotherm. This data obtained at the start of the isotherm was easier to interpret due to the lesser effects of adsorbate-adsorbate interaction. When diffusion within the porous solid is accompanied by adsorption, the usual diffusion equation must be modified for this:

$$\frac{\partial C}{\partial t} = \frac{D}{H+1}\left[\frac{\partial^2 C}{\partial r^2} + \frac{2}{r}\frac{\partial C}{\partial r}\right] \qquad (6\text{-}8)$$

where H = constant of proportionality between the concentrations of the adsorbed phase and the freely diffusing phase.

6.5 Results and Discussion

6.5.1 Ethane Adsorption Isotherms

The adsorption isotherms of ethane on PtH-ZSM-5 catalysts were measured at 10, 20 and 30 $^{\circ}$C. Ethane adsorption isotherms at different adsorption temperatures for the fresh PtH-ZSM-5(30) catalyst are shown in Figure 6.3. The shape of the isotherms are of Type I, where a distinct plateau was observed at saturation, indicating that the pores are in micropore region, i.e. < 2nm. Similar results have been reported previously

for the sorption of ethane in ZSM-5 sorbent [12-13]. The adsorption capacity of ethane decreased as the temperature of sorption was increased. As adsorption is an exothermic process, an increase in temperature shifts the equilibrium towards the region unfavourable to adsorption because of the combination effects of the bombardment rate of bulk molecules and increase in vibrational energy of the ethane molecules. Hence, smaller amount of ethane molecules are adsorbed at equilibrium when the temperature of adsorption is increased.
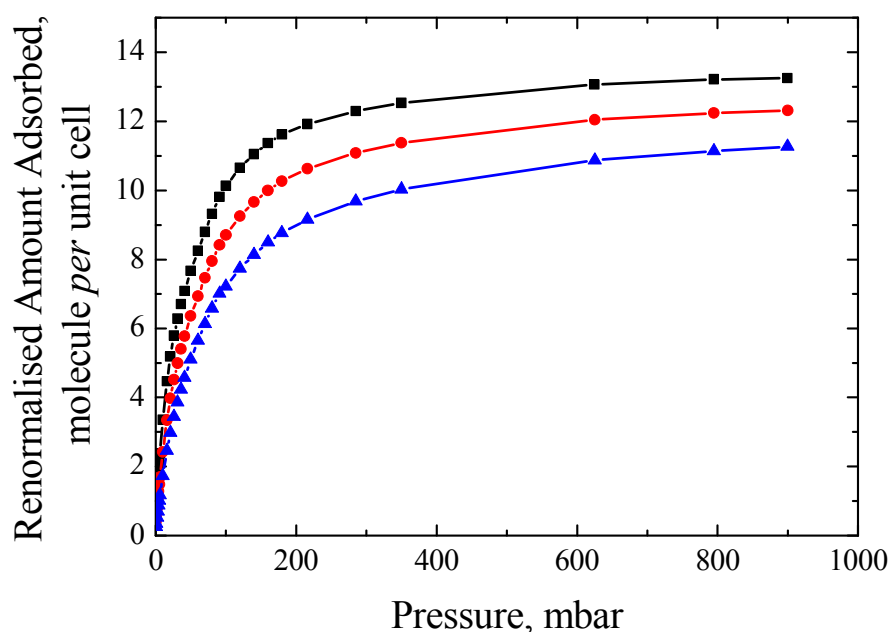
Figure 6.3 – Ethane adsorption isotherms for fresh PtH-ZSM-5(30) catalyst at 10°C (-■-), 20 ^{o}C (-●-) and 30 ^{o}C (-▲-)

The experimental adsorption capacity, q_{exp} of ethane on the fresh PtH-ZSM-5(30) catalyst was compared with the theoretical sorption capacity, q_{theo}, evaluated by Richards and Rees [10] (Table 6.2). The effective channel length calculated (Table 6.2) for ethane in the PtH-ZSM-5(30) sample was comparable with the calculated lengths evaluated by Richards and Rees [10]. It should be noted that the total sorption capacities were evaluated at equilibrium pressures P_e which were well below the saturation vapour pressure, P_o of ethane. To further validate the experimental data obtained, the experimental adsorption capacity of ethane was also compared with experimental data

of Sun et al. [14]. It was found that, results obtained in this study were in good agreement with previous finding of Sun et al. [14].

Table 6-2 – Sorption Capacities for ZSM-5/Silicalite-1

Adsorbate	Adsorbate Length (nm)	Theoretical Sorption Capacity [a], q_{theo} (molecules *per* unit cell)		Experimental Sorption Capacity [b], q_{exp} (molecules *per* unit cell)	max P_e/P_o	Effective Channel Length (nm *per* unit cell)	
		2molec/int	1molec/int				
Ethane	0.526	16.7	12.6	12.3	0.0198	5.57 [a]	6.00 [b]

[a] Adapted from reference [10] , [b] Based on average adsorption capacity of ethane at 10, 20 and 30 °C

6.5.1.1 *Effect of Coke on Adsorption Capacity of Ethane*

The effect of coke deposition on the adsorption of the key reactant, ethane was also studied, and is presented in Figure 6.4 for PtH-ZSM-5 (30) catalysts and Figure 6.5 for PtH-ZSM-5(80) catalysts. The total amount of ethane adsorbed was corrected for the amount of coke formed, as described for nitrogen and argon adsorption. As with the nitrogen and argon sorption results, the coke formed during the alkylation reaction caused a decrease in the adsorption capacity of the bi-functional PtH-ZSM-5 catalysts to ethane. The reduction in the adsorption capacity for ethane as a result of coke formation is very similar to that observed for nitrogen and argon (discussed in Chapter 4).
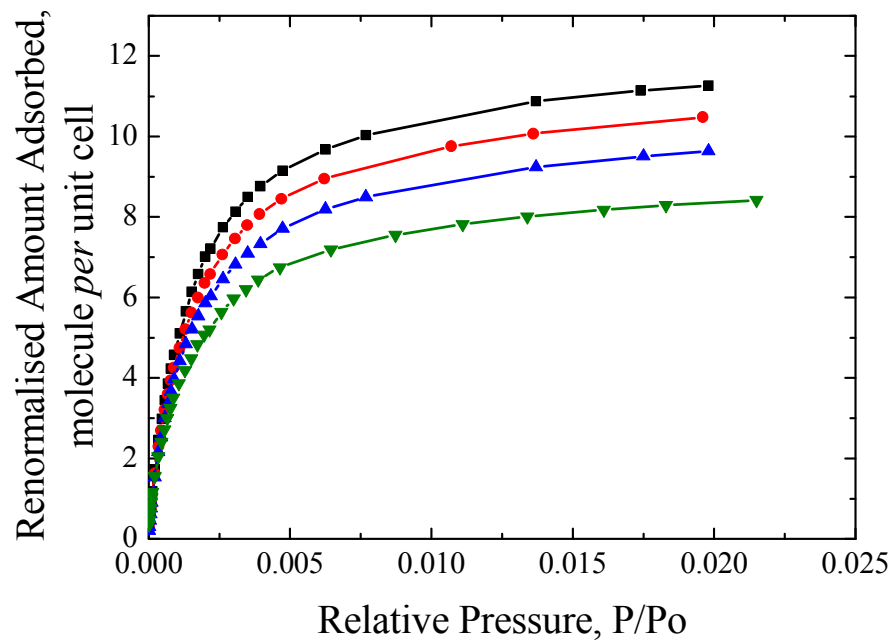
Figure 6.4 – Ethane adsorption isotherms for fresh (-■-), 4 h (-●-), 24 h (-▲-) and 48 h (-▼-) coked PtH-ZSM-5(30) catalysts at 30 ^{o}C
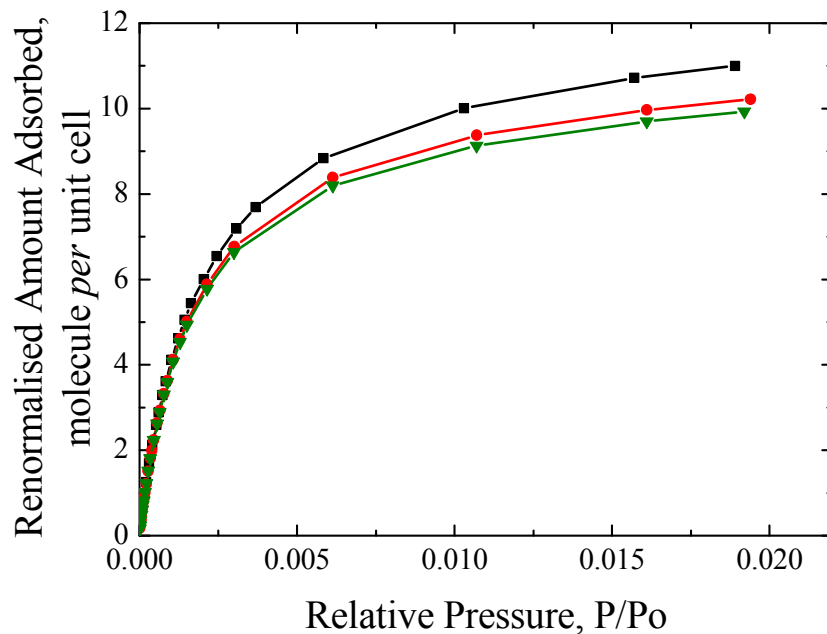
Figure 6.5 – Ethane adsorption isotherms for fresh (-■-), 4 h (-●-), and, 48 h (-▼-) coked PtH-ZSM-5(80) catalysts at 30 ^{o}C

At saturation, the total amount of ethane adsorbed for the fresh PtH-ZSM-5(30) sample is 12.3 molecules *per* unit cell while the adsorption capacity for the uncoked PtH-ZSM-5(80) catalyst is 12 molecules *per* unit cell, based on an average obtained from three different adsorption temperatures. This value corresponds to the theoretical value of 12.6 molecules *per* unit cell calculated based on adsorption of 1 molecule in the intersection at 16 ^{o}C [10]. After 48 h on-stream, the coke content increases to 5.6 mass %, decreasing ethane adsorption capacity in the PtH-ZSM-5(30) sample from 12.3 molecules *per* unit cell to 8.4 molecules *per* unit cell. A less significant decrease in adsorption capacity was observed for the PtH-ZSM-5(80) catalyst after 48 h on-stream. An increase of 2 mass % of coke content resulted in 12.5 % adsorption capacity loss of the PtH-ZSM-5(80) catalyst.

The comparison of ethane adsorption capacity in terms of molecules *per* unit cell and effective channel length *per* unit cell for both PtH-ZSM-5 catalysts with TOS is shown in Table 6.3.

Table 6-3 – Variation of adsorption capacity of PtH-ZSM-5 with TOS

Time on Stream (h)	Experimental Adorption Capacity, q_{exp} (molecules *per* unit cell)		Effective Channel Length (nm *per* unit cell)	
	PtH-ZSM-5(30)	PtH-ZSM-5(80)	PtH-ZSM-5(30)	PtH-ZSM-5(80)
0	12.3	12.0	6.49	6.29
4	11.2	10.8	5.86	5.70
24	10.5	-	5.53	-
48	8.4	10.5	4.42	5.49

6.5.2 Isosteric Heat of Adsorption, Q_{st}
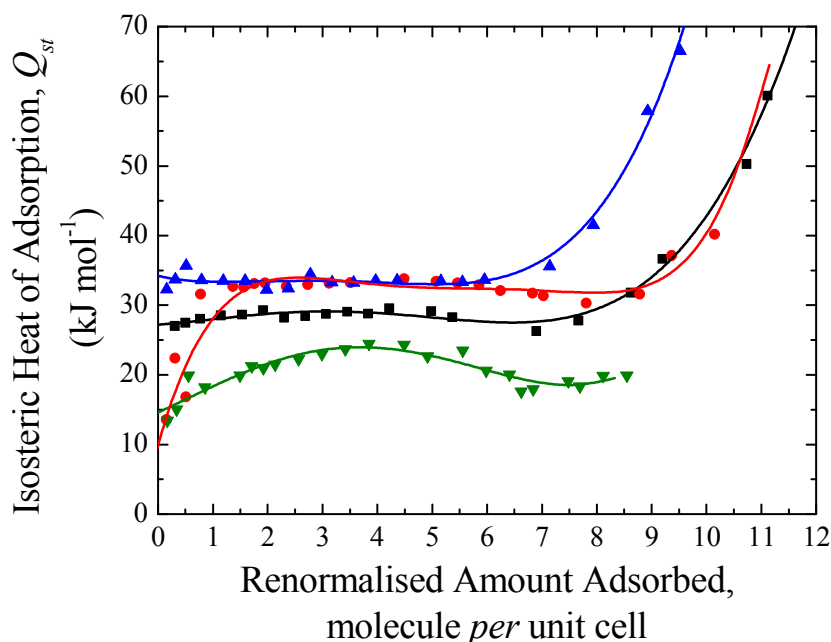
Figure 6.6 – Variation of isosteric heat of sorption, Q_{st} for fresh (-■-), 4 h coked (-●-), 24 h coked (-▲-) and 48 h coked (-▼-) PtH-ZSM-5(30) catalyst

The Q_{st} at different coverage of ethane was determined from the isotherms by the Clausius-Clapeyron equation as described in Section 6.4.3.2. Q_{st} calculated for ethane adsorption is the sum of the interaction between zeolite pore walls and ethane molecules, and also between ethane molecules. In ZSM-5 zeolites, the Q_{st} is believed to be dominated by sorbate-sorbent interaction because of the highly energetic interaction between the alkane hydrogen atoms and the oxygen atoms of the channel walls [15]. The sorbate-sorbate interaction is restricted to only end methyl-methyl group interactions in the narrow pore system [16] as described by Richard and Rees [10] for the adsorption of n-alkanes in H-ZSM-5.

The variation of Q_{st} of ethane for the fresh and coked PtH-ZSM-5(30) catalysts is illustrated in Figure 6.6. Q_{st} for the fresh catalyst remained constant at approximately 28 kJ mol^{-1} for ethane loading up to 8 molecules *per* unit cell. The constancy of the Q_{st} for ethane loading up to 8 molecules *per* unit cell indicated an energetic homogeneous surface for the adsorption of ethane molecules. Based on previous findings, either experimentally [10, 17-18] or by simulations [12-13, 19], Q_{st} for ethane molecules on

ZSM-5/Silicalite was reported to be in the range of 28-45 kJ mol^{-1}. Therefore, the reported value coincides with the findings of other studies, verifying the experimental data obtained.

A more pronounced variation in the initial Q_{st} was observed with increasing coke content. The initial Q_{st} increased to ~34 kJ mol^{-1} for the 4 h and 24 h coked catalysts, and then as TOS is increased to 48 h, the Q_{st} decreased below the Q_{st} for fresh catalyst. For the 48 h coked sample, Q_{st} increased to a maximum value of 23.5 kJ mol^{-1} at 50 % of the maximum uptake of 8 molecules *per* unit cell. A further increase in the ethane loading for this sample led to a decrease in the Q_{st} due to the balance between the two opposing interactions (attractive and repulsive) of the ethane molecules. The presence of coke modifies the adsorption potential inside the crystallites. This causes a change in the Q_{st} with TOS for a given amount of adsorbed ethane.

Richards and Rees [10] proposed a packing arrangement for molecules adsorbed within the ZSM-5 pores, based on the variation of Q_{st} with coverage. The same approach was applied in this study to predict the possible arrangement of ethane molecules in the pore structure at equilibrium with the effect of coke being taken into consideration. As adsorption first took place in the highest energy adsorption sites, ethane molecules were initially adsorbed in the straight and zig-zag channels. Q_{st} remained constant initially for the fresh, 4 h and 24 h on-stream catalysts because the ethane molecules can be positioned in the channel segments without interaction from other ethane molecules.

Even though the ZSM-5 zeolite has been considered to be an energetically homogeneous sorbent, the interaction energy for the ethane molecules in the channels would be different from those at the intersections. As the amount adsorbed was increased above 8 molecules *per* unit cell for the fresh sample, ethane molecules must have adsorbed in sites within the channel intersections that had lower adsorbate-adsorbent interactions but higher adsorbate-adsorbate interactions. The increasing net Q_{st} for the adsorption of the molecules in the intersections suggests that the adsorbate-adsorbate interactions dominate in the channel intersections.

Due to the formation of dead-end pores with higher pore potential as a result of coke deposition, as proven by the shift to smaller pore diameter in the PSD (Figure 4.37 in Chapter 4), Q_{st} for the 4 h and 24 h coked PtH-ZSM-5(30) catalyst rose above the Q_{st} for the fresh sample. For the 48 h coked catalyst, Q_{st} was found to increase with amount adsorbed, with a peak/maximum at 4 molecules *per* unit cell, and then decreased. As the ethane coverage was increased, the attractive adsorbate-adsorbate interactions led to increased Q_{st} until the molecular packing becomes so tight that repulsive adsorbate-adsorbate interactions increased significantly causing the Q_{st} to fall.

6.5.3   Mass Transfer Coefficient (MTC)

The term mass transfer coefficient (MTC) has been used by Sircar and Hufton [6] to characterise mass transfer in an adsorbent particle, and will be used in this study. The kinetics data obtained from the ethane adsorption experiment were used to determine the relationship between the MTC and the effect of coking. It can be seen from Figure 6.2 that the LDF model fits perfectly the upper part of the uptake curve of the experimental data. Fitting the LDF model to the upper part of the curve is better as it is further away from potential disturbance caused by the pressure step change which is not ideal [6]. In addition, at the lower part of the adsorption curve, the heat transfer effect is more pronounced due to large amounts of ethane adsorbed in the pores of the catalyst [6]. The large amount of heat released increases the MTC, k [6], thus giving rise to inaccuracy in the value of k calculated.

In some cases, the LDF model does not fit perfectly to the experimental data. This is due to the non ideality of the step shape during the pressure step causing the system to not reach equilibrium. During the adsorption analysis, it is preferably to use small pressure steps but in order to improve the signal-to-noise ratio in the data, larger pressure steps are usually used [6]. It is therefore important to check that all the data points reached equilibrium prior to using them for adsorption rate calculation.
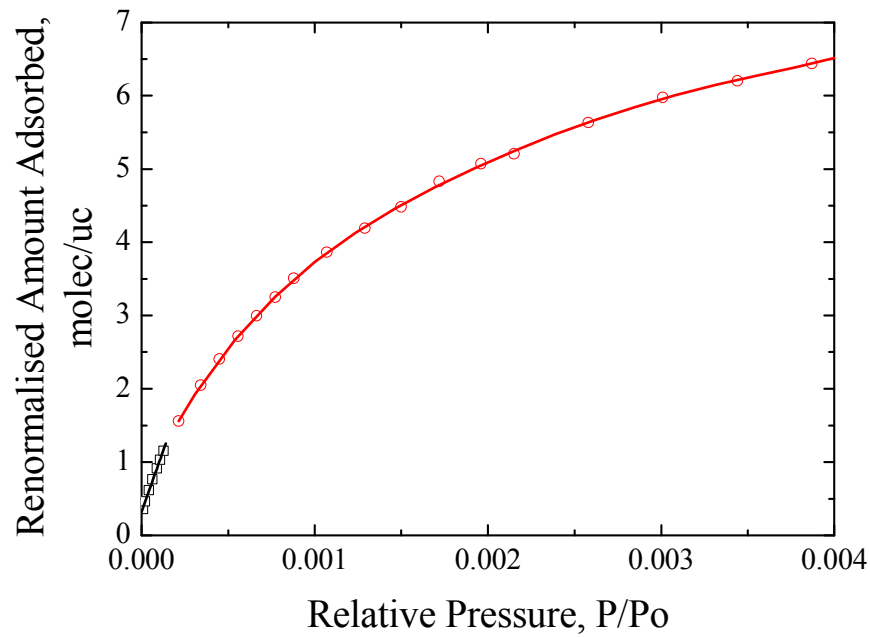
Figure 6.7 – Ethane adsorption isotherm for PtH-ZSM-5(30) catalyst coked for 48 hours at 30 °C.

Also shown are a fit of points for *P/Po* up to 2E-04 to a linear plot (-□-) (*y = 0.2094+7.870E+3x, R²=0.9660*), and a 6th order polynomial fit (-○-) (y = 7.833E +14x⁶ + 5.758E+12x⁵ - 1.518E+11x⁴ + 9.051E+8x³ - 2.643E=6x² + 5.008E+3x + 0.60273, R²=0.9998) to points with P/P₀ above 2E-04

The resistance to diffusion was enhanced as the loading of ethane on the surface of the catalyst increases. To correct the calculated MTC in order to take into account of diffusion with adsorption, the slope of the isotherm, *H* at that particular pressure point needs to be calculated. The isotherms show that the amount adsorbed increases linearly with pressure at the beginning of the isotherm, but deviates from linearity as pressure increases. The initial part of the ethane adsorption isotherms were fitted to a straight line while the upper part of the curve is fitted to a 6th order polynomial fit. The gradient of the straight line gives Henry's constant. For the upper part of the curve, the gradient of a polynomial fit at a particular pressure point will be used to correct the calculated mass transport coefficient from Equation 6.2. Example of fit of the straight line and polynomial curve is shown in Figure 6.7.
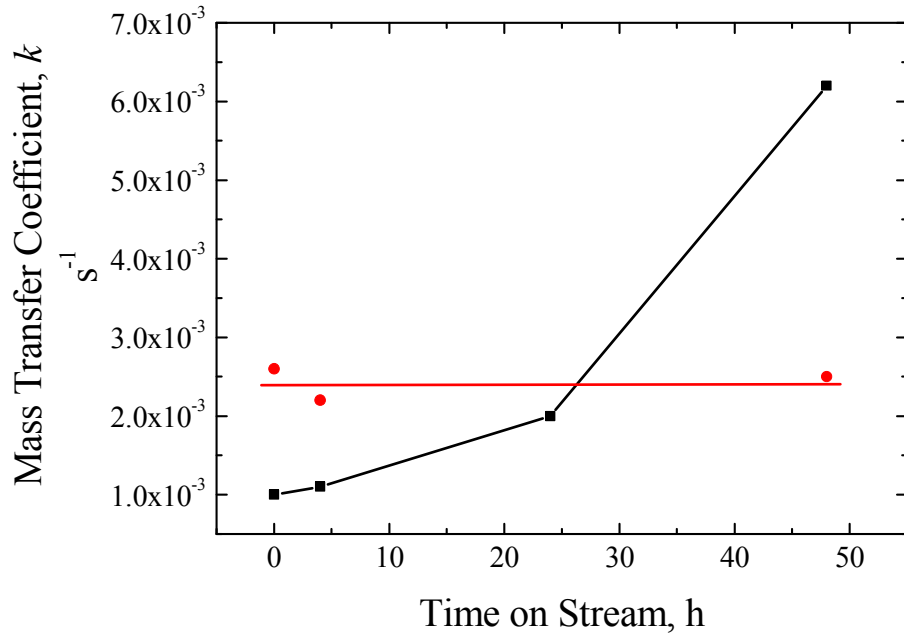
Figure 6.8 – Variation of LDF mass transfer coefficients with TOS for PtH-ZSM-5(30) (-■-) and PtH-ZSM-5(80) (-●-) at ethane loading of 6 molecules *per* unit cell

Figure 6.8 shows the change of the MTC with TOS, obtained from fitting the LDF model. It can be seen that, at a constant amount of ethane adsorbed, an increase in the MTC was observed with TOS for the PtH-ZSM-5(30) catalyst.

The diffusion of molecules on surfaces can be considered as a series of activated hops between adsorption sites. If the diffusion is modelled as a random walk [20], then diffusivity, D is given by:

$$D = \frac{k_D \lambda^2}{\tau} \tag{6-9}$$

where λ is the jump distance, τ is the correlation time and k_D is the numerical factor which depends on the dimensionality of the system. If the diffusion of molecules is an activated process, in which the diffusivity varies with temperature, the diffusivity may be correlated with an Arrhenius expression of the form of:

$$D = A_o \exp\left(\frac{E_D}{RT}\right) \tag{6-10}$$

where A_o is the pre-exponential factor and E_D is the activation energy for diffusion.

157

As the activation energy for the correlation time is a monotonically increasing function of the heat of adsorption, Q_{st} [20], the correlation time of diffusion should increase from 0-24 h on-stream as the interaction between ethane molecules and the pore walls is increased. This is supported by the increase in Q_{st} for the coked PtH-MFI-15 catalysts as described in Section 6.5.2. As a result of site blockage, or increasing adsorption coverage, the jump length of the molecule is reduced due to intermolecular collisions. Hence, the contribution of both the jump length and the correlation time suggest that the diffusivity of the ethane molecules should decrease with TOS.

Since the diffusivity of ethane did not increase with coking, then the observation of an increase in MTC ($k = 15D/a^2$) with coking (Figure 6.8) can only be explained by a decrease in the length of the diffusion pathway, which is equivalent to an apparent decrease in crystallite size of the zeolite catalyst. The decrease in the diffusion path length but lack of impact on diffusivity can be explained by the preferential deposition of coke towards the centre of the zeolite crystallites, thereby partially blocking the internal pore structure of the zeolite catalysts [2, 21].

In contrast to the PtH-ZSM-5(30) catalyst, coke deposition up to 2 mass % did not affect diffusion of ethane in the PtH-ZSM-5(80) catalyst. The MTC for the coked PtH-ZSM-5(80) catalysts was the same as that in the fresh catalyst. After 48 h on-stream, the PtH-ZSM-5(30) catalyst yielded a larger MTC as compared to the PtH-ZSM-5(80) catalyst, at a specific amount of ethane adsorbed. Therefore, the diffusion pathlength of the PtH-ZSM-5(80) catalyst remained long with TOS when compared to the PtH-ZSM-5(30) catalyst, as demonstrated by the larger MTC for the PtH-ZSM-5(30) catalyst.

6.6 Conclusions

The effect of coke formation on mass transport within PtH-ZSM-5 catalysts was studied by ethane adsorption. The results have shown that coke formation decreased the adsorption capacity for ethane in PtH-ZSM-5 catalysts. The variation of Q_{st} of ethane with loading suggested the possible arrangement of ethane molecules in the pore network of the zeolite catalysts.

It was observed that, the mass transfer coefficients for ethane, corrected for the slope of the equilibrium isotherm, showed an increase with TOS, at constant amount adsorbed for the PtH-ZSM-5(30) catalysts. This result probably indicates a decrease in diffusion length, rather than an increase in diffusivity. The reduction in the length of diffusional pathway suggested that coke deposition preferentially starts to occur in the center of the pores within the PtH-ZSM-5(30) crystallites.

6.7 References

[1]   W.T. Mo, and J. Wei, Chemical Engineering Science 41 (1986) 703-710.

[2]   D. Chen, H.P. Rebo, K. Moljord, and A. Holmen, Chemical Engineering Science 51 (1996) 2687-2692.

[3]   B. Paweewan, P.J. Barrie, and L.F. Gladden, Applied Catalysis A: General 167 (1998) 353-362.

[4]   C.R. Reid, and K.M. Thomas, Langmuir 15 (1999) 3206-3218.

[5]   E. Glueckauf, and J.I. Coates, Journal of Chemical Society (1947) 1315-1321.

[6]   M.J. Watt-Smith, S.T. Kolaczkowski, S.P. Rigby, and J.A. Chudek, AIChE Journal 52 (2006) 3278-3289.

[7]   J. Karger, H. Pfeifer, J. Caro, M. Bulow, H. Schlodder, R. Mostowicz, and J. Volter, Applied Catalysis 29 (1987) 21-30.

[8]   Y. Schuurman, C. Delattre, I. Pitault, J.P. Reymond, and M. Forissier, Chemical Engineering Science 60 (2005) 1007-1017.

[9]   M.A. Uguina, D.P. Serrano, R. Van Grieken, and S. Venes, Applied Catalysis A: General 99 (1993) 97-113.

[10]   R.E. Richards, and L.V.C. Rees, Langmuir 3 (1987) 335-340.

[11]   S.J. Gregg, and K.S.W. Sing, Adsorption, Surface Area and Porosity. London : Academic Press, 1982.

[12]   Z. Du, G. Manos, T.J.H. Vlugt, and B. Smit, AIChE Journal 44 (1998) 1756-1764.

[13]   W. Zhu, F. Kapteijn, and J.A. Moulijn, Physical Chemistry Chemical Physics 2 (2000) 1989-1995.

[14]   M.S. Sun, D.B. Shah, H.H. Zu, and O. Talu, 102 (1998) 1466-1473.

[15]   D.H. Olson, G.T. Kokotailo, S.L. Lawton, and W.M. Meier, Journal of Physical Chemistry 85 (1981) 2238-2243.

[16]   H. Thamm, H. Stach, and W. Fiebig, Zeolites 3 (1983).

[17]   V.R. Choudhary, and S. Mayadevi, Zeolites 17 (1996) 501-507.

[18]   H. Thamm, Zeolites 7 (1987).

[19]   M.D. Macedonia, and E.J. Maginn, Fluid Phase Equilibria 158-160 (1999) 19-27.

[20]   E.R. Gilliland, R.F. Baddour, G.P. Perkinson, and K.J. Sladek, Industrial & Engineering Chemistry Research 13 (1974) 95-100.

[21]   J.L. Sotelo, M.A. Uguina, J.L. Valverde, and D.P. Serrano, Applied Catalysis A: General 114 (1994) 273-285.

Chapter 7 : Investigation of the Cause of Coke Location during Benzene Alkylation with Ethane

7.1 Introduction

Results described above from different characterisation techniques, combined with Monte Carlo simulation, have indicated intra- or intercrystalline coke depositions, during benzene alkylation with ethane over PtH-ZSM-5 catalysts with SiO_2/Al_2O_3 ratios of 30 and 80, respectively. Intracrystalline coke deposition was seen for the PtH-ZSM-5(30) catalyst while coke was found on the surface of the PtH-ZSM-5(80) crystallites. It is therefore the aim of this chapter to find the possible explanation for the different locations of coke observed.

The Pt distribution differs for the two PtH-ZSM-5 catalysts, as seen from BSE images in Chapter 4 (Figures 4.13 and 4.14). A higher concentration of Pt was found on the surface of the PtH-ZSM-5(80) crystallites when compared with the PtH-ZSM-5(30) sample. Since Pt metal act as active sites for reactions to take place, the difference in the Pt location could possibly affect the location of coke formation. The effect of Pt incorporation on the pore structure of the H-ZSM-5 catalysts will be shown using nitrogen sorption results, while mass transport effects will be studied using pulsed field gradient (PFG) NMR technique. In order to access the effect of microporosity in a zeolite catalyst, self-diffusion and tortuosity of probe molecules imbibed in a pure mesoporous silica pellet will also be investigated in this Chapter.

7.2 Theory

In order to recognize the potential of gas sorption for pore structure characterisation and pulsed field gradient (PFG) NMR for transport phenomena investigation in porous solids, it is important to understand the basic principles of these techniques. Since the theory of gas sorption has already been discussed in Chapter 4, only the NMR theory will be described in this section.

7.2.1 Nuclear Magnetic Resonance (NMR) Theory

Nuclear magnetic resonance (NMR) has been widely applied for molecular structure characterisation in different fields such as physics, biology and medical science. However, the application of nuclear magnetic resonance (NMR) technique for diffusion studies has become one of its main applications following the first report by Tanner and Stejskal [1] who used PGSE NMR to measure diffusion in aqueous solutions. NMR spectroscopy is based on the resonant absorption of radiofrequency (RF) radiation by nuclei exposed to a magnetic field [2]. Molecules usually contain nuclei which may be characterised by a nuclear spin quantum number, I, which may take values greater than or equal to zero, and are multiples of ½. If $I = 0$, then the nucleus possesses no nuclear spin, and hence cannot exhibit nuclear magnetic resonance. However, when $I > 0$, the nuclei possess a magnetic moment with a constant magnitude and an orientation. In the presence of a magnetic field, B_o, the magnetic moments align themselves relative to the field in a number of orientations ($2I+1$) because the energy states involved are quantised.
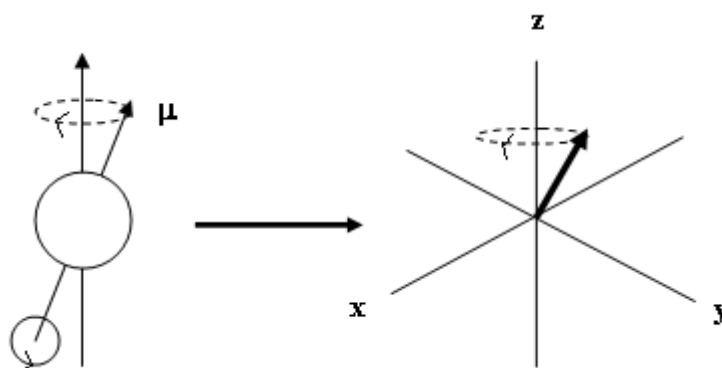
Figure 7.1 – A spinning nucleus with a magnetic moment, μ (left) and a Cartersian coordinate frame with the motion of nucleus represented as a vector moving on the surface of a cone (right) (Adapted from ref [3])

As a result of the static magnetic field, a torque is imposed on the magnetic moment, hence resulting in the moment tracing a circular path about the applied field (Figure 7.1). The motion of the magnetic moment is termed the Larmor precession, and the rate of precession is proportional to the applied magnetic field. The frequency of the Larmor precession, v is given by:

$$\nu = -\frac{\gamma B_o}{2\pi} \qquad (7-1)$$

where γ is the magnetogyric ratio, and B_o is the applied magnetic field.

In this study, we only consider hydrogen nuclei, which have a spin quantum number $I = \frac{1}{2}$. These spins may adopt two different orientations with respect to the static field, a parallel (the α-state), $+ \frac{1}{2}$ ($\uparrow$) or antiparallel (the β-state), $- \frac{1}{2}$ ($\downarrow$). When no magnetic field is present, the spins have the same energy level. However, when an external magnetic field is applied, the spins move from a lower energy level to a higher energy level, changing the population of the two spin states, hence resulting in a net magnetization, M_o along the z-axis. [2] Since there is nothing to define a preferred orientation for the spins in the transverse direction, there is no net magnetization in the transverse (x-y) plane. By application of a 90° radiofrequency pulse of frequency $\gamma\beta_1/2\pi$, the magnetization precesses into the xy-plane. Therefore, applying the radiofrequency field along the x-axis will drive the vector to the y-axis, and the magnetization vector is now rotating in the xy-plane at the Larmor frequency. Electrical signals produced by the rotating magnetization vector give rise to the NMR signal. As time passes, the transverse magnetization vector shrinks, while simultaneously growing along the z-axis. This process of returning to the equilibrium state is known as relaxation, and causes the NMR signal to decay with time, producing the observed Free Induction Decay (FID). The disappearance of the transverse magnetization is known as the spin-spin relaxation, while the recovery of the magnetization in the z-axis is termed as longitudinal spin-spin relaxation.
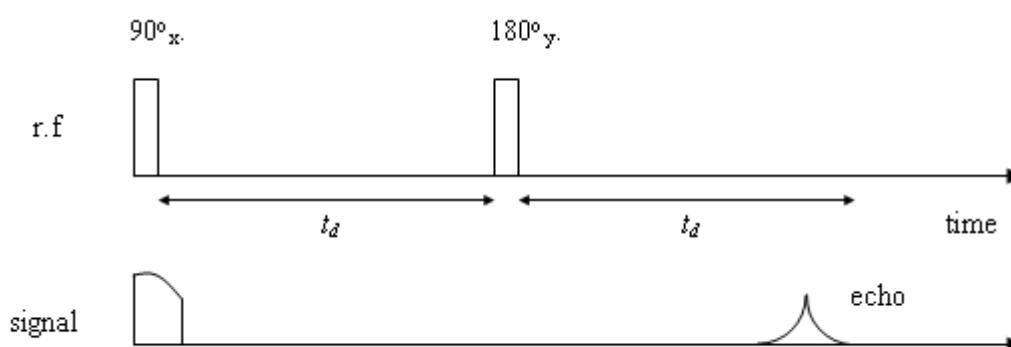
Figure 7.2 – NMR spin echo pulse sequence [4]
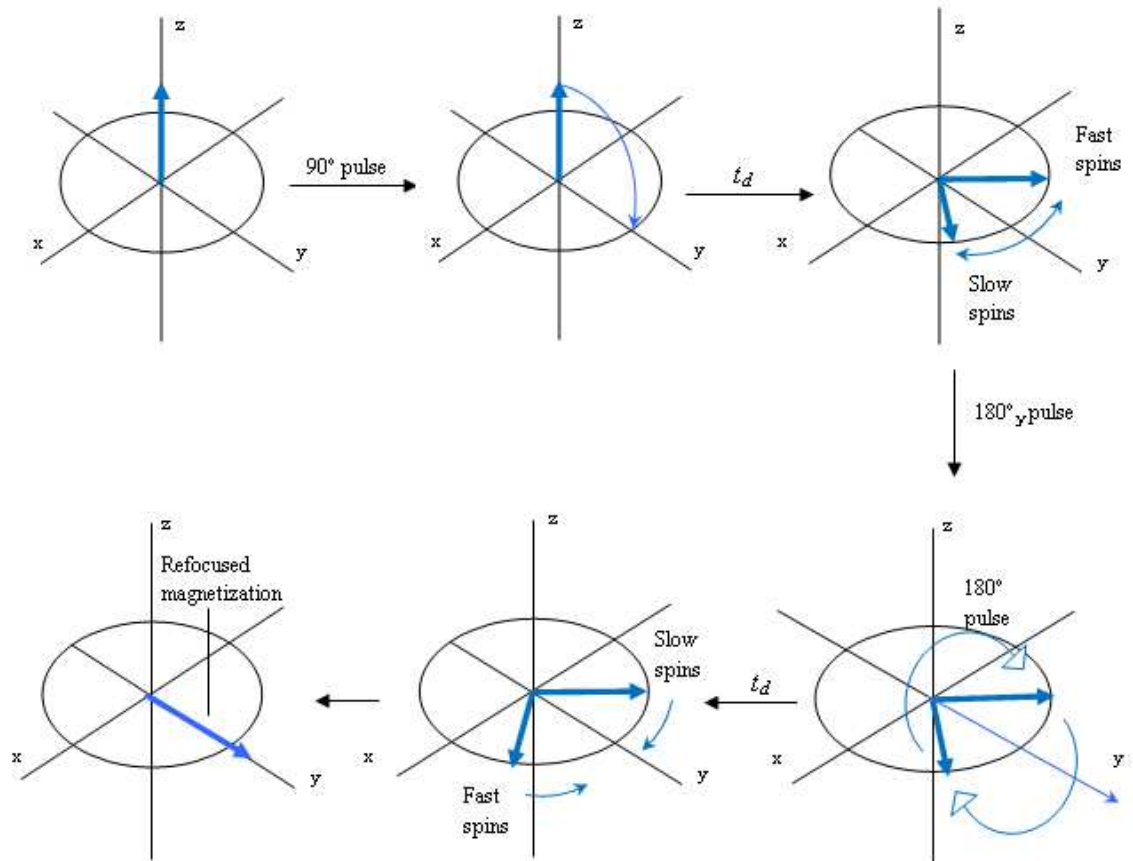
Figure 7.3 – Vector model representation of the spin echo pulse sequence [2]

During an NMR experiment, a set of radiofrequency pulses (pulse sequence) is usually applied to produce a specific form of NMR signal. The spin echo pulse sequence is illustrated in Figures 7.2 and 7.3. During a spin echo pulse sequence, a 90° pulse is applied along the x-axis, creating transverse magnetization along the y-axis. The nuclear spins begin to fan out because they have different Larmor frequencies, since some of the spins precess at a higher rate compared to the others. After a time period of t_d, a 180° pulse (along the y-axis) is applied to the sample. This 180° pulse rotates the magnetization vectors of the fast and slow spins. Therefore, the fast spins are now behind the slow spins, and the fan begins to close up again. Thus, the 180° pulse causes the magnetization to rephase, and the resultant signal is called an echo.
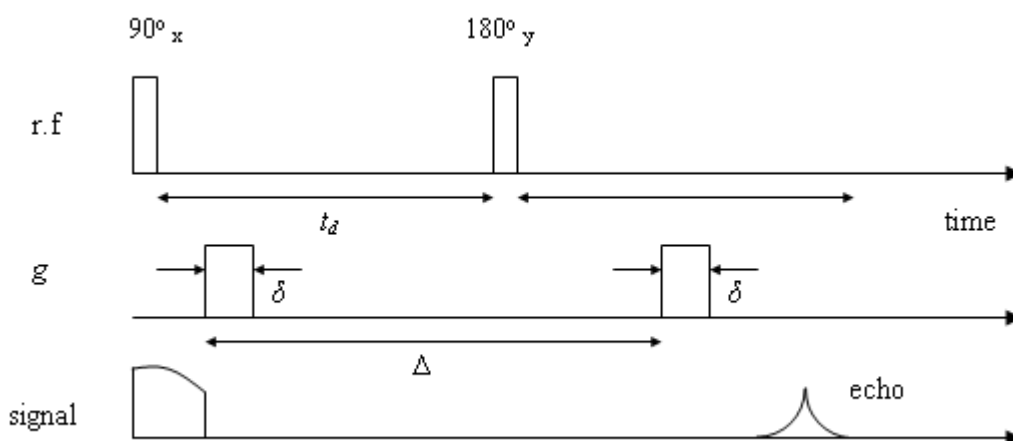
Figure 7.4 – NMR pulse sequence – pulsed gradient spin echo sequence where pulsed field gradient, *g* is applied (Adapted from ref [4])

The pulsed-field gradient (PFG) spin echo is the most commonly used scheme for the characterisation of diffusion in porous materials. The PFG spin echo sequence is based on the spin echo sequence described earlier, with two gradient pulses of identical magnitude, g and width, δ. The two pulsed gradients are applied after the 90° and 180° pulses, with a separation time between pulses of Δ (Figure 7.4). When pulsed gradients are employed, the complete refocusing of the signal will only occur when the local field experienced by a spin is identical during the two gradient pulses. If molecules diffuse away from its initial position during the observation time, Δ, then the local field experienced during the second PFG would not exactly match that of the first, and only partial refocusing of the signal would occur [3]. Therefore, attenuation of the detected signal would be observed, depending on how far the molecules have moved during the time Δ, and by its diffusion coefficient. However, if the particles have not moved in between the two pulses, the effect of both pulses is cancelled out.

The echo intensity obtained from the experiment varies with the diffusion time, Δ, length of the gradient pulse, δ, and the strength of the gradient pulses, g. It is usually assumed that the displacements during the time interval, δ are negligibly small in comparison with those during the diffusion time, Δ. The signal intensity, *I* for the PFG spin echo experiment is given by:

$$\frac{I}{I_0} = \exp\left[-D_{PFG}\gamma^2 g^2 \delta^2 \left(\Delta - \frac{\delta}{3} - \frac{\tau}{2}\right)\right] \qquad (7\text{-}2)$$

where I is the observed echo intensity, I_0 is the echo intensity in the absence of gradient pulses, D_{PFG} is the self-diffusion coefficient, γ is the gyromagnetic ratio of ^1H, g is the applied gradient, δ is the gradient pulse duration, Δ is the diffusion time, and τ is the correction time for the phasing and dephasing between bipolar gradients. The plot of $\ln (I/I_0)$ vs $\gamma^2 g^2 \delta^2 \left(\Delta - \frac{\delta}{3} - \frac{\tau}{2}\right)$ yields the diffusion coefficient from the slope of the linear plot obtained.

The diffusion coefficient calculated from the PFG NMR experiment, D_{PFG}, contains a contribution from the spin density which is related to the voidage [4], and is related to the effective diffusion coefficient :

$$D_{eff} = \varepsilon D_{PFG} \qquad (7\text{-}3)$$

where D_{eff} is the effective diffusion coefficient, and ε is the voidage of the material. For diffusion of a liquid in a porous solid, the effective diffusion coefficient is related to the molecular self-diffusion of bulk liquid, D, tortuosity, τ_p and voidage, ε:

$$D_{eff} = D\frac{\varepsilon}{\tau_p} \qquad (7\text{-}4)$$

Tortuosity of the pore network is a measure of the deviation from the linear path that a diffusing molecule may experience. It describes the geometry of the flow paths and defines the complexity of the porous medium. Therefore, the greater the tortuosity measured, the smaller is the displacement of the spins during the diffusion time [4]. From Equation 7.3 and 7.4, the tortuosity of the catalyst can be determined by Equation 7.5.

$$\tau_p = \frac{D}{D_{PFG}} \qquad (7\text{-}5)$$

where D is the molecular self-diffusion coefficient of the bulk liquid and D_{PFG} is the self-diffusivity.

During the diffusion time, Δ, the molecules diffuse from its initial position, and its displacement from this initial position can be determined by the diffusion coefficient,

D_{PFG}, measured from the NMR experiment. The distance travelled by the molecules gives indication of the effect of the pore structure on the molecular diffusion within the porous material. The relationship between the molecular mean squared displacement and the self-diffusion coefficient is given by the Einstein equation:

$$\langle r(t)^2 \rangle = 6D_{PFG}\Delta \qquad (7\text{-}6)$$

where D_{PFG} is the self-diffusivity, and $\langle r(t)^2 \rangle$ is the mean squared displacement

In this study, two different cyclic hydrocarbon molecules were used to study the transport properties of the two PtH-ZSM-5 zeolite catalysts. Cyclo-hexane (C_6H_{12}) and cyclo-octane (C_8H_{16}) were chosen as probe molecules because C_6H_{12} molecules can adsorb within the crystallites of the ZSM-5 catalyst [5] while C_8H_{16} molecules was reported to be too large to enter the micropore channels of the ZSM-5 zeolites [5-6]. The two probe molecules have similar shape to benzene, the main reactant used in the reaction studied in Chapter 3. Therefore, results gained from the PFG studies of these molecules could give an indication of the transport resistance for benzene during the alkylation reaction. In addition, C_6H_{12} has been increasingly used as a substitute for benzene due to the high toxicity level of benzene [7]. In the next section, the experimental set-up and procedure will be described, followed by the discussion of results obtained in this study.

7.3   Experimental Procedure

7.3.1   Nitrogen Sorption

Nitrogen sorption experiments were carried out using a Micromeritics ASAP 2020 volumetric apparatus at 77 K. The experimental procedure for the gas sorption experiment was discussed in detailed in Chapter 4 Section 4.3.5.

7.3.2   PFG NMR Experiments

7.3.2.1   Sample Preparation

Prior to exposing the catalyst to the hydrocarbon liquids, the zeolite catalysts were first heated up to 250 ^{o}C under vacuum condition to remove any physisorbed

species. Then, the catalysts were immersed in the liquid for at least 24 hours. After immersion, the catalysts were removed, and dabbed gently on pre-wetted tissue to remove the excess liquid from the external surface, before placing the catalysts between two susceptibility plugs within a 5 mm diameter NMR tube. A piece of tissue soaked in the hydrocarbon liquid was placed at the top of the NMR tube to maintain the vapour pressure and reduce evaporative loss from the catalysts.
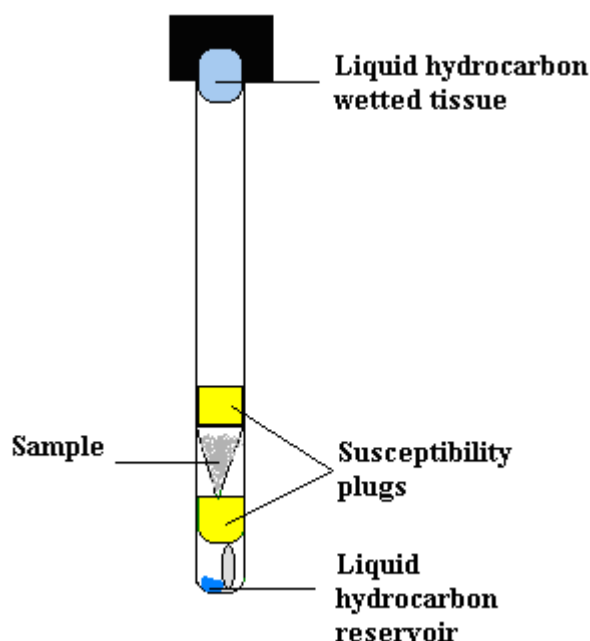
Figure 7.5 – NMR experimental set-up for diffusion measurement

7.3.2.2 PFG Experiments

The PFG NMR experiments were performed on the Bruker Avance 400 MHz spectrometer with static field strength of 9.4 T corresponding to a resonance frequency of 400.13 MHz for ^{1}H nuclei.

PFG experiments were conducted by varying the gradient strength, g in the range of 0.674 to 32.030 G cm^{-1}, while keeping diffusion time, Δ, gradient length, δ, and bipolar correction delay, τ constant. Three different diffusion times, Δ was used in this study; 0.015 s, 0.025 s and 0.05 s. Each experiment had 8 data points, of 16 scans each. Signal attenuation was used to calculate the diffusion coefficient, D_{PFG} and tortuosities, τ_p.

7.4 Results

7.4.1 Nitrogen Sorption

Figures 7.6 and 7.7 compare the nitrogen sorption isotherms of H-ZSM-5(30) and H-ZSM-5(80) catalysts before and after Pt impregnation. Since the total mass of the PtH-ZSM-5 sample includes the mass of H-ZSM-5 as well as the mass of Pt, it is necessary to take into account the Pt content before comparing isotherms of H-ZSM-5 and PtH-ZSM-5 samples. Therefore, the total sorption capacity measured from gas sorption experiments were renormalized to take into account of the mass of Pt on the catalyst.
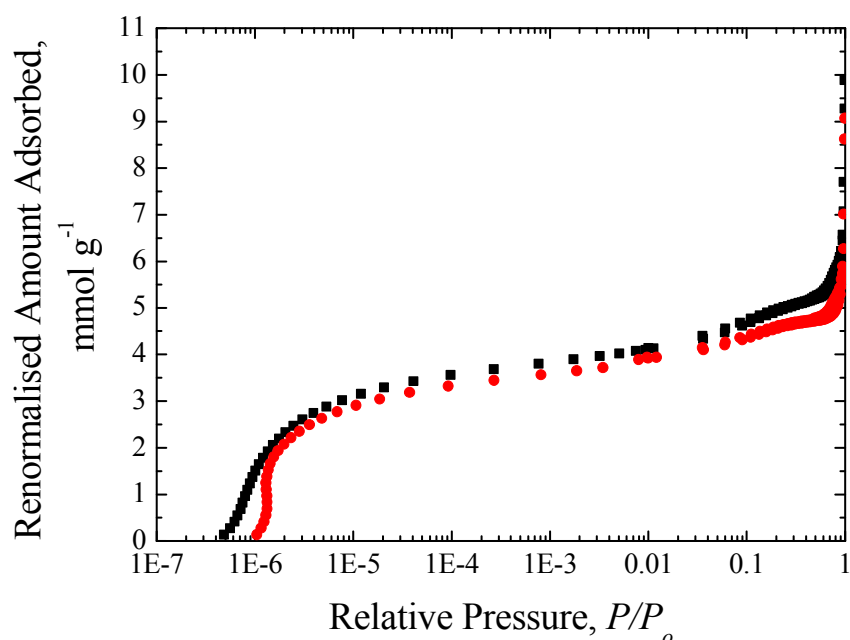
Figure 7.6 – Nitrogen sorption isotherms for H-ZSM-5(30) (-■-) and PtH-ZSM-5(30) (-●-) catalysts

The nitrogen sorption isotherms in Figures 7.6 and 7.7 showed that after the impregnation of Pt, the nitrogen sorption capacity of the PtH-ZSM-5 catalysts decreased when compared with the H-ZSM-5 samples. In Figure 7.7, the changes in the shape of the isotherms at very low relative pressure ($P/P_o \sim 10^{-6}$) may be due to the lower experimental sensitivity at such low pressures, and hence was considered as noise. In order to distinguish between the adsorption in the dual pore system of the zeolite catalyst, the reversible regions of the adsorption isotherms of the H-ZSM-5 and PtH-

ZSM-5 catalysts were fitted to a two-component model comprising of Langmuir and BET components, as described in Chapter 4. From Table 7.1, it can be seen that the ratio of the Langmuir component adsorption capacity parameter showed little change relative to the BET component, after Pt impregnation on the H-ZSM-5(80) catalyst. Contrary to the results for the H-ZSM-5(80) catalyst, a more significant drop was observed for the adsorption capacity ratio for the Langmuir component after the incorporation of Pt on the H-ZSM-5(30) catalyst
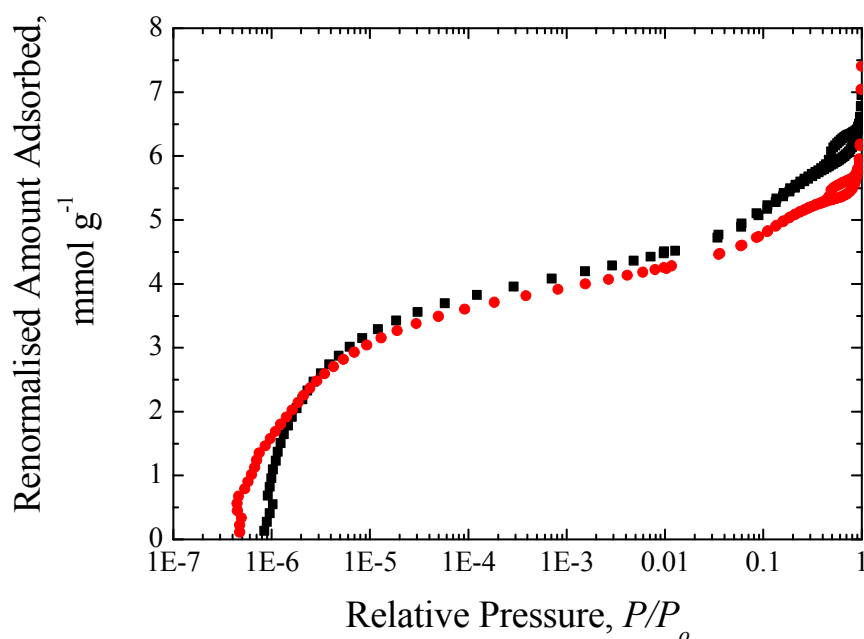
Figure 7.7 – Nitrogen sorption isotherms for H-ZSM-5(80) (-■-) and PtH-ZSM-5(80) (-●-) catalysts

Table 7-1 – Results of Langmuir and BET composite model fit to nitrogen adsorption isotherms for H-ZSM-5 and PtH-ZSM-5 catalysts.
Notes: W/W_o is the ratio of the adsorption capacity parameter of the relevant component, W, for the PtH-ZSM-5 sample, to the corresponding total value, W_o, for the H-ZSM-5 catalyst

W/W_o	H-ZSM-5(30)	PtH-ZSM-5(30)	H-ZSM-5(80)	PtH-ZSM-5(80)
Langmuir	0.80 ± 0.02	0.73 ± 0.02	0.76 ± 0.03	0.73 ± 0.03
BET	0.20 ± 0.02	0.18 ± 0.02	0.24 ± 0.01	0.20 ± 0.01

7.4.2 PFG NMR Results

7.4.2.1 *Determination of bulk diffusivity, D_B of C_6H_{12} and C_8H_{16}*

The plot shows $\ln (I/I_o)$ on the y-axis versus $g^2\gamma^2\delta^2(D-\delta/3-\tau/2)$, $(\times 10^9 \text{ s m}^{-2})$ on the x-axis.

$D_B (C_8H_{16}) = 5.84 \times 10^{-10} \text{ m}^2 \text{ s}^{-1}$

$D_B (C_6H_{12}) = 1.66 \times 10^{-9} \text{ m}^2 \text{ s}^{-1}$
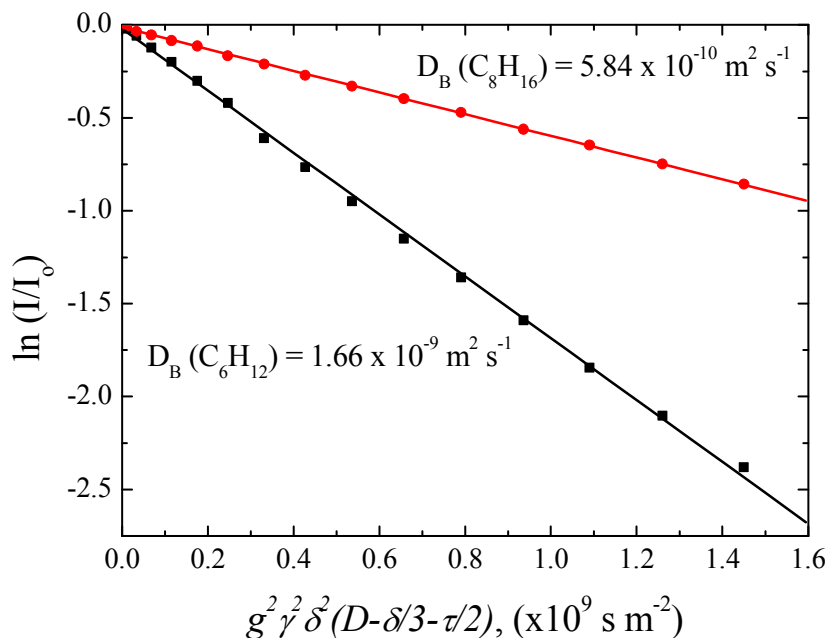
Figure 7.8 – Comparison of log attenuation plot for bulk liquid C_6H_{12} (-■-) and C_8H_{16} (-●-)

Figure 7.8 shows the log attenuation plot for bulk cyclo-hexane (C_6H_{12}) and cyclo-octane (C_8H_{16}). The diffusion coefficient of the bulk liquids was determined from the slope of the graph. The bulk diffusivity of C_6H_{12} was found to be $(1.66 \pm 0.01) \times 10^{-9} \text{ m}^2 \text{ s}^{-1}$, while the bulk diffusivity of C_8H_{16} was calculated to be $(5.84 \pm 0.01) \times 10^{-10} \text{ m}^2 \text{ s}^{-1}$. Previous studies on the sorption of cyclic hydrocarbons found that the diffusivities decrease with increase in the sorbate size/molecular diameter [8-10]. Since C_8H_{16} has a molecular diameter of 0.80 nm [11], and the diameter of C_6H_{12} was reported to be 0.60 nm [12], the difference in their molecular sizes (with C_8H_{16} having a smaller molecular diameter) can explain the lower diffusivity of C_8H_{16} compared with C_6H_{12}.

7.4.2.2 *Molecular size effect on tortuosity of a mesoporous silica pellet (C10)*

The diffusivity of C_6H_{12} and C_8H_{16} when it was imbibed in an industrially supplied sol gel silica pellet (labelled as C10 pellets) is shown in Table 7.2. The C10

pellets are 5 mm in diameter, with surface area of 280 m^2 g^{-1} and BJH median pore size of 10 nm. The PFG-NMR experiments on the C10 pellets were aimed to identify the effect of molecular size of probe molecules on self-diffusion and tortuosity without the influence of the micropore network that are present in zeolite catalysts discussed in the next section.

The motion of a sorbed molecule is much slower than the bulk diffusion in liquid when it is imbibed in a porous material. Due to the restrictions by the pore structure experienced by the molecules, the diffusivity of C_6H_{12} and C_8H_{16} decreased when compared with the bulk diffusivity measured. The fraction of reduction in the diffusivity in comparison with the bulk diffusivity is known as the tortuosity factor, τ_p. It is noted from Table 7.2 that the tortuosity for C_8H_{16} is higher than for C_6H_{12}, possibly due to the bigger molecular size of C_8H_{16} molecule, hindering passage of the molecules through the pore network of the C10 pellet. The results shown are consistent with the previous work of Wood et al. [13] who reported that the tortuosity of pentane is lower than that of heptane due to the smaller molecular size of pentane.

Table 7-2 – Comparison of bulk diffusion coefficient, D_{PFG} of C_6H_{12} and C_8H_{16} in C10 pellets at diffusion time, Δ = 0.05 s

Molecule	D_{PFG} (m^2 s^{-1})	Tortuosity, τ_p
C_6H_{12}	$(1.18 \pm 0.01) \times 10^{-9}$	1.41 ± 0.02
C_8H_{16}	$(3.32 \pm 0.01) \times 10^{-10}$	1.74 ± 0.02

7.4.2.3 Comparison of the PFG NMR results for PtH-ZSM-5(30) and PtH-ZSM-5(80) catalysts

The average distance travelled by the C_6H_{12} and C_8H_{16} molecules during the different observation times was compared with the crystallite and particle sizes of the PtH-ZSM-5 samples. Table 7.3 shows the root mean squared displacement (RMSD) in PtH-ZSM-5(30) and PtH-ZSM-5(80) catalyst. The size of the PtH-ZSM-5 particles is between 250-710 μm (sieve fraction), while the thickness of the particles has an average value of 400 μm. The RMSD travelled by both the C_6H_{12} and C_8H_{16} molecules over the different observation times employed in the PFG experiments is much smaller than the

smallest dimensions of the PtH-ZSM-5 particles (250 μm), and larger than the size of the crystallites (measured from SEM images). Therefore, the diffusing molecules are moving through the void space in between the crystallites.

Table 7-3 – RMSD of C_6H_{12} and C_8H_{16} imbibed within PtH-ZSM-5 catalysts

Sample	Diffusion Time, Δ (s)	RMSD (μm)	
		C_6H_{12}	C_8H_{16}
PtH-ZSM-5(30)	0.015	10.96 ± 0.10	7.24 ± 0.11
	0.025	13.91 ± 0.44	9.17 ± 0.20
	0.050	19.64 ± 0.70	12.94 ± 0.12
PtH-ZSM-5(80)	0.015	11.89 ± 0.11	6.79 ± 0.12
	0.025	15.20 ± 0.33	8.63 ± 0.15
	0.050	21.44 ± 0.45	12.14 ± 0.31
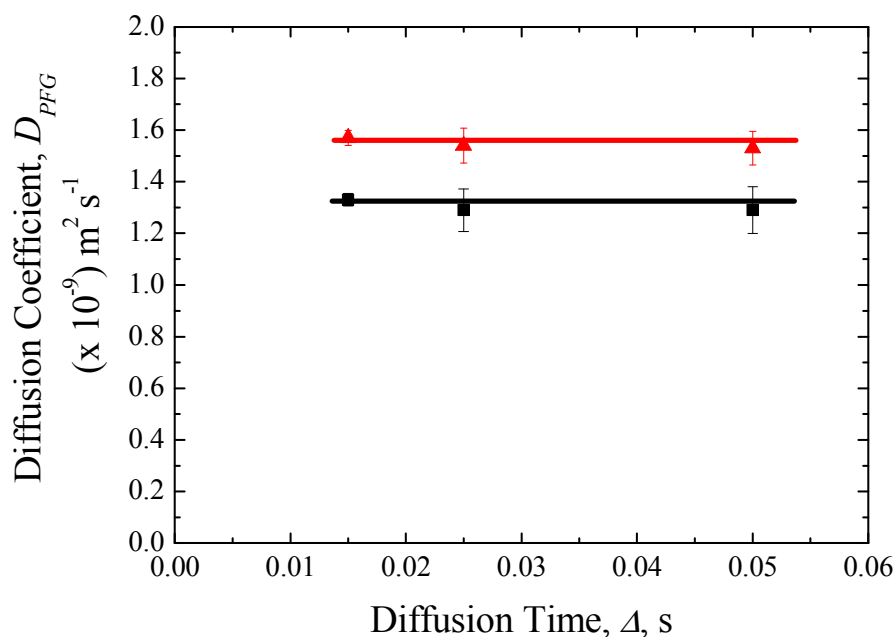
Figure 7.9 – Diffusion coefficient, D_{PFG} of C_6H_{12} imbibed in PtH-ZSM-5(30) (-■-) and PtH-ZSM-5(80) (-▲-) catalysts as a function of diffusion time, Δ
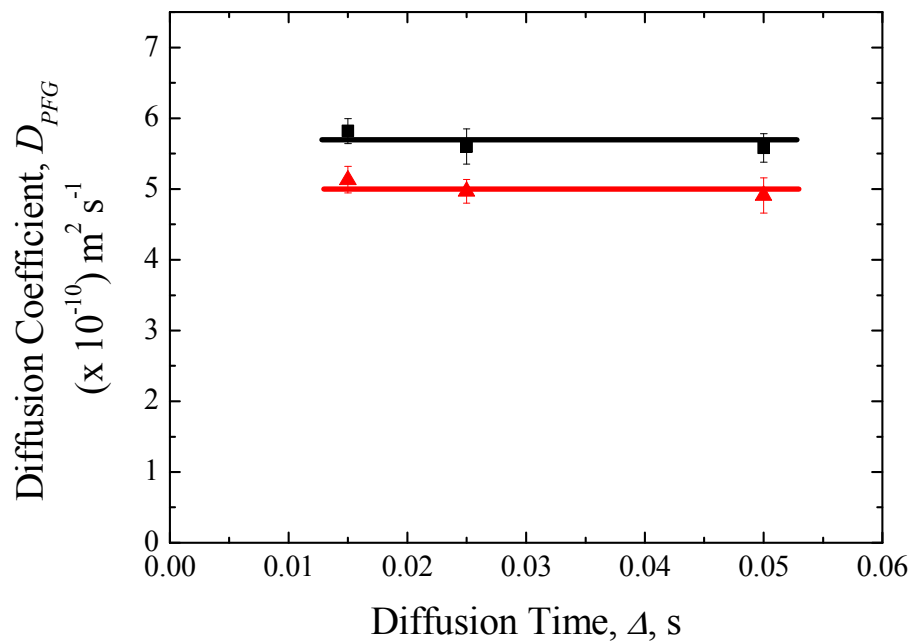
Figure 7.10 – Diffusion coefficient, D_{PFG} of C_8H_{16} imbibed in PtH-ZSM-5(30) (-■-) and PtH-ZSM-5(80) (-▲-) catalysts as a function of diffusion time, Δ
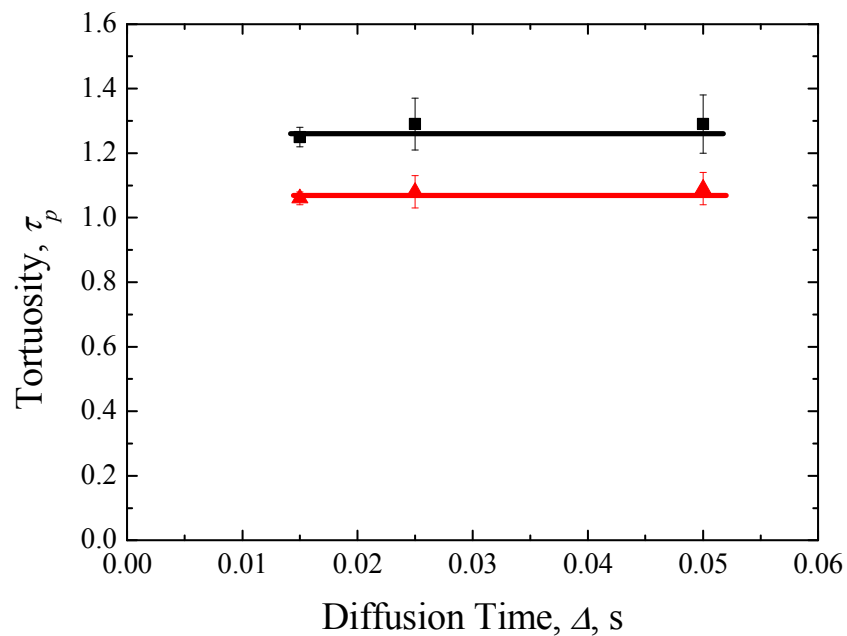
Figure 7.11 – Tortuosity, τ_p of PtH-ZSM-5(30) (-■-) and PtH-ZSM-5(80) (-▲-) catalysts as a function of diffusion time, Δ for C_6H_{12} probe molecules
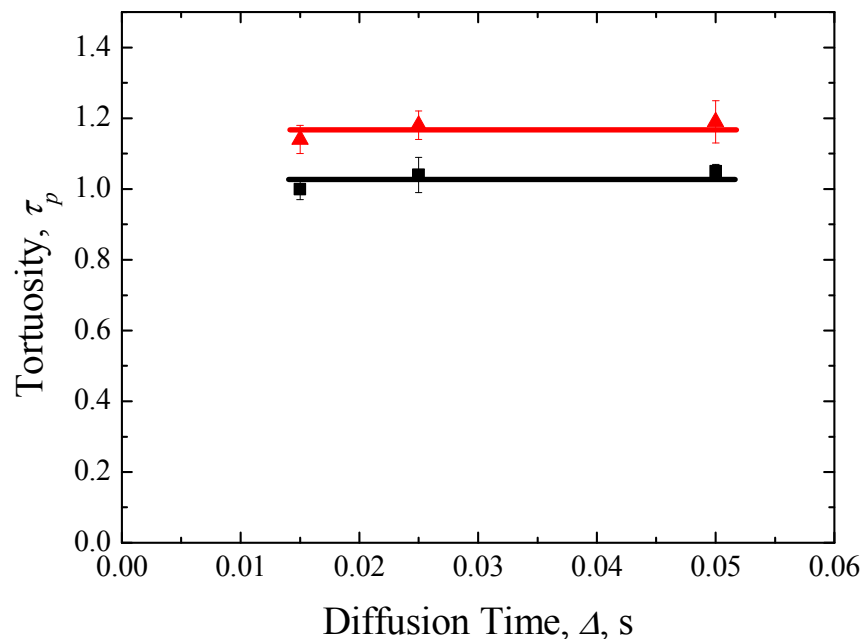
Figure 7.12 – Tortuosity, τ_p of PtH-ZSM-5(30) (-■-) and PtH-ZSM-5(80) (-▲-) catalysts as a function of diffusion time, Δ for C_8H_{16} probe molecules

The variation of self diffusion coefficient, D_{PFG} with diffusion time, Δ of C_6H_{12} and C_8H_{16} molecules when imbibed in the PtH-ZSM-5 samples are illustrated in Figures 7.9 and 7.10. The graphs show that the measured D_{PFG} is independent of the diffusion time, Δ. Therefore, the molecules do not encounter (surface) barriers with increasing diffusion time.

Figures 7.11 and 7.12 compare the tortuosity, τ_p of PtH-ZSM-5(30) and PtH-ZSM-5(80) catalysts measured by C_6H_{12} and C_8H_{16} molecules. When evaluating the effect of molecular size on the diffusion within the PtH-ZSM-5(80) catalyst, the diffusion path was found to be slightly more tortuous for the C_8H_{16} molecules than for the C_6H_{12} molecules, consistent with the results shown in Table 7.2 for C10, a pure mesoporous silica pellet. Contrary to the results obtained for the PtH-ZSM-5(80) catalyst, the tortuosity of PtH-ZSM-5(30) catalyst was found to be higher when C_6H_{12} was imbibed in the catalyst, as opposed to when C_8H_{16} was probing the pore space of the PtH-ZSM-5(30) sample.

7.4.3 Discussion

7.4.3.1 *Effect of Pt impregnation on the pore structure of H-ZSM-5 catalysts*

The adsorption capacity parameters obtained from the Langmuir-BET fit was compared for the PtH-ZSM-5 catalyst of different SiO_2/Al_2O_3 ratio. The change in the ratios of the adsorption capacity parameters gives indication of the location of the metal particle, either within or on the external surface of the crystallites. The decrease in nitrogen sorption capacity in the mesopores, and the more significant reduction in the BET component adsorption capacity parameter for the PtH-ZSM-5(80) catalyst when compared with the Langmuir component, could be due to the deposition of Pt particles on the surface of the zeolite crystallite. This result is consistent with the BSE images shown in Chapter 4, which showed that more Pt particles were present on the surface of the PtH-ZSM-5(80) crystallites. The Pt particles probably block the pore openings on the external surface of the crystallite, hence hindering the access of nitrogen to the interior of the crystallite.

While the adsorption capacity ratio for the BET component remained constant before and after Pt impregnation on the H-ZSM-5(30) catalyst, the Langmuir component adsorption capacity ratio decreased after Pt incorporation. This suggests preferential deposition of Pt particles within the PtH-ZSM-(30) crystallite, as opposed to surface metal deposition for the PtH-ZSM-5(80) catalyst.

7.4.3.2 *Influence of Pt on the transport properties of PtH-ZSM-5 catalysts*

As mentioned earlier, the C_6H_{12} molecules can adsorb in the crystallites of the ZSM-5 catalyst [5] while C_8H_{16} molecules only probe the surface of the zeolite crystallites [5-6] within the mesoporosity. However, the presence of the Pt particles on the surface of the H-ZSM-5(80) crystallites could block the pore openings and hinder the access/diffusion of C_6H_{12} molecules into the crystallites. In that case, the C_6H_{12} molecules only probe the pore space in the intercrystalline regions of the PtH-ZSM-5(80) catalyst, similar to the C_8H_{16} molecule. Since both C_6H_{12} and C_8H_{16} molecule are diffusing in the same regions, the lower diffusivity measured for the C_8H_{16} molecule compared to the diffusivity of C_6H_{12} can be explained by its larger molecular diameter [8-10].

As for the PtH-ZSM-5(30) sample, the diffusion path was more tortuous for C_6H_{12} than it was for C_8H_{16}. Previous studies have shown that the SiO_2/Al_2O_3 ratio does not have a major influence on the heat of adsorption of hydrocarbons in a H-ZSM-5 catalyst [14-15]. Arik et al. [15] reported that the heat of adsorption increased by only 10 kJ mol^{-1} when the SiO_2/Al_2O_3 ratio was increased from 24 to 800. Therefore, the increase in the interaction of hydrocarbons with the pore walls can be assumed to be insignificant when the SiO_2/Al_2O_3 ratio of the PtH-ZSM-5 catalyst was varied from 30 to 80, in our experiments. In addition, Jentys et al. [16] found that the sorption of benzene is controlled by the interaction of the molecule with the pore walls, and that the localized interaction with the bridging hydroxyl group gives rise to only minor energetic contributions. Hence, the tortuosity trend observed for the PtH-ZSM-5(30) catalyst can not be due to the difference in the SiO_2/Al_2O_3 ratio of the catalysts. In order for the C_6H_{12} molecules to experience an increase in tortuosity when probing the pore structure of the PtH-ZSM-5(30), as compared to C_8H_{16} molecules, the C_6H_{12} molecules have to interact stronger on the surface of the PtH-ZSM-5(30) catalyst. Therefore, only if the impregnation of Pt metal with the surface of the PtH-ZSM-5(30) catalyst leads to an enhanced specific interaction for the C_6H_{12} molecule with the surface, and not for the C_8H_{16} molecule, then the effect of Pt impregnation can also be excluded as a possibility for the tortuosity results observed.

For the above reasons, the higher tortuosity experienced by the C_6H_{12} molecules could only be explained by the molecular exchange between intra- and intercrystalline void space of the PtH-ZSM-5(30) catalyst. The C_6H_{12} molecules could adsorb within the crystallites of a H-ZSM-5 catalyst since the Pt particles within the H-ZSM-5(30) crystallites do not hinder the molecular exchange of C_6H_{12} between the dual pore systems of the PtH-ZSM-5(30) catalyst as they did for PtH-ZSM-5(80). The C_6H_{12} molecules could possibly enter the zeolite crystallites, thereby experiencing a higher restriction to diffusion due to more confined geometry in the micropore network. This thus leads to a more tortuous path for the C_6H_{12} molecules, when compared with the tortuosity experienced by the C_8H_{16} molecule that only probes the surface of the PtH-ZSM-5(30) crystallites.

7.4.3.3 *Analysis of the different location of coke deposition during benzene alkylation with ethane over PtH-ZSM-5 catalysts*

The first stage of the alkylation of benzene with ethane is the dehydrogenation of ethane on metal sites. Therefore, the formation of ethene, the product of ethane dehydrogenation could take place on the surface of the PtH-ZSM-5(80) catalyst since Pt particles are present on the surface of the crystallite. The PFG results showed that the Pt particles on the surface of the PtH-ZSM-5(80) sample hindered the accessibility of the C_6H_{12} molecules from going into the micropore network of the catalyst, but not for the PtH-ZSM-5(30) catalyst since the Pt particles are predominantly located within the crystallite for this sample. Therefore, ethene (formed from dehydrogenation of ethane) and benzene, the main reactants for benzene alkylation, would experience more difficulty to enter the micropore network of the PtH-ZSM-5(80) catalyst when compared with PtH-ZSM-5(30). It has been reported that the formation of aromatics could take place over with high metal oxide surface area, with little measurable Brønsted acidity [16]. In addition, carbonaceous species formation catalysed by metal surface has also been reported for catalytic systems without acidic support [17]. If this is the case, ethene formed could possibly undergo oligomerization and aromatization to form bulky aromatics, which could then lead to the formation of coke on the external surface of the crystallite.

Since most Pt particles are located within the crystallites, and the pore openings on the surface of the PtH-ZSM-5(30) was not obstructed by the Pt particles, ethane molecules could diffuse into the crystallite, react on the metal surface to form ethene, and further react with benzene to form ethylbenzene (EB). Side reactions such as oligomerization, aromatization and isomerization could take place within the zeolite crystallite to form coke precursors such as methyl-naphtalene, as proposed by Lukyanov and Vazhnova [18]. Hence, coke formation takes place within the PtH-ZSM-5(30) crystallite, supporting earlier results from gas sorption and diffraction experiments.

7.5 Conclusion

Nitrogen adsorption and PFG results have shown that, after the impregnation process, most Pt particles are located within the micropore network for the PtH-ZSM-5(30) catalyst, while most of the Pt particles are found on the surface of the PtH-ZSM-

5(80) crystallite. The preferential deposition of Pt particle on the surface of the PtH-ZSM-5(80) catalyst was found to block access of C_6H_{12} into the crystallite. As for the PtH-ZSM-5(30) catalyst, molecular exchange of C_6H_{12} with the two pore systems of the catalyst resulted in a higher tortuosity experienced by the C_6H_{12} molecule when compared with the C_8H_{16} molecule that only probes the intercrystalline region of the catalyst.

Explanation for the different location coke deposition for the two PtH-ZSM-5 catalysts was proposed. The Pt particles on the surface of the PtH-ZSM-5(80) crystallite made it more difficult for the reactants to penetrate into the crystallite. Hence, ethene, the product of ethane dehydrogenation on the metal sites on the surface could possibly undergo further reactions on the active sites present on the surface to form bulky aromatics that could lead to coke formation. With Pt particles located within micropore network of the PtH-ZSM-5(30) catalyst, ethane dehydrogenation and benzene alkylation would take place in the crystallite. Side reactions that lead to the formation of large aromatic products could initiate the formation of coke within the crystallite.

7.6   References

[1]   E.O. Stejskal, and J.E. Tanner, The Journal of Chemical Physics 42 (1965) 288-292.

[2]   P.W. Atkins, Atkins' Physical Chemistry Oxford University Press, Oxford, 2002.

[3]   T.D.W. Claridge, High-Resolution NMR Techniques in Organic Chemistry. Pergamon, Amsterdam;Oxford 1999, 382.

[4]   M.P. Hollewand, and L.F. Gladden, Chemical Engineering Science 50 (1995) 309-326.

[5]   Y. Traa, S. Sealy, and J. Weitkamp, in: H.G. Karge, and J. Weitkamp, (Eds.), Characterization II, Springer, Berlin / Heidelberg. 103-154.

[6]   F. Stallman, and J. Karger, Adsorption 5 (1999) 117-133.

[7]   E. Browning, British Journal of Industrial Medicine 16 (1959) 23-39.

[8]   H. Ban, J. Gui, L. Duan, X. Zhang, L. Song, and Z. Sun, Fluid Phase Equilibria 232 (2005) 149-158.

[9]   D.M. Ruthven, and B.K. Kaul, Industrial & Engineering Chemistry Research 32 (1993) 2053-2057.

[10]   C.L. Cavalcante, and D.M. Ruthven, Industrial & Engineering Chemistry Research 34 (1995) 185-191.

[11]   T. Makino, T. Nakamura, T. Sugahara, and K. Ohgaki, Fluid Phase Equilibria 218 (2004) 235-238.

[12]   S. Mitra, V.S. Kamble, A.K. Tripathi, N.M. Gupta, and R. Mukhopadhyay, PRAMANA - Journal of Physics 63 (2004) 443-448.

[13]   J. Wood, and L.F. Gladden, Applied Catalysis A: General 249 (2003) 241-253.

[14]   A.V. Ivanov, G.W. Graham, and M. Shelef, Applied Catalysis B: Environmental 21 (1999) 243-258.

[15]   I.C. Arik, J.F. Denayer, and G.V. Baron, Microporous and Mesoporous Materials 60 (2003) 111-124.

[16]   K.M. Dooley, T.F. Guidry, and G.L. Price, Journal of Catalysis 157 (1995) 66-75.

[17]   M. Guisnet, and P. Magnoux, Applied Catalysis:A General 212 (2001) 83-96.

[18]   D.B. Lukyanov, and T. Vazhnova, Journal of Catalysis 257 (2008) 382-389.

Chapter 8 : Conclusions and Future Work

8.1 Conclusions

A novel multi-technique approach has been shown, in this thesis, to be successful in identifying the coking behaviour of two bifunctional Pt-H-ZSM-5 catalysts (SiO_2/Al_2O_3 = 30 and 80) during benzene alkylation with ethane.

The following points summarise the main findings of the work in this thesis.

1. Activity of PtH-ZSM-5 catalysts

Benzene alkylation with ethane over two Pt-incorporated H-ZSM-5 catalysts was carried out at $370^{\circ}C$. During the alkylation of benzene with ethane over the PtH-ZSM-5(30) catalysts, the conversion of benzene and ethane decreased with TOS as a result of catalyst deactivation. On the other hand, the PtH-ZSM-5(80) catalyst remained stable during the reaction, even with increasing coke content, as determined by thermogravimetric analysis. Due to the higher acidity of the PtH-ZSM-5(30) catalyst, the alkylation of benzene with ethene was enhanced, hence drawing the ethane dehydrogenation forward. As a result, the selectivity to ethene for the PtH-ZSM-5(30) catalyst is lower than that observed for the PtH-ZSM-5(80) catalyst. Benzene conversion over the PtH-ZSM-5(30) catalysts yields conversion higher than the equilibrium conversion. This suggests that benzene was also converted to other side products apart from the transformation of benzene into the desired product, ethylbenzene (EB). When the reaction is carried out over PtH-ZSM-5(30) catalysts, it was observed that the partially deactivated catalysts were more *para*-selective for DEB and xylene isomers than the fresh catalysts. On the contrary, the selectivity of the DEB isomers remained constant with time-on-stream (TOS) when the reaction was catalysed by the PtH-ZSM-5(80) catalysts.

2. Pore Structure Modification of PtH-ZSM-5 Catalysts by Coking during Benzene Alkylation with Ethane

Results from nitrogen, argon and ethane adsorption on the fresh and partially deactivated PtH-ZSM-5 catalysts have illustrated the effect of coke on the catalyst's

pore structure. The difference between the total adsorption capacity for nitrogen, argon and ethane of the fresh and deactivated PtH-ZSM-5 catalysts is believed to be associated with the increasing coke content as TOS increases. The nitrogen and argon isotherm shift observed at low P/P_o has indicated the effect of coke on the pore architecture of the zeolite catalysts. In addition, the shift in the micropore size distribution observed, in the case of the 4 h and 24 h coked PtH-ZSM-5(30) catalysts suggested that more dead-end pores are formed as coke is deposited within the core of the crystallites.

3. *Location of Coke Deposition*

Successful determination of the location of coke deposition during the alkylation reaction of both the PtH-ZSM-5 catalysts has been obtained. Changes in the relative position and intensities of XRD peaks for the PtH-ZSM-5(30) catalysts provided evidence for intracrystalline coking, as opposed to the external location of the coke formed during benzene alkylation over the PtH-ZSM-5(80) catalyst. The nitrogen and argon adsorption data, fitted to a dual-component Langmuir-BET fit has shown to be capable of differentiating coke deposition within the zeolite crystallites and in the intercrystalline regions. The significant drop in the ratio of the BET component adsorption capacity parameter suggested that the mesopores in-between the zeolite crystallites were modified by coke for the PtH-ZSM-5(80) catalysts. The intracrystalline coke deposition proposed by the XRD spectra for the PtH-ZSM-5(30) catalysts was supported by the changes in the ratio of the Langmuir component adsorption capacity parameter with TOS.

4. *Simulation of accessibility and diffusion within PtH-ZSM-5 crystallites*

The Monte Carlo simulations performed have successfully generated the accessibility plot for a ZSM-5 type lattice. The percolation threshold, f_c for a ZSM-5 lattice, assuming random distribution of coke in the channels and intersections was found to be 0.65. Percolation analysis of the nitrogen and argon adsorption data indicated that the random coke distribution inside the zeolite crystallites is incorrect for the PtH-ZSM-5(30) catalyst. This was shown by the still high accessibility of the PtH-ZSM-5(30) pore network to nitrogen and argon even when the percolation threshold for random deposition of coke is reached.

The results from the self-diffusivity simulations showed that, the relationship between the self-diffusivity and molecular occupancy is highly sensitive to the connectivity of a lattice, with a more significant non-linearity effect on lattices with lower connectivity. The intra-crystalline diffusivity was found to decrease with increasing pore blockage, but declined rapidly when the percolation limit is reached.

5. *Effect of coke formation on kinetics and thermodynamic of ethane adsorption*

Analysis of the kinetics data from ethane adsorption experiments has identified changes in the mass transfer coefficient ($k = D/a^2$) with TOS, at a constant amount of ethane adsorbed. The observation of an increase in the MTC with coking is accounted for by a decrease in the length of the diffusion pathway, which is equivalent to an apparent decrease in crystallite size of the zeolite catalysts. The decrease in the diffusion path length but lack of impact on diffusivity is consistent with the preferential deposition of coke towards the centre of the zeolite crystallites, thereby partially blocking the internal pore structure of the zeolite catalysts.

6. *The deactivation behaviour of PtH-ZSM-5 catalysts during benzene alkylation with ethane*

A direct correlation between the structural evolution of the zeolite pore structure as a result of coke deposition, which alters the adsorption kinetics and transport properties, and the product selectivity was achieved in this study.

a. *PtH-ZSM-5(30)*

When alkylation of benzene with ethane was carried out over the PtH-ZSM-5(30) catalysts, the selectivity to *para*-DEB was decreased, while the selectivity to *meta*-DEB was increased, with TOS. The formation of DEB is due to further alkylation reaction of ethylbenzene with ethene on the acid sites of the zeolite catalyst. Due to the steric constraints of the two ethyl groups, *ortho*-DEB was not observed in the product distribution. This finding is rare in comparison with the typical effect of coking, which would enhance the selectivity of *para*- isomers, as the effective channel size of the catalyst is reduced, and the diffusion resistance increased, with coke deposition [1].

Kaeding [2] showed that, when the alkylation or disproportionation of ethylbenzene was carried out over large crystals of ZSM-5 zeolites, the selectivity to *para*-DEB isomer was enhanced as a result of increasing diffusional pathlength [2]. When the diffusion path length is increased, the DEB isomers would then have to travel a long distance before they left the crystallites. Therefore, in a restricted pore network like in the ZSM-5 type zeolite, the formation of *para*-DEB would be favoured.

Results from the accessibility study suggested that coke molecules were initially formed in the core of the crystallites, and when the coke content was increased, these coke molecules block the channels and intersections in such a way that the coke was progressively building up from the middle of the structure, moving outwards to the crystal surface, hence decreasing the diffusion length of the zeolite crystallites. The increase in the MTC with TOS also indicated that the diffusion pathway of the zeolite crystallites was decreased as a result of coking. Therefore, the observed increasing selectivity to *meta*-DEB with TOS in this work could be due to the effect of coke, decreasing the diffusion pathway within the zeolite crystallite. As a result, *meta*-DEB did not isomerize to form *para*-DEB (Equation 8.1) in the pores of the zeolite catalyst.

$$(8\text{-}1)$$
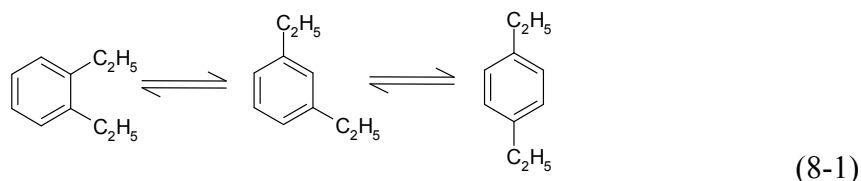
As for the variation of the xylene isomers distribution with TOS, the deactivated catalysts, which have smaller diffusion length, are always less *para*-selective than the fresh Pt-modified H-ZSM-5(30) catalyst. The relationship between the xylene isomers selectivity with TOS shows that the *ortho*-xylene selectivity was increasing at the expense of the *meta*- + *para*- xylene selectivity. This result was consistent with previous research on toluene alkylation with methanol by Sotelo et al. [3], who suggested that the pore blockage by coke molecules lead to a decrease in the diffusion pathway length, thus decreasing the *para*-selectivity of the xylene isomers.

b. PtH-ZSM-5(80)

As opposed to the effect of coke seen on the PtH-ZSM-5(30) catalysts, the coking phenomenon had no effect on the shape selectivity reactions when the reaction was carried out with the PtH-ZSM-5(80) catalysts. The selectivity to DEB isomers did not change with TOS, as shown in Figure 3.18 in Chapter 3. It was proposed that the

deposition of coke within the zeolite crystallites and the reduction of the diffusion length of the PtH-ZSM-5(30) catalyst were responsible for the changes in the selectivity of different isomers with TOS.

For the PtH-ZSM-5(80) catalyst, no evidence of coke deposition in the internal pore structure of the zeolite crystallites was found. The changes in the ratios of adsorption capacity parameters, from the Langmuir-BET adsorption fits, with TOS suggested that the deposition of coke on PtH-ZSM-5(80) catalyst was dominated by pore blockage, where the entrance to the zeolite channels was blocked by coke forming on the outside of zeolite crystallites. The diffraction spectra also indicated that no deformation of the zeolite framework was detected with increasing coke content. In addition, the diffusion pathlength of the PtH-ZSM-5(80) catalyst remained long with TOS when compared to the PtH-ZSM-5(30) catalyst, as demonstrated by the larger MTC for the PtH-ZSM-5(30) catalyst. As a result, no variations in the DEB isomers with TOS were observed.

7. *Spatial distribution of Pt metal on PtH-ZSM-5 catalysts*

The spatial distribution of Pt particles has been successfully identified by nitrogen adsorption and electron microscopy images. BSE images of the crystallite surface indicated that the concentration of surface Pt particle was higher on the PtH-ZSM-5(80) catalyst than on the PtH-ZSM-5(30) sample. The drop in the BET component adsorption capacity parameter for the PtH-ZSM-5(80) catalyst when compared with that of the H-ZSM-5(80) catalyst confirmed the location of Pt metal on the crystallite surface, hence reducing the N_2 adsorption capacity in the mesopore region. The intracrystalline location of Pt particles for the PtH-ZSM-5(30) catalyst was suggested by the significant drop in the ratio of the Langmuir component adsorption capacity parameter, as compared to the BET component.

PFG-NMR results have shown the effect of Pt location on the diffusivities of C_6H_{12} and C_8H_{16} probe molecules imbied in the PtH-ZSM-5 catalysts. The Pt particles on the surface of the PtH-ZSM-5(80) surface hindered the accessibility of C_6H_{12} molecule into the crystallite. Therefore, similar to C_8H_{16}, C_6H_{12} only probes the pore space in between the PtH-ZSM-5(80) crystallites. As a result of intracrystalline deposition of Pt metal, C_6H_{12} can migrate between the two regions of the zeolite pore network as the Pt particles are not blocking access to the micropore network of the PtH-

ZSM-5(30) catalyst, as it did for the PtH-ZSM-5(80) sample. Molecular exchange of C_6H_{12} was indicated by the increase in tortuosity experienced by C_6H_{12} molecules when compared with C_8H_{16} molecules.

8. *Analysis of the different locations of coke deposition for the PtH-ZSM-5(30) and PtH-ZSM-5(80) catalysts*

A proposal to explain the different spatial distribution of coke observed during benzene alkylation with ethane over the two PtH-ZSM-5 catalysts was put forward in this study.

a. *PtH-ZSM-5(30)*

Intracrystalline coking phenomenon that took place when the reaction was carried out over the PtH-ZSM-5(30) catalyst could be explained by the preferential deposition of Pt metal within the zeolite crystallite. Ethane dehydrogenation proceeds on the Pt sites within the crystallite to form ethene, which will then react with benzene on the acid sites to form ethylbenzene. Further conversions over the active sites lead to coke formation within the PtH-ZSM-5(30) crystallite.

b. *PtH-ZSM-5(80)*

As a result of the deposition of Pt particles on the crystallite surface, the dehydrogenation of ethane and alkylation of benzene took place on the surface of the crystallites when the reaction was carried out over the PtH-ZSM-5(80) catalysts. The Pt particles block the pore openings on the external surface of the crystallite, making it more difficult for ethene and benzene to penetrate into the micropore network. Hence, further reactions such as oligomerization, alkylation, and aromatization proceed on the surface of the crystallites. The formation of bulky aromatic molecules from these reactions initiates the coking process in the intercrystalline region of the PtH-ZSM-5(80) catalyst.

8.2 Future Work

The combination of experimental techniques and simulation studies contained in this work has been proven to yield valuable information on the deactivation mechanism

of a zeolite catalyst. In this section, the possible ideas for further developments in this area are considered.

1. Effect of metal/acid balance in PtH-ZSM-5 catalysts on the alkylation of benzene with ethane

In the current study, the metal loading was kept constant at 1 wt%, but the two PtH-ZSM-5 catalysts have different acidity. The balance between the acid and metal site density is an important factor that determines the reactivity of a bifunctional catalyst, and the selectivity of the products. Hence, it would be useful to investigate the influence of the metal/acid balance on the performance of the zeolite catalyst in the benzene alkylation reaction.

a. Acidity measurement of PtH-ZSM-5 catalysts

The acidity of PtH-ZSM-5 catalysts can be measured by employing the FTIR technique. However, in order to determine the distribution of acid sites on the external and internal surface, suitable probe molecules have to be used. The acid sites located on the external surface can be characterised by large probe molecule such as di-tert-butyl-pyridine (DTBPy) [4], while ammonia and pyridine can be used to probe the total acidity of the catalyst [5].

b. Pt distribution on the PtH-ZSM-5 catalysts

In order to determine the amount of interzeolite and intrazeolite Pt particles, a combination of nonane pre-adsorption and H_2 or CO chemisorption characterisation method was proposed. The PtH-ZSM-5 samples will first be exposed to nonane, so that the micropores are completely filled with nonane, and then followed by chemisorption experiment. This method will allow the determination of interzeolite Pt particle since H_2 or CO only interacts with Pt metal on the external surface of the zeolite crystallites.

2. Effect of coke formation on the acidic properties of PtH-ZSM-5 catalysts

The two PtH-ZSM-5 zeolites have different number of acid sites, with the PtH-ZSM-5(30) catalyst having greater number of acid sites when compared with the PtH-ZSM-5(80) catalyst. The number and strength of acid sites in a catalyst are important

parameters that can influence the activity and product selectivity in various hydrocarbon transformation reactions [6]. By carrying out IR spectroscopy and calorimetric measurements on the fresh and coked catalysts, the changes in the total acidity and acid strength distribution as a function of TOS can be determined. In addition, the chemical identity and nature of coke components can also be identified by the IR technique. Analysis of the product distribution with the acidity properties of the catalyst could give a better understanding of the catalyst deactivation phenomenon.

8.3 References

[1]   X. Lin, Y. Fan, G. Shi, H. Liu, and X. Bao, Energy and Fuels 21 (2007) 2517-2524.

[2]   W.W. Kaeding, Journal of Catalysis 95 (1985) 512-519.

[3]   J.L. Sotelo, M.A. Uguina, J.L. Valverde, and D.P. Serrano, Applied Catalysis A: General 114 (1994) 273-285.

[4]   A. Corma, V. Fornes, L. Forni, F. Marquez, J. Martinez-Triguero, and D. Moscotti, Journal of Catalysis 179 (1998) 451-458.

[5]   R.W. Weber, J.C.Q. Fletcher, K.P. Moller, and C.T. O'Connor, Microporous Materials 7 (1996) 15-25.

[6]   S.K. Sahoo, N. Viswanadham, N. Ray, J.K. Gupta, and I.D. Singh, Applied Catalysis A: General 205 (2001) 1-10.

Appendix

A1 – Gas Chromatogram (GC) Analysis

A1-1 – Typical chromatogram of chemical components detected by TCD
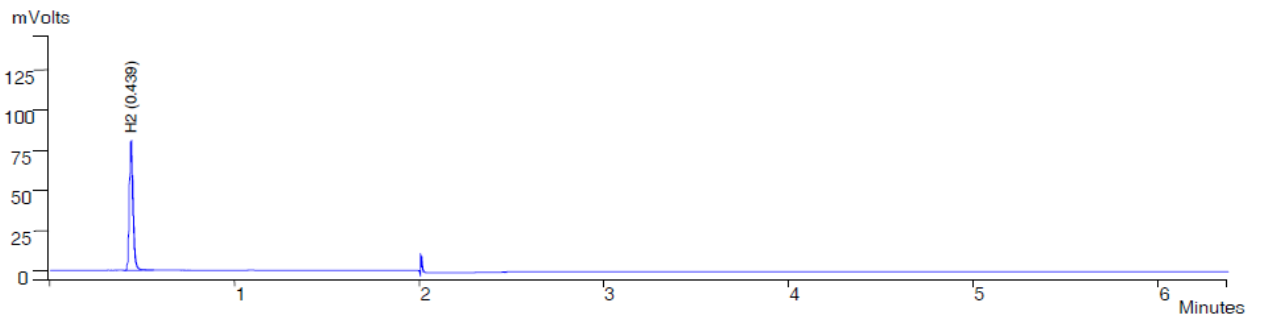
A1-2 – Typical chromatogram of chemical components detected by FID
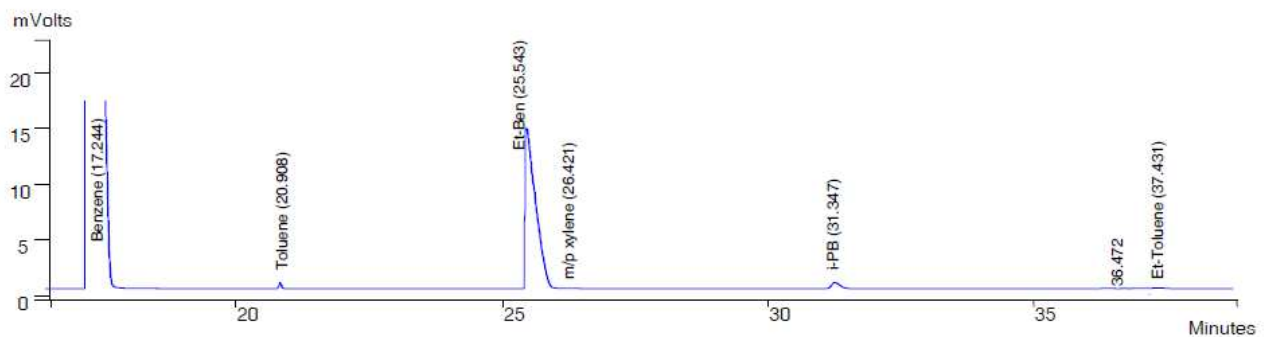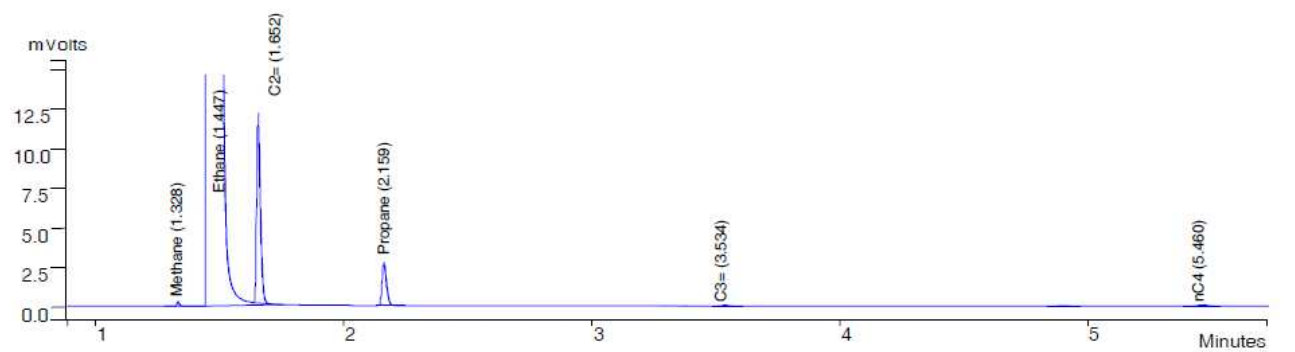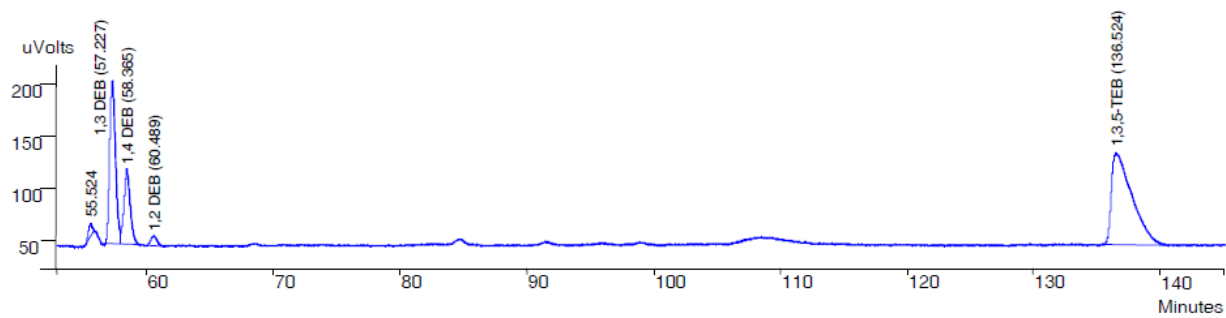
A2 – Thermodynamic Calculations

A2-1 – Benzene Alkylation with Ethane

$$C_6H_6 + C_2H_6 \rightarrow C_6H_5(C_2H_5) + H_2$$
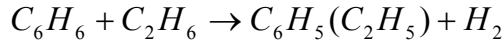
Thermodynamics data at 298 K, Cp/R = a+bT+cT^2+d/T^2 (Yaw, 1992):

Components	Enthalpy, ΔH (J mol^{-1})	Entropy, ΔS (J mol^{-1} K^{-1})	a	b	c	d
Ethane	-84000	229.2	1.131	0.0192	-5.6E-06	-
Benzene	82880	269.3	-0.206	0.0391	-1.3E-05	-
EB	29920	360.63	1.124	0.0554	-1.8E-05	-
Hydrogen	0	130.7	3.249	0.0004	-	8.3E-07
Ethene	29920	360.63	1.424	0.0144	-4.4E-06	-

$$\Delta H_{298} = \Delta H_{EB} + \Delta H_{H2} - \Delta H_{C2} - \Delta H_{Ben}$$
$$= \underline{31040 \ J \ mol^{-1}}$$

$$\Delta S_{298} = \Delta S_{EB} + \Delta S_{H2} - \Delta S_{C2} - \Delta S_{Ben}$$
$$= \underline{-7.17 \ J \ mol^{-1} K^{-1}}$$

$$\Delta H_{643} = \Delta H_{298} + CpdT$$
$$= \Delta H_{298} + \int_{298}^{643} (a + bT + cT^2 + \frac{d}{T^2} dT) \times R$$
$$= \underline{37829 \ J \ mol^{-1}}$$

$$\Delta S_{643} = \Delta S_{298} + \frac{Cp}{T} dT$$
$$= \Delta S_{298} + \int_{298}^{643} (\frac{a}{T} + b + cT + \frac{d}{T^3} dT) \times R$$
$$= \underline{8.78 \ J \ mol^{-1} K^{-1}}$$

The Gibbs free energy of reaction at 370°C

$$\Delta G_{643} = \Delta H_{643} - T\Delta S_{643}$$
$$= 37718 - (643 \times 8.78)$$
$$= \underline{32181.35 \ J \ mol^{-1}}$$

The equilibrium constant of reaction at 370°C

$$\ln K_P = \frac{-\Delta G_r}{RT_r}$$
$$= \frac{-32181.35}{8.314 \times 643}$$
$$= \underline{-6.02}$$

$$K_p = \underline{2.42 \times 10^{-3}}$$

The equilibrium conversion of benzene

$$X_{Ben} = \underline{13.2\%}$$

A2-2 – Ethane Dehydrogenation
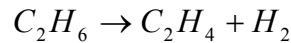
$$C_2H_6 \rightarrow C_2H_4 + H_2$$

$$\Delta H_{298} = \Delta H_{C2=} + \Delta H_{H2} - \Delta H_{C2}$$
$$= \underline{136400 \ J \ mol^{-1}}$$

$$\Delta S_{298} = \Delta S_{C2=} + \Delta S_{H2} - \Delta S_{C2}$$
$$= \underline{120.8 \ J \ mol^{-1} K^{-1}}$$

$$\Delta H_{643} = \Delta H_{298} + CpdT$$
$$= \Delta H_{298} + \int_{298}^{643} (a + bT + cT^2 + \frac{d}{T^2} dT) \times R$$
$$= \underline{141384 \ J \ mol^{-1}}$$

$$\Delta S_{643} = \Delta S_{298} + \frac{Cp}{T} dT$$

$$= \Delta S_{298} + \int_{298}^{643} (\frac{a}{T} + b + cT + \frac{d}{T^3} dT) \times R$$

$$= \underline{133.96 \ J \ mol^{-1} K^{-1}}$$

The Gibbs free energy of reaction at 370°C

$$\Delta G_{643} = \Delta H_{643} - T\Delta S_{643}$$
$$= 141384 - (643 \times 133.96)$$
$$= \underline{55251.32 \ J \ mol^{-1}}$$

The equilibrium constant of reaction at 370°C

$$\ln K_P = \frac{-\Delta G_r}{RT_r}$$
$$= \frac{-55251.32}{8.314 \times 643}$$
$$= \underline{-10.34}$$

$$K_p = \underline{3.21 \times 10^{-5}}$$

The equilibrium conversion of ethane

$$X_{C2} = \underline{0.52\%}$$

A3 – Alkylation of Benzene with Ethane Experimental Data

A3-1 – Concentration of products (mol %) produced over PtH-ZSM-5(30) catalyst at 370°C

Conversion of ethane-benzene over 1%PtHZSM5(30) catalyst at 370°C.

Feed: 90mol% ethane, 10mol% Benzene

Comments: cat. weight = 0.5002 g

Feed flowrate = Ethane 16 ml/min

Experiment	5.0000	5001.0000	5002.0000	5003.0000	5004.0000	5005.0000	5006.0000	5007.0000
Temper.,°C	370	0	370	370	370	370	370	370
Tsat, oC	20.0	0.0	20.0	20.0	19.5	19.5	19.5	20.0
TOS, h	1.02	8.02	15.03	22.03	29.05	36.07	43.07	48.07
WHSV, h-1	3.10	3.02	3.02	3.04	3.06	3.06	3.06	3.02
Cont.time,h	0.3226	0.3311	0.3311	0.3289	0.3268	0.3268	0.3268	0.3311
Conv. C2	6.623	4.718	3.989	3.519	3.249	3.000	2.765	2.644
Conv Benz	20.470	18.685	18.089	16.078	14.862	14.241	14.730	13.765
S1(E+B=EB)	6.36	10.46	12.53	15.37	17.36	19.24	21.35	22.54
S2(B=EB)	37.19	51.89	59.66	67.34	71.97	75.54	78.73	80.35
S3(C2=)	0.83	1.30	1.70	2.00	2.21	2.83	2.75	2.81
S4 (H2)	16.13	21.60	22.71	25.00	26.64	29.11	30.22	31.92
Yield Et-Benz	7.612	9.695	10.793	10.827	10.696	10.758	11.597	11.061
H2	1.6616	1.5731	1.3949	1.3697	1.3460	1.3712	1.3166	1.3377
C1	5.9986	3.5477	2.8233	2.2996	1.9799	1.6594	1.4249	1.2795
C2	82.7555	86.1455	87.8619	87.8711	87.8311	87.9364	88.6850	88.3161
C2=	0.0850	0.0948	0.1042	0.1094	0.1118	0.1332	0.1196	0.1178
C3	0.7306	0.5517	0.4852	0.4109	0.3610	0.3157	0.2840	0.2537
C3=	0.0138	0.0111	0.0105	0.0094	0.0085	0.0075	0.0071	0.0062
i-C4	0.0182	0.0139	0.0123	0.0102	0.0091	0.0079	0.0071	0.0064
n-C4	0.0240	0.0195	0.0181	0.0163	0.0152	0.0142	0.0136	0.0129
trans -C4=	0.0012	0.0010	0.0009	0.0009	0.0008	0.0008	0.0008	0.0000
1-C4=	0.0000	0.0000	0.0000	0.0000	0.0000	0.0000	0.0000	0.0000
iso-C4=	0.0022	0.0018	0.0017	0.0016	0.0015	0.0014	0.0014	0.0013
cis-C4=	0.0000	0.0000	0.0000	0.0000	0.0000	0.0000	0.0000	0.0000
C5	0.0011	0.0008	0.0007	0.0000	0.0000	0.0000	0.0000	0.0000
16.1000	0.0000	0.0000	0.0000	0.0000	0.0000	0.0000	0.0000	0.0000
Benzene	6.9463	6.5707	5.9966	6.6509	7.1159	7.3528	6.9582	7.4929
Toluene	0.9164	0.5058	0.3510	0.2823	0.2244	0.1862	0.1539	0.1338
Et-Benzene	0.6552	0.7619	0.7694	0.8418	0.8774	0.9061	0.9303	0.9445
m/p Xylene	0.0496	0.0259	0.0181	0.0132	0.0101	0.0081	0.0071	0.0060
o-Xylene	0.0130	0.0073	0.0054	0.0038	0.0029	0.0024	0.0021	0.0017
iPB	0.0066	0.0093	0.0108	0.0118	0.0130	0.0138	0.0148	0.0150

PB	0.0025	0.0020	0.0018	0.0016	0.0016	0.0014	0.0013	0.0011
Et-Toluene	0.0733	0.0760	0.0665	0.0495	0.0442	0.0388	0.0293	0.0311
A	0.0052	0.0037	0.0027	0.0017	0.0015	0.0008	0.0012	0.0005
B	0.0087	0.0117	0.0086	0.0066	0.0072	0.0058	0.0055	0.0051
1,3-DEB	0.0057	0.0093	0.0110	0.0101	0.0118	0.0127	0.0137	0.0140
1,4-DEB	0.0039	0.0052	0.0054	0.0049	0.0055	0.0060	0.0068	0.0069
1,2-DEB	0.0000	0.0000	0.0000	0.0000	0.0000	0.0000	0.0000	0.0000
C	0.0000	0.0085	0.0080	0.0000	0.0000	0.0000	0.0000	0.0000
TEB	0.0217	0.0417	0.0309	0.0228	0.0196	0.0173	0.0156	0.0158
SUM DEB	0.0096	0.0145	0.0164	0.0150	0.0172	0.0187	0.0206	0.0209
SUM Xyl	0.0626	0.0332	0.0235	0.0170	0.0130	0.0105	0.0092	0.0077
Total	100.0000	100.0000	100.0000	100.0000	100.0000	100.0000	100.0000	100.0000

A3-2 – Concentration of products (mol %) produced over PtH-ZSM-5(80) catalyst at 370°C

Conversion of ethane-benzene over 1%PtHZSM5(80) catalyst at 370°C.

Feed: 90mol% ethane, 10mol% Benzene

Comments: cat. weight = 0.5002 g

Feed flowrate = Ethane 16 ml/min

Experiment	3.0000	3001.0000	3002.0000	3003.0000	3004.0000	3005.0000	3006.0000	3007.0000
Temper.,°C	370	0	370	370	370	370	370	370
Tsat, oC	20.0	0.0	20.0	19.5	20.0	20.0	19.5	20.0
TOS, h	1.12	8.13	15.15	22.17	29.17	36.18	43.20	48.00
WHSV, h-1	3.10	3.30	3.30	3.20	3.12	3.16	3.18	3.14
Cont.time,h	0.3226	0.3030	0.3030	0.3125	0.3205	0.3165	0.3145	0.3185
Conv. C2	2.436	1.822	1.569	1.445	1.390	1.336	1.294	1.332
Conv Benz	10.473	11.035	10.728	10.320	10.472	10.270	10.149	10.045
S1(E+B=EB)	16.96	26.53	30.32	32.88	34.54	36.00	35.96	37.68
S2(B=EB)	73.28	83.84	87.52	90.18	91.20	92.42	93.19	93.86
S3(C2=)	3.77	4.81	5.32	5.53	5.81	6.02	6.16	5.93
S4 (H2)	31.12	41.43	46.36	49.18	50.65	51.33	52.78	52.20
Yield Et-Benz	7.675	9.252	9.390	9.307	9.551	9.491	9.458	9.429
H2	1.2039	1.2520	1.2597	1.2656	1.2629	1.2364	1.2571	1.2599
C1	1.2831	0.4978	0.2601	0.1487	0.0820	0.0433	0.0208	0.0100
C2	88.3534	89.1150	89.3214	89.1588	89.3171	89.2837	89.3740	88.8008
C2=	0.1458	0.1455	0.1444	0.1423	0.1449	0.1449	0.1466	0.1430
C3	0.3106	0.1510	0.0965	0.0677	0.0508	0.0394	0.0330	0.0285
C3=	0.0090	0.0047	0.0030	0.0021	0.0017	0.0013	0.0012	0.0000
i-C4	0.0061	0.0040	0.0031	0.0024	0.0019	0.0014	0.0011	0.0010
n-C4	0.0127	0.0098	0.0081	0.0064	0.0052	0.0039	0.0029	0.0022
trans -C4=	0.0009	0.0000	0.0000	0.0000	0.0000	0.0000	0.0000	0.0000
1-C4=	0.0000	0.0000	0.0000	0.0000	0.0000	0.0000	0.0000	0.0000
iso-C4=	0.0016	0.0012	0.0009	0.0000	0.0000	0.0000	0.0000	0.0000
cis-C4=	0.0000	0.0000	0.0000	0.0000	0.0000	0.0000	0.0000	0.0000
C5	0.0000	0.0000	0.0000	0.0000	0.0000	0.0000	0.0000	0.0000
16.1000	0.0000	0.0000	0.0000	0.0000	0.0000	0.0000	0.0000	0.0000
Benzene	7.7778	7.8627	7.9613	8.2677	8.1894	8.3076	8.2442	8.7855
Toluene	0.1755	0.0829	0.0542	0.0373	0.0260	0.0177	0.0120	0.0089
Et-Benzene	0.6561	0.8019	0.8240	0.8462	0.8612	0.8670	0.8565	0.9096
m/p Xylene	0.0038	0.0020	0.0015	0.0011	0.0009	0.0006	0.0005	0.0005
o-Xylene	0.0011	0.0006	0.0005	0.0000	0.0000	0.0000	0.0000	0.0000
iPB	0.0109	0.0173	0.0185	0.0193	0.0201	0.0203	0.0205	0.0215
PB	0.0018	0.0009	0.0005	0.0000	0.0000	0.0000	0.0000	0.0000
Et-Toluene	0.0187	0.0111	0.0112	0.0087	0.0079	0.0066	0.0039	0.0036
A	0.0000	0.0000	0.0000	0.0000	0.0000	0.0000	0.0000	0.0000

B	0.0024	0.0019	0.0009	0.0000	0.0000	0.0000	0.0000	0.0000
1,3-DEB	0.0071	0.0112	0.0111	0.0115	0.0123	0.0120	0.0122	0.0122
1,4-DEB	0.0038	0.0053	0.0060	0.0052	0.0057	0.0062	0.0061	0.0064
1,2-DEB	0.0000	0.0007	0.0000	0.0000	0.0006	0.0000	0.0005	0.0005
C	0.0000	0.0000	0.0000	0.0000	0.0000	0.0000	0.0000	0.0000
TEB	0.0140	0.0207	0.0132	0.0092	0.0096	0.0077	0.0069	0.0060
SUM DEB	0.0109	0.0171	0.0171	0.0166	0.0187	0.0182	0.0187	0.0191
SUM Xyl	0.0049	0.0026	0.0019	0.0011	0.0009	0.0006	0.0005	0.0005
Total	100.0000	100.0000	100.0000	100.0000	100.0000	100.0000	100.0000	100.0000
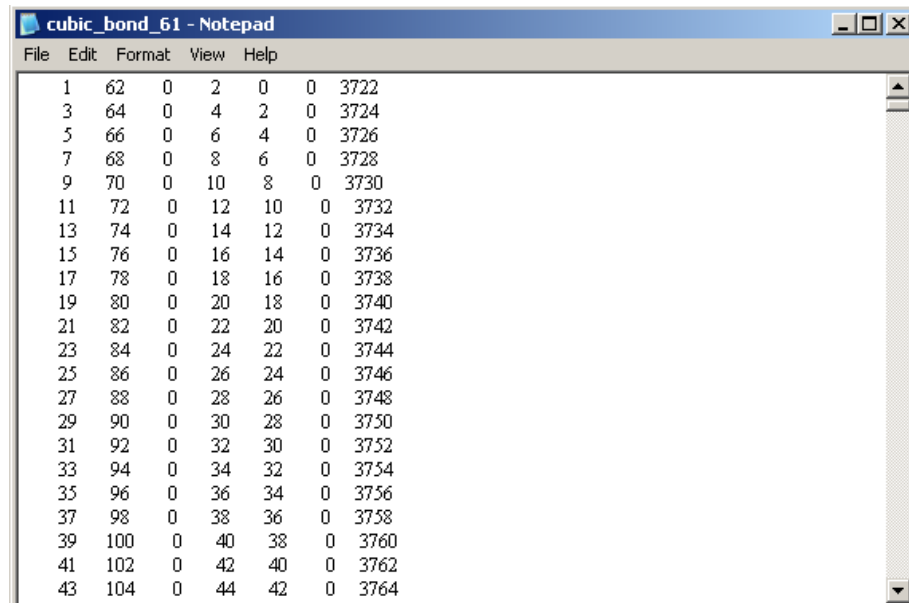
A4 – Fortran Programming

The FORTRAN codes given in Appendix A4-1, A4-2, A4-3 and A4-4 were written as part of the PhD thesis.

The accessibility and self-diffusivity study can be performed by following the steps given:

1. Generating a cubic lattice
   a. Open the file PROGRAM Cubic_structure (A1-1)
   b. Input the number of LATSIDE required
   c. State the number of LATSIZE (LATSIZE=LATSIDE^3)
   d. Run PROGRAM Cubic_structure
   e. The file generated will be stored in the same folder as the program file.
   f. The output appears similar to the diagram shown :

```
cubic_bond_61 - Notepad
File  Edit  Format  View  Help
  1     62    0    2     0    0    3722
  3     64    0    4     2    0    3724
  5     66    0    6     4    0    3726
  7     68    0    8     6    0    3728
  9     70    0   10     8    0    3730
 11     72    0   12    10    0    3732
 13     74    0   14    12    0    3734
 15     76    0   16    14    0    3736
 17     78    0   18    16    0    3738
 19     80    0   20    18    0    3740
 21     82    0   22    20    0    3742
 23     84    0   24    22    0    3744
 25     86    0   26    24    0    3746
 27     88    0   28    26    0    3748
 29     90    0   30    28    0    3750
 31     92    0   32    30    0    3752
 33     94    0   34    32    0    3754
 35     96    0   36    34    0    3756
 37     98    0   38    36    0    3758
 39    100    0   40    38    0    3760
 41    102    0   42    40    0    3762
 43    104    0   44    42    0    3764
```

2. Generating a ZSM-5 lattice
   a. Open the file PROGRAM ZSM_5structure (A1-2)
   b. Input the number of LATSIDE required
   c. State the number of LATSIZE (LATSIZE=LATSIDE^3)
   d. Run PROGRAM ZSM_5structure
   e. The file generated will be stored in the same folder as the program file.
   f. The output appears similar to the diagram shown :

3. Accessibility Analysis

    a. Open the file PROGRAM MC_ZSM_ACCESSIBILITY (A1-3)

    b. Copy the cubic lattice or ZSM-5 lattice file generated (from Step 1 or 2) in the same folder as the PROGRAM MC_ZSM_ACCESSIBILITY

    c. Input LATSIDE, LATSIZE and number of COL and ROW based on the file generated (cubic/ZSM-5) lattice.

    d. Calculate the total volume of straight channel (VS), zig-zag channel (VZ) and intersection (VI) for the ZSM-5 lattice generated.

    e. Set the total volume of coke (VC), then calculate the amount of coke in the straight channel (VCS), zig-zag channel (VCZ), and intersection (VCI) based on the probability weighted by their volumes in the real zeolite.

    f. Run PROGRAM MC_ZSM_ACCESSIBILITY

    g. Repeat step (d) with different volumes of coke.

4. Random Walk

    a. Open the file PROGRAM MC_CUBIC_DSELF (A1-4)

    b. Copy the ZSM-5 lattice file generated (from Step 2) in the same folder as the PROGRAM MC_ZSM_ACCESSIBILITY

    c. Input the number of LATSIDE required

    d. State the number of LATSIZE (LATSIZE=LATSIDE^3)

e. Set a value for INOM (between 20 – LATSIZE), and calculate THETA (THETA=INOM/LATSIZE)

f. Run PROGRAM MC_CUBIC_DSELF

g. Repeat step (d) with different INOM to cover the range of 0≤THETA≤1

A4-1 – Cubic Lattice Generation

```
PROGRAM Cubic_structure

!adsorption sites taken to be on alpha and beta sites
   IMPLICIT NONE

INTEGER                         I,IR,J,K,DJ,SLICE,ROW,E,W,S,N,U,D,ROW_S,
                                ROW_E,NM,WM,SM,EM,UM,DM
INTEGER, PARAMETER          :: LATSIZE=226981,LATSIDE=61,
                                LATSDX=61,LATSDY=61,LATSDZ=61
INTEGER, DIMENSION(LATSIZE,8)  :: NODE
INTEGER, DIMENSION(0:LATSIZE)  :: X,Y,YR,Z,PIX
INTEGER, DIMENSION(250)         :: CARTX,CARTY,CARTZ   ! for a cubic lattice

       !'(6I9)'  FORMAT(6I9)

       OPEN(870, FILE = 'cubic_bond_61')

! memory place holder
WRITE(870,'(8I9)') 0,0,0,0,0,0,0,0

  SLICE = 0
  DO WHILE (SLICE<LATSDX)

       SLICE= SLICE+1

       ! odd numbered slices (connection 1 - slice 1,3,5)

       IF (MOD(SLICE,2) ==1) THEN

   ROW = 0

        DO WHILE (ROW<21)  !(ROW<INT((LATSDX*LATSDY)/(2*LATSDX)))
! limit of number of rows per slice

        ROW = ROW+1

         IF ( ROW == 1) THEN
          ROW_S =LATSDX*LATSDY*(SLICE-1)+1
          ROW_E = ROW_S + (LATSDX-1)

         ELSE
          ROW_S =ROW_S+2*LATSDX
          ROW_E = ROW_S + (LATSDX-1)
         END IF

         DO J = ROW_S,ROW_E,2

   CALL CONNEX1(N,S,E,W,U,D,NM,SM,EM,WM,UM,DM,J,LATSIZE,LATSIDE)

   WRITE(870,'(8I9)') J,NM,SM,EM,WM,DM,UM

        END DO
   END DO
  END IF

  IF (MOD(SLICE,2)==1) THEN

   ROW=0
```

```
  DO WHILE (ROW<21)

   ROW=ROW+1

  IF (ROW==1) THEN
    ROW_S=LATSDX*LATSDY*(SLICE-1)+2
    ROW_E=ROW_S+(LATSDX-2)

   ELSE
    ROW_S=ROW_S+(2*LATSDX)
    ROW_E=ROW_S+(LATSDX-2)

   END IF

   DO J=ROW_S,ROW_E,2

       CALL CONNEX3(EM,WM,J,LATSIZE,LATSDX,LATSDY,LATSDX)

   WRITE(870,'(8I9)') J,EM,WM,0,0,0,0

   END DO
   END DO
  END IF

 IF (MOD(SLICE,2)==1) THEN

  ROW=0

  DO WHILE (ROW<20)

   ROW=ROW+1
  IF (ROW==1) THEN
    ROW_S=LATSDX*LATSDY*(SLICE-1)+(LATSDX+1)
    ROW_E=ROW_S+(LATSDX-1)
   ELSE
    ROW_S=ROW_S+(2*LATSDX)
    ROW_E=ROW_S+(LATSDX-1)
   END IF

   DO J=ROW_S,ROW_E,2

       CALL CONNEX4(NM,SM,J,LATSIZE,LATSDX,LATSDY,LATSDX)

   WRITE(870,'(8I9)') J,NM,SM,0,0,0,0

   END DO
   END DO
  END IF

  ! even numbered slices (2,4,6)

  IF (MOD(SLICE,2)==0.AND.SLICE<=LATSDX) THEN

   ROW=0

   DO WHILE (ROW<21) !(ROW<INT((LATSDX*LATSDY)/(2*LATSDX)))

    ROW=ROW+1
```

```fortran
     IF (ROW==1) THEN
         ROW_S =LATSDX*LATSDY*(SLICE-1)+1
         ROW_E = ROW_S + (LATSDX-1)

      ELSE
       ROW_S =ROW_S+2*LATSDX
       ROW_E = ROW_S + (LATSDX-1)
      END IF

      DO J = ROW_S,ROW_E,2

      CALL CONNEX2(U,D,UM,DM,J,LATSIZE,LATSDX,LATSDY,LATSDX)

      !PRINT*, SLICE,J,DDM, UPM,0,0
      WRITE(870,'(8I9)') J,DM,UM,0,0,0,0,

      END DO
      END DO
      END IF

   END DO

    CONTAINS

      SUBROUTINE
CONNEX1(NO,SO,EA,WE,UP,DD,NOM,SOM,EAM,WEM,UPM,DDM,P,LZ,LD)
INTEGER           P,NO,EA,SO,WE,UP,DD,NOM,EAM,SOM,

                        WEM,UPM,DDM,LZ,LD
!       subroutine to determine neighbouring pixels

      IF(MOD(P,(LD**2)).GT.(LD**2-LD)) THEN
       NO=0
      ELSE IF(MOD(P,(LD**2)).EQ.0) THEN
       NO=0
      ELSE
       NO=P+(2*LD)
      ENDIF

   IF(MOD(P,(LD**2)).GT.(LD**2-LD)) THEN
       NOM=0
      ELSE IF(MOD(P,(LD**2)).EQ.0) THEN
       NOM=0
      ELSE
       NOM=P+(LD)
      ENDIF

      IF ((MOD(P,LD)).EQ.0) THEN
       EA=0
      ELSE
       EA=P+2
      ENDIF

   IF ((MOD(P,LD)).EQ.0) THEN
       EAM=0
      ELSE
       EAM=P+1
      ENDIF

      IF ((MOD(P,LD)).EQ.1) THEN
       WE=0
```

```fortran
          ELSE
           WE=P-2
          ENDIF

     IF ((MOD(P,LD)).EQ.1) THEN
           WEM=0
          ELSE
           WEM=P-1
          ENDIF

     IF(((MOD(P,(LD**2))).LE.LD).AND.((MOD(P,(LD**2))).NE.0))THEN
           SO=0
          ELSE
           SO=P-(2*LD)
          ENDIF

     IF(((MOD(P,(LD**2))).LE.LD).AND.((MOD(P,(LD**2))).NE.0))THEN
           SOM=0
          ELSE
           SOM=P-LD
          ENDIF

          IF(P.GT.(LZ-(LD**2))) THEN
           UP=0
          ELSE
           UP=P+(2*(LD**2))
          ENDIF

     IF(P.GT.(LZ-(LD**2))) THEN
           UPM=0
          ELSE
           UPM=P+(LD**2)
          ENDIF

          IF(P.LE.(LD**2)) THEN
           DD=0
          ELSE
           DD=P-(2*(LD**2))
          ENDIF

          IF(P.LE.(LD**2)) THEN
           DDM=0
          ELSE
           DDM=P-(LD**2)
          ENDIF

          END SUBROUTINE CONNEX1

! even numbered slices

          SUBROUTINE CONNEX2(UP,DD,UPM,DDM,P,LZ,LDX,LDY,LDZ)
          INTEGER                    P,UP,DD,UPM,DDM,LZ,LDX,LDY,LDZ

     IF(P.GT.(LZ-(2*LDX*LDY))) THEN
           UP = 0 ! periodic boundary -top
          ELSE
           UP=P+(2*LDX*LDY)
          ENDIF

     IF(P.GT.(LZ-(LDX*LDY))) THEN
```

```fortran
       UPM = 0 ! periodic boundary -top
       ELSE
       UPM =P+(LDX*LDY)
       ENDIF

       IF(P.LE.(2*LDX*LDY)) THEN
        DD= 0
       ELSE
        DD=P+(2*LDX*LDY)
       ENDIF

 IF(P.LE.(LDX*LDY)) THEN
        DDM= 0
       ELSE
        DDM=P-(LDX*LDY)
       ENDIF

       END SUBROUTINE CONNEX2

! mid points for the odd number slice

SUBROUTINE CONNEX3(EAM,WEM,P,LZ,LDX,LDY,LDZ)
       INTEGER                P,EAM,WEM,LZ,LDX,LDY,LDZ

 IF ((MOD(P,LDX)).EQ.0) THEN
        EAM=0
       ELSE
        EAM=P+1
       ENDIF

       IF ((MOD(P,LDX)).EQ.1) THEN
        WEM=0
       ELSE
        WEM=P-1
       ENDIF

       END SUBROUTINE CONNEX3

       SUBROUTINE CONNEX4(NOM,SOM,P,LZ,LDX,LDY,LDZ)

       INTEGER                        P,NOM,SOM,LZ,LDX,LDY,LDZ

 IF(MOD(P,(LDX**2)).GT.(LDX**2-LDX)) THEN
        NOM=0
       ELSE IF(MOD(P,(LDX**2)).EQ.0) THEN
        NOM=0
       ELSE
        NOM=P+(LDX)
       ENDIF

       IF(((MOD(P,(LDX**2))).LE.LDX).AND.((MOD(P,(LDX**2))).NE.0))THEN
        SOM=0
       ELSE
        SOM=P-LDX
       ENDIF
       END SUBROUTINE CONNEX4

END PROGRAM Cubic_structure
```

A4-2 – ZSM-5 Lattice Generation

```
PROGRAM ZSM_5structure
!adsorption sites taken to be on alpha and beta sites
   IMPLICIT NONE

INTEGER                        I,IR,J,K,DJ,SLICE,ROW,NE,NW,SE,SW,UP,DD,
                               ROW_S,ROW_E,NEM,NWM,SEM,SWM,UPM,DDM
INTEGER, PARAMETER             :: LATSIZE=884736,LATSDX=96,
                                  LATSDY=96,LATSDZ=96
INTEGER, DIMENSION(884736,4)   :: NODE
INTEGER, DIMENSION(0:LATSIZE)  :: X,Y,YR,Z,PIX

       !'(6I9)'  FORMAT(6I9)

       OPEN(870, FILE = 'ZSM5_structure_96')

 ! memory place holder
 WRITE(870,'(6I9)') 0,0,0,0,0,0

 SLICE = 0
  DO WHILE (SLICE<LATSDX)

       SLICE= SLICE+1

       ! odd numbered slices (connection 1 - slice 1,5,9)

       IF (MOD(SLICE,4) ==1) THEN

   ROW = 0
       DO WHILE (ROW<INT((LATSDX*LATSDY)/(4*LATSDX))) ! limit of number of rows per slice

       ROW = ROW+1

       IF ( ROW == 1) THEN
        ROW_S =LATSDX*LATSDY*(SLICE-1)+1
        ROW_E = ROW_S + (LATSDX-1)

       ELSE
        ROW_S =ROW_S+4*LATSDX
        ROW_E = ROW_S + (LATSDX-1)
       END IF

       DO J = ROW_S,ROW_E,4

       CALL
CONNEX1(NE,NEM,NW,NWM,UP,UPM,DD,DDM,J,LATSIZE,LATSDX,LATSDY,LATSDX)

       IF(J.LE.(LATSDX*LATSDY)) THEN  ! periodic boundary - base
        CALL CONNEX3(UP,UPM,DD,DDM,J,LATSIZE,LATSDX,LATSDY,LATSDX)
       END IF

       NODE(J,1) = NWM
       NODE(J,2) = NEM
       NODE(J,3) = DDM
       NODE(J,4) = UPM

       !PRINT*,  SLICE,J,NWM,NEM,DDM,UPM
       WRITE(870,'(6I9)') J,SLICE,NWM,NEM,DDM,UPM
```

```
                END DO
                END DO
                END IF


! odd numbered slices (connection 2 - slice 1,5,9) - neighbours for position NE/NW of P
        ! sites are actually determined as if they were SW/SE of J

        IF (MOD(SLICE,4) ==1) THEN

   ROW = 0

        DO WHILE (ROW<INT((LATSDX*LATSDY)/(4*LATSDX)))

        ROW = ROW+1

        IF ( ROW == 1) THEN
         ROW_S =LATSDX*LATSDY*(SLICE-1)+ (2*LATSDX+3)
         ROW_E = ROW_S + (LATSDX-3)

         ELSE
          ROW_S =ROW_S+4*LATSDX
          ROW_E = ROW_S + (LATSDX-3)

         END IF

         DO J = ROW_S,ROW_E,4

         CALL
CONNEX2(SE,SEM,SW,SWM,UP,UPM,DD,DDM,J,LATSIZE,LATSDX,LATSDY,
LATSDX)

IF(J.LE.(LATSDX*LATSDY)) THEN   ! periodic boundary - base

         CALL
CONNEX3 (UP,UPM       ,DD,DDM,J,LATSIZE,LATSDX,LATSDY,LATSDX)
         END IF
    !PRINT*, SLICE,J,SWM,SEM,DDM,UPM
        WRITE(870,'(6I9)') J,SLICE,SWM,SEM,DDM,UPM

        END DO
        END DO
        END IF

  ! zig zag channel sites neighbours

        ! NEM and SWM neighbours
        IF (MOD(SLICE,4) ==1) THEN

   ROW = 0

        DO WHILE (ROW<INT((LATSDX*LATSDY)/(4*LATSDX))) ! limit of number of rows per slice

        ROW = ROW+1

        IF ( ROW == 1) THEN
         ROW_S =LATSDX*LATSDY*(SLICE-1)+LATSDX+2
         ROW_E = ROW_S + (LATSDX-2)
```

```
        ELSE
         ROW_S =ROW_S+4*LATSDX
         ROW_E = ROW_S + (LATSDX-2)
        END IF

        DO J = ROW_S,ROW_E,4
        CALL CONNEX4(NEM,NWM,SEM,SWM,J,LATSIZE,LATSDX,LATSDY,LATSDX)

    !PRINT*, SLICE,J,SWM,NEM,NWM,SEM
        WRITE(870,'(6I9)') J,SLICE,SWM,NEM,NWM,SEM

        END DO
       END DO
      END IF

! NWM and SEM neighbours
 IF (MOD(SLICE,4) ==1) THEN

    ROW = 0

        DO WHILE (ROW<INT((LATSDX*LATSDY)/(4*LATSDX))) ! limit of number of rows per slice

        ROW = ROW+1

        IF ( ROW == 1) THEN
         ROW_S =LATSDX*LATSDY*(SLICE-1)+LATSDX+4
         ROW_E = ROW_S + (LATSDX-3)

        ELSE
         ROW_S =ROW_S+4*LATSDX
         ROW_E = ROW_S + (LATSDX-3)
        END IF

        DO J = ROW_S,ROW_E,4

        CALL CONNEX5(NEM,NWM,SEM,SWM,J,LATSIZE,LATSDX,LATSDY,LATSDX)
     !PRINT*, SLICE,J,NWM,SEM,NEM,SWM
        WRITE(870,'(6I9)') J,SLICE,NWM,SEM,NEM,SWM

        END DO
       END DO
      END IF

  ! odd numbered slices (connection 2 - slice 3,7)

        IF (MOD(SLICE,4) ==3) THEN

    ROW = 0

        DO WHILE (ROW<INT((LATSDX*LATSDY)/(4*LATSDX)))

        ROW = ROW+1

        IF ( ROW == 1) THEN
         ROW_S =LATSDX*LATSDY*(SLICE-1)+1
         ROW_E = ROW_S + (LATSDX-1)

        ELSE
         ROW_S =ROW_S+4*LATSDX
         ROW_E = ROW_S + (LATSDX-1)
```

```fortran
          END IF

          DO J = ROW_S,ROW_E,4

          CALL CONNEX2(SE,SEM,SW,SWM,UP,UPM,DD,DDM,J,LATSIZE,LATSDX,LATSDY,
LATSDX)

          !PRINT*, SLICE,J,SWM,SEM,DDM,UPM
    WRITE(870,'(6I9)') J,SLICE,SWM,SEM,DDM,UPM

          END DO
         END DO
        END IF
   ! odd numbered slices (connection 2 - slice 3,7) - neighbours for position SE/SW of P

         IF (MOD(SLICE,4) ==3) THEN

    ROW = 0

         DO WHILE (ROW<INT((LATSDX*LATSDY)/(4*LATSDX)))

         ROW = ROW+1

         IF ( ROW == 1) THEN
          ROW_S =LATSDX*LATSDY*(SLICE-1)+(2*LATSDX+3)
          ROW_E = ROW_S + (LATSDX-3)

         ELSE
          ROW_S =ROW_S+4*LATSDX
          ROW_E = ROW_S + (LATSDX-3)
         END IF

         DO J = ROW_S,ROW_E,4

         CALL
CONNEX1(NE,NEM,NW,NWM,UP,UPM,DD,DDM,J,LATSIZE,LATSDX,LATSDY,LATSDX)

          !PRINT*, SLICE,J,NWM,NEM,DDM,UPM
          WRITE(870,'(6I9)') J,SLICE,NWM,NEM,DDM,UPM

          END DO
         END DO
        END IF

         ! zig zag channel sites neighbours

         ! NWM and SEM neighbours
        IF (MOD(SLICE,4) ==3) THEN

    ROW = 0

         DO WHILE (ROW<INT((LATSDX*LATSDY)/(4*LATSDX)))

         ROW = ROW+1

         IF ( ROW ==1) THEN
          ROW_S =LATSDX*LATSDY*(SLICE-1)+(LATSDX*3+2)
          ROW_E = ROW_S + (LATSDX-1)

         ELSE
```

```fortran
      ROW_S =ROW_S+4*LATSDX
      ROW_E = ROW_S + (LATSDX-1)
      END IF

      DO J = ROW_S,ROW_E,4

      CALL CONNEX5(NEM,NWM,SEM,SWM,J,LATSIZE,LATSDX,LATSDY,LATSDX)
!PRINT*, SLICE,J,SEM,NWM,NEM,SWM
      WRITE(870,'(6I9)') J,SLICE,NWM,SEM,NEM,SWM

      END DO
      END DO
      END IF

      ! NEM and SWM neighbours
      IF (MOD(SLICE,4) ==3) THEN

ROW = 0

      DO WHILE (ROW<INT((LATSDX*LATSDY)/(4*LATSDX)))

      ROW = ROW+1

      IF ( ROW ==1) THEN
      ROW_S =LATSDX*LATSDY*(SLICE-1)+(LATSDX*3+4)
      ROW_E = ROW_S + (LATSDX-4)

      ELSE
      ROW_S =ROW_S+4*LATSDX
      ROW_E = ROW_S + (LATSDX-4)
      END IF

      DO J = ROW_S,ROW_E,4

      CALL CONNEX4(NEM,NWM,SEM,SWM,J,LATSIZE,LATSDX,LATSDY,LATSDX)

 !PRINT*, SLICE,J,SWM,NEM,NWM,SEM
      WRITE(870,'(6I9)') J,SLICE,SWM,NEM,NWM,SEM

      END DO
      END DO
      END IF

! even numbered slices - intermediates (up and down connection)

      IF (MOD(SLICE,2) ==0 .AND. SLICE<=LATSDX) THEN

ROW = 0

      DO WHILE (ROW<INT((LATSDX*LATSDY)/(4*LATSDX)))
      ROW = ROW+1

      IF ( ROW == 1) THEN
       !ROW_S =LATSDX*LATSDY*(SLICE-1)+LATSDX+1
       ROW_S =LATSDX*LATSDY*(SLICE-1)+1
       ROW_E = ROW_S + (LATSDX-1)

      ELSE
       ROW_S =ROW_S+4*LATSDX
       ROW_E = ROW_S + (LATSDX-1)
```

```fortran
      END IF

      DO J = ROW_S,ROW_E,4

      CALL CONNEX3(UP,UPM,DD,DDM,J,LATSIZE,LATSDX,LATSDY,LATSDX)

      !PRINT*, SLICE,J,DDM, UPM,0,0
      WRITE(870,'(6I9)') J,SLICE,DDM, UPM,0,0

       END DO
      END DO
     END IF

 ! even numbered slices - intermediates (up and down connection 4 NW/NE neighbours of P)

      IF (MOD(SLICE,2) ==0 .AND. SLICE<=LATSDX) THEN

   ROW = 0

       DO WHILE (ROW<INT((LATSDX*LATSDY)/(4*LATSDX)))

       ROW = ROW+1

       IF ( ROW == 1) THEN
       ROW_S =LATSDX*LATSDY*(SLICE-1)+(2*LATSDX+3)
       ROW_E = ROW_S + (LATSDX-3)

       ELSE
       ROW_S =ROW_S+4*LATSDX
       ROW_E = ROW_S + (LATSDX-3)
       END IF

       DO J = ROW_S,ROW_E,4


       CALL CONNEX3(UP,UPM,DD,DDM,J,LATSIZE,LATSDX,LATSDY,LATSDX)
       !PRINT*, SLICE,J,DDM, UPM,0,0
      WRITE(870,'(6I9)') J,SLICE,DDM, UPM,0,0

       END DO
      END DO
     END IF

  END DO

  CLOSE(870)

  CONTAINS

   SUBROUTINE CONNEX1(NNE,NNEM,NNW,NNWM,UUP,UUPM,DDD,DDDM,P,LZ,LDX,LDY,
 LDZ)
       INTEGER       NNE,NNEM,NNW,NNWM,UUP,UUPM,DDD,DDDM,P,
 LZ,LDX,LDY,LDZ
   INTEGER, DIMENSION(0:LATSIZE)    :: PIXX


  IF ((MOD(P,(LDX*LDY)))== 0) THEN
       NNW=0                                !flag 4 appropriate periodic boundary
       ELSE IF ((MOD(P,LDX))== 1) THEN
       NNW= 0 !P+(2*LDY-1)                  !periodic boundary for the edge
```

```
ELSE IF ((MOD(P,LDX))== 2) THEN
     NNW=0                                         !flag 4 appropriate periodic boundary
     ELSE IF(MOD(P,(LDX*LDY))> (LDX*LDY-2*LDX)) THEN
     NNW=0
     ELSE IF((MOD(P,LDX)) /= 1) THEN
     NNW=P+2*LDY-2
     ENDIF

IF ((MOD(P,(LDX*LDY)))== 0) THEN
     NNWM=0
     ELSE IF ((MOD(P,LDX))== 1) THEN
     NNWM=0 !P+(2*LDY-1)                           !edge 1 periodic boundary
     ELSE IF(MOD(P,(LDX*LDY))> (LDX*LDY-LDX)) THEN
     NNWM=0
     ELSE IF((MOD(P,LDX)) /= 1) THEN
     NNWM=P+LDY-1
     ENDIF

     IF ((MOD(P,LDX))==0) THEN
     NNE= P-(2*LDY-1)
     ELSE IF(MOD(P,(LDX*LDY))> (LDX*LDY-2*LDX)) THEN
     NNE=0
ELSE IF ((MOD(P,LDX))==(LDX-1)) THEN
     NNE=0
     ELSE
     NNE=P+2*LDY+2
     ENDIF

IF ((MOD(P,LDX))==0) THEN
     NNEM=0
     ELSE IF(MOD(P,(LDX*LDY))> (LDX*LDY-LDX)) THEN
     NNEM=0
     ELSE
     NNEM=P+LDY+1
     ENDIF

     IF(P.GT.(LZ-(2*LDX*LDY))) THEN
     UUP = 0
     ELSE
     UUP=P+(2*LDX*LDY)
     ENDIF

IF(P.GT.(LZ-(LDX*LDY))) THEN
     UUPM = 0
     ELSE
     UUPM =P+(LDX*LDY)
     ENDIF

     IF(P.LE.(2*LDX*LDY)) THEN
     DDD= 0
ELSE
     DDD=P-(2*LDX*LDY)
     ENDIF

IF(P.LE.(LDX*LDY)) THEN
     DDDM= 0
     ELSE
     DDDM=P-(LDX*LDY)
     ENDIF
```

```fortran
              END SUBROUTINE CONNEX1

    SUBROUTINE CONNEX2(SSE,SSEM,SSW,SSWM,UUP,UUPM,DDD,DDDM,P,LZ,LDX,LDY,
LDZ)
              INTEGER              SSE,SSEM,SSW,SSWM,UUP,UUPM,DDD,DDDM,P,
LZ,LDX,LDY,LDZ
    INTEGER, DIMENSION(0:LATSIZE)    :: PIXX

  IF ((MOD(P,(LDX*LDY)))== 0) THEN
        SSW=P-2*LDY-2
        ELSE IF ((MOD(P,LDX))== 1) THEN
        SSW=0

  ELSE IF ((MOD(P,LDX))== 2) THEN
        SSW=0

        ELSE IF ((MOD(LDX*LDY-LDX+P,LDX*LDY))==0) THEN
        SSW=0

        ELSE IF(MOD(P,(LDX*LDY))<= 2*LDX) THEN
         SSW=0
        ELSE
         SSW=P-2*LDY-2
        ENDIF

  IF ((MOD(P,LDX))== 1 .AND. MOD(P,(LDX*LDY))==1) THEN
        SSWM= 0 !P+ (LDX*LDY-1) !periodic boundary for first point of odd # planes

        ELSE IF ((MOD(P,LDX))== 1) THEN
         SSWM= 0 !P-1                          !periodic boundary for edge 1

        ELSE IF ((MOD(P,LDX))== 1) THEN
         SSWM=0

        ELSE IF ((MOD(LDX*LDY-LDX+P,LDX*LDY))==0) THEN
         SSWM=0

        ELSE IF(MOD(P,(LDX*LDY))<LDX) THEN
        SSWM= 0 !P+ (LDX*LDY-(LDX+1))       !periodic boundary for edge 3
        ELSE
         SSWM=P-LDY-1
        ENDIF

        IF ((MOD(P,LDX))==0) THEN
         SSE=0
  ELSE IF ((MOD(P,LDX))==(LDX-1)) THEN
         SSE=0
        ELSE IF(MOD(P,(LDX*LDY))<=2*LDX) THEN
         SSE=0
        ELSE
         SSE=P-2*LDY+2
        ENDIF

        IF ((MOD(P,LDX))==0) THEN
         SSEM=0
        ELSE IF(MOD(P,(LDX*LDY))<LDX) THEN
         SSEM= 0 !P+ (LDX*LDY-(LDX-1))          !periodic boundary for edge 3
         ELSE
         SSEM=P-LDY+1
         ENDIF
```

```fortran
        IF(P.GT.(LZ-(2*LDX*LDY))) THEN
         UUP = 0
         ELSE
         UUP=P+(2*LDX*LDY)
         ENDIF

IF(P.GT.(LZ-(LDX*LDY))) THEN
         UUPM = 0
         ELSE
         UUPM =P+(LDX*LDY)
         ENDIF


        IF(P.LE.(2*LDX*LDY)) THEN
         DDD= 0
         ELSE
         DDD=P-(2*LDX*LDY)
         ENDIF

IF(P.LE.(LDX*LDY)) THEN
         DDDM= 0
         ELSE
         DDDM=P-(LDX*LDY)
         ENDIF

        END SUBROUTINE CONNEX2

        ! straight channel sites neighbours
SUBROUTINE CONNEX3(UUP,UUPM,DDD,DDDM,P,LZ,LDX,LDY,LDZ)

        INTEGER          UUP,UUPM,DDD,DDDM,P,LZ,LDX,LDY,LDZ
INTEGER, DIMENSION(0:LATSIZE)    :: PIXX

        IF(P.GT.(LZ-(2*LDX*LDY))) THEN
         UUP = 0 !P-LDX*LDY*(LDX-1) ! periodic boundary -top
         ELSE
         UUP=P+(2*LDX*LDY)
         ENDIF

IF(P.GT.(LZ-(LDX*LDY))) THEN
         UUPM = 0 !P-LDX*LDY*(LDX-1) ! periodic boundary -top
         ELSE
         UUPM =P+(LDX*LDY)
         ENDIF

        IF(P.LE.(2*LDX*LDY)) THEN
         DDD= 0 !P+LDX*LDY*(LDX-1)
         ELSE
         DDD=P+(2*LDX*LDY)
         ENDIF

IF(P.LE.(LDX*LDY)) THEN
         DDDM= 0 !P+LDX*LDY*(LDX-1)
         ELSE
         DDDM=P-(LDX*LDY)
         ENDIF

        END SUBROUTINE CONNEX3
```

```fortran
SUBROUTINE CONNEX4(NNEM,NNWM,SSEM,SSWM,P,LZ,LDX,LDY,LDZ)
      INTEGER                NNEM,NNWM,SSEM,SSWM,P,LZ,LDX,LDY,LDZ
 INTEGER, DIMENSION(0:LATSIZE)    :: PIXX

 NNWM = 0
      SSEM = 0

      IF((MOD(P,(LDX*LDY)))==0 ) THEN
       NNEM= 0 !P-(LDX*LDY-1)        !highest # in a slice periodic boundary

 ELSE IF ((MOD(P,LDX))==0) THEN                 ! edge 2 periodic boundary
      !NNEM= P-(LDY*2-1)
       NNEM= 0 !P+1

      ELSE IF((MOD(P,(LDX*LDY)))> (LDX*LDY-LDX)) THEN

       NNEM= 0 !P-(LDX*LDY-(LDX+1))       !edge 4 periodic boundary

      ELSE IF(MOD(P,(LDX*LDY))> (LDX*LDY-2*LDX)) THEN
       NNEM = 0
      ELSE
       NNEM=P+LDY+1
      ENDIF

      IF ((MOD(P,LDX))== 1) THEN      ! edge 1 periodic boundary
       SSWM = 0! P+(LDY*2-1)

 ELSE
       SSWM=P-(LDY+1)
      ENDIF

      END SUBROUTINE CONNEX4

      SUBROUTINE CONNEX5(NNEM,NNWM,SSEM,SSWM,P,LZ,LDX,LDY,LDZ)
      INTEGER              NNEM,NNWM,SSEM,SSWM,P,LZ,LDX,LDY,LDZ
 INTEGER, DIMENSION(0:LATSIZE)    :: PIXX

 NNEM = 0
      SSWM = 0

 IF((MOD(P,(LDX*LDY)))> (LDX*LDY-LDX)) THEN

       NNWM= 0 !P-(LDX*LDY-(LDX-1))                !edge 4 periodic boundary
      ELSE
       NNWM=P+LDY-1
      ENDIF

      IF ((MOD(P,LDX))==0) THEN          ! edge 2 periodic boundary
       SSEM= 0! P-(2*LDY-1)

      ELSE IF ((MOD(P,LDX))== 1) THEN
       SSEM = 0                          !flag demand appropriate periodic boundary

 ELSE
       SSEM=P-(LDY-1)
      ENDIF


      END SUBROUTINE CONNEX5
```

END PROGRAM ZSM_5structure

A4-3 – ZSM-5 Accessibility Program

```
PROGRAM MC_ZSM_ACCESSIBILITY
   IMPLICIT NONE

INTEGER                  I,J,K,N,E,S,W,U,D,RAND,LPSTART,LPEND,LPCOUNT,
RCOUNT,RLIM,OP,NP,H_DIR, N_DIR,LDX,LDY,LDZ,M,VI,VS,VZ,ICOUNT,
SCOUNT,ZCOUNT
INTEGER, PARAMETER                          :: COL=6,ROW=165888,
LATSIZE=884736,LATSIDE=96,LDX=96,LDY=96
INTEGER, DIMENSION(COL,ROW)        :: NODE,SST
REAL                                         SEED,VP, VC, VINT,VSTR,VZZ,
VOPEN,VCI,VCS,VCZ

   SEED = 0.986 !0.009547!0.9106!0.000047286275
   VINT = 2.68E-22 !2.01E-22
   VSTR = 1.09E-22 !8.198E-23
   VZZ = 1.46E-22 !1.09E-22
        VP = 2.89E-17
   !VC = 8.45E-21

   OPEN(900, FILE = 'ZSM5_structure_96')
   OPEN(910, FILE = 'cubic_results_12')
   OPEN(911, FILE = 'cubic_boundary')
   OPEN(912, FILE = 'cubic_lattice')
   OPEN(913, FILE = 'cubic_lattice_2')
   OPEN(914, FILE = 'percolation_results')

        ! read cubic lattice nodes and their neighbours
   READ(900,*) NODE

   DO J=1,COL
    DO I=1, ROW !DO I=1,LATSIZE
        SST(J,I) = 0 !SST(N_HOP,I)
!PRINT*, J,I,SST(J,I)
        !WRITE(910,*) J,I,SST(J,I)
                END DO
    END DO

        ! random blocking of sites in the lattice

   LPCOUNT = 0
   RCOUNT = 0
   ICOUNT = 0
   SCOUNT = 0
   ZCOUNT = 0
   VCI = 4.767E-18 !1.39E-20
   VCS = 1.943E-18
   VCZ = 2.589E-18

   DO WHILE (VCI.GT.0) !DO WHILE (LPCOUNT<=(10))
    RCOUNT= RCOUNT+1

    CALL RANDOM_POS(SEED)

    LPSTART=1
    LPEND=ROW

        !IF ((SEED.LE.0.513).AND.(SEED.GT.0)) THEN
```

```fortran
      RAND = (1+INT(ROW*SEED))
      !PRINT*, 'INTERSECTION'
      IF ((MOD(NODE(2,RAND),2)==1).AND.NODE(6,RAND)/=0) THEN

          CALL  MOL_BLOCK1  (LPSTART,LPEND,RAND,SST,VCI,NODE,VINT,LPCOUNT,ICOUNT)
! FOR INTERSECTIONS

      END IF

   END DO

   DO WHILE (VCS.GT.0)
     RCOUNT= RCOUNT+1

   CALL RANDOM_POS(SEED)

   LPSTART=1
    LPEND=ROW

   !ELSE IF ((SEED.LE.0.722).AND.(SEED.GT.0.513)) THEN

    RAND = (1+INT(ROW*SEED))
    !PRINT*, 'STRAIGHT'

    IF ((MOD(NODE(2,RAND),2)==0).AND.NODE(5,RAND)==0.AND.NODE(6,RAND)==0) THEN

        CALL                                         MOL_BLOCK2
(LPSTART,LPEND,RAND,SST,VCS,NODE,VSTR,LPCOUNT,SCOUNT)        !    FOR    STRAIGHT
CHANNELS

      END IF

   END DO

  DO WHILE (VCZ.GT.0)
    RCOUNT= RCOUNT+1

  CALL RANDOM_POS(SEED)

  LPSTART=1
  LPEND=ROW

      !ELSE IF ((SEED.LE.1).AND.(SEED.GT.0.722)) THEN

    RAND = (1+INT(ROW*SEED))

   IF ((MOD(NODE(2,RAND),2)==1).AND.NODE(5,RAND)==0.AND.NODE(6,RAND)==0) THEN

        CALL  MOL_BLOCK3  (LPSTART,LPEND,RAND,SST,VCZ,NODE,VZZ,LPCOUNT,ZCOUNT)
! FOR ZIG-ZAG CHANNELS

      END IF

    !END IF

   END DO

        ! calculate f, fraction of unplugged pores - without percolation effects
```

```
VC= 9.3E-18
VP = 2.89E-17

        VOPEN=VP-VC

  PRINT*, VP, VC, VOPEN

  !set boundaries of adsorbate molecules

  DO I= 1, ROW
    IF ((MOD(NODE(1,I),LDX)==1).AND.SST(1,I)==0.AND.MOD(NODE(2,I),2)==1) THEN
      SST (1,I)=2

      ELSE  IF  ((MOD(NODE(1,I),(LDX*LDY))<LDX).AND.SST(1,I)==0.AND.MOD(NODE(2,I),2)==1)
  THEN
        SST (1,I) =2

      ELSE                  IF                  ((MOD(NODE(1,I),(LDX*LDY))>(LDX*LDY-
  LDX)).AND.SST(1,I)==0.AND.MOD(NODE(2,I),2)==1) THEN
        SST (1,I) =2

    END IF
    !PRINT*, I, NODE(1,I), SST(1,I)
    WRITE (911,*) I, SST(1,I), NODE(1,I)
  END DO

        ! set neighbours to the right sst

  DO I=1,ROW

    IF (SST(1,I)==2) THEN

      CALL ADJ_SITES(N,E,S,W,I,NODE,SST)

      WRITE (912,*) I, NODE(1,I),SST(1,I),SST(3,I),SST(4,I),SST(5,I),SST(6,I)

      ELSE

      CALL ADJ_SITES(N,E,S,W,I,NODE,SST)
      WRITE (912,*) I, NODE(1,I),SST(1,I),SST(3,I),SST(4,I),SST(5,I),SST(6,I)

    END IF

  END DO

  ! move molecules inwards

  RCOUNT=0
  DO WHILE (RCOUNT.LE.90)

      DO I=1,ROW

  !PRINT*, I,SST(1,I),SST(2,I),SST(3,I),SST(4,I),SST(5,I)

  !CALL ADJ_SITES2(N,E,S,W,U,D,I,NODE,SST)

      IF (SST(1,I)==0) THEN

   CALL ADJ_SITES2(N,E,S,W,I,NODE,SST)
```

```fortran
    ELSE IF (SST(1,I)==2) THEN

      CALL ADJ_SITES3(N,E,S,W,I,NODE,SST)

    END IF


    END DO

  RCOUNT=RCOUNT+1
  PRINT*, RCOUNT
  END DO
  DO I=1,ROW

    IF (SST(1,I)==2) THEN

     CALL ADJ_SITES(N,E,S,W,I,NODE,SST)

    ELSE IF (SST(1,I)==0) THEN

      CALL ADJ_SITES(N,E,S,W,I,NODE,SST)

     END IF

  WRITE (913,*) I, NODE(1,I),SST(1,I),SST(3,I),SST(4,I),SST(5,I),SST(6,I)

   END DO

  !taking into account percolation effect

   VI=0
   VS=0
   VZ=0

        DO I=1,ROW

    IF (SST(1,I)==2) THEN

     IF (MOD(NODE(1,I),2)==1.AND.NODE(6,I)/=0) THEN

        VI=VI+1

     ELSE IF (MOD(NODE(1,I),2)==0.AND.NODE(5,I)==0.AND.NODE(6,I)==0) THEN

        VS=VS+1

     ELSE IF (MOD(NODE(1,I),2)==1.AND.NODE(5,I)==0.AND.NODE(6,I)==0) THEN

        VZ=VZ+1

     END IF

    END IF

   END DO

  PRINT*, VOPEN, VI, VS, VZ
  WRITE(914,*) VOPEN, VI, VS, VZ
```

```fortran
CONTAINS

    SUBROUTINE RANDOM_POS (X)

  INTEGER                                IX, K,J,M
  REAL                                   X,IRAND,RM

     DATA K,J,M,RM / 5702,3612,566927,566927.0/
     IX=INT(X*RM)
     IRAND=MOD(J*IX+K,M)
     X=(REAL(IRAND)+0.5)/RM

     END SUBROUTINE RANDOM_POS

 SUBROUTINE MOL_BLOCK1 (LS,LE,RD,ST,VCI,DNODE,VINT,LC,IC)

     INTEGER                          LS,LE,RD,LC,ND,IC
     INTEGER, DIMENSION(ROW)      :: R
     INTEGER, DIMENSION(COL,ROW) :: ST
     INTEGER, DIMENSION(COL,ROW),INTENT(IN) :: DNODE
     REAL                                        VCI, VINT

      !random placement of molecules in lattice
       DO I=LS,LE
       R(I) = RD
   !PRINT*, RD
        ! occupied sites cannot be recounted
        IF ( ST(1,I)==0 .AND.I== R(I)) THEN
        ST(1,I) = 1
             VCI=VCI-VINT

      END IF

        END DO

     END SUBROUTINE MOL_BLOCK1

 SUBROUTINE MOL_BLOCK2 (LS,LE,RD,ST,VCS,DNODE,VSTR,LC,SC)

     INTEGER                          LS,LE,RD,LC,ND,SC
     INTEGER, DIMENSION(ROW)     :: R
     INTEGER, DIMENSION(COL,ROW)       :: ST
     INTEGER, DIMENSION(COL,ROW),INTENT(IN) :: DNODE
     REAL                                         VCS, VSTR

      !random placement of molecules in lattice
       DO I=LS,LE
       R(I) = RD
       ! occupied sites cannot be recounted
        IF   (   ST(1,I)==0   .AND.I==   R(I))   THEN   !IF   (   ST(1,I)==0   .AND.I==
R(I).AND.(MOD(DNODE(2,RD),2)==0).AND.DNODE(5,RD)==0.AND.DNODE(6,RD)==0) THEN
        ST(1,I) = 1
             VCS=VCS-VSTR

      END IF

        END DO

     END SUBROUTINE MOL_BLOCK2
```

```fortran
SUBROUTINE MOL_BLOCK3 (LS,LE,RD,ST,VCZ,DNODE,VZZ,LC,ZC)

      INTEGER                               LS,LE,RD,LC,ND,ZC
      INTEGER, DIMENSION(ROW)     :: R
      INTEGER, DIMENSION(COL,ROW)        :: ST
      INTEGER, DIMENSION(COL,ROW),INTENT(IN) :: DNODE
      REAL                                      VCZ, VZZ


      !random placement of molecules in lattice
       DO I=LS,LE
        R(I) = RD

       ! occupied sites cannot be recounted
        IF      (ST(1,I)==0      .AND.I==      R(I))     THEN    !IF    (ST(1,I)==0
.AND.I==R(I).AND.(MOD(DNODE(2,RD),2)==1).AND.DNODE(5,RD)==0.AND.DNODE(6,RD)==0)
THEN

         ST(1,I) = 1
            VCZ=VCZ-VZZ

     END IF

       END DO

     END SUBROUTINE MOL_BLOCK3

  SUBROUTINE ADJ_SITES(NO,EA,SO,WE,J,DNODE,ST)

INTEGER                                        I,J,K,NO,EA,SO,WE
INTEGER, DIMENSION(COL,ROW)                 :: ST
INTEGER, DIMENSION(COL,ROW),INTENT(IN) :: DNODE

  ! search for site location in ZSM5 structure array

  LOOP1:  DO I=1,ROW

      IF (DNODE(3,J)==DNODE(1,I)) THEN
       WE = I
       IF (SST(1,I)==2) THEN
       ST(3,J)=2

       ELSE IF (ST(1,I)==1) THEN
         ST(3,J)=1
       IF (ST(3,J) ==2) EXIT LOOP1 ! 2 map once to array memory

       ELSE
       WE = 0

       END IF

       END IF

  END DO LOOP1

  LOOP2:  DO I=1,ROW

      IF ( DNODE(4,J)==DNODE(1,I)) THEN
       EA = I
       IF (ST(1,I)==2) THEN
```

```
        ST(4,J)=2

      ELSE IF (ST(1,I)==1) THEN
        ST(4,J)=1

      IF (ST(4,J) ==2) EXIT LOOP2 ! 2 map once to array memory

      ELSE
      EA = 0
      END IF

      END IF

   END DO LOOP2

   LOOP3:  DO I=1,ROW

      IF ( DNODE(5,J)==DNODE(1,I)) THEN
      SO = I
      IF (ST(1,I)==2) THEN
      ST(5,J)=2

      ELSE IF (ST(1,I)==1) THEN
        ST(5,J)=1

      IF (ST(5,J) ==2) EXIT LOOP3 ! 2 map once to array memory

      ELSE
      SO = 0

      END IF

      END IF

   END DO LOOP3

   LOOP4:  DO I=1,ROW

      IF ( DNODE(6,J)==DNODE(1,I)) THEN
      NO = I
      IF (ST(1,I)==2) THEN
      ST(6,J)=2

      ELSE IF (ST(1,I)==1) THEN
        ST(6,J)=1

      IF (ST(6,J) ==2) EXIT LOOP4 ! 2 map once to array memory

      ELSE
      NO = 0

      END IF

      END IF

   END DO LOOP4

   END SUBROUTINE ADJ_SITES

  SUBROUTINE ADJ_SITES2(NO,EA,SO,WE,J,DNODE,ST)
```

```fortran
        INTEGER                                        I,J,K,NO,EA,SO,WE
        INTEGER, DIMENSION(COL,ROW)            :: ST
        INTEGER, DIMENSION(COL,ROW),INTENT(IN) :: DNODE

! search for site location in ZSM5 structure array

LOOP1:  DO I=1,ROW

     IF (DNODE(3,J)==DNODE(1,I)) THEN
      WE = I
      IF (SST(1,I)==2) THEN
      ST(1,J)=2
      ST(3,J)=2

      IF (ST(3,J) ==2) EXIT LOOP1 ! 2 map once to array memory
      ELSE
      WE = 0

      END IF

      END IF

END DO LOOP1

LOOP2:  DO I=1,ROW

     IF ( DNODE(4,J)==DNODE(1,I)) THEN
      EA = I
      IF (ST(1,I)==2) THEN
        ST(1,J)=2
      ST(4,J)=2

      IF (ST(4,J) ==2) EXIT LOOP2 ! 2 map once to array memory

      ELSE
      EA = 0

      END IF

      END IF

END DO LOOP2

LOOP3:  DO I=1,ROW

     IF ( DNODE(5,J)==DNODE(1,I)) THEN
      SO = I
      IF (ST(1,I)==2) THEN
        ST(1,J)=2
      ST(5,J)=2

      IF (ST(5,J) ==2) EXIT LOOP3 ! 2 map once to array memory

      ELSE
      SO = 0

      END IF

      END IF
```

```fortran
      END DO LOOP3

LOOP4:  DO I=1,ROW

      IF ( DNODE(6,J)==DNODE(1,I)) THEN
      NO = I
      IF (ST(1,I)==2) THEN
        ST(1,J)=2
      ST(6,J)=2

      IF (ST(6,J) ==2) EXIT LOOP4 ! 2 map once to array memory

      ELSE
      NO = 0

      END IF

      END IF

  END DO LOOP4

  END SUBROUTINE ADJ_SITES2

  SUBROUTINE ADJ_SITES3(NO,EA,SO,WE,J,DNODE,ST)

      INTEGER                                      I,J,K,NO,EA,SO,WE
      INTEGER, DIMENSION(COL,ROW)                  :: ST
      INTEGER, DIMENSION(COL,ROW),INTENT(IN) :: DNODE

! search for site location in ZSM5 structure array

LOOP1:  DO I=1,ROW

      IF (DNODE(3,J)==DNODE(1,I)) THEN
      WE = I
      IF (ST(1,I)==0) THEN
      ST(1,I)=2
      ST(3,J)=2

      ELSE IF (ST(1,I)==2) THEN
        ST(3,J)=2

      IF (ST(3,J) ==2) EXIT LOOP1 ! 2 map once to array memory

      ELSE
      WE = 0

      END IF

      END IF

END DO LOOP1

LOOP2:  DO I=1,ROW

      IF ( DNODE(4,J)==DNODE(1,I)) THEN
      EA = I
      IF (ST(1,I)==0) THEN
        ST(1,I)=2
```

```
                      ST(4,J)=2

                      ELSE IF (ST(1,I)==2) THEN
                        ST(4,J)=2

                      IF (ST(4,J) ==2) EXIT LOOP2 ! 2 map once to array memory

                      ELSE
                      EA = 0

                      END IF

                      END IF

              END DO LOOP2

              LOOP3:  DO I=1,ROW

                      IF ( DNODE(5,J)==DNODE(1,I)) THEN
                      SO = I
                      IF (ST(1,I)==0) THEN
                        ST(1,I)=2
                      ST(5,J)=2

                      ELSE IF (ST(1,I)==2) THEN
                        ST(5,J)=2

                      IF (ST(5,J) ==2) EXIT LOOP3 ! 2 map once to array memory

                      ELSE
                      SO = 0

                      END IF

                      END IF

              END DO LOOP3

                LOOP4:  DO I=1,ROW

                      IF ( DNODE(6,J)==DNODE(1,I)) THEN
                      NO = I
                      IF (ST(1,I)==0) THEN
                        ST(1,I)=2
                      ST(6,J)=2

                      ELSE IF (ST(1,I)==2) THEN
                        ST(6,J)=2

                      IF (ST(6,J) ==2) EXIT LOOP4 ! 2 map once to array memory

                      ELSE
                      NO = 0

                      END IF

                      END IF

              END DO LOOP4
```

END SUBROUTINE ADJ_SITES3

END PROGRAM MC_ZSM_ACCESSIBILITY

A4-4 – ZSM-5 Random Walk

```
PROGRAM MC_CUBIC_DSELF
IMPLICIT NONE


!  program acquires CUBIC nodes and uses MC simulations to evaluate
!  self diffusivity peridic boundaries apply on all edges


! interface to system clock for reseeding random number generation
        INTERFACE
   SUBROUTINE HOP_DIR4 (SEED,N_DIR,RAND)
        INTEGER                          RAND,N_DIR
        REAL                   SEED
        END SUBROUTINE
   END INTERFACE


INTEGER                 I,J,K,N,E,S,W,U,D,INOM,RAND,LPSTART,LPEND,
LPCOUNT,RCOUNT,RLIM,OP,NP,H_DIR,N_DIR,
N_HOP,NH,HOPS,HOPCOUNT,XG,YG,ZG,COG,R1,R2,R3,OPR,cycount,R4,R5,R6,cylim2,COUNT,SIT
ES,M
INTEGER, PARAMETER ::        COL=6,ROW=2592,LATSIZE=13824,
LATSIDE=24,MAX_HOP= 1000000
INTEGER, DIMENSION(COL,ROW)        :: NODE,SST
INTEGER, DIMENSION(ROW)              ::XC,YC,ZC,XOG,YOG,ZOG
INTEGER, DIMENSION(2,ROW)         :: XCT,YCT,ZCT
INTEGER, DIMENSION(3,ROW)              :: STT,STTNODE
INTEGER, DIMENSION(ROW)    ::IMAGE_X,IMAGE_Y,IMAGE_Z
REAL    THETA,DNOM,SEED,INSEED,TAU,JRATE1,TIME_A,
TIME_X,DELT1,r2t,r2tx,r2ty,r2tz,SEED1,P,JRATE2,
DELT2,T
 REAL, DIMENSION(ROW)                         :: x0,y0,z0,XD,YD,ZD


INOM= 1296
DNOM=INOM
SITES=1728  ! number of sites in the lattice
P=0.36  ! fraction of sites blocked
M=P*SITES
TAU = 1  !3E+9
T=0.5
        N_HOP=1
        HOPCOUNT=0
   RCOUNT=0
        RLIM= 30000
        INSEED= 0.942
        SEED = INSEED
        THETA=DNOM/LATSIZE
        COG = 1246 !158 !(LATSIZE+1)/2 1246        ! coordinates origin
        R1=450
        R2=2598
        R3=9872
   TIME_X=0
   TIME_A=0
   OP=0
   cycount=0
   R4=451
   R5=1974
   R6=6947


500  FORMAT(15I5)
510  FORMAT (I5,T10,I10,T30,E15.6,T54,E15.6,T76,E15.6, T98,  E15.6,T120,E15.6,T142,E15.6,T164)
```

```fortran
520  FORMAT (I5,T10,I10,T30,D15.6,T54,D15.6,T76,D15.6, T98,  D15.6,T120,D15.6,T142,D15.6)

   OPEN(100, FILE = 'RANDOM_NUMBER')
   OPEN(110, FILE = 'RANDOM_NUMBER2')
   OPEN(200, FILE = 'rand_numbers', POSITION= 'APPEND')
   OPEN(210, FILE = 'rand_numbers1', POSITION= 'APPEND')
   OPEN(211, FILE = 'rand_numbers2', POSITION= 'APPEND')
   OPEN(212, FILE = 'rand_numbers3', POSITION= 'APPEND')
   OPEN(213, FILE = 'rand_numbers4', POSITION= 'APPEND')
   OPEN(214, FILE = 'rand_numbers5', POSITION= 'APPEND')
        OPEN(900, FILE = 'ZSM5_structure_24')
        OPEN(910, FILE = 'results_12')
   OPEN(911, FILE = 'results_12a')
   OPEN(912, FILE = 'results_12b')
   OPEN(920, FILE = 'mean2displacement_12_a', POSITION='APPEND')
   OPEN(930, FILE = 'mean2displacement_12_b', POSITION='APPEND')
   OPEN(950, FILE = 'mean2displacement_12_c', POSITION='APPEND')
   OPEN(960, FILE = 'mean2displacement_12_d', POSITION='APPEND')
   OPEN(970, FILE = 'mean2displacement_12_e', POSITION='APPEND')
   OPEN(980, FILE = 'mean2displacement_12_f', POSITION='APPEND')
   OPEN(990, FILE = 'mean2displacement_12_g', POSITION='APPEND')
   OPEN(1000, FILE = 'mean2displacement_12_h', POSITION='APPEND')
   OPEN(1100, FILE = 'mean2displacement_12_i', POSITION='APPEND')
   OPEN(1200, FILE = 'mean2displacement_12_j', POSITION='APPEND')
   OPEN(1300, FILE = 'mean2displacement_12', POSITION='APPEND')

! read cubic lattice nodes and their neighbours
   READ(900,*) NODE

   DO J=1,COL
    DO I=1, ROW !DO I=1,LATSIZE
         SST(J,I) = 0 !SST(N_HOP,I)
   !PRINT*, J,I,SST(J,I)
         !WRITE(910,*) SST(J,I)
                END DO
     END DO

   DO J = 1,3
         DO I=1,ROW !DO I=1,LATSIZE
                 STT(J,I) = 0 !SST(N_HOP,I)
         END DO
         END DO

  ! random allocation of molecules in the lattice
   LPCOUNT =1
   RCOUNT = 0

   DO WHILE (LPCOUNT<=INOM)
   RCOUNT = RCOUNT + 1

    CALL RANDOM_POS(SEED)
    RAND = (1+INT(ROW*SEED))
    CALL ADJ_SITES(N,E,S,W,RAND,NODE,SST)

    LPSTART = 1
    LPEND =  ROW !LATSIZE

CALL MOL_ADD(LPSTART,LPEND,RAND,SST,LPCOUNT,W,E,S,N)

   END DO
```

```fortran
   DO I=1,ROW
     IF (SST(1,I)==1) THEN
     END IF
   END DO

! random blocking of sites in the lattice

   LPCOUNT = 1
   RCOUNT = 0

   DO WHILE (LPCOUNT<=(P*SITES))
    RCOUNT= RCOUNT+1

    CALL RANDOM_POS(SEED)

    RAND = (1+INT(ROW*SEED))

    LPSTART=1
    LPEND=ROW

CALL MOL_BLOCK (LPSTART,LPEND,RAND,SST,LPCOUNT,NODE)

END DO

   !DO J=1,1
     DO I=1,ROW
       IF (SST(1,I)==2) THEN
       END IF
     END DO

   DO I=1,ROW !DO I=1,LATSIZE

     IF ( SST(1,I)==1) THEN
     STT(2,I)=I  ! tag 4 hopping molecule

     END IF
     STT(1,I) = STT(2,I)    ! initial state
     STTNODE(1,I)=NODE(1,I)
     STTNODE(2,I)=NODE(1,I) ! current which becomes previous position after a hop
     STTNODE(3,I)=NODE(1,I) ! new hop position
     SST(2,I)=SST(1,I)
     !PRINT*, I,SST(1,I),SST(2,I)
     !WRITE(910,*) I,NODE(1,I),SST(1,I), SST(2,I)
         END DO

   DO I=1,ROW

       CALL ADJ_SITES(N,E,S,W,I,NODE,SST)

     IF (SST(1,I)==1) THEN
       IF (S==0.AND.N==0) THEN
        !PRINT*, I,SST(1,W),SST(1,E)
       ELSE
        !PRINT*, I,SST(1,W),SST(1,E),SST(1,S),SST(1,N)
       END IF

     END IF

   END DO
```

```fortran
! establishing origin of the coordinate system
                CALL xyz_cordinates(N_HOP,STTNODE,XC,YC,ZC)

                XG = XC(COG)
                YG = YC(COG)
                ZG = ZC(COG)
                !PRINT*, M
                PRINT*, 247,N_HOP,STTNODE(1,COG),XC(COG),YC(COG),ZC(COG)

           DO I=1,ROW
                STTNODE(3,I)=0  ! reset new hop position
           END DO

! random search of molecule 2 hop
   HOPMOLECULE: DO WHILE (N_HOP<=MAX_HOP-1)

   RCOUNT = RCOUNT+1
   HOPCOUNT=HOPCOUNT+1

CALL RANDOM_POS2(HOPCOUNT,R1,R2,R3,ROW,RAND,cycount,N_HOP)

    IF (MOD(HOPCOUNT,RLIM)==0) THEN
     N_DIR = ROW
     ! initiate the seed from the current time
     CALL HOP_DIR4(SEED,N_DIR,RAND)
     RCOUNT=0
     !PRINT*, SEED, RAND
    END IF

! REPLACE J WITH A NUMBER OF AN OCCUPIED SITE eg 45,111,265,323 etc
     J = RAND  ! ( memory access between 0-LATSIZE)

    IF ( STT(2,J)/=0 ) THEN

     CALL ADJ_SITES(N,E,S,W,J,NODE,SST)
     !random serach of hop direction
     !using a different random generation routine

     HOPCOUNT=HOPCOUNT+1

     IF (S==0.AND.N==0) THEN
       N_DIR=2
     ELSE
       N_DIR=4
     END IF

CALL RANDOM_POS2(HOPCOUNT,R1,R2,R3,N_DIR,RAND,cycount, N_HOP)

     H_DIR = RAND

     CALL RANDOM_POS(SEED)
     JRATE1 = 1/(TAU*INOM)
     DELT1=-(JRATE1)*LOG(SEED)
     JRATE2 = 1/(TAU*INOM*T) ! T=FOR BLOCKED SITE
     DELT2=-(JRATE2)*LOG(SEED)

    IF(N_HOP>=10001) THEN
     IF (S==0.AND.N==0) THEN
       IF (SST(2,W)==2.OR.SST(2,E)==2) THEN
```

```fortran
      TIME_X = TIME_X + DELT2
      ELSE
      TIME_X = TIME_X + DELT1
      END IF
     ELSE IF (W/=0.AND.E/=0.AND.S/=0.AND.N/=0) THEN
      IF(SST(2,W)==2.OR.SST(2,E)==2.OR.SST(2,S)==2.OR.SST(2,N)==2) THEN
      TIME_X = TIME_X + DELT2
      ELSE
      TIME_X = TIME_X + DELT1
      END IF
     END IF
    END IF

    IF (RCOUNT <=10) THEN
    END IF

    ! determination of the site a molecule hops to
    ! molecule bounces back if hop site is occupied

    !W= NODE(3,J)!SW/NW
    !E= NODE(4,J)!SE/NE
    !S= NODE(5,J)!D
    !N= NODE(6,J)!U

      IF                               (MOD(NODE(2,J),2)==1.AND.H_DIR==1.AND.W
/=0.AND.SST(2,W)==0.AND.STT(2,W)==0)THEN
        DO I=1,ROW
         IF (STT(2,I)/=0) THEN ! new occupancy set to previous
          STT(3,I) = STT(2,I)
         END IF
        END DO

      SST(2,W) = 1
      SST(2,J) = 0
      OP = STT(2,J)
      OPR = NODE(1,J)
      STT(3,W) =  OP
      STT(3,J) = 0
      N_HOP = N_HOP+1          ! only successful hops counted
      NP = NODE(3,J)
      STTNODE(3,OP)= NP

      !PRINT*, N_HOP,H_DIR,J,NP, OP,STTNODE(3,OP)

      ELSE                               IF(MOD(NODE(2,J),2)==1.AND.H_DIR==2.AND.E
/=0.AND.SST(2,E)==0.AND.STT(2,E)==0)THEN

         DO I=1,ROW
          IF (STT(2,I)/=0) THEN ! new occupancy set to previous
           STT(3,I) = STT(2,I)
          END IF
         END DO

      SST(2,E) = 1
      SST(2,J) = 0
      OP = STT(2,J)
      OPR = NODE(1,J) !ACTUAL POSITION IN ZSM5 GRID
      STT(3,E) = OP
      STT(3,J) = 0
      NP = NODE(4,J)
```

```fortran
              N_HOP = N_HOP+1
              STTNODE(3,OP)= NP

             !PRINT*, N_HOP,H_DIR,J,NP, OP,STTNODE(3,OP)

             ELSE                              IF(MOD(NODE(2,J),2)==1.AND.H_DIR==3.AND.S
        /=0.AND.SST(2,S)==0.AND.STT(2,S)==0)THEN

                  DO I=1,ROW
                   IF (STT(2,I)/=0) THEN ! new occupancy set to previous
                    STT(3,I) = STT(2,I)
                   END IF
                   END DO

              SST(2,S) = 1
              SST(2,J) = 0
              OP = STT(2,J)
              OPR = NODE(1,J)
              STT(3,S) = OP
              STT(3,J) = 0
              NP = NODE(5,J)
              N_HOP = N_HOP+1
              STTNODE(3,OP)= NP
              !PRINT*, N_HOP,H_DIR,J,NP, OP ,STTNODE(3,OP)

             ELSE                              IF(MOD(NODE(2,J),2)==1.AND.H_DIR==4.AND.N
        /=0.AND.SST(2,N)==0.AND.STT(2,N)==0)THEN
                  DO I=1,ROW
                   IF (STT(2,I)/=0) THEN ! new occupancy set to previous
                    STT(3,I) = STT(2,I)
                   END IF
                   END DO

              SST(2,N) = 1
              SST(2,J) = 0
              OP = STT(2,J)
              OPR = NODE(1,J)
              STT(3,N) = OP
              STT(3,J) = 0
              NP = NODE(6,J)
              N_HOP = N_HOP+1
              STTNODE(3,OP)= NP
              !PRINT*, N_HOP,H_DIR,J,NP, OP,STTNODE(3,OP)

            ELSE IF(MOD(NODE(2,J),2)==0.AND.H_DIR==1.AND.W/=0
         .AND.SST(2,W)==0.AND.STT(2,W)==0)THEN

                  DO I=1,ROW
                   IF (STT(2,I)/=0) THEN ! new occupancy set to previous
                    STT(3,I) = STT(2,I)
                   END IF
                   END DO

              SST(2,W) = 1
              SST(2,J) = 0
              OP = STT(2,J)
              OPR = NODE(1,J)
              STT(3,W) =  OP
              STT(3,J) = 0
              NP = NODE(3,J)
```

```
          N_HOP = N_HOP+1
          STTNODE(3,OP)= NP

          ELSE                                    IF(MOD(NODE(2,J),2)==0.AND.H_DIR==2.AND.E
/=0.AND.SST(2,E)==0.AND.STT(2,E)==0)THEN
          !ELSE IF(H_DIR==6.AND.U /=0.AND.STT(2,U)==0)THEN
          !PRINT*, N_HOP,H_DIR,J,SST(2,J),SST(2,E)
            DO I=1,ROW
             IF (STT(2,I)/=0) THEN ! new occupancy set to previous
              STT(3,I) = STT(2,I)
             END IF
            END DO

          SST(2,E) = 1
          SST(2,J) = 0
          OP = STT(2,J)
          OPR = NODE(1,J)
          STT(3,E) =  OP
          STT(3,J) = 0
          NP = NODE(4,J)
          N_HOP = N_HOP+1
          STTNODE(3,OP)= NP
          !PRINT*, N_HOP,H_DIR,J,NP, OP,STTNODE(3,OP)

          END IF


          ! reset values of boundary overlap
          DO I=1,ROW
           IMAGE_X(I)=0
           IMAGE_Y(I)=0
           IMAGE_Z(I)=0
          END DO

IF ( OP/=0) THEN  !  accounts 4 high occupancy when STT=1 but cannot hop

     NEWPOSITION: DO I=1,ROW

IF (STT(1,I)/=0 .AND. STT(2,I)/=0 .AND. STT(3,I)==0) THEN
! particle did hop

          ! search new position of particle
          DO J=1,ROW
           IF (STT(3,J)==OP) THEN
           STTNODE(3,OP)= NP
           !PRINT*, OP,J
           END IF
          END DO
         ELSE IF (STT(2,I)/=0 .AND. STT(2,I)==STT(3,I)) THEN

          NH = STT(3,I)

          DO J=1,ROW
           IF (STT(3,J)==NH) THEN
           STTNODE(3,NH)= NODE(1,J)
! search 4 particles which did not hop
           END IF
          END DO

          END IF
```

! flag whenever a molecule passes the boundary

```
IF(MOD(STTNODE(2,OP),LATSIDE)==1 .AND. MOD(STTNODE(3,OP),LATSIDE)==0) THEN
        IMAGE_X(OP)=-1
ELSE IF(MOD(STTNODE(2,OP),LATSIDE)==0 .AND. MOD(STTNODE(3,OP),LATSIDE)==1) THEN
        IMAGE_X(OP)=1

ELSE IF (STTNODE(3,OP)-STTNODE(2,OP)==1.AND.MOD(STTNODE(2,OP),LATSIDE)==0 &
.AND.MOD(STTNODE(3,OP),LATSIDE)==1) THEN
        IMAGE_Y(OP)=1

ELSE              IF              (STTNODE(3,OP)-STTNODE(2,OP)==(LATSIDE*2-
1).AND.MOD(STTNODE(2,OP),LATSIDE)==1 &
.AND.MOD(STTNODE(3,OP),LATSIDE)==0) THEN
        IMAGE_Y(OP)=1

ELSE IF (STTNODE(2,OP)-STTNODE(3,OP)==1.AND.MOD(STTNODE(2,OP),LATSIDE)==1 &
.AND.MOD(STTNODE(3,OP),LATSIDE)==0) THEN
        IMAGE_Y(OP)=-1

ELSE              IF              (STTNODE(2,OP)-STTNODE(3,OP)==(LATSIDE*2-
1).AND.MOD(STTNODE(2,OP),LATSIDE)==0 &
.AND.MOD(STTNODE(3,OP),LATSIDE)==1) THEN
        IMAGE_Y(OP)=-1

ELSE       IF       (STTNODE(2,OP)-STTNODE(3,OP)==(LATSIDE**2-(LATSIDE-1))       &
.AND.MOD(STTNODE(2,OP),LATSIDE**2)<(LATSIDE**2)&
.AND.MOD(STTNODE(2,OP),LATSIDE**2)>(LATSIDE**2-
.AND.MOD(STTNODE(3,OP),LATSIDE**2)>0 &
.AND.MOD(STTNODE(3,OP),LATSIDE**2)<=LATSIDE) THEN

        IMAGE_Y(OP)=1

ELSE IF (STTNODE(2,OP)-STTNODE(3,OP)==(LATSIDE**2-(LATSIDE+1)) &
.AND.MOD(STTNODE(2,OP),LATSIDE**2)<(LATSIDE**2)&
.AND.MOD(STTNODE(2,OP),LATSIDE**2)>(LATSIDE**2-(LATSIDE-1)) &
.AND.MOD(STTNODE(3,OP),LATSIDE**2)>0 &
.AND.MOD(STTNODE(3,OP),LATSIDE**2)<=LATSIDE) THEN
        IMAGE_Y(OP)=1

ELSE IF (STTNODE(3,OP)-STTNODE(2,OP)==(LATSIDE**2-(LATSIDE-1)) &
.AND.MOD(STTNODE(3,OP),LATSIDE**2)<(LATSIDE**2)&
.AND.MOD(STTNODE(3,OP),LATSIDE**2)>(LATSIDE**2-(LATSIDE-1)) &
.AND.MOD(STTNODE(2,OP),LATSIDE**2)>0 &
.AND.MOD(STTNODE(2,OP),LATSIDE**2)<=LATSIDE) THEN
        IMAGE_Y(OP)=-1

ELSE       IF       (STTNODE(3,OP)-STTNODE(2,OP)==(LATSIDE**2-(LATSIDE+1))       &
.AND.MOD(STTNODE(3,OP),LATSIDE**2)<(LATSIDE**2)&
.AND.MOD(STTNODE(3,OP),LATSIDE**2)>(LATSIDE**2-(LATSIDE-1)) &
.AND.MOD(STTNODE(2,OP),LATSIDE**2)>0 &
.AND.MOD(STTNODE(2,OP),LATSIDE**2)<=LATSIDE) THEN
        IMAGE_Y(OP)=-1

ELSE IF (STTNODE(2,OP)-STTNODE(3,OP)==(LATSIDE**2-(LATSIDE-2))&
.AND.MOD(STTNODE(2,OP),LATSIDE**2)==0 &
.AND.MOD(STTNODE(3,OP),LATSIDE**2)<=LATSIDE) THEN
        IMAGE_Y(OP)=-1

ELSE IF (STTNODE(3,OP)-STTNODE(2,OP)==(LATSIDE**2-(LATSIDE-2))&
```

```
            .AND.MOD(STTNODE(3,OP),LATSIDE**2)==0 &
            .AND.MOD(STTNODE(2,OP),LATSIDE**2)<=LATSIDE) THEN
                    IMAGE_Y(OP)=1


      ELSE IF (STTNODE(3,OP)<=(LATSIDE**2) .AND.
      STTNODE(2,OP)>(LATSIZE-(LATSIDE**2))) THEN
                    IMAGE_Z(OP)= 1


      ELSE   IF   (STTNODE(3,OP)>(LATSIZE-(LATSIDE**2))   .AND.   STTNODE(2,OP)<=(LATSIDE**2))
      THEN
                    IMAGE_Z(OP)=-1
                  END IF



      END DO NEWPOSITION

      ! determining the mean2 displacement
            CALL xyz_cordinates(N_HOP,STTNODE,XC,YC,ZC )

            XYZ_DIS: DO I=1,ROW

               IF (N_HOP==10000) THEN

                 XCT(1,I) = 0!XC(I)-XG
                 YCT(1,I) = 0!YC(I)-YG
                 ZCT(1,I) = 0!ZC(I)-ZG
                 XCT(2,I) = 0!XC(I)-XG
                 YCT(2,I) = 0!YC(I)-YG
                 ZCT(2,I) = 0!ZC(I)-ZG
                END IF

                IF(N_HOP>=10001) THEN

                 XOG(I) = XC(I)-XG
                 YOG(I) = YC(I)-YG
                 ZOG(I) = ZC(I)-ZG

      ! coordinates value at time = 0
                IF(N_HOP==10001) THEN
                  x0(I) = XOG(I)
                  y0(I) = YOG(I)
                  z0(I) = ZOG(I)
                  XD(I)= 0!XOG(I)
                  YD(I)= 0!YOG(I)
                  ZD(I)= 0!ZOG(I)
                  END IF

                IF ( MOD(N_HOP,2)/=0) THEN
                  XCT(1,I) = XOG(I)
                  YCT(1,I) = YOG(I)
                  ZCT(1,I) = ZOG(I)
                 ELSE IF(MOD(N_HOP,2)==0) THEN
                  XCT(2,I) = XOG(I)
                  YCT(2,I) = YOG(I)
                  ZCT(2,I) = ZOG(I)
                   END IF

      ! molecule did not hop
            IF (STT(2,I)/=0 .AND. STT(2,I)==STT(3,I)) THEN
            XD(I) = XD(I)
```

```
        YD(I) = YD(I)
        ZD(I) = ZD(I)


! molecule hopped over the boundary to the east(+)
        ELSE IF(IMAGE_X(I)==1)THEN
        IF (N_HOP==10001) THEN
          XD(I)=x0(I)
        ELSE
        XD(I) = XD(I)+1
        END IF


! molecule hopped over boundaries to the west(-)
        ELSE IF(IMAGE_X(I)==-1)THEN
        IF (N_HOP==10001) THEN
          XD(I)=x0(I)
        ELSE
        XD(I) = XD(I)-1
        END IF


! molecule did not overlap boundary
        ELSE IF(IMAGE_X(I)==0)THEN
        IF (XCT(2,I)==XCT(1,I)) THEN
        XD(I)=XD(I)


! swap current positions
        ELSE IF ( MOD(N_HOP,2)/=0) THEN
        XD(I) = XD(I)+(XCT(1,I)-XCT(2,I))
        ELSE IF(MOD(N_HOP,2)==0) THEN
        XD(I) = XD(I)+(XCT(2,I)-XCT(1,I))
        END IF
        END IF


! molecule hopped over the boundary to the north(+)
        IF(IMAGE_Y(I)==1)THEN
        IF (N_HOP==10001) THEN
          YD(I)=y0(I)
        ELSE
        YD(I) = YD(I)+1
        END IF


! molecule hopped over boundaries to the south(-)
        ELSE IF(IMAGE_Y(I)==-1)THEN
        IF (N_HOP==10001) THEN
          YD(I)=y0(I)
        ELSE
        YD(I) = YD(I)-1
        END IF


! molecule did not overlap boundary
        ELSE IF(IMAGE_Y(I)==0)THEN
        IF (YCT(2,I)==YCT(1,I)) THEN
         YD(I)=YD(I)


! swap current positions
        ELSE IF ( MOD(N_HOP,2)/=0) THEN
        YD(I) = YD(I)+(YCT(1,I)-YCT(2,I))
        ELSE IF(MOD(N_HOP,2)==0) THEN
         YD(I) = YD(I)+(YCT(2,I)-YCT(1,I))
        END IF
        END IF
```

```fortran
! molecule hopped over the boundary upwards(+)
        IF(IMAGE_Z(I)==1)THEN
        !IF (N_HOP==MAX_HOP/3) THEN
        IF (N_HOP==10001) THEN
          ZD(I)=z0(I)
        ELSE
        ZD(I) = ZD(I)+1
        END IF

! molecule hopped over the boundary downwards(-)
        ELSE IF(IMAGE_Z(I)==-1)THEN
        !IF (N_HOP==MAX_HOP/3) THEN
        IF (N_HOP==10001) THEN
          ZD(I)=z0(I)
        ELSE
         ZD(I) = ZD(I)-1
        END IF
        ! molecule did not overlap boundary
        ELSE IF(IMAGE_Z(I)==0)THEN
        IF (ZCT(2,I)==ZCT(1,I)) THEN
         ZD(I)=ZD(I)

         ! swap current positions
        ELSE IF ( MOD(N_HOP,2)/=0) THEN
        ZD(I) = ZD(I)+(ZCT(1,I)-ZCT(2,I))

        ELSE IF(MOD(N_HOP,2)==0) THEN
         ZD(I) = ZD(I)+(ZCT(2,I)-ZCT(1,I))
        END IF
        END IF

        END IF

      END DO XYZ_DIS

      IF(N_HOP>=10001) THEN
       r2tx=0
       r2ty=0
       r2tz=0
       r2t=0

      DISPLACEMENT: DO I =1,ROW
       IF (STTNODE(3,I)/=0) THEN
        r2tx= r2tx + (XD(I)-x0(I))**2
        r2ty= r2ty + (YD(I)-y0(I))**2
        r2tz= r2tz + (ZD(I)-z0(I))**2
        r2t= r2t+(XD(I)-x0(I))**2+(YD(I)-y0(I))**2+(ZD(I)-z0(I))**2
       END IF
      END DO DISPLACEMENT

      IF(N_HOP>=10001) THEN
      IF (MOD(N_HOP,10000)==0) THEN
WRITE(1300,510)INOM,N_HOP,TIME_X,TIME_A,r2tx,r2ty,r2tz,r2t!,STTNODE(2,OP)
       PRINT*, N_HOP,r2tx,r2ty,r2tz,r2t!,H_DIR
      END IF
      END IF

IF (N_HOP<=MAX_HOP/10) THEN          !IF (N_HOP<=10000000) THEN !
      IF (MOD(N_HOP,1000)==0) THEN
```

```fortran
WRITE(920,510) INOM,N_HOP,TIME_X,TIME_A,r2tx,r2ty,r2tz,r2t
     END IF
     END IF

IF ((N_HOP.LE.(2*MAX_HOP/10)).AND.(N_HOP.GT.(MAX_HOP/10))) THEN
     IF (MOD(N_HOP,1000)==0) THEN
WRITE(930,510) INOM,N_HOP,TIME_X,TIME_A,r2tx,r2ty,r2tz,r2t
     END IF
     END IF

IF((N_HOP.LE.(3*MAX_HOP/10)).AND.(N_HOP.GT.(2*MAX_HOP/10))) THEN
     IF (MOD(N_HOP,1000)==0) THEN
WRITE(950,510) INOM,N_HOP,TIME_X,TIME_A,r2tx,r2ty,r2tz,r2t
     END IF
     END IF

IF((N_HOP.LE.(4*MAX_HOP/10)).AND.(N_HOP.GT.(3*MAX_HOP/10))) THEN
     IF (MOD(N_HOP,1000)==0) THEN
WRITE(960,510) INOM,N_HOP,TIME_X,TIME_A,r2tx,r2ty,r2tz,r2t
     END IF
     END IF

IF((N_HOP.LE.(5*MAX_HOP/10)).AND.(N_HOP.GT.(4*MAX_HOP/10))) THEN
     IF (MOD(N_HOP,1000)==0) THEN
WRITE(970,510) INOM,N_HOP,TIME_X,TIME_A,r2tx,r2ty,r2tz,r2t
     END IF
     END IF

IF((N_HOP.LE.(7*MAX_HOP/10)).AND.(N_HOP.GT.(6*MAX_HOP/10))) THEN
     IF (MOD(N_HOP,1000)==0) THEN
WRITE(990,510) INOM,N_HOP,TIME_X,TIME_A,r2tx,r2ty,r2tz,r2t
     END IF
     END IF

IF((N_HOP.LE.(8*MAX_HOP/10)).AND.(N_HOP.GT.(7*MAX_HOP/10))) THEN
     IF (MOD(N_HOP,1000)==0) THEN
WRITE(1000,510) INOM,N_HOP,TIME_X,TIME_A,r2tx,r2ty,r2tz,r2t
     END IF
     END IF

IF((N_HOP.LE.(9*MAX_HOP/10)).AND.(N_HOP.GT.(8*MAX_HOP/10))) THEN
     IF (MOD(N_HOP,1000)==0) THEN
WRITE(1100,510) INOM,N_HOP,TIME_X,TIME_A,r2tx,r2ty,r2tz,r2t
     END IF
     END IF

IF((N_HOP.LE.(10*MAX_HOP/10)).AND.(N_HOP.GT.(9*MAX_HOP/10))) THEN
     IF (MOD(N_HOP,1000)==0) THEN
WRITE(1200,510) INOM,N_HOP,TIME_X,TIME_A,r2tx,r2ty,r2tz,r2t
     END IF
     END IF

     END IF

     ! swap particle's position before next hop attempt
     SWAP: DO I =1,ROW
      STT(2,I)=STT(3,I)
      STTNODE(2,I)=STTNODE(3,I)
     END DO SWAP
```

```fortran
      OP = 0 ! reset value of hopping particle
    END IF

  END IF

  CALL RANDOM_POS(SEED)
  JRATE1 = 1/(TAU*INOM)
  DELT1=-(JRATE1)*LOG(SEED)
  IF(N_HOP>=10001) THEN
    TIME_A = TIME_A + DELT1  ! time incremented 4 all hops
  END IF

  IF (N_HOP==MAX_HOP/10) THEN
    CLOSE (920)
  END IF

  IF (N_HOP==2*MAX_HOP/10) THEN
    CLOSE (930)
  END IF

  IF (N_HOP==3*MAX_HOP/10) THEN
    CLOSE (950)
  END IF

  IF (N_HOP==4*MAX_HOP/10) THEN
    CLOSE (960)
  END IF

  IF (N_HOP==5*MAX_HOP/10) THEN
    CLOSE (970)
  END IF

  IF (N_HOP==7*MAX_HOP/10) THEN
    CLOSE (990)
  END IF

  IF (N_HOP==8*MAX_HOP/10) THEN
    CLOSE (1000)
  END IF

  IF (N_HOP==9*MAX_HOP/10) THEN
    CLOSE (1100)
  END IF

  IF (N_HOP==10*MAX_HOP/10) THEN
    CLOSE (1200)
  END IF

  END DO HOPMOLECULE

 PRINT*, TIME_X,TIME_A, HOPCOUNT

 CONTAINS

SUBROUTINE RANDOM_POS (X)

  INTEGER                   IX, K,J,M
  REAL                         X,IRAND,RM

      DATA K,J,M,RM / 5702,3612,566927,566927.0/
```

```
              IX=INT(X*RM)
              IRAND=MOD(J*IX+K,M)
              X=(REAL(IRAND)+0.5)/RM

END SUBROUTINE RANDOM_POS

SUBROUTINE RANDOM_POS2 (dcount,i1, i2, i3,d_dir,hd,cycount,nhop)
IMPLICIT NONE
INTEGER          :: b,i1, i2, i3, i,dcount,cylim,d_dir,hd,cycount,nhop
INTEGER, PARAMETER :: dp = SELECTED_REAL_KIND(14, 60)
INTEGER, SAVE :: s1 = 1234, s2 = -4567, s3 = 7890
REAL (dp)                :: random_numb


cylim=3E+7
  IF(dcount==cylim)THEN
    s1=450
    s2=2598
    s3=9872
    dcount=0
    cycount=cycount+1
    PRINT*, 'GENERATOR RESEEDED',cycount

    WRITE(100,*) 'GENERATOR RESEEDED',cycount,nhop

  END IF

  IF (IAND(s1,-2) == 0) s1 = i1 - 1023
  IF (IAND(s2,-8) == 0) s2 = i2 - 1023
  IF (IAND(s3,-16) == 0) s3 = i3 - 1023

  b  = ISHFT( IEOR( ISHFT(s1,13), s1), -19)
  s1 = IEOR( ISHFT( IAND(s1,-2), 12), b)
  b  = ISHFT( IEOR( ISHFT(s2,2), s2), -25)
  s2 = IEOR( ISHFT( IAND(s2,-8), 4), b)
  b  = ISHFT( IEOR( ISHFT(s3,3), s3), -11)
  s3 = IEOR( ISHFT( IAND(s3,-16), 17), b)
  random_numb = IEOR( IEOR(s1,s2), s3) * 2.3283064365E-10_dp + 0.5_dp

  hd = 1+INT(d_dir*random_numb)

END SUBROUTINE RANDOM_POS2


SUBROUTINE MOL_ADD (LS,LE,RD,ST,LC,W,E,S,N)

INTEGER                                    LS,LE,RD,LC,W,E,S,N
INTEGER, DIMENSION(ROW)     :: R
INTEGER, DIMENSION(COL,ROW) :: ST


!        random placement of molecules in lattice
         DO I=LS,LE
           R(I) = RD
! occupied sites cannot be recounted
 IF ( ST(1,I)==0 .AND.I== R(I)) THEN
      IF (N==0.AND.S==0) THEN
       IF (ST(1,W)/=2.AND.ST(1,E)/=2) THEN
                ST(1,I) = 1
                  LC = LC +1
```

```
          END IF
        ELSE IF (ST(1,W)/=2.AND.ST(1,E)/=2.AND.ST(1,N)/=2.AND.ST(1,S)/=2) THEN
          ST(1,I) = 1
                LC = LC +1
        END IF
      END IF

          END DO

END SUBROUTINE MOL_ADD

SUBROUTINE xyz_cordinates(DHOP,DNODE,CARTX,CARTY,CARTZ)

INTEGER                                        I,DI,IR,LATSDX,LATSDY,DHOP
INTEGER, DIMENSION(ROW)    :: X,Y,YR,Z
INTEGER, DIMENSION(ROW),INTENT(OUT)::CARTX,CARTY,CARTZ
INTEGER, DIMENSION(3,ROW),INTENT(IN)         :: DNODE

LATSDX= LATSIDE
LATSDY= LATSIDE

! determine the cartesian coordinates of the nodes
        DO I=1,ROW

        X(I)=MOD(DNODE(3,I),LATSDX*LATSDY)
      X(I)=MOD(X(I),LATSDX)
        IF(X(I).NE.0) THEN
         CARTX(I)=X(I)
         ELSE
          CARTX(I)=LATSDX
         ENDIF

         Y(I)=MOD(DNODE(3,I),LATSDX*LATSDY)
         YR(I)=Y(I)
         Y(I)=INT(YR(I)/LATSDX)
         IF(MOD(DNODE(3,I),LATSDX)==0.AND.MOD(DNODE(3,I),LATSDX*LATSDY)/=0)    THEN
! edge 2
         CARTY(I)=Y(I)
         ELSE IF(MOD(DNODE(3,I),LATSDX*LATSDY).NE.0) THEN
         CARTY(I)=Y(I)+1
         ELSE IF(MOD(DNODE(3,I),LATSDX*LATSDY)==0) THEN
          CARTY(I)=LATSDY
         ELSE
          CARTY(I)=Y(I)
         ENDIF

     IR=DNODE(3,I)
        Z(I)=INT(IR/(LATSDX*LATSDY))
        CARTZ(I)=Z(I)
        IF(MOD(DNODE(3,I),LATSDX*LATSDY).NE.0) THEN
     CARTZ(I)=CARTZ(I)+1
    ENDIF

    END DO

END SUBROUTINE xyz_cordinates

SUBROUTINE ADJ_SITES(NO,EA,SO,WE,J,DNODE,ST)

INTEGER                                        I,J,K,NO,EA,SO,WE
```

```fortran
INTEGER, DIMENSION(COL,ROW)                          :: ST
INTEGER, DIMENSION(COL,ROW),INTENT(IN) :: DNODE

        ! search for site location in ZSM5 structure array

        LOOP1:          DO I=1,ROW
            IF (DNODE(3,J)==DNODE(1,I)) THEN
                            WE = I
                            ST(3,I)=1
        IF (ST(3,I) ==1) EXIT LOOP1      ! 2 map oncce to array memory
                ELSE
                WE = 0
                END IF

        END DO LOOP1

        LOOP2:          DO I=1,ROW
            IF ( DNODE(4,J)==DNODE(1,I)) THEN
                            EA = I
                            ST(4,I)=1
        IF (ST(4,I) ==1) EXIT LOOP2 ! 2 map once to array memory
                            ELSE
                            EA = 0
                            END IF

        END DO LOOP2

        LOOP3:          DO I=1,ROW
            IF ( DNODE(5,J)==DNODE(1,I)) THEN
                            SO = I
                            ST(5,I)=1
        IF (ST(5,I) ==1) EXIT LOOP3      ! 2 map once to array memory
                            ELSE
                            SO = 0
                            END IF

        END DO LOOP3

        LOOP4:          DO I=1,ROW
            IF ( DNODE(6,J)==DNODE(1,I)) THEN
                            NO = I
                            ST(6,I)=1
        IF (ST(6,I) ==1) EXIT LOOP4      ! 2 map once to array memory
                            ELSE
                            NO = 0
                            END IF

        END DO LOOP4
    END SUBROUTINE ADJ_SITES

SUBROUTINE RANDOM_POS3 (i1, i2, i3,d_dir,hd)
IMPLICIT NONE
INTEGER         :: b,i1, i2, i3, i,dcount,cylim,d_dir,hd,cycount,nhop
INTEGER, PARAMETER :: dp = SELECTED_REAL_KIND(14, 60)
INTEGER, SAVE :: s1 = 2345, s2 = -6789, s3 = 1035
REAL (dp) :: random_numb


        cylim=3E+7
```

```fortran
        IF (IAND(s1,-2) == 0) s1 = i1 - 1023
        IF (IAND(s2,-8) == 0) s2 = i2 - 1023
        IF (IAND(s3,-16) == 0) s3 = i3 - 1023

        b  = ISHFT( IEOR( ISHFT(s1,13), s1), -19)
        s1 = IEOR( ISHFT( IAND(s1,-2), 12), b)
        b  = ISHFT( IEOR( ISHFT(s2,2), s2), -25)
        s2 = IEOR( ISHFT( IAND(s2,-8), 4), b)
        b  = ISHFT( IEOR( ISHFT(s3,3), s3), -11)
        s3 = IEOR( ISHFT( IAND(s3,-16), 17), b)
        random_numb = IEOR( IEOR(s1,s2), s3) * 2.3283064365E-10_dp + 0.5_dp

   hd = 1+INT(d_dir*random_numb)
   !PRINT*, hd,cycount

        END SUBROUTINE RANDOM_POS3

SUBROUTINE MOL_BLOCK (LS,LE,RD,ST,LC,DNODE)

INTEGER                                     LS,LE,RD,LC,ND
INTEGER, DIMENSION(ROW)      :: R
INTEGER, DIMENSION(COL,ROW) :: ST
INTEGER, DIMENSION(COL,ROW),INTENT(IN) :: DNODE

!random placement of molecules in lattice
        DO I=LS,LE
          R(I) = RD
! occupied sites cannot be recounted
     IF ( ST(1,I)==0 .AND.I== R(I)) THEN
           ST(1,I) = 2
                 LC = LC +1

     END IF
         END DO
        END SUBROUTINE MOL_BLOCK

 END PROGRAM MC_CUBIC_DSELF


! PROGRAM HOP_DIR4
  SUBROUTINE HOP_DIR4 (SEED,D_DIR,RAND4)

INTEGER                           COUNT,INCR,D_DIR,RAND4
INTEGER, DIMENSION(1)         :: SEED1
REAL                          SEED

INCR=1

OPEN(940, FILE = 'hop_numbers', POSITION= 'APPEND')

CALL SYSTEM_CLOCK(COUNT)
        SEED1 = COUNT
        CALL RANDOM_SEED( PUT = SEED1)
        RAND4= 1+INT(D_DIR*SEED)

!WRITE(940,*) RAND4
!PRINT*, RAND4
        INCR =INCR+1
  END SUBROUTINE HOP_DIR4
```